Adaptive Optics for Small Aperture Telescopes

Author:
Cegarra Polo, Manuel

Publication Date:
2015

DOI:
https://doi.org/10.26190/unsworks/18564

Adaptive Optics for Small Aperture Telescopes

Manuel Cegarra Polo

A thesis in fulfilment of the requirements for the degree of
Doctor of Philosophy

School of Engineering and Information Technology
University of New South Wales
Canberra

February 16, 2015

PLEASE TYPE

THE UNIVERSITY OF NEW SOUTH WALES
Thesis/Dissertation Sheet

Surname or Family name: **Cegarra Polo**

First name: **Manuel** Other name/s:

Abbreviation for degree as given in the University calendar: **PhD**

School: **School of Engineering and Information Technology** Faculty: **UNSW Canberra**

Title: **Adaptive Optics for Small Aperture Telescopes**

Abstract 350 words maximum: (PLEASE TYPE)

Adaptive Optics (AO) is one of the techniques to reduce aberrations caused by atmosphere turbulence in the light coming from objects above this layer that reaches ground based optical telescopes. It was proposed 62 years ago, and since then it has undergone a fast evolution due to the technical developments in mechanics, optics and electronics. Due to these advances and the efforts of the research community, AO nowadays is widely used in big and moderate size telescopes and it has become an essential instrument in this telescope segment.

The research for its use in small aperture telescopes has been limited for different factors: it is an expensive technique; small aperture involves less gathered light that could reduce AO performance; and also low altitudes where usually these telescopes are located result in severe aberrations. This research has been focused in the investigation of new techniques and procedures that facilitate the engineering of an AO system for small aperture telescopes.

For this purpose an AO testbed has been developed, which includes a portable opto-mechanical platform adapted specifically for its use in small aperture telescopes, which has been tested in laboratory and assessed with on-sky experiments.

In this research, an original AO real time processing control architecture has been defined, that can be fully implemented in a low cost standalone Field Programmable Gate Array (FPGA) device, unlike standard AO configurations, which typically rely in complex distributed hardware architectures which make the system more expensive and less portable.

The lack of gathered light inherent to small aperture telescopes constitutes a severe limitation for an AO system. Hence is crucial to develop optimized image processing algorithms that balance this drawback. Here a novel fast implementation of a centroiding algorithm has been accomplished, adapted to severe low light conditions, and from this a closed loop AO system has been demonstrated.

There is wide potential demand in the scientific and amateur astronomy community in this field, and the innovations and engineering concepts introduced here constitute a valid and proven AO system applied for small aperture telescopes.

ORIGINALITY STATEMENT

'I hereby declare that this submission is my own work and to the best of my knowledge it contains no materials previously published or written by another person, or substantial proportions of material which have been accepted for the award of any other degree or diploma at UNSW or any other educational institution, except where due acknowledgement is made in the thesis. Any contribution made to the research by others, with whom I have worked at UNSW or elsewhere, is explicitly acknowledged in the thesis. I also declare that the intellectual content of this thesis is the product of my own work, except to the extent that assistance from others in the project's design and conception or in style, presentation and linguistic expression is acknowledged.'

Signed ....

Date 26-11-2015

COPYRIGHT STATEMENT

'I hereby grant the University of New South Wales or its agents the right to archive and to make available my thesis or dissertation in whole or part in the University libraries in all forms of media, now or here after known, subject to the provisions of the Copyright Act 1968. I retain all proprietary rights, such as patent rights. I also retain the right to use in future works (such as articles or books) all or part of this thesis or dissertation.

I also authorise University Microfilms to use the 350 word abstract of my thesis in Dissertation Abstract International (this is applicable to doctoral theses only).

I have either used no substantial portions of copyright material in my thesis or I have obtained permission to use copyright material; where permission has not been granted I have applied/will apply for a partial restriction of the digital copy of my thesis or dissertation.'

Signed ....

Date ......26 - 11 - 2015......

AUTHENTICITY STATEMENT

'I certify that the Library deposit digital copy is a direct equivalent of the final officially approved version of my thesis. No emendation of content has occurred and if there are any minor variations in formatting, they are the result of the conversion to digital format.'

Signed ....

Date ......26 - 11 - 2015......

Abstract

Adaptive Optics (AO) is one of the techniques to reduce aberrations caused by atmosphere turbulence in the light coming from objects above this layer that reaches ground based optical telescopes. It was proposed 62 years ago, and since then it has undergone a fast evolution due to the technical developments in mechanics, optics and electronics. Due to these advances and the efforts of the research community, AO nowadays is widely used in big and moderate size telescopes and it has become an essential instrument in this telescope segment.

The research for its use in small aperture telescopes has been limited for different factors: it is an expensive technique; small aperture involves less gathered light that could reduce AO performance; and also low altitudes where usually these telescopes are located result in severe aberrations. This research has been focused in the investigation of new techniques and procedures that facilitate the engineering of an AO system for small aperture telescopes.

For this purpose an AO testbed has been developed, which includes a portable opto-mechanical platform adapted specifically for its use in small aperture telescopes, which has been tested in laboratory and assessed with on-sky experiments.

In this research, an original AO real time processing control architecture has been defined, that can be fully implemented in a low cost standalone Field Programmable Gate Array (FPGA) device, unlike standard AO configurations, which typically rely in complex distributed hardware architectures which make the system more expensive and less portable.

The lack of gathered light inherent to small aperture telescopes constitutes a severe limitation for an AO system. Hence is crucial to develop optimized image processing algorithms that balance this drawback. Here a novel fast

implementation of a centroiding algorithm has been accomplished, adapted to severe low light conditions, and from this a closed loop AO system has been demonstrated.

There is wide potential demand in the scientific and amateur astronomy community in this field, and the innovations and engineering concepts introduced here constitute a valid and proven AO system applied for small aperture telescopes.

Table of Contents

Acknowledgments

Thanks to my supervisor, Andrew Lambert, for giving me the chance to work in the exciting field of Astronomy, for his constant and positive support, and for giving me plenty of flexibility to develop my own research, but at the same time "nudging" me in the correct direction when I lose the right way.

Thanks to my wife, Yoshiko, for her endless patience, close support and encouragement during the highs and lows of the whole PhD journey. Thanks to my father, Manuel, for teaching me to love science, and to my mother, Candelaria, for teaching me to love. Thanks to my sisters Rosario and Matilde for, despite the long distance, make me feel that they are by my side. Thanks to my Spanish friends in Australia, specially Maria José and Ramón, for bringing to Australia a piece of Spanish soul.

Thanks to my colleagues and friends: Steve Weddell from University of Canterbury (New Zealand) for his invaluable help in the testing of the AO system in Mt.John Observatory; Evgeny Mironov from UNSW Canberra for his useful proofreading; Fanpeng Kong, Shanggang Lin and Ping Li from UNSW Canberra for their good company and support.

Thanks to UNSW Canberra staff, specially to Elvira Berra and Craig Edwards for their diligent and helpful feedback to any administrative issue, and to Darryl Budarick, Ban Hotrieu and Rick Whyte from UNSW Canberra Technology Support Group, for their fast response to any technical problem.

Finally thanks to Rudyard Kipling and Walt Whitman, though they are not among us, with their poems "If" and "When I heard the Learn'd Astronomer" respectively, provide me with the necessary inspiration, the former to follow my own path regardless of other people's opinion, and the latter to enjoy "from time to time, Look'd in perfect silent at the stars".

List of Symbols

r_0	Fried parameter or Fried coherence length
E_{rms}	Root mean square error
θ_0	Anisoplanatic angle
τ_0	Greenwood time
L_0	Outer scale of Kolmogorov model
l_0	Inner scale of Kolmogorov model
Re	Reynolds number
ϵ	Energy input and dissipation rate
Φ_T	Power spectrum of atmosphere temperature fluctuations
κ	Spatial wave number
n	Refractive index
Φ_N	Power spectrum of atmosphere refractive index fluctuations
C_N^2	Refractive index structure constant
D_V	Velocity structure function
C_V^2	Velocity structure constant
D_T	Temperature structure function
C_T^2	Temperature structure constant
D_N	Refractive index structure function
D_Φ	Wavefront structure function
B_h	Coherence function
B_0	Coherence function at ground
ζ	Zenith angle
B	Atmospheric transfer function
f_G	Greenwood frequency
σ	Standard deviation
σ^2	Variance

σ_p	Phase standard deviation
Z_i	Zernike polynomials
w_i	Zernike coefficients
$W(x, y)$	Wavefront respect x and y axes
f	Focal distance
C	Calibration matrix
I	Influence matrix
CLK_{in}	Input clock signal from wavefront sensor
CLK_{out}	Output clock signal from FPGA
CLK_{50}	50 MHz oscillator clock signal
H_{sync}	Horizontal synchronism signal from wavefront sensor
V_{sync}	Vertical synchronism signal from wavefront sensor
D_{IN}	Pixel intensity data from wavefront sensor
$Cent_x$	Calculated centroid in x axis
$Cent_y$	Calculated centroid in y axis
$I(x_i, y_i)$	Intensity data of wavefront sensor pixels respect x and y axes
C_x	Phase correction term for x axis in 1FC centroiding algorithm
C_y	Phase correction term for y axis in 1FC centroiding algorithm
m_v	Apparent magnitude
M_v	Absolute magnitude
λ	Wavelength

List of Abbreviations

1FC	First Fourier Coefficient Algorithm
AO	Adaptive Optics
AOA	Adaptive Optics Associates
ASIC	Application Specific Integrated Circuit
ASM	Adaptive Secondary Mirror
BGA	Ball Grid Array
BJT	Bipolar Junction Transistor
C	Calibration matrix
CCD	Charged Coupled Device
CLB	Configurable Logic Block
CMOS	Complementary Metal Oxide Semiconductor
CoG	Center of Gravity
CORDIC	Coordinate Rotation Digital Computer
COTS	Common of the Shelf
CPLD	Complex Programmable Logic Device
CPU	Central Processing Unit
CUR	Curvature
CZV	Centroids, Zernike coefficients and Voltages for actuators
D/A	Digital to Analog
DCM	Digital Clock Manager
DEC	Declination
DM	Deformable Mirror
DSP	Digital Signal Processor
DWFS	Deconvolution from Wavefront Sensing
EEPROM	Electrically Erasable Programmable Read Only Memory
ESO	European Southern Observatory

FFT	Fast Fourier Transform
FIFO	First In, First Out
FOV	Field of View
FPGA	Field Programmable Gate Array
FPU	Floating Point Unit
FWHM	Full Width Half Maximum
GPU	Graphics Processing Unit
GUI	Graphical User Interface
HV	Hufnagel-Valley
I	Influence matrix
IP	Intellectual Property
LC	Logic Cell
LGS	Laser Guide Star
LUT	Look-Up Table
LVDS	Low Voltage Differential Signaling
MAC	Multiplier-Accumulator
MC	Multi Conjugate
MLA	Micro Lenslet Array
MM	Membrane Micromachined
MOAO	Multiple Object Adaptive Optics
MPM	Monolithic Piezoelectric Mirror
MTF	Modulation Transfer Function
NGS	Natural Guide Star
OA	Operation Amplifier
OPD	Optical Path Difference
PDM	Piezoelectric Deformable Mirror
PSF	Point Spread Function
PYR	Pyramid
RA	Right Ascension
RAM	Random Access Memory
RMS	Root Mean Square
ROI	Region of Interest
RT	Real Time
RTC	Real Time Controller
RTL	Register Transfer Level
S/N	Signal to Noise

SC	Science Camera
SCAO	Single Conjugate Adaptive Optics
SH	Shack-Hartmann
SI	Shearing Interferometer
SPI	Serial Peripheral Interface
SR	Strehl Ratio
SRAM	Static Random Access Memory
TDM	Time Division Multiplexing
TTL	Transistor-Transistor Logic
UI	User Interface
UNSW	University of New South Wales
USB	Universal Serial Bus
VHDL	VHSIC Hardware Description Language
VHSIC	Very High Speed Integrated Circuit
WFS	Wavefront Sensor

List of Figures

List of Tables

CHAPTER 1

Introduction

1.1 Approach to the problem

The curiosity of man has lead him to observe the surrounding nature, like astronomers, who want to observe what is outside the Earth, and try to comprehend what they are seeing. When talking about visible light, unaided eyes have been enough for the brighter stars, the Moon or some planets. But if someone wants to observe these objects with more resolution, or reach more distant objects, optical instrumentation such as telescopes are an important aid. For ground-based telescopes there is a problem which prevents reaching the theoretical resolution of a particular telescope, the atmospheric turbulence. The heating of the Earth generates this turbulence, and creates aberrations in the light coming from objects that traverses the atmosphere. As a consequence, objects are presented as blurry and also scintillation can be observed. One solution is use a telescope outside the atmosphere in an Earth orbit, like Hubble or Gaia, but apart from the obvious high cost of the project and tricky maintenance, another disadvantage is that is too far to have a good control over it. If observations have to be performed from the Earth surface, solutions have to be provided to avoid these disturbances. Among others, adaptive optics (AO) is one of the techniques used. It includes active mirrors to correct light aberration using data coming from wavefront sensors that detect aberrations, all commanded by a control system in a closed loop fashion.

The use of AO has been generalised in big telescope facilities. A survey of the current adoption of AO in these large telescopes is given in table 1.1, sorted by the telescope primary mirror size. All these adaptive optics systems are in continuous improvement, and in this table are presented the more recent specifications, as they can be found in the literature.

Nevertheless use of AO in moderate and small size telescopes is less widespread, limiting the access of curious observers to a lucky few. One of the factors of this trend is the cost, as AO systems are formed by expensive and specialized components, which can be justified for use in high budget telescope installations. On the other hand, there are no AO standard technology products in the market to be used with particular telescopes, but this technique is designed, tested, and implemented for dedicated installations, increasing the cost due to the need of professional teams which work in a particular system for long periods of time. Big telescope installations usually are owned, supported and maintained by a partnership of countries, which ease the funding of materials and professionals. That said, this doesn't mean that it's an easy task; on the contrary, it requires lots of resources and time, and typically installations are finished over several years. AO also requires similarly expensive improvements.

The use of AO in small aperture telescopes has been less investigated, although some authors have made some progress in this field, as shown in section 1.4. Different challenges have to be faced in the design of an adaptive optics system for a small telescope. Normally these telescopes belong to small research organizations, universities or amateur astronomers, that usually have to struggle to get money for their different projects or ideas, so the low cost nature of the project is an important factor. This means that some parts of the inputs have to be cut, reducing the cost as much as possible, and also the professional teams have to be small, typically consisting in very diverse backgrounded professionals, who must specialise in more than one field.

Apart from the cost, other issues derived in this type of designs are: low signal to noise (S/N) ratio, mechanical vibrations (due to its weight compared to the telescope tube), and limited space and portability. Also in AO for small telescopes another problem is the lack of man-made guide stars, so the natural guide star or self-referencing objects must be available in the field of view.

Table 1.1: AO systems of worldwide main telescopes, running or planned, as reported in the literature at January 2015 (footnotes in next page).

AO Name	Telescope	Site	Ap [1]	Guide [2]	WFS [3]	DM [4]	Performance	Ref
KAPAO	AstroMech.	TMO[5](CA)	0.6	NGS	SH	MM 140	SR[6]=0.26, optical filter	[64]
ACE	60-inch	Mt.Wilson(CA)	1.5	NGS	SI	MPM 69	FWHM[7]=0.17", 700nm, m_v[8]=5.9	[65]
ROBO-AO	60-inch	Mt.Palomar(CA)	1.5	LGS	SH 121	489	SR=0.64, seeing=0.69", J band	[3]
ShARCS	Shane	Lick (CA)	3.0	LGS	SH	MM 1024	SR=0.52, FWHM=0.188", m_v=5	[43]
ALFA	Calar Alto	Almeria (Spain)	3.5	LGS	SH 100	PDM 97	SR=0.5, 2.2μm	[76],[11]
COME-ON-+	ESO 3.6m	La Silla(Chile)	3.6	LGS	SH 100	PDM 52	FWHM=0.1, bright star, J H bands	[23]
CANARY	WHT	Canary i.(Spain)	4.2	Both	SH 49	52	SR=0.27 in SCAO[9]	[45]
PALM-3000	Hale	Mt.Palomar(CA)	5.1	Both	SH 4096	3368	SR=0.86, m_v=7, K band	[10]
MMT AO	MMT	MMTO[10] (AZ)	6.5	Both	SH 144	ASM 336	E_{rms}[11]=450nm, seeing=0.77"	[50]
GeMS	GEMINI-S	C.Pachon(Chile)	8.1	LGS	SH 256	MC[12]	SR=0.3, seeing= 0.45", K band	[69]
NIRI-ALTAIR	GEMINI-N	Mauna Kea (HI)	8.1	Both	SH 144	177	SR=0.3, seeing= 0.4"	[33]
AO188	SUBARU	Mauna Kea (HI)	8.2	Both	CUR 188	Bimorph	SR=0.45, good seeing, K band	[26]
NAOS	VLT	Chile	8.2	NGS	SH 196	185	SR=0.5, K Band	[1],[59]
LBT AO	LBT	Mt.Graham (AZ)	8.4 [13]	NGS	PYR	ASM 672	SR=0.9, poor seeing, 4μm	[2]
Keck AO	Keck 1, 2	Mauna Kea (HI)	9.8	Both	SH	349	SR=0.4, bright star, K band	[14]
	GMT [14]	L.Camp. (Chile)	24.5	Both	SH	ASM	SR=0.75, 2.2μm (NGS)	[7]
	TMT [15]	Mauna Kea (HI)	30.0	LGS	SH	MC	E_{rms}=187nm, avg. seeing, J,H,K	[8]
	E-ELT [16]	C.Arma. (Chile)	40.0	Both	SH	MC	SR=0.6, 2.16μm (MC)	[12],[16]

[1] Aperture diameter of telescope primary mirror in metres.

[2] Star reference type: NGS (Natural Guide Star), LGS (Laser Guide Star), Both (Could work in two modes, NGS or LGS).

[3] Type of wavefront sensor (PYR: Pyramid, SH: Shack-Hartmann, SI: Shearing Interferometer, CUR: Curvature) and number of subapertures.

[4] Type of deformable mirror (MM: Membrane Micromachined, MPM: Monolithic Piezoelectric Mirror, PDM: Piezoelectric Deformable Mirror, ASM: Adaptive Secondary Mirror) and number of actuators in deformable mirror.

[5] TMO: Table Mountain Observatory.

[6] SR: Strehl Ratio.

[7] FWHM: Full Width at Half Maximum.

[8] m_v: Relative magnitude of star.

[9] SCAO: Single Conjugate Adaptive Optics.

[10] MMTO: Multi Mirror Telescope Observatory.

[11] E_{rms}: Root Mean Square Error.

[12] MC: Multi Conjugate.

[13] 2 primary mirrors of 8.4 metres each which provides a collecting area equivalent to an 11.8 metres.

[14] Commissioning in 2021.

[15] Commissioning in 2022.

[16] Commissioning in 2024.

Nevertheless, some products have been developed and exist in the market, aimed at supporting a wider and common of the shelf (COTS) adoption of the benefits of AO in both amateur and research markets. In table 1.2 is shown a list of these systems, with their more important features. Some companies, such as Santa Barbara or Stellar Products, have introduced in the market ready-to-go products, meanwhile others propose more customizable solutions for the customers, such as OKO.

Table 1.2: AO commercial systems as reported in the literature at January 2015.

Name	Company	Modes[1]	Status	Price	Ref
AO-8T	SBIG	2	Commercial	974 AUD	note[2]
AO-X	SBIG	2	Commercial	2690 AUD	note[2]
AO-2	Stellar Products	2	Discontinued	N/A	note[3]
AO-5	Stellar Products	5	In development	N/A	note[3]
QuickSilver	Starpoint AO	–	Prototype	N/A	note[4]
AO system	OKO	–	Prototype	24000 AUD	note[5]
Kit,Metric	AOS	–	Not astronomy	14700 AUD	note[6]

Big telescopes normally are sited at high altitudes, which permit to obtain better resolution, avoiding the first layers of turbulence close to the Earth's surface. A small aperture telescope normally is sited at moderate altitudes, in most of cases close to the research center, the university or the abode of a particular amateur astronomer. This constitutes an increase in the layers of turbulence that light has to cross before reaching the telescope, as well as other complications, both technical and logistical. A typical measure of the turbulence is the ratio D/r_0, where D is the telescope diameter, and r_0 is the Fried coherence length, a parameter which describes the fraction of the telescope aperture that is not affected by turbulence (more details about r_0 are provided in chapter 2). At high altitudes, air is less turbulent because light crosses less layers, but this ratio scales with telescope diameter. Nevertheless, in poorer air, small diameter telescopes have a similar or worse D/r_0 than large ones.

[1] Number of classical aberration modes corrected.
[2] www.sbig.com
[3] www.stellarproducts.com
[4] www.starpointao.com
[5] www.okotech.com
[6] www.activeopticalsystems.com

The small aperture of these telescopes also involves that comparatively less photons reach the detector, typically a digital image sensor, which constitutes another of the important limitations in the design of the AO system to be considered. This means lower signal to noise ratio, which will affect severely the design of the whole system, including the optical design and the number of actuators in the active mirrors.

1.2 Correcting for the atmosphere turbulence

In figure 1.1 is shown the more important techniques to correct atmosphere turbulence, that can be divided in three main categories: post processing, real time and hybrid techniques. Post processing methods apply specialised image processing to the recorded output of the optical system, with no constraints in the processing time. The more important methods are based in speckle imaging, where a set of short exposure images (called speckle images due to their particular shape) are recorded with the image sensor and subsequently processed by different techniques.

Unlike post processing methods, in adaptive optics the images are corrected by mechanical devices in real time, and this is the technique investigated in this research.

Hybrid methods combine both techniques, post processing and real time, where images are corrected partially by adaptive optics, while at the same time these images are recorded and subsequently processed. Different authors have investigated these hybrid techniques, such as speckle imaging and adaptive optics [46], the application of specific techniques of astronomy to ophthalmology [34] or deconvolution using wavefront sensor data [20].

Speckle interferometry techniques have proven to produce good diffraction limited images. It is an open loop solution and high computational calculations are necessary to obtain these images. Other techniques are blind deconvolution and its extensions, such as the sparse prior deconvolution [75], or the pupil wavefront folding interferometry [9].

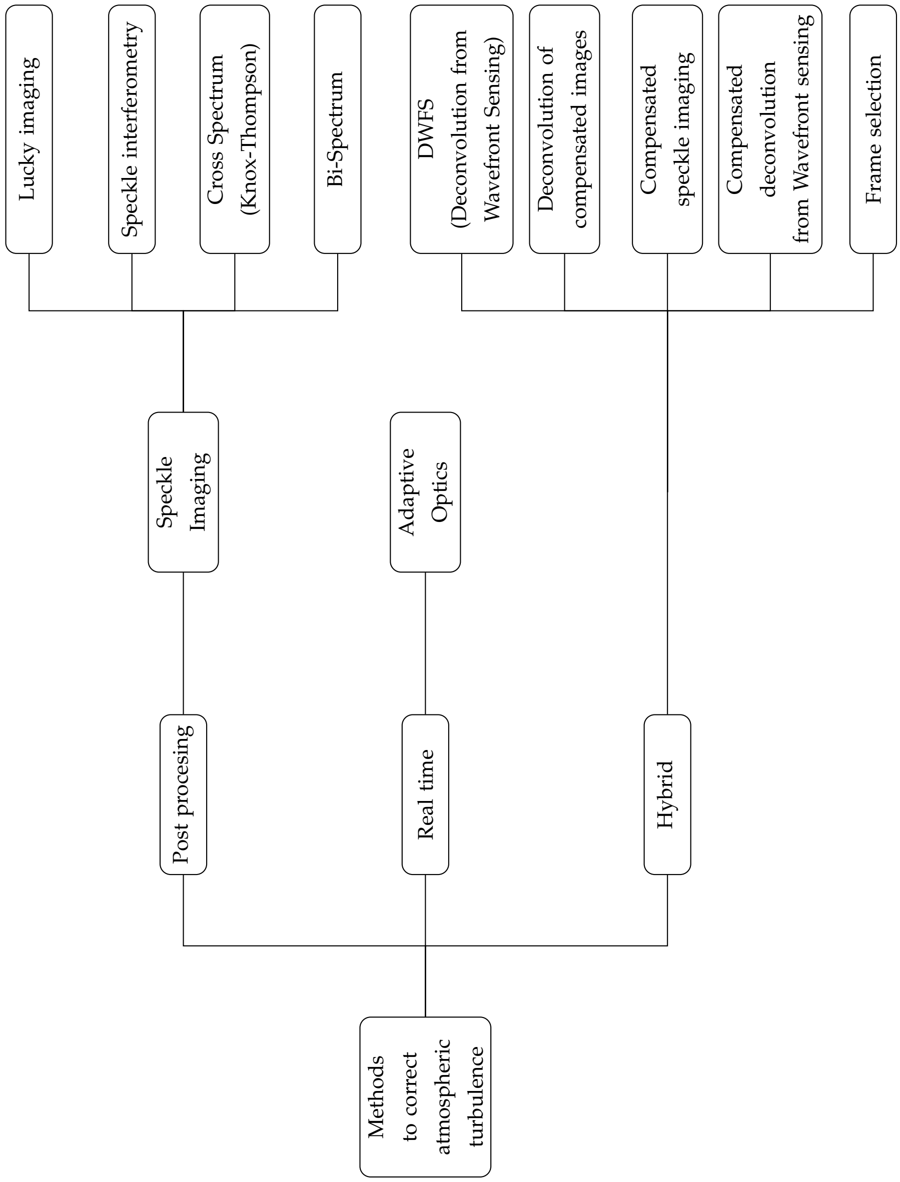

Figure 1.1: Techniques to correct atmosphere turbulence.

1.3 Adaptive optics

Adaptive optics is a real time technique to correct the aberrations in the optical wavefront of a light beam that travels through a medium. In figure 1.2 is shown the operation of this technique with its main blocks indicated. A traditional AO system is formed by three main components: control system, wavefront sensor (WFS) to measure the aberrations, and deformable and tip-tilt mirrors to correct them mechanically. The control system, which is implemented in a CPU or other computing devices, obtains the aberrations information of the incoming wavefront from the WFS, and processes it in order to obtain the signals to be applied to the actuators of the deformable and tip-tilt mirrors, to reproduce a conjugate shape to the aberrated wavefront, in a real time closed loop process.

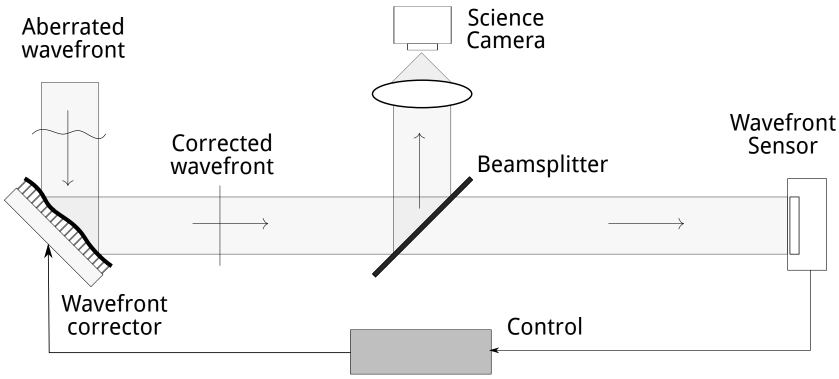

Figure 1.2: Basic operation of an adaptive optics system (closed loop method).

One of the main applications of AO is astronomy, when the aberrations are created by the Earth's atmosphere, although it can be also applied in many different fields as ophthalmology (retinal imaging), confocal microscopy, ultra-short laser pulse shaping, machine vision, quality laser beam measurement, optics testing or optical system alignment.

AO doesn't have a long history. Its origins date back around the 1950's. In 1953, Babcock proposed the possibility of an adaptive optics technique, and later Linnick suggested the use of a segmented correction mirror in 1957. At that moment, the implementation of the systems proposed by Babcock or Linnick involved a very high cost. So it was not actively used until 1977, when Hardy was capable to build the first adaptive optics system. In 1982, a larger version of Hardy's system was built in Air Force Maui Optical Site in Haleakala (Hawaii), and by the end of tht decade, AO systems were developed for defense applications. But the main target of these systems were satellites, and astronomers needed a more sensitive system to detect fainter objects in the sky. A share effort between the ESO (European Southern Observatory), defence research experts, and industry, lead to the development of the COME-ON AO prototype, which was used in the infrared spectrum, because the compensation requirements were more relaxed than in the visible spectrum.

On the other hand, researchers at NOAO (National Optical Astronomy Observatory) investigated the use of novel devices, as the curvature sensor instead of the Shack-Hartmann (SH) sensor of the COME-ON system, or the bimorph deformable mirror, that was successfully tested in the CFHT (Canada-France-Hawaii Telescope) on Mauna Kea (Hawaii) in 1993. In the mid-90s AO systems were in the planning stages for the current big aperture telescopes.

Since then AO has experienced a fast evolution, in part due to the enhancements in computer processing, sensors, and actuators, which are the three main technologies on which adaptive optics is based [70]. In figure 2.1 in next chapter is shown a timeline with the main milestones in the AO history, along with the telescope evolution.

1.4 Advances in AO for small aperture telescopes

Different authors have investigated the application of adaptive optics for small and moderate aperture telescopes.

In table 1.3 is summarized the efforts accomplished by some researchers with the aim to develop AO systems that could be used in small aperture telescopes.

Roland et al.[58] proposed the use of low cost adaptive optics systems that could include any kind of telescopes, not only the big ones. They described a general purpose AO system based in quite off-the-shelf components, using a simplified design with a real time modal control approach, based on Motorola VME boards.

Ivanescu et al.[30] developed a low cost adaptive optics system for the 1.6 m diameter telescope in Mont-Mégantic Observatory, correcting 5 terms of aberration: tip, tilt, defocus, astigmatism and one trefoil term.

Paterson, Munro and Dainty [48] built a flexible low cost AO system, with an estimated cost of 28000 AUD. They used a membrane deformable mirror of 37 piezoelectric actuators, a SH wavefront sensor, with the control implemented on a single processor, achieving frame rates up to 800 Hz, with all the components commercially available. They stated that it would be possible to correct tip and tilt aberrations with the membrane mirror, but with limited correction available, depending on the application.

Teare et al.[67] developed an AO prototype based on an Ebert-Fastie mirror re-imaging system. They built a prototype for a 0.4 metres diameter telescope, that eventually would be applied to a 1.4 metres.

Table 1.3: Research in AO systems for small aperture telescopes.

Year	Ap[1]	WFS[2]	DM[3]	RTC[4]	Price	Ref
1994	2-4	SH 25	Bimorph13	CPU	–	[58]
2000	–	SH	MM 37	DSP	28000 AUD	[48]
2003	1.6	7	PDM 6	–	–	[30]
2006	0.4	–	MM	–	–	[67]
2007	–	–	PM	MC	8500 AUD	[38]
2008	<1	SH 45	MM	CPU	7500 AUD	[36]
2009	2.2	SH 25	MM 39	CPU	50000 AUD	[11]
2014	1.3	SH 144	MM 48	CPU	–	[21]
2014	0.6-1.6	SH 81	MAG 69	CPU	–	[52]
2014	–	SH 1600	MAG 277	CPU	–	[63]

Mansell et al.[38] described a commercial system with a estimated cost of 8500 AUD, using a deformable mirror with polymer membranes and a stochastic parallel gradient descent control algorithm.

Loktev et al.[36] developed an integrated AO system to be attached to telescopes up to 1 meter in diameter. It used natural guide stars of at least magnitude 4 in a telescope of 25 cm, where the tests were performed. The target price for this prototype was 7500 AUD without computer, and the dimensions were 188 × 291 × 145 mm. The optical system was based in an afocal Offner configuration with two spherical mirrors, and a membrane deformable mirror. The SH wavefront sensor had 45 subapertures, and the software used was FrontSurfer, a commercial solution provided by OKO Technologies. In the laboratory tests, the system corrected static

[1] Aperture diameter of telescope primary mirror in metres.

[2] Type of wavefront sensor (SH: Shack-Hartmann) and number of subapertures.

[3] Type of deformable mirror (MM: Membrane Micromachined, PM: Polymer Membrane, PDM: Piezoelectric Deformable Mirror, MAG: Magnetic) and number of actuators in deformable mirror.

[4] RTC: Real Time Control hardware (CPU: Central Processing Unit of PC, MC: Microcontroller, DSP: Digital Signal Processor).

aberrations of the system, and dynamic aberrations when a rotating disk aberrator was used. In their experimental results, the system could correct static aberrations with a natural star of magnitude 2.21.

Aceituno [11] developed a low cost adaptive optics prototype, based on a membrane deformable mirror and a SH wavefront sensor for 1 to 2 meter class telescopes. This prototype was called SAOLIM and had an overall cost about 50000 AUD. It was tested in the 1 meter telescope of Calar Alto Observatory in Almeria (Spain). The control system was based on a CPU supported by a desktop computer. It was capable to correct 15 modes of aberration. According to the experimental results, the system was capable to improve the Full Width at Half Maximum (FWHM) from 1.14" to 0.42", in average seeing conditions.

Fujishiro et al.[21] developed a low cost AO system, based on a refractive optical design, and using off-the-shelf components. They tested the AO system in a 1.3 metres telescope, although the system was intended to be used in any telescope ranging from 1 to 30 metres aperture size. Using only tip-tilt correction, they improved the performance of the telescope, from 2.6" to 2.0" in the seeing disk size, although they stated that improvements should be made in the reduction of the residual wavefront error created in the deformable mirror. The control hardware was based on a multi-core CPU architecture (Intel i5 at 2.8 MHz).

Ren et al.[52] developed a portable AO system to be used in solar and stellar applications, optimized for near infrared wavelength range. They used off-the-shelf components and a control hardware based on a high speed multi-core CPU architecture (2 8-Core Intel Xenon at 3.1 GHz) supported by LabView. They stated a good performance in the on-sky results obtained, with a average Strehl Ratio (SR) of about 0.8 in H band. Still their work is in progress, with the goal to adapt this system to 4 meter class telescopes.

Schimpf et al.[63] developed an AO system using off-the-shelf components running at 1.5 KHz for general adaptive optics applications. The control was based in a high performance CPU/GPU architecture (2 Intel Xeon E5520 and 4 GPU Nvidia Tesla S1070), running the Alpao AO MATLAB toolbox ACE.

All these research efforts, aimed to the application of AO for small telescopes, are based in control architectures with external hardware to run the AO real time control algorithm. This hardware is based mostly in high performance CPU devices, that can cope with high parallel calculations in real time. As we will see in the next chapters of this thesis, the approach for this topic is different. An optimized control algorithm implemented in a low cost Field Programmable Gate Array (FPGA) will be used, that is incorporated to an AO opto-mechanical platform, which reduces the complexity, and increases the flexibility and portability of the system. Nevertheless, the use of FPGA as computing device in an AO system has been proposed and evaluated mainly for big aperture telescopes, as is shown in section 2.5.3 in chapter 2 about AO systems for Astronomy.

1.5 Motivations and purpose

The aim of this work is to contribute significantly in AO techniques when applied to small aperture telescopes in non privileged spots, which can be found in small research centres or universities, or for amateur astronomy. To follow this aim it was required the development of an AO testbed for a particular small aperture telescope, shown in figure 1.3, attached to a 16" inches telescope, used for the experimental part of this research. Aspects such low cost, integration, compact design, lightweight, portability, consumption and ease of use had a crucial importance in this research.

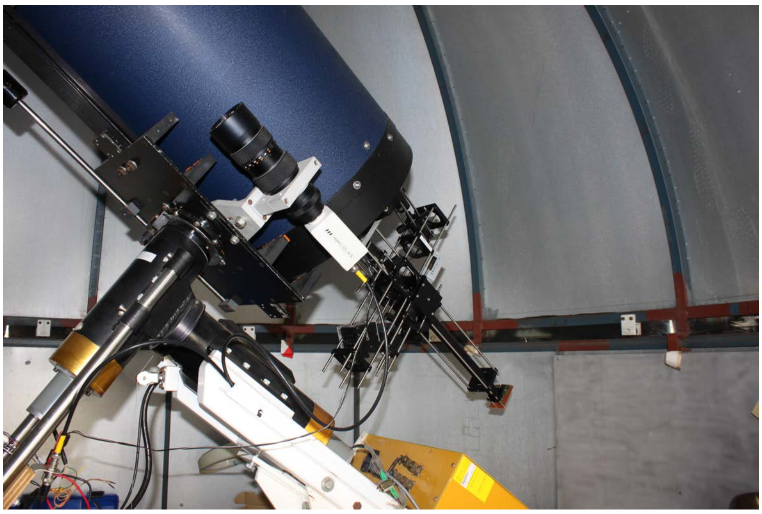

Figure 1.3: Adaptive Optics testbed built for experimental part of research attached to 16" telescope.

Regarding the mechanics of the system, one of the goals of the thesis, was to obtain an opto-mechanical testbed which could be applied to small aperture telescopes. This testbed should be a low cost system (an estimated budget of the AO system is shown in the appendix A.5).

Regarding the optics, inexpensive and off the shelf optical components have been chosen. Another consideration is that the number of optical components has been reduced as much as possible, due the low photon flux existent in small aperture telescopes, compared to the big ones.

Regarding the control, an FPGA device constitutes the hardware platform for the AO system, supported externally by other control devices which provide auxiliary systems, as communication interfaces with a support computer. Some of the motivations for choosing FPGA technology as a basis for the AO control, is due to its inherent pipeline and parallel design possibilities, its low cost nature, and the high speed that these devices can achieve nowadays. Also FPGAs can be easily reprogrammed, thus providing a high degree of flexibility, and a way to test different algorithms in a convenient way. The reduced size of electronic devices nowadays opens the possibility to be used in portable AO systems, which could be eventually attached to small aperture telescopes.

In small aperture telescopes, one of the crucial factors to consider is the poor S/N ratio due to the low photon flux that reaches the aperture. Also it is more difficult to align the system optically, when compared to big telescopes structures, because factors as wind, weight and balance have more importance, making the system more unstable to vibrations and sag, since it is mounted at the extremity of a moment arm and experiences large vibrational torque.

As a testbed we seek to show that an AO system can be done and done well, following the engineering decisions and steps in this work. We therefore don't try to solve all issues associated with AO but show it can be accomplished in an inexpensive way.

1.6 Contents and structure of thesis

This thesis describes the engineering and operation of an AO testbed for small telescopes. In the first chapter the problem is presented and a study of the different solutions existent in the market is shown, including the state of the art of adaptive optics system built or under development, for big and small aperture telescopes. This was useful to show the possible limitations or system specific design criteria, and propose new ideas and solutions to develop.

In the second chapter the basic concepts of an AO system applied to astronomy are shown, where main concepts and mathematical background that will be used during the rest of the thesis are presented. A description about the different components used in AO such as deformable mirrors or wavefront sensors is introduced, and section 2.3.6. focuses in the limitations of this system when applied to small aperture telescopes.

In the third chapter the optical and mechanical design of the testbed are described, with their main specifications. The process and different stages that lead to the current testbed are detailed, as well as the justification of the different design decisions. Optical simulations in ZEMAX[1], an industry standard software in optical design, were performed during this stage. Various mechanical 3D models (AUTODESK INVENTOR) were presented, and based on them, the best solution for the final prototype was chosen. The different aspects related to mechanical integration, weight and power supply were considered, including ergonomics, to ratify the correctness and fidelity of the system.

In the fourth chapter the control of adaptive optics system is shown. The control architecture, designed with a software combination of Altium Designer[2], Xilinx PlanAhead[3] and System Generator[4], is described in detail, specifying the different modules that form the control system. Similarly the software platform developed for this purpose in MATLAB[5] Simulink[6] will be described, including the interfaces of the AO system with the debug and control computer. Different centroiding algorithm designs are presented, including a comparative study, when used in a SH wavefront sensor configuration. Also this chapter includes a study of the proposed 1st Fourier coefficient centroiding algorithm implemented in the FPGA architecture.

[1]ZEMAX is an optical design and ray tracing software from Radiant Zemax LLC (www.zemax.com).

[2]Altium Designer is an electronic design automation software from Altium Limited (www.altium.com).

[3]Xilinx PlanAhead is a software tool to design and program logic devices from Xilinx Inc. (www.xilinx.com).

[4]System Generator is high abstraction tool to design DSP systems from Xilinx Inc. (www.xilinx.com).

[5]MATLAB is a numerical computing software and programming language from MathWorks Inc. (www.matlab.com).

[6]Simulink is a graphical programming environment to model dynamic systems from MathWorks Inc. (www.matlab.com).

In the fifth chapter experimental results are shown, in the laser laboratory and on-sky with the real telescope, and the performance of the AO system is evaluated, including the deformable mirror behaviour. Simulation results are shown regarding the floating point and fixed point precision, and also analysis of the timing performance, the FPGA utilization, the D/A converters linearity and the interaction matrix calculation. Results in closed loop configuration are shown, including the performance of the different stages of the control loop. Section 5.5 shows the performance of the different centroiding algorithms, tested with real on-sky images.

Sixth chapter presents the conclusions and future developments of the AO system.

After the bibliography, the appendices show: a relevant part of the AO system code, a description of the tracking system, the user manual of the real time control software, the estimated budget of the system, optical design details and pictures of different parts of the AO system.

1.7 Research contributions

An AO platform has been developed for use with small telescopes, tested in laboratory and on-sky. The optical configuration shows that with low cost and off-the-shelf components, a configurable light path can be studied. The whole control algorithm was implemented in a low cost standalone FPGA, a Xilinx Spartan XC3S3400A model, without requiring extra computing devices. If more computing operations, such as filters, were required, the VHDL based code could be easily exported to a more powerful FPGA device. Results from simulation and implementation of the control algorithm shows a correct behaviour with low latency, which is the time since the last pixel of a frame is read until the voltages are applied simultaneously to all deformable mirror actuators.

As a result of this process, we have achieved a flexible platform that works as a on-sky testbed to try different technologies in different parts of the adaptive optics workflow. So this leads to design and techniques paths to follow in the research of these kind of systems.

A testbed has been designed and tested in laboratory and on-sky with a telescope of 16" aperture size. This testbed includes low cost and lightweight mechanical components in a flexible setup, which makes it suitable for fast reconfiguration of its different components. The prototype is easily portable, so it can be mounted in a platform for experimentation in a laser laboratory, but also can be installed in the rear port of a telescope through a flange, which avoids designing different setups for laboratory or for telescope uses.

Specific Contributions are:

1. Prototype: A compact lightweight low cost adaptive optics testbed for small aperture telescopes has been developed, which can be used in different telescopes, as is a highly configurable system regarding the optics and mechanics. It allows the use of different configurations in the same platform. It's lightweight, with a overall weight around 10 kg. Also is a low cost system, based on off-the-shelf components, with a estimated cost around 24000 AUD (more details in appendix A.5).

2. Control: An AO control electronic architecture has been implemented in a low cost FPGA, and connected through standard USB communication interfaces to a real time software platform running in a support computer, where debugging, control and recording tasks are performed.

3. Algorithm: A centroids estimation algorithm based on 1st Fourier coefficient has been implemented in an FPGA, adapted to low light and noisy image signals from highly aberrated atmosphere areas.

4. Real-time software platform: A MATLAB based real time software has been developed, which shows centroids, Zernike coefficients and actuator voltages in real time, and snapshots images of reference wavefronts. All parameters of the SH wavefront sensor can be controlled from the platform, as well as the speed control of the tracking system of the telescope. Results can be recorded for further analysis.

5. Operative: The AO system operates on-sky, in laboratory, and with simulations accomplished both in a Meade 16" telescope but also adapted to 1 metre McLellan telescope at Mt.John Observatory (New Zealand).

CHAPTER 2

Adaptive Optics for Astronomical Imaging

2.1 Introduction

In this chapter, after a review of telescope and adaptive optics evolution where their main milestones are indicated, the theoretical principles established mainly by Kolmogorov, Takarskii and Fried, are shown. Expressions for the key parameters that define the atmosphere turbulence are obtained, namely, r_0, θ_0 and τ_0, which are Fried parameter, anisoplanatic angle and Greenwood time respectively, and also the main expressions of the Strehl ratio (SR), which is an standardized method to measure the performance of adaptive optics system, are shown. Also the concept of angular anisoplanatism is explained, and a final section with considerations for small aperture telescopes in low altitudes is shown.

Next a general description of the main blocks of an adaptive optics system for astronomy is detailed. It is not in the scope of this thesis to do a comprehensive survey of the current advances in wavefront sensing and wavefront correctors technologies. These two topics constitute *per se* very broad fields in continuous research. In the current thesis two technologies have been selected for the design, particularized for the constraints of the project. Both Shack-Hartmann wavefont sensors and piezoelectric deformable mirrors (PDM) are two well known solutions for adaptive optics in astronomy, tested and used thoroughly in different current systems. This is an important asset for the purpose of this research, where more efforts were employed in the control architecture. Later in this chapter the theoretical principles of both technologies are detailed. The wavefront reconstruction and control principles are shown, including stages of the process in the modal reconstruction method, which is followed in this research.

In the last section hardware technologies for AO control are detailed, including a description of FPGAs devices, the hardware technology in which this research is based for the control stage, with a survey of the advances of the scientific community in this aspect.

2.2 Astronomical telescopes

2.2.1 Evolution of telescopes and adaptive optics

The invention of the telescope dates back more than 400 years ago. Since that moment, designs of refractor and reflector telescopes have been constantly improved, the first composed by lenses, and the second by mirrors. Both types have experienced technical advances during their evolution, facing each of them different problems which defined their limitations. In any case, during the telescope history, many developments and findings were performed and built by amateur astronomers, which states the importance of the amateur community, even today, in astronomical instrumentation. In figure 2.1 is shown a timeline of the telescope evolution where the most important events are indicated, along with a similar approach for AO history.

In 1663 James Gregory built the first reflector telescope, but it showed a poor performance, because at that moment, the technology to manufacture and test mirrors was not too advanced. In 1677, Guillaume Cassegrain built a telescope with a secondary convex mirror in front of the primary mirror, design that nowadays is known as Cassegrain telescope. Around 1774, William Herschel began constructing reflector telescopes, and he was capable to built one with 1.2 meters aperture, that was the largest telescope of this kind in the world for a long time. Today, a telescope of 4.2 metres sited in Canary Islands (Spain) has his name, the William Herschel Telescope. Around the middle of 19th century, all telescope mirrors were made of metal, but Leon Foucault, using the silvering process invented by Justus von Liebig, made a big step building glass mirrors. Nowadays, reflector telescopes are preferred among refractor designs for professional research.

In 1668, Isaac Newton constructed a prototype of the first useful refractor telescope, which design is still used nowadays in amateur astronomy. Nevertheless his design showed severe chromatic aberration, an issue that was not fixed until 1729, when Chester Moore Hall built an achromatic objective, combining lenses with different

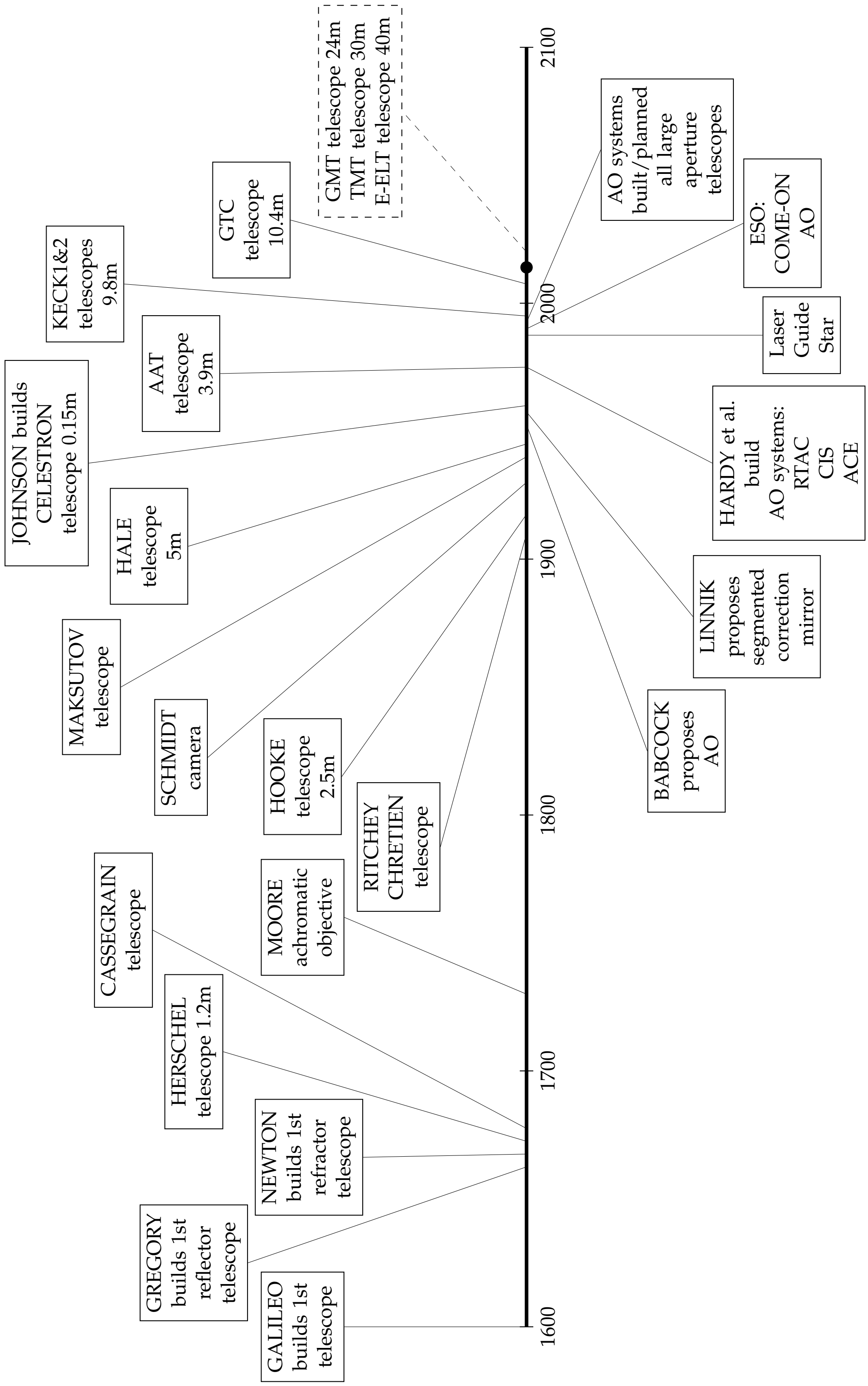

Figure 2.1: Timeline of milestones in evolution of Telescope(top) and Adaptive Optics(bottom)

dispersion coefficients. At the end of 19th century, it was possible to build reflector telescopes up to 1 metre in diameter, and even today this size is the upper limit for this kind of telescopes.

In the beginning of 20th century, both technologies, reflector and refractor were combined, giving birth to the catadioptric telescopes. The pioneer of this system was Bernhard Schmidt, who was the creator of the first Schmidt camera, where he used a large spherical mirror combined with a correcting lens situated in the center of curvature or the mirror. With his invention, telescopes could combine the good features of both reflective or refractive telescopes: large aperture, wide field of view and sharp images.

At that time the size of refractor telescopes reached its limit, so efforts were invested to increase the size of reflector telescopes. This would permit astronomers to gather more light and therefore observe galaxies and distant objects that before were out of reach of current telescopes. In 1917 was finished a 100 inches ($\approx$ 2.5 metres aperture) the Hooker telescope in Mount Wilson (California), and with the support of George Ellery Hale, the telescope that has his name, a 200 inches ($\approx$ 5 metres) aperture sited in Mt. Palomar (California) and finished in 1947. The Hale Telescope was the world's largest until the BTA-6, of 6 metres aperture, achieved its first light in 1975 in Russia. A number of 4-metre class telescopes were built during 1970s and 1980s in both hemispheres, as the AAT (Anglo-Australian Telescope) of 3.89 metres in New South Wales (Australia) in 1974, the MPI-CAHA of 3.5 metres in Almería (Spain) in 1984, the ESO NTT 3.6 m Telescope in La Silla (Chile) in 1989, the CFHT of 3.58 metres in Hawaii (USA) in 1979, or the Nicholas U. Mayall of 4 metres in Arizona (USA) in 1973, to mention a few.

To even get larger apertures, the research during those years were focused in new techniques for casting single mirrors with diameters around 8 metres, or the use of arrays of telescopes and segmented mirrors. The idea of an array of telescopes was first put into practice with the MMT Telescope in Arizona (USA) in 1979, but after 19 years, technology permitted the substitution of this array by a 6.5 meters single mirror, with its first light in 2000. The first segmented telescope was one of the Keck twins in Mauna Kea, Hawaii (USA), finished in 1993. At that moment the use of segmented mirrors was an appropriate technical solution for large telescopes, hence from that date more segmented mirror telescopes were built, such as the Hobby Eberly of 9.2 metres in Texas (USA) finished in 1996, the SALT of 9.2 metres finished in 2005, or the GTC of 10.4 meters in La Palma (Spain) finished in 2007.

The increase of the telescope aperture size allowed to gather more light and therefore the possibility to observe more distant objects, but that was not suitable for large fields of view of the sky. The ideas of Bernard Schmidt were put into practice by Ronald R. Willey Jr in 1962, who developed a Schmidt-Cassegrain compact telescope that offered sharpened images on and off-axis. Tom Johnson manufactured a model called Celestron, a compact 200 mm f/10 Schmidt-Cassegrain telescope. Matsukov and others discovered independently, that a deep meniscus lens has more or less the same effect as the Schmidt lens, correcting the spherical aberration inherent to spherical mirrors. This gave birth to the nowadays known as Matsukov-Cassegrain, a very popular amateur telescope. At that time, other improvements based on the two mirrors Cassegrain telescope lead to the Ritchey-Chrétien configuration telescope, with better performance over the previous ones.

Most reflector telescopes have a central obscuration created by the secondary mirror, which reduces contrast and sharpnesses, specially in low contrast objects, such as planetary details. On the other hand, refractors suffer from chromatic aberration. So in the 1950s, Anton Kutter developed a reflector without obstruction, called schiefspieglers, which is the most important telescope model which belongs to the family of TCT, or Tilted Component Telescopes.

Nowadays the trend to build larger apertures is synthesized in three ambitious and long term projects: GMT (Giant Magellan Telescope), TMT (Thirty Meter Telescope) and E-ELT (European Extremely Large Telescope). The GMT telescope will consist of six segments of 8.4 metres each, equivalent to a single optical surface of 24.5 metres in diameter. It will be installed in Las Campanas Observatory (Chile) and its commissioning is scheduled to begin in 2021. The TMT telescope will have also a segmented primary mirror, covering an optical surface of 30 metres in diameter, and it will be installed in Mauna Kea (Hawaii) with a expected first light in 2022. Finally the E-ELT will have a segmented primary mirror of 40 metres in diameter and it will be installed in Cerro Armazones (Chile) with its expected first light in 2024.

2.2.2 Ritchey-Chrétien telescope

The Ritchey-Chrétien telescope configuration is the most widely used in the professional field. Most of the telescopes mentioned in the previous section have this configuration, even the space observatories as Herschel, Hubble or Spitzer.

It consists in a variation of a classical Cassegrain system, where both primary and secondary mirrors have an hyperboloid shape. They are more difficult to build due to the bigger sphericity of their mirror surfaces. These shapes are intended to correct coma aberration, although they show certain degree of astigmatism and curvature field. Compared with other Cassegrain configurations, they have a larger field of view. The moderate and small aperture Ritchey-Chrétien telescopes are a good option for the top end segment of amateur astronomy, or universities and modest research centres, and among their applications are satellite tracking or astrophotography. In figure 2.2 is shown the Meade 16" LX200-ACF Ritchey-Chrétien telescope installed in the School of Engineering and Information Technology (SEIT) of the University of New South Wales (UNSW) Canberra, used in this research.

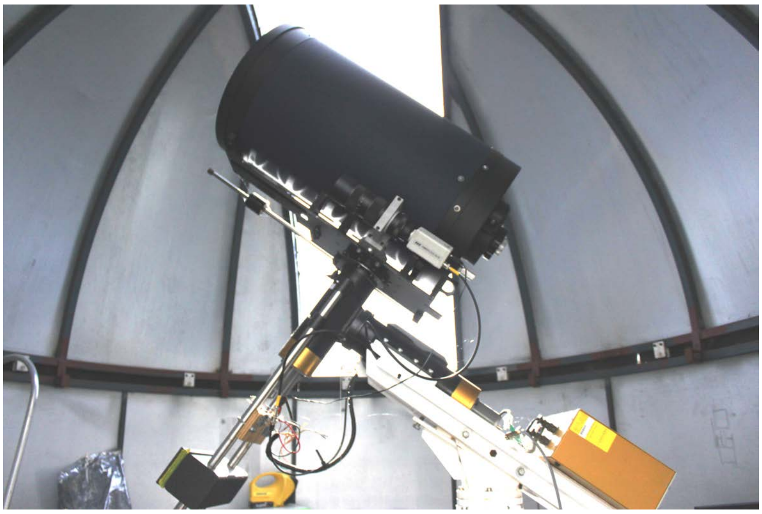

Figure 2.2: 16 inches Ritchey-Chrétien telescope in UNSW Canberra.

All this optical engineering, overlooks one huge limitation; that of the corruption of imagery by the intervening atmosphere turbulence that would limit the precision to the likes of 5 to 10 cm telescopes.

2.3 Optical propagation through atmosphere turbulence

Different researchers have investigated the optical effects created by atmosphere turbulence, but among them, Kolgomorov plays an important role because he developed a statistical model for turbulent air flow, which is a seminal work for subsequent research in this topic. Also Tatarskii and Fried works stand out, the former for applying Kolgomorov model to wave propagation and imaging through volumes with random index of refraction, and the latter for extending Tatarskii work to the optics community. This section summarizes some of their results, stating important relations that will help in the characterization an optimization of the AO system.

2.3.1 Statistics of atmosphere turbulence

The sunlight heats the Earth surface in a cyclic way, and this differential heating creates large areas of air with different temperatures in the atmosphere. The air movement, that typically follows a turbulent model, breaks this large areas in smaller ones that are distributed randomly, due to the unpredictable nature of a turbulent fluid. This air pockets have different temperatures, and because index of refraction of air is sensitive to temperature, this index varies randomly in space and time. Thus turbulence air motion in the atmosphere creates spatial and temporal random variations in its refractive index.

Kolmogorov proposed a model for turbulent air where the kinetic energy of large turbulent areas of air is transferred to smaller spatial scale motions. The air pockets are commonly denominated turbulent eddies and because their temperature is constant, they have uniform index of refraction. Kolmogorov considered different scale sizes for these eddies, and defined L_0 as the outer scale and l_0 as the inner scale, representing the dimensions of the largest and the smallest turbulent eddies respectively. These two values are related by the equation:

$$l_0 = \frac{L_0}{Re^{3/4}}, \tag{2.1}$$

where Re is the Reynolds number. When the turbulent flow breaks up, the kinetic energy is transferred to smaller and and smaller eddies, until the critical Reynolds number is reached, and in this stage, the kinetic energy is transformed in heat by viscous dissipation. If the process is stable, the turbulent energy input rate should be equal to the rate of viscous dissipation. Taking into account dimensional considerations, this condition can be expressed in the next equation:

$$V \propto \epsilon^{1/3} l^{1/3}, \tag{2.2}$$

where V is the velocity of fluctuations, ϵ is the energy input and dissipation rate and l is the eddie size.

The eddies size has been investigated by different authors. Roddier [53] says that l_0 values are around 1 mm near the ground, increasing to about 1 cm near the tropopause layer. However the size of L_0 shows more variability, ranging from 1 m to 100 m.

The power spectrum of temperature fluctuations in the atmosphere, Φ_T, can be deduced from equation 2.2 and expressed in the next equation:

$$\Phi_T(\kappa) \propto \kappa^{-5/3}, \tag{2.3}$$

which is known as the Kolmogorov law, where $\kappa = 2\pi/l$ is the spatial wave number for an eddy of size l, and only valid in the range $l_0<l<L_0$. These temperature fluctuations change the air density, and therefore its refractive index n. Based in Kolmogorov law, Tatarskii obtained a equation to express the power spectrum of the variations of the refractive index Φ_N:

$$\Phi_N(\vec{\kappa}) = 0.033\, C_N^2\, \kappa^{-11/3}, \tag{2.4}$$

where C_N^2 is the refractive index structure constant, parameter which varies with altitude and time.

The variation of atmospheric turbulence with height can be expressed through the parameter C_N^2. Different models have been proposed to describe the turbulence at different layers, but one of the more accepted is the Hufnagel-Valley (HV) model, based on empirical measurements of the turbulence at different heights, performed by many observers. This profile is shown in figure 2.3, in two versions, the daytime HV profile, and the modified HV profile for nighttime. Also the Greenwood model is shown, for comparison purposes.

The HV model has an exponential component up to approximately 1500 metres height, that decreases with altitude, plus a peak value at the tropopause around 10 km.

2.3.2 Wave propagation through turbulence

When a plane wavefront propagates through a turbulent region in the atmosphere, the refraction index variations create perturbations in its phase, and through propagation, this phase perturbations evolve in both phase and amplitude

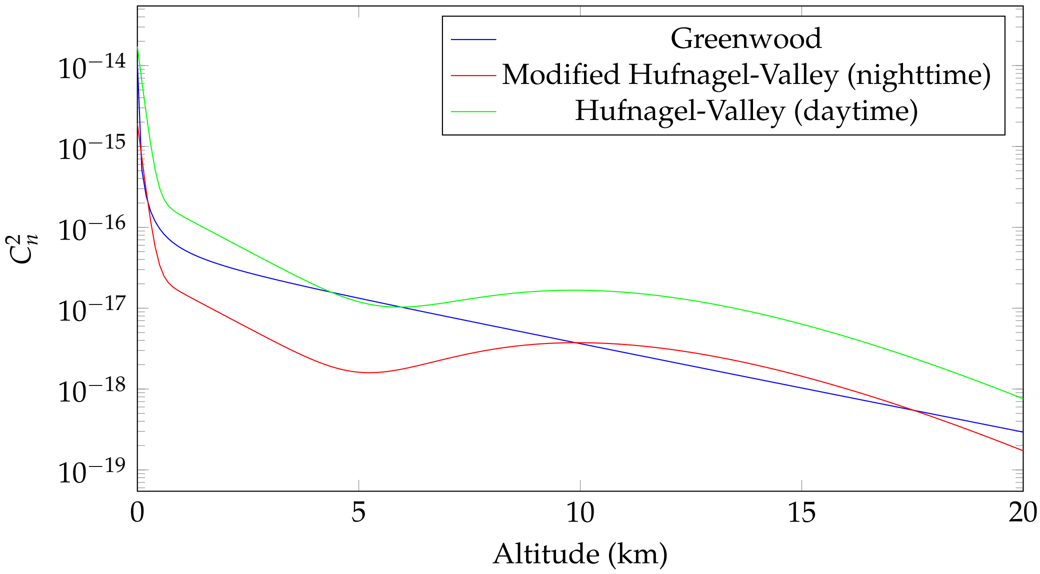

Figure 2.3: Three models of C_N^2 profiles

variations. To measure the effect of turbulent layers in an incident wavefront, first a simplified approach can be used, considering an incident plane wavefront of magnitude unity which crosses a thin turbulent layer [53]. Also the layer thickness is considered to be large compared with the eddies in that particular layer, but small enough to consider diffraction effects negligible.

The average values of many atmosphere characteristic parameters, as temperature or pressure, change with a large time scale, as minutes or hours. To distinguish changes in the average values of these parameters from these slow fluctuations, Kolmogorov introduced structure functions to describe these random functions. From equation 2.2, and considering that the medium is locally homogeneous and isotropic, a structure function between two velocity components, V(x), separated a distance r along x axis, can be defined with the next equation:

$$D_V(r) = |V(x) - V(x+r)|^2 = C_V^2 r^{2/3}, \tag{2.5}$$

where $D_V(r)$ is the velocity structure function, r is the distance between the two velocity components, and C_V^2 is the velocity structure constant, which depends on the energy of the process.

According to Kolmogorov analysis, a similar result can be obtained for the temperature as follows:

$$D_T(r) = |T(x) - T(x+r)|^2 = C_T^2\, r^{2/3}, \tag{2.6}$$

where $D_T(r)$ is the temperature structure function, and C_T^2 the temperature structure parameter.

The air refractive index depends on temperature, pressure and water vapor concentration, but pressure and vapor concentration effects are negligible in the case of vertical propagation. So similarly to equation 2.6, the refractive index structure function can be expressed with the next equation:

$$D_N(r) = C_N^2\, r^{2/3}. \tag{2.7}$$

In the case of a incident plane wavefront that cross a thin turbulent layer of thickness ∂h, an expression for the phase structure function of that wavefront can be obtained from equation 2.7:

$$D_\Phi(r) = 2.914\, k^2\, C_N^2\, \partial h\, r^{5/3}. \tag{2.8}$$

The phase shift produced in the wavefront by the index of refractions fluctuations can be defined as follows:

$$\Phi(x) = k \int_h^{\partial h} dz\, n(x,z), \tag{2.9}$$

which is the sum of a great number of independent variables, therefore it has Gaussian statistics. Considering this, the coherence function $B_h(r)$ can be expressed in terms of the phase structure function as follows:

$$B_h(r) = exp[-\frac{1}{2} D_\Phi(r)], \tag{2.10}$$

and from equation 2.8:

$$B_h(r) = exp[-\frac{1}{2}(2.914\, k^2\, C_N^2\, \partial h\, r^{5/3})]. \tag{2.11}$$

If near field conditions are assumed, that is, the turbulence layer is close enough to the pupil plane of the telescope , the coherence function at ground $B_0(r)$ is

$$B_0(r) = exp[-\frac{1}{2}D_\Phi(r)] = exp[-\frac{1}{2}(2.914\, k^2\, C_N^2\, \partial h\, r^{5/3})]. \quad (2.12)$$

The near field assumption implies that perturbations at the pupil plane consist on phase perturbations and not amplitude perturbations.

Extending the result obtained for a single turbulence layer in equation 2.11 to a continuous distribution of turbulence in different layers, the next formula is obtained for the coherence function at the output of all layers near the pupil plane of the telescope:

$$B_0(r) = exp[-\frac{1}{2}(2.914\, k^2\, r^{5/3} \int_h C_N^2(h)dh], \quad (2.13)$$

which can be generalized for any angle from the zenith ζ (ζ=0 in case of vertical propagation) in the next expression:

$$B_0(r) = exp[-\frac{1}{2}(2.914\, k^2\, (sec\zeta)\, r^{5/3} \int_h C_N^2(h)dh]. \quad (2.14)$$

A usual way to measure the turbulence severity is the Fried's parameter (or atmosphere coherence length), r_0, which can be interpreted as the aperture size from which any increase in this diameter won't yield in more increase in resolution [44]. Quantitatively this defines an aperture on which the phase distortion error in the incoming beam has a mean square value of 1 rad^2.

Fried [20] defined an expression for the atmospheric transfer function B(f) in terms of r_0 as follows:

$$B(f) = exp[-3.44(\frac{r}{r_0})^{5/3}]. \quad (2.15)$$

From equations 2.13 and 2.14 the value of r_0 for the integrated turbulence over the pupil plane of the telescope can be obtained:

$$r_0 = [0.423\, k^2(sec\zeta) \int_h C_N^2(h)dh]^{-3/5}, \quad (2.16)$$

where $k=2\pi/\lambda$ is the wave number.

From equations 2.8 and 2.16 the expression of the phase structure in terms of r_0 can be deduced:

$$D_{\Phi}(r) = 6.88(\frac{r}{r_0})^{5/3}. \tag{2.17}$$

Strong turbulence yields low values of r_0, while weak turbulence is expressed in high r_0 values. Typical values are expressed for a wavelength of 0.5µm, and could range from 5 cm for strong turbulence to 20 cm for weak turbulence, but average values are among 7-12 cm [28]. From that formula, when λ increases r_0 decreases, so the seeing improves, which in turn means that telescope used at larger wavelengths suffer to lesser extent the turbulence effect. That explains why AO has been more successful when correcting these wavelengths, and therefore this gives shorter wavelengths, as the visible spectrum, more potential in research opportunity as they are harder to be corrected.

Fried parameter r_0 provides a way to interpret the turbulence severity, but this is an incomplete description, as it combines all the atmosphere layers that the light has to traverse in its way downwards the telescope. To determine the performance of a particular adaptive optics system, is useful to know the distribution of turbulence with altitude. The atmospheric turbulence profile can be divided in three main layers: surface to about 1 km above the ground, planetary boundary from 1 to 8-10 km height, and tropopause around 10 km height. Above this height turbulence decreases quickly and around 25 km height turbulence effects vanish. Turbulence in surface layer depends strongly of local climatic conditions and is where usually most of the wavefront aberrations are produced.

The angular resolution of a telescope improves when the ratio λ/D decreases, so for a particular wavelength, the larger the aperture of telescope, the better its resolution. But when turbulence exists in the optical path coming to the telescope this is not true anymore, and now the angular resolution will be limited to the ratio λ/r_0. Therefore for an uncompensated telescope with aperture larger than these values of r_0, the angular resolution will be limited by atmosphere turbulence and not for the physical limitations of the telescope. In other words, the seeing disk, that is the area occupied by a long exposure image, is determined by the ratio λ/r_0 and not for λ/D. Typical values of seeing range from 0.5 arc seconds in the best case (average seeing value in Mauna Kea (Hawaii), one of the best astronomical spots in the world) to 2 arc seconds or more in worse cases.

2.3.3 Temporal characteristics of atmosphere turbulence

An AO system needs to apply the wavefront correction to the deformable and tip-tilt mirrors fast enough to compensate turbulence dynamics. The atmosphere turbulence dynamics depend on the effect of winds which moves the turbulent layers, and the motion inside the turbulence. Greenwood [25] defined an expression the measure the frequency of changes of turbulence dynamics with the next equation:

$$f_G = [0.102\, k^2 (sec\zeta) \int_0^\infty C_n^2(h)\, v^{5/3}(h) dh]^{3/5}. \tag{2.18}$$

In this expression can be observed that the value of Greenwood frequency is determined by the turbulence and wind profiles of the atmosphere in a particular site. The knowledge of f_G allows to estimate the error introduced by time delays in an AO system. From empirical data of different researchers, turbulence rate variations are difficult to predict, because depends of local conditions, time, geographical situation and other factors, but for practical purposes approximately 1 kHz can be considered a good target to aim for an AO design working in average atmosphere conditions.

2.3.4 Angular anisoplanatism

Anisoplanatism is an important limitation in AO systems. Strictly speaking, the wavefront measured from a reference point source is only valid for an object that is situated in the same direction of the reference. If there is only one layer of turbulence close to the telescope entrance pupil, then the wavefront error could be corrected in any input angle if the wavefront corrector is situated at the conjugate of the pupil. However, in fact the turbulence is distributed along the beam path when it traverses the atmosphere, which makes it so the overall wavefront error is not related with a particular layer, so the effect is stronger as the angle of arrival increases.

In equation 2.8 was shown the expression for the phase structure function in the case of an incident plane wavefront that crosses a thin turbulent layer of thickness ∂h, that is reproduced here:

$$D_\Phi(r) = 2.914\, k^2\, C_N^2\, \partial h\, r^{5/3}. \tag{2.19}$$

If this expression is generalized for the case of a continuous distribution of turbulence layers and for any angle ζ from the zenith, the next equation is obtained:

$$D_{\Phi}(r) = \langle\sigma_{\theta}^{2}\rangle = 2.914\,k^{2}(sec\zeta)\,r^{5/3}\int_{h} C_{N}^{2}(h)dh, \tag{2.20}$$

which express the mean-square wavefront error between two points situated in that wavefront and separated a distance r. This distance can be expressed as a function of z, the beams range, with the next expression:

$$r(z) = \theta z = \theta h sec(\zeta). \tag{2.21}$$

Substituting expression 2.21 in 2.20 we obtain:

$$\langle\sigma_{\theta}^{2}\rangle = 2.914\,k^{2}(sec(\zeta))\int_{h} C_{N}^{2}(\theta\,h\,sec(\zeta))^{5/3}dh = 2.914\,k^{2}(sec(\zeta))^{8/3}\theta^{5/3}\int_{h} C_{N}^{2}\,h^{5/3}dh. \tag{2.22}$$

If θ_0 is the angle defined as

$$\theta_0 = [2.914\,k^{2}(sec(\zeta))^{8/3}\int_{h} C_{N}^{2}(h)\,h^{5/3}dh]^{-3/5}, \tag{2.23}$$

then the anisoplanatic error for any angle θ can be obtained through the expression:

$$\langle\sigma_{\theta}^{2}\rangle = (\frac{\theta}{\theta_0})^{5/3}, \tag{2.24}$$

where θ_0 is known as the anisoplanatic angle.

It's interesting to relate the anisoplanatic angle θ_0 in terms of the coherence length r_0. In equation 2.16 it was obtained an expression for the coherence length r_0, that is reproduced here:

$$r_0 = [0.423k^{2}(sec(\zeta))\int_{h} C_{n}^{2}(h)dh]^{-3/5}. \tag{2.25}$$

Combining equations 2.25 and 2.23 the next expression is obtained:

$$\frac{\theta_0}{r_0} = [6.88(sec(\zeta))^{5/3}\frac{\int_h C_{N}^{2}(h)h^{5/3}dh}{\int_h dhC_{n}^{2}(h)dh}]^{-3/5}. \tag{2.26}$$

If the mean turbulence height is defined as:

$$\bar{h} = [\frac{\int_h C_N^2(h) h^{5/3} dh}{\int_h C_n^2(h) dh}]^{3/5}, \tag{2.27}$$

equation 2.26 can be expressed as follows:

$$\frac{\theta_0}{r_0} = 6.88^{-3/5}(sec(\zeta))^{-1}(\bar{h})^{-1}, \tag{2.28}$$

or what is the same:

$$\theta_0 = 0.314(cos(\zeta))\frac{r_0}{\bar{h}}. \tag{2.29}$$

The previous expression is useful to estimate typical values of the anisoplanatic angle. Both r_0 and θ_0 depend on the wavelength and the refractive index structure constant C_N^2. C_N^2 has a profile which depends strongly on the height above sea level, and also varies with the day time and the location. Values or r_0 have been obtained by different authors, but as indicated in section 2.3.2, typical values of r_0 in the visible spectrum can range from 5 cm for strong turbulence, to 20 cm for weak turbulence.

To simplify calculations in equation 2.29 only one layer of turbulence is considered, being $\bar{h}$ the height of that particular layer. In table 2.1 typical values of the anisoplanatic angle θ_0 for a single turbulence layer situated at three different heights are shown. Three different turbulence conditions in the visible spectrum, and a zenith angle $\zeta = 0$ are considered.

Table 2.1: Typical values of anisoplanatic angle for different turbulence strength and three different single turbulence layers, at 1, 5 and 10 km height, obtained with the formula 2.29.

Turbulence strength	r_0 (cm)	θ_0 (arcsec) 1 km height	θ_0 (arcsec) 5 km height	θ_0 (arcsec) 10 km height
Strong	5	3.24	0.65	0.32
Medium	12	7.80	1.50	0.78
Weak	20	13	2.60	1.30

2.3.5 Performance of adaptive optics systems: Strehl ratio

The performance of a telescope can be evaluated through the ability to focus the light of a distant astronomical point source in the smallest possible disc. One way to measure this performance is with the Strehl ratio, which is defined as the ratio of the actual peak intensity in a point source image, to the peak intensity of that image when this is produced by a diffraction limited telescope.

Different approximate expressions have been developed to determine the Strehl ratio from the mean-square wavefront error, that in general terms should be used with care. For small phase errors, up to about 0.6 rad rms, Born and Wolf [6] deduced an expression for SR:

$$SR \approx 1 - (\sigma_p)^2, \tag{2.30}$$

where σ_{p} is the standard deviation of the phase.

A similar expression was derived by Marechal [41]:

$$SR \geq [1 - \frac{1}{2}(\sigma_p)^2]^2, \tag{2.31}$$

which for small phase errors up to 0.5 rad rms yields approximately the same values of Born and Wolf expression. Marechal suggested as a criterion, that a optical system with SR equal or greater than 0.8 can be considered acceptable. Hardy [28] states that this expression could be valid for fixed optical systems formed by lenses or mirrors, but this could be restrictive when evaluating the performance of an AO system. Another expression called the extended Marechal approximation is:

$$SR \approx e^{-(\sigma_p)^2}. \tag{2.32}$$

This equation seems to be valid with larger phase errors that the other two expressions, up to around 2 rad rms, and is regularly used as a performance measurement for adaptive optics systems.

2.3.6 Considerations for small aperture telescopes in low altitudes

In the surface layer of the atmosphere (up to approximately 1 km height) is where most of contributions to wavefront aberrations are produced. When telescopes are sited in high mountains, as is the usual case for big telescopes, aberrations are greatly reduced. In this research the proposed AO system is sited at low altitudes, which increases the wavefront aberrations. This can be observed in the Hufnagel-Valley model of figure 2.3, where C_N^2 values range between 10^{-15} $m^{-2/3}$ near the ground, to 10^{-17} $m^{-2/3}$ at 1 km.

The small size of the telescope aperture will limit the degrees of freedom of the wavefront correcting devices and also the photon flux that the wavefront sensor device receives. Eventually the telescope aperture size will limit the extension and the order of the aberrations that can be corrected.

For cost and logistic reasons, the AO system developed in this research is meant to work with natural guide star (NGS), which means that the number of targets that could be covered with the AO system will have a limitation (more information about NGS systems in section 2.4 of this chapter).

In figure 2.4 is shown the resolution of a telescope expressed in terms of its normalized image size, for different values of the telescope aperture, for long and short exposure images. For practical purposes short exposure is considered when time is less than about 1/50 seconds.

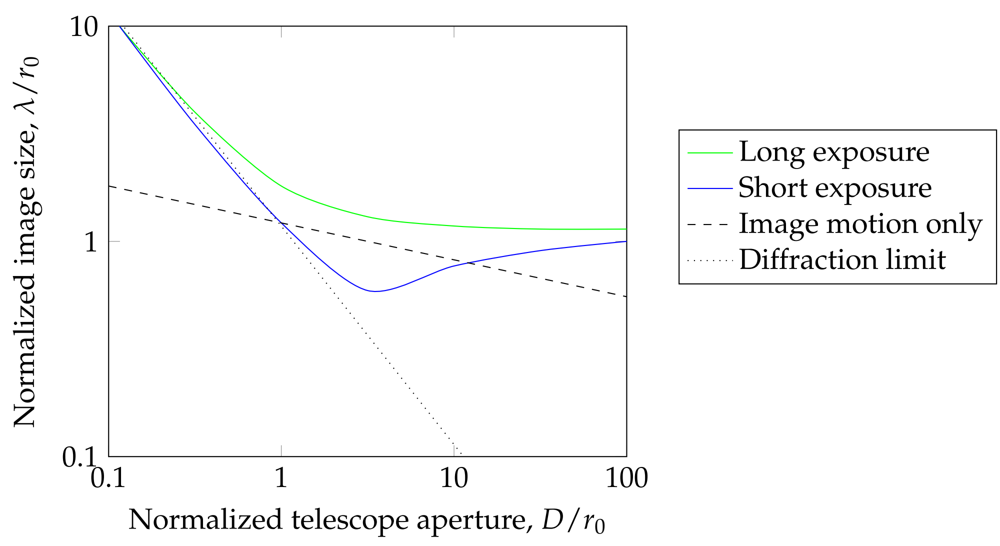

Figure 2.4: Telescope resolution as a function of D/r_0 (adapted from [28]).

In this chart the angular image size is normalized to the coherence length r_0, in units of λ/r_0, and also the telescope aperture, in units of D/r_0. According to Hardy [28], some important properties of the uncorrected image can be deduced from this figure depending on the telescope aperture size:

- If the aperture of the telescope is small ($D/r_0 < 1$), the effect of the turbulence in the image is minimal (long exposure and short exposure curves are close to diffraction limit), and the wavefront distortion mainly produces image motion, that is, tip and tilt. The image motion curve is below the diffraction limit, so with this size of telescope, AO has little room for improvement.

- For values of D/r_0 between 1 and 10 the image motion is significant, and also the difference between the long and short exposure curves. With this telescope apertures and for certain values of r_0 (that is, the turbulence strength), there is a potential improvement with the use of an AO system, demonstrated by the difference between short and long exposure curves, and the diffraction limit curve. The correction of image motion improves the image significantly but still there is margin to improve higher orders of aberrations. These conditions can be applied for the telescope of this research, with a 0.4 metres aperture diameter, so that under certain turbulence conditions, low and some high orders of aberration could be corrected. We will show however that with this scenario there is worthwhile gains to be made.

- For values of D/r_0 greater than 10, that is, big telescopes, or small telescopes in poor air, the potential improvement of the image quality with adaptive optics (difference between short and long exposure curves and the diffraction limit curve) is greater that in the previous case, and also difference seen in figure 2.4 between long and short exposure reduces. Image motion now is not an important effect. That's the reason telescopes around the world with apertures greater than 3 to 4 metres include an AO correction system, or there is a plan to install it.

2.4 AO systems for astronomy

An AO system for astronomy consists of three main components: the wavefront sensor to obtain information about aberrations in the incoming beam, the wavefront correctors (typically tip-tilt and deformable mirrors) to correct mechanically these aberrations, and the control system, which transforms the wavefront sensor information into the appropriate signals to drive the actuators of the wavefront correctors. In figure 2.5 is shown the basic operation and main components of a traditional AO system for astronomy applications.

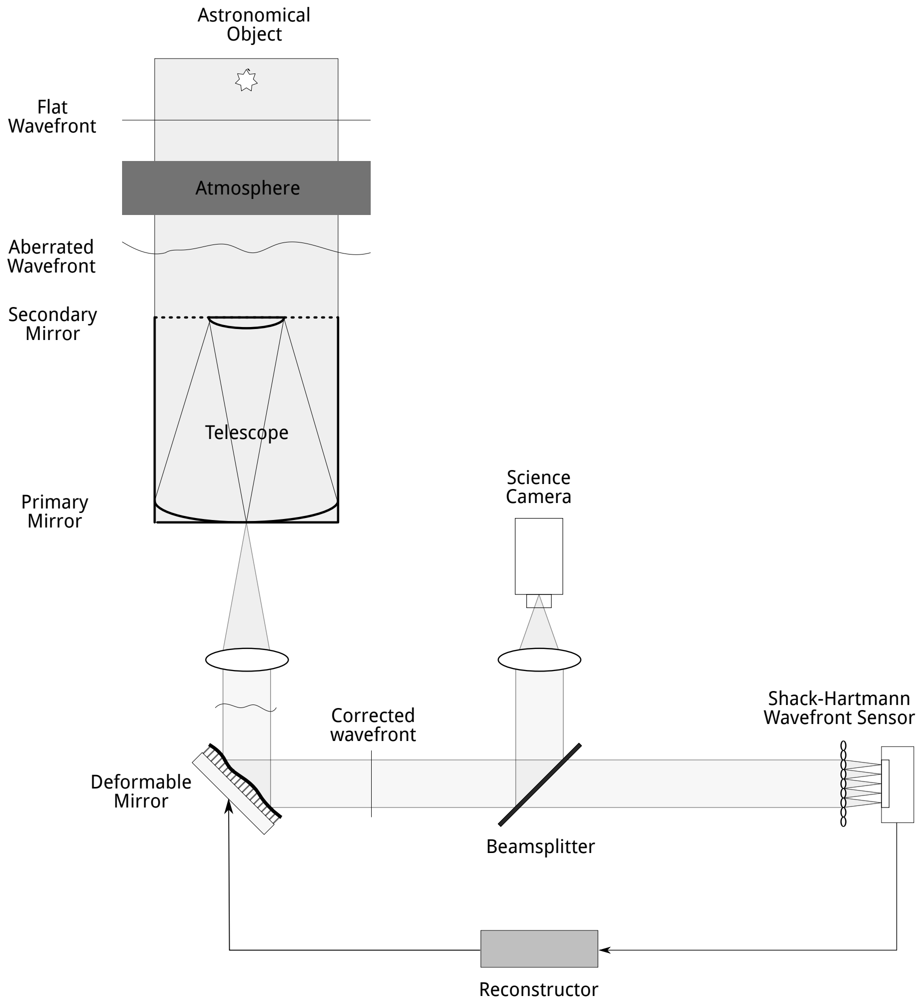

Figure 2.5: Operation of an AO system for astronomy.

In this diagram, initially the light wavefront coming from distant astronomical light sources don't show aberrations, but after traversing the atmosphere, some aberrations will appear in the wavefront. At the telescope output a collimation lens system reproduces the aberrated wavefront at a smaller scale, and then passes it through the wavefront corrector, tip-tilt and deformable mirrors, towards a beamsplitter which divides the wavefront into two beams with the same information but half of the energy each (in case of a 50/50 beamsplitter). One of the beams coming from the beamsplitter is directed towards the wavefront sensor, which is the device which measures the aberration, in the case of a SH wavefront sensor detecting slopes in subapertures which indicates change in the wavefront phase, and transforms this information into signals that can be interpreted by the control system. The control system processes these data transforming them into signals that can be applied to the deformable and tip-tilt mirror actuators, to correct the wavefront mechanically, and closing the control loop. Finally the corrected image could be observed in the science camera.

Natural Guide Star/Laser Guide Star

To gather the light that will be used to extract information about the wavefront aberration, different sources could be used. In the first place, light coming from the object under study itself or from a nearby natural source can be used, which is known as a NGS (Natural Guide Star). But also an artificial guide star can be used created with a laser source originated in the adaptive optics system itself, which is known as a LGS (Laser Guide Star).

In many cases, the light coming from the source under study is not bright enough to extract the aberration information in the wavefront sensor. The beamsplitter, the number of subapertures in which the beam is divided and the integration time, generally in the order of milliseconds to cope with the change rate of atmosphere turbulence, are limiting factors which restrict the photon flux that reaches the wavefront sensor. All these factors define how dim an object can be in order to be corrected with enough quality. A NGS nearby the object under study can be used as reference. This can increase the number of photons that reach the wavefront sensor, but this time the limiting factor is the anisoplanatism effect that was explained in section 2.3.4. The anisoplanatic angle generally is in the order of a few arc seconds, so the possible astronomical objects that can be studied are limited severely to a few. In any case, this doesn't mean that a NGS adaptive optics system is not useful, just that is important to be aware of its limitations which will determine its scope, applications and performance.

A solution that was proposed in the 1980s is the use of artificial beacons that utilize the back scatter light or fluorescence of a laser that is originated close to the adaptive optics system. This solution corrects in some degree the lack of photons that reach the image sensor and also broaden drastically the astronomical objects under study, but also presents some issues, as the focal anisoplanatism, or still the necessity of a natural reference in order to stabilize its position. These are generally not within the realms of amateur astronomer so are discussed no further herein.

Adaptive Optics/Active Optics

Adaptive optics is not limited to correct atmosphere turbulence, although this is the most important limitation in ground based telescopes. It can also corrects errors in the telescope mirrors created by low temporal frequency variations as temperature or gravity. But generally these low frequency disturbances are corrected in a separate system, known as active optics. Active optics makes reference to the techniques to control or correct the distortions introduced by mechanical, thermal or optical effects in the telescope itself, where the nature of these variations is slow, typically below 1 Hz [5]. Adaptive optics corrects the distortions caused by the atmosphere, which occurs at a high rate, typically 1 kHz or more, compared to active optics, so the correction devices have to be situated in the image of the pupil for instance, where fast and small correctors can be used.

2.4.1 Wavefront sensing

The WFS function is to obtain phase data of the incident wavefront and transform this data as signals that can be interpreted by the control stage. As a data transducer, it transforms the light into electric signals, and for this purpose includes an image sensor. Typically an optical system is situated before the light is received in the image sensor, to adapt the light for the functionality of the particular wavefront sensor. Two techniques can be applied to obtain the phase information, direct and indirect [28]. In direct techniques, a particular property of the wavefront, as the slope or the curvature, is measured in the optical pupil of the telescope. Direct methods can be subdivided in zonal or modal. Indirect techniques are based in the measure of a related parameter to the wavefront phase, usually the intensity distribution of the wavefront in the image plane.

Among all the wavefront sensor types, three of them stand out, which are Shack-Hartmann (SH), Curvature and Pyramidal. The SH wavefront sensor has become the more common sensor in adaptive optics for astronomy, due to its robustness and ease of design, and later in this section a more detailed description of this sensor is given. As shown in table 1.1 of chapter 1, most of the WFS used in current or planned AO systems for big telescopes are Shack-Hartmann type. Curvature and Pyramidal, proposed by Roddier [54] and Ragazzoni [51] respectively, are interesting alternatives to SH wavefront sensor, and nowadays some AO systems include them.

Different parameters influence the efficiency of a particular wavefront sensor [28], namely:

- Phase to intensity conversion efficiency in the image sensor.
- Fraction of incident light which reaches the WFS.
- Quantum efficiency of image sensor.
- Signal to noise ratio of image sensor.
- Algorithm efficiency to convert photons detected to phase measurements.

The first two parameters depend on the optical design, which is covered in this research in chapter 3, and the type of wavefront sensor chosen. The next two parameters depend on the technology of the particular model of image sensor. The last parameter depends on the control algorithm to convert the measured parameter (subaperture slopes in case of a SH WFS) into phase values, and this topic is covered in chapter 4 about the control system.

CMOS/CCD

It is difficult to make an statement about which technology, CCD (Charged Coupled Device) or CMOS (Complementary Metal Oxide Semiconductor), is better in general terms for astronomical imaging, and in particular for wavefront sensing. What is truth is that the use of CMOS image sensor in astronomy has experienced an increase, a field that traditionally has been mostly populated by CCD image sensors. This is due to the development of more sensitive and fast CMOS image sensors and also with better resolution. Nowadays we can find in the market inexpensive CMOS image sensors with similar features to their CCD counterparts.

In the case of the design of a small form factor adaptive optics system, as is the case of this research, CMOS sensors show several advantages, as low cost and ease of integration. CMOS sensor can be populated with the rest of integrated circuits in a single and small size board. Also signals coming from a CMOS sensor are digital, so there is no need of an external analog to digital conversion stage, as in the case of CCD image sensors.

In figure 2.11 at the end of the chapter is shown a picture of the board developed in UNSW Canberra and used in this research as the AO control board, which includes a CMOS image sensor. In section 3.3.2 of chapter 3 are listed the main specifications of the CMOS image sensor used in this research.

Shack-Hartmann wavefront sensor

The SH wavefront sensor is formed by a micro lenslet array (MLA) and a image sensor. The light beam incident on the lenslet array is divided into several small beams corresponding with each of the subapertures which form the lenslet. The image sensor is positioned in the focal plane of the subaperture beams. The positions of the focused beams are shifted in a perpendicular plane if the phase of the incident wavefront changes with respect to a reference wavefront, obtained with a non-aberrated beam, that is, a plane wave. A measurement of the local slopes of the beam phases in each subaperture can be obtained from the positions of these local focused beams, as it will be shown in section 2.4.3 about wavefront reconstruction. In figure 2.6 is shown the SH wavefront sensor operating principle, where gray dots and black dots represent the array of focused beams from a non-aberrated and an aberrated wavefront respectively.

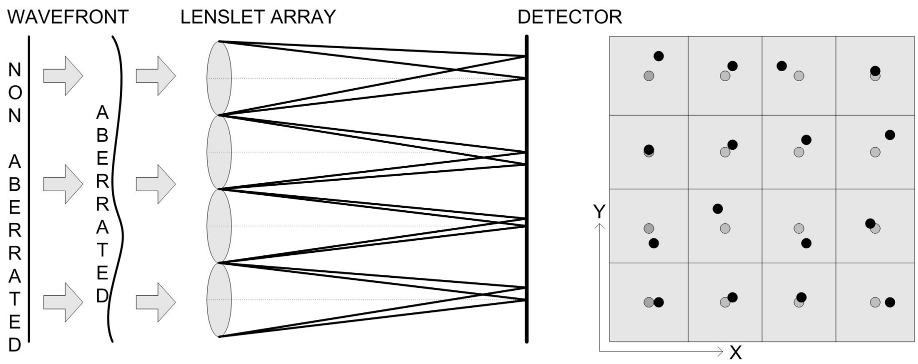

Figure 2.6: SH wavefront sensor operation principle.

The three main parameters which define the design of a SH sensor are the number of subapertures, the number of pixels per subaperture and the pixel size. The number of subapertures will define the numbers of beams in which the incident wavefront will be divided, which will influence the photon flux in each beam that reaches the detector. This is an important parameter when low light conditions exist, as is the case of this research. The number of pixels per subaperture will determine the resolution of the computed gradients. The minimum number of pixels per subaperture consist of a quadcell detector, formed by four orthogonal cells, but these number of pixels can be increased. Increasing the number of pixels will increase the resolution, but also this will affect adversely the processing time and the photon noise induced in the phase measurements. The pixel size influences in the linearity and the dynamic range. Small pixels show good linearity but small dynamic range. As pixel size increases, the dynamic range will improve at the expense of linearity.

2.4.2 Wavefront corrector

The wavefront correctors generally consist of two types of devices, where each corrects some part of the aberrations: tip-tilt mirror to correct tilts in orthogonal axes perpendicular to the incident wavefront, and deformable mirror to correct a number of the classical higher order optical aberrations, as defocus, astigmatism or trefoil.

The gap existent between the Babcock conceptual proposal of an adaptive optics system, and the first feasible system in the 1970s, was partly due to the lack of a suitable wavefront corrector, that were capable to cope with the needed specifications. Nowadays the deformable mirror is the most common used device to correct aberrations of higher order than tip and tilt.

There are different mirror technologies to correct mechanically a wavefront with a deformable mirror, such as segmented, bimorph, membrane or continuous faceplate mirrors. It is not in the scope of this thesis to show the characteristics and performance of each of these types, but it is interesting to describe the continuous faceplate mirror, and more specifically the piezoelectric deformable mirror (PDM) in some detail, which is the one used in this research.

Piezoelectric Deformable Mirror (PDM)

In figure 2.7 is represented a schematic of the structure of a PDM, that essentially consists of a series of discrete actuators fixed to a stable base and bonded to a thin flexible deformable plate.

Some of the main parameters that characterize a deformable mirror are: type and number of actuators, dynamic range, time response, surface flatness, hysteresis, influence functions and power dissipation. In section 3.3.2 of chapter 3 about the optical design are enumerated some specifications for the deformable mirror used in this research, and below is detailed the influence of some of these parameters in the AO system design.

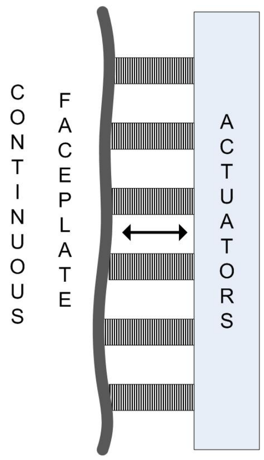

Figure 2.7: Structure of a piezoelectric deformable mirror.

The number of actuators of a DM, also known as degrees of freedom, defines the order of the compensation that can be obtained. For circular apertures it is convenient that the actuators are positioned in an array of hexagonal shape, in order to have a more uniform spacing between them. Also this spacing or pitch defines the fitting error when compared to the coherence length r_0. Piezoelectric actuators are based on the piezoelectric effect, that is, the creation of stress in certain materials due to the application of an electric field. To create a useful shift of the actuators, a relatively high voltage has to be applied between their electrodes. Therefore a high voltage power supply is needed to drive the actuators, and driver boards are needed to adapt the low voltage signals coming from the control stage to the actuators. In the case of the design of a compact and small form factor AO system such as the one in this research, this involves the design of drivers adapted to these constraints. In chapter 4 about the control system is shown the design built in UNSW Canberra for this purpose.

The dynamic range of the correction is defined by the stroke of the actuators, that is, the maximum excursion peak-to-valley that the actuators can be moved. The value of the stroke, ranging typically from 2 µm to 10 µm, will determine the severity of the turbulence that can be corrected. A relative high stroke value (as the one of the PDM used in this research which is 8 µm) will be theoretically enough to correct tip and tilt and also aberrations of higher order, but this can decrease the dynamic range available to correct these high order distortions. That's why sometimes it can be convenient to correct wavefront tip and tilt with a separate fast steering mirror, dedicated exclusively to correct these low order aberrations.

The time response of a deformable mirror is an important design factor, as it influences in the overall delay of the closed loop control. This delay must be considered in the control system design as it will determine the maximum gap time available for the calculations in the control stage.

The influence functions of a deformable mirror are defined as the shapes created in the overall faceplate when only one actuator is driven. The influence functions are mainly determined by the stiffness of the faceplate and actuators, and depend on the mechanical structure of a particular deformable mirror.

2.4.3 Wavefront reconstruction and control

The control system obtains the gain and phase information of the incoming wavefront from the sensor, and processes it in order to obtain signals that will be applied to the actuators of the deformable and tip-tilt mirrors, to reproduce a conjugate of the aberrated wavefront. This is a real time closed loop process. In order to achieve the real time requirement of the feedback loop, the whole computation time has to be within the variation rate of the refraction index distortions introduced by atmosphere, typically 10 ms for well sited telescopes, but potentially much shorter for the situations considered herein, in the order of a few milliseconds. The computation time since the data are acquired by the wavefront sensor until signals drive the actuators of the wavefront correctors is called latency.

Open loop/Closed loop

An AO system can operate in two modes: open loop or feed-forward and closed loop or feedback. These two modes are represented schematically in figure 2.8 (open loop above the light beam and closed loop below it). In open loop mode the aberrated wavefront is measured in the first place with one of the beams in which the incoming light is divided, and from these measurements, the wavefront reconstructor calculates the required signals for the actuators of the wavefront correctors, that are situated after the beamsplitter. This mode requires a precise calibration of both the wavefront sensor and the wavefront corrector for any magnitude in the phase error. This makes the AO system difficult to calibrate, and for that reason, generally the closed loop operation is preferred over the open loop.

In closed loop mode, the wavefront sensor detects the difference between the incoming wavefront and the last correction made in the wavefront corrector, that

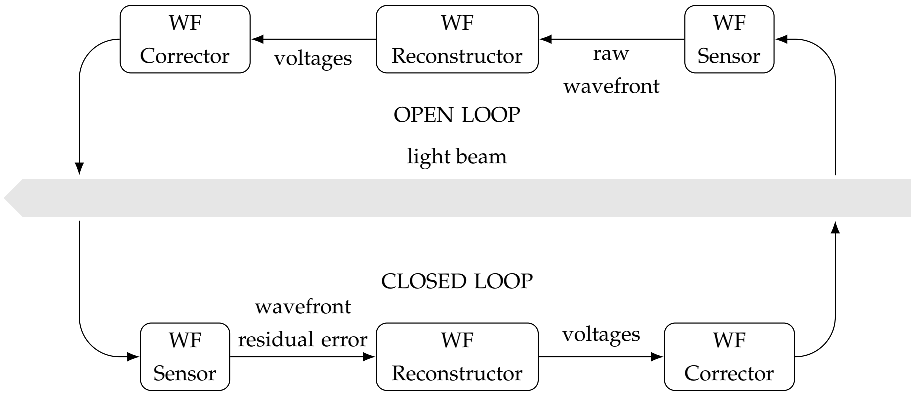

Figure 2.8: Open loop mode (above the light beam) and closed loop mode (below the light beam). Light beam travels from right to left.

is, the residual error. This way, controlling the closed loop gain, residual error can be forced to zero, to avoid instability in the feedback loop.

Zonal/Modal reconstruction

There are two ways to represent the wavefront over an aperture, zonal and modal. In the first case, the aperture is divided in a number of areas or subapertures, and the aberrations in the wavefront, as tip, tilt or curvature, are specified for each of these subapertures. In modal reconstruction, the wavefront is considered as a sum of mathematical functions over the whole aperture. In optics, Zernike polynomials are the traditional functions to represent a wavefront over a circular aperture, where each of the lower order polynomials represents a specific optical aberration. In the next subsection Zernike polynomials expressions are shown. Another set of functions that are used to describe a wavefront are the Karhunen-Love polynomials. Both Zernike and Karhunen-Love low order terms are very similar, so there are no too many differences when analysing first optical aberrations with any of them [28]. From this reference, the next paragraph has been extracted to clarify the difference between both (Zernike and Karhunen-Love) polynomials: "Zernike polynomials are not statistically independent, so wavefronts generated directly from the sum of Zernike coefficients do not have zero mean values over time. A similar set of orthonormal functions with completely uncorrelated elements maybe generated using the Karhunen-Love expansion. Fried (David. L.Fried. Probability of getting a lucky short-exposure image through turbulence. J. Opt. Soc. Am. 68, 1651-1657) has shown that for a given number of modal corrections, the Karhunen-Love expansion is optimal in that it gives a better fit to atmospherically distorted wavefronts than any other orthogonal set, in terms of minimizing the mean-square residual error. However, the difference in performance between Zernike and Karhunen-Love functions is not large, producing at most 10% improvement in the peak value of normalized resolution when 21 correction terms are used (Wang and Markey. Modal compensation of atmospheric turbulence phase distortion. J. Opt. Soc. Am. 68, 78-87). For low-order correction of up to 10 terms (through coma), the Zernike polynomials are close to optimum."

For practical purposes, both wavefront sensor and wavefront corrector usually are built using a zonal configuration. Nevertheless, the modal approach is more appropriate for computation, so an interesting approach is convert the data coming from a zonal wavefront sensor to modal functions in order to ease the processing stage. Then these modal data are transformed again to zonal data, required for a wavefront corrector comprising a finite number of actuators, that is, applying a zonal correction. This is the approach followed in this research.

Zernike polynomials

Zernike polynomials are a convenient way to represent the optical wavefront over the telescope aperture. In this way, the aberrated wavefront can be decomposed in a series of polynomials terms, each of them corresponding to a particular optical aberration. The Zernike polynomials in polar coordinates on a unit circle are defined with the next expression:

$$\begin{aligned} Z_{even} &= \sqrt{n+1}R_n^m(r)\sqrt{2}cos(m\theta) && m \neq 0 \\ Z_{odd} &= \sqrt{n+1}R_n^m(r)\sqrt{2}sin(m\theta) && m \neq 0 \\ Z &= \sqrt{n+1}R_n^0(r) && m = 0, \end{aligned} \tag{2.33}$$

where

$$R_n^m(r) = \sum_{S=0}^{(n-m)/2} \frac{(-1)^S (n-S)!\, r^{n-2S}}{S!\,[(n+m)/2-S]!\,[(n-m)/2-S]!}. \tag{2.34}$$

Substituting $x = r\,cos\theta$ and $y = r\sin\theta$, the Zernike polynomials in cartesian coordinates are obtained. In table 2.2 are shown the first 10 Zernike polynomials, normalized on a unit circle, both in polar and cartesian coordinates. In figures 2.9 and 2.10 are represented graphically these 10 first Zernike modes, indicating their corresponding classical optical aberration, according to Noll index [47].

Table 2.2: First 10 Zernike polynomials normalized on a unit circle, in polar and cartesian coordinates.

	Azimuthal Frequency (m)			
Radial (n)	0	1	2	3
0	$Z_1 = 1$ Constant			
1		$Z_2 = 2rcos\theta = 2x$ $Z_3 = 2rsin\theta = 2y$ x and y tilts		
2	$Z_4 = \sqrt{3}(2r^2 - 1)$ $= \sqrt{3}(2x^2 + 2y^2 - 1)$ Defocus		$Z_5 = \sqrt{6}r^2 sin2\theta$ $= \sqrt{6}\, 2xy$ $Z_6 = \sqrt{6}r^2 cos2\theta$ $\sqrt{6}\,(x^2 - y^2)$ Astigmatism	
3		$Z_7 = \sqrt{8}(3r^3 - 2r)sin\theta$ $= \sqrt{8}\, 3y(x^2 + y^2) - 6y$ $Z_8 = \sqrt{8}(3r^3 - 2r)cos\theta$ $= \sqrt{8}\, 3x(x^2 + y^2) - 6x$ Coma		$Z_9 = \sqrt{8}r^3 sin3\theta$ $= \sqrt{8}y(3x^2 - y^2)$ $Z_{10} = \sqrt{8}r^3 cos3\theta$ $= \sqrt{8}x(x^2 - 3y^2)$ Trefoil

Modal reconstruction based on zonal wavefront sensing. Stages of the process

The operations performed by the control system are:

- Obtaining the positions of the focal spots (centroids).
- Conversion of these positions to gradients (difference with a reference wavefront).
- Reconstruction of the wavefront.

In the second stage, the centroids shift computation can be performed by several algorithms. A detailed study of the centroiding algorithm is shown in chapter 4 about the control system. The Center of Gravity (CoG) calculation is a straightforward method to obtain these deviations, though it has some limitations with real spots [22]. With the aim to show the centroiding algorithm operation, the CoG is used for centroids computation, although in the implementation of the AO system, more algorithms have been tested and implemented.

In the case of the CoG algorithm, if W(x,y) is the wavefront captured in the detector with respect to axis x and y, by geometry these differences can be related with the corresponding slopes in each of the subapertures with the next expression:

$$\frac{1}{s}\int_{s}\frac{\partial W(x,y)}{\partial x}ds = \frac{\Delta x(x,y)}{f}. \tag{2.35}$$

In equation 2.35 this relation is expressed in x axis, where $\Delta x(x,y)$ is the gradient in the centroid position in x axis for a subaperture, and f is the focal distance of each of the lens of the micro lenslet array. An analogous expression can be deduced for the y axis.

The next step is the reconstruction process, where the control system receives the centroids positions of each subaperture from the detector, and produces the signals that will be sent to the actuators of the tip-tilt and deformable mirrors, with minimum latency.

To reconstruct the aberrated wavefront, a modal approach is used, whereby W(x,y) can be expressed as a weighted sum of Zernike polynomials, with each of terms representing a different optical aberration, as follows:

$$W(x,y) = \sum_{i=1}^{N} w_i Z_i(x,y), \tag{2.36}$$

where term w_i represents the Zernike coefficients of each of the aberrations, Z_i (x,y) the Zernike polynomials, and N the number of aberrations considered.

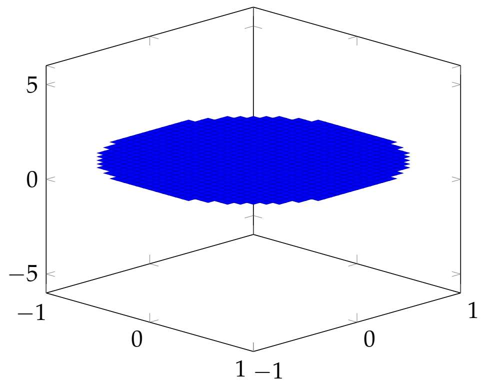

(a) Z_1 Constant n=0, m=0

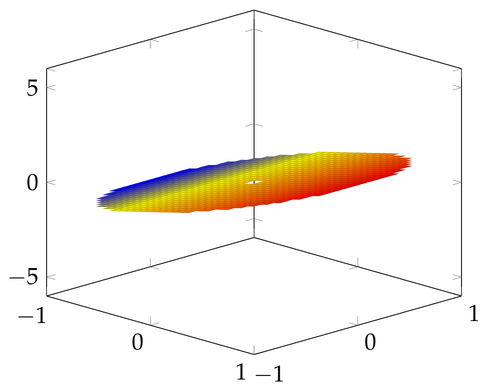

(b) Z_2 Tilt x n=1, m=1

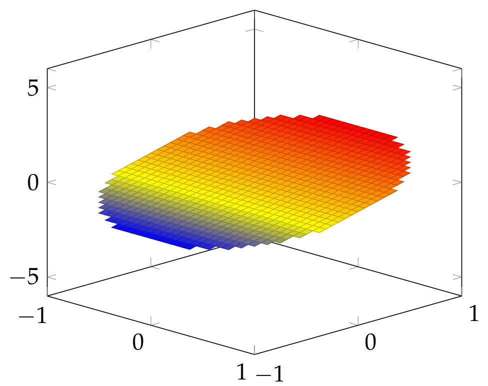

(c) Z_3 Tilt y n=1, m=-1

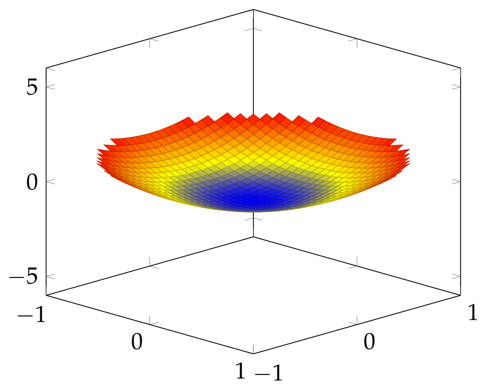

(d) Z_4 Defocus n=2, m=0

Figure 2.9: Zernike polynomials 1 to 4 graphical representation with their corresponding names of classical optical aberrations.

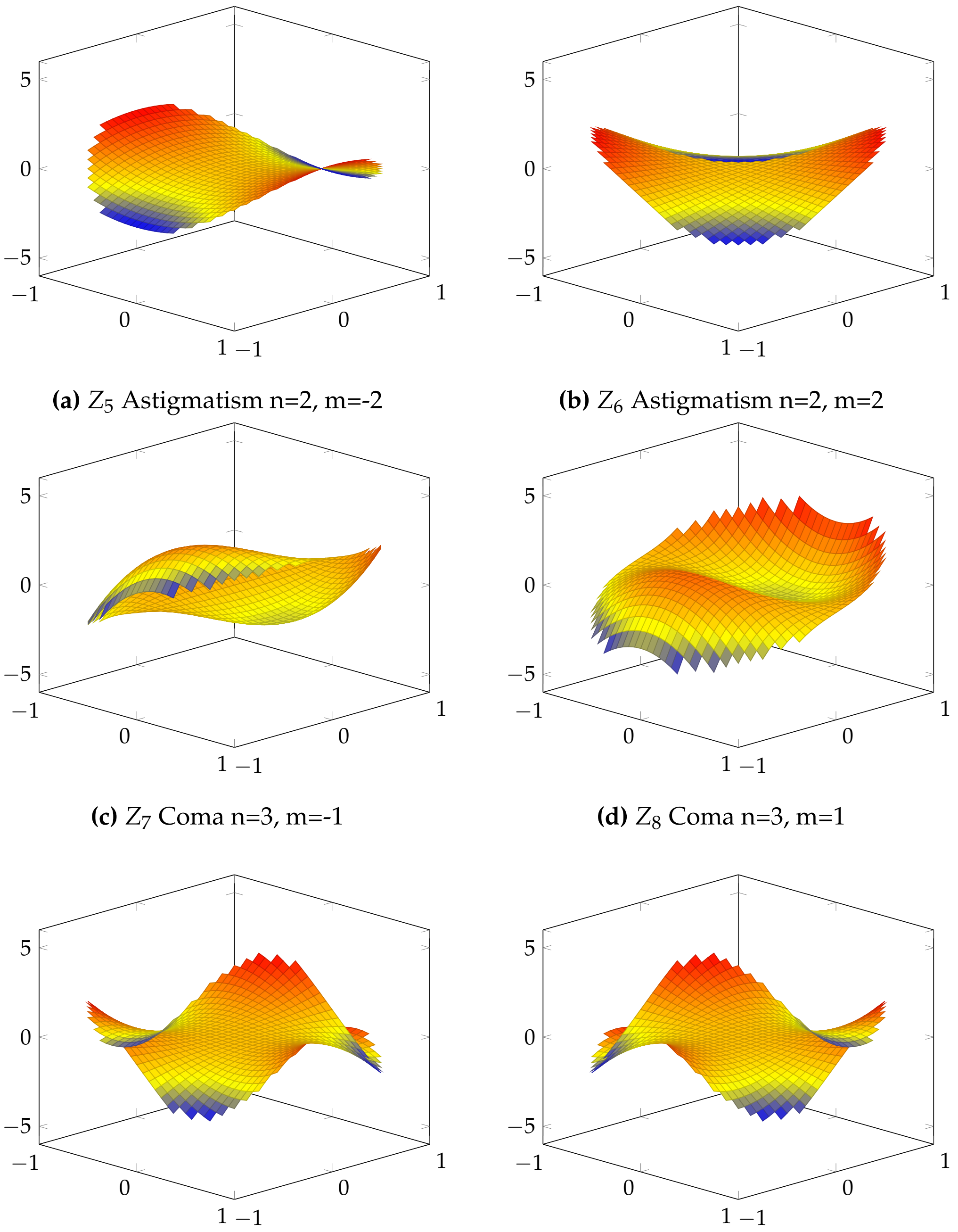

(a) Z_5 Astigmatism n=2, m=-2

(b) Z_6 Astigmatism n=2, m=2

(c) Z_7 Coma n=3, m=-1

(d) Z_8 Coma n=3, m=1

(e) Z_9 Trefoil n=3, m=-3

(f) Z_{10} Trefoil n=3, m=3

Figure 2.10: Zernike polynomials 6 to 10 graphical representation with their corresponding names of classical optical aberrations.

From equations 2.36 and 2.35, the gradients of each of the subapertures can be related with a weighted sum of Zernike polynomials, as follows:

$$\frac{\Delta x(x,y)}{f} = \frac{1}{s}\int_s \sum_{i=1}^{N} w_i \frac{\partial Z_i(x,y)}{\partial x} ds. \tag{2.37}$$

Considering all the subapertures in both axes, equation 2.37 can be expressed in matrix form as follows:

$$\boldsymbol{\Delta}_{2k\times 1} = \boldsymbol{Z}_{2k\times N}\boldsymbol{W}_{N\times 1}. \tag{2.38}$$

In equation 2.38 k is the number of subapertures, Δ is the gradients matrix with 2k × 1 dimension, Z is the partial derivative of Zernike polynomial matrix in both axes with dimension 2k × N, and W is the Zernike coefficients matrix of dimension N × 1. In order to obtain the Zernike coefficients from equation 2.38, the least square estimation method is applied to obtain the pseudo-inverse matrix of Z, resulting in the next equation:

$$\boldsymbol{W}_{N\times 1} = \boldsymbol{C}_{N\times 2k}\boldsymbol{\Delta}_{2k\times 1}; \boldsymbol{C} = (\boldsymbol{Z}^T\boldsymbol{Z})^{-1}\boldsymbol{Z}^T, \tag{2.39}$$

where C is called the calibration matrix, with dimension N × 2k.

In order to obtain the signals to be applied to the mirror actuators, the influence functions have to be derived, each of them representing the bi-dimensional profile generated for each of the actuators. Each of the actuators will have a value to represent each of the Zernike coefficients. The matrix which relates these parameters is called the influence matrix (I).

Finally, from equation 2.39 and the influence matrix, the voltages required by the actuators to reproduce a specific wavefront can be obtained as follows:

$$\boldsymbol{V}_{1\times j} = \boldsymbol{W}^T_{1\times N}\boldsymbol{I}_{N\times j}, \tag{2.40}$$

where V is the voltages actuator matrix, and j is the number of actuators.

Details about how to obtain matrices C and I are shown in chapter 4 about the control system.

2.5 Hardware architectures for AO systems

2.5.1 Reconfigurable computing: FPGA

FPGA: Definition and features

A FPGA is an integrated circuit which contains configurable logic blocks (CLB) and interconnections, which can be programmed *in situ*. The first FPGA was introduced in the market by Xilinx in 1984, to fill the existing gap between CPLDs (Complex Programmable Logic Device) and ASICs (Application Specific Integrated Circuit), other digital integrated circuits which appeared previously. Each CLB is formed by a LUT (Look-up Table), a multiplexer, a register and fast carry logic for arithmetic operations. This logic blocks are structured in a hierarchy of LCs (Logic Cell), slices and CLBs (in Xilinx terminology). Apart from these building blocks, a typical FPGA includes other hardwired blocks as RAM (Random Access Memory), Multipliers or MACs (Multiplier-Accumulator). In figure 2.11 is shown the internal architecture of the core building block, a logic cell, in Xilinx FPGA devices.

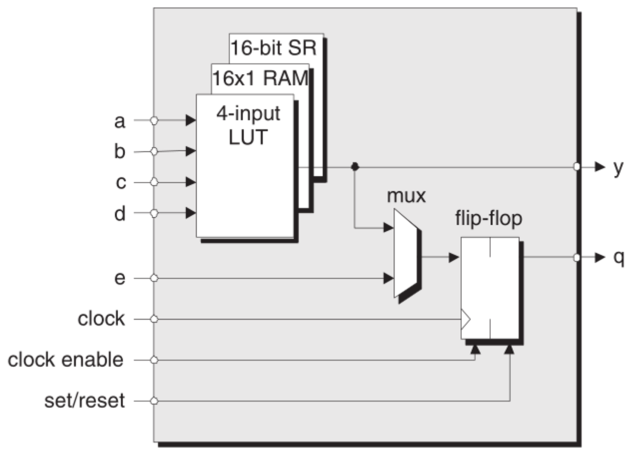

Figure 2.11: Internal architecture of an LC in Xilinx FPGA devices (source [42]).

There are different technologies to program the logic blocks and interconnections in a FPGA, as SRAM (Static Random Access Memory) cells, Flash or anti-fuse. Most of the current FPGAs today are based in SRAM cells, which allows its reprogrammability. This approach is well suited for designs that need to be implemented in a short time, which makes FPGAs an invaluable asset in computer engineering research. FPGAs based in SRAM programming technology have volatile memory, hence they need to be reconfigured each time the system is powered up. Normally an external memory device, typically an EEPROM (Electrically Erasable Programmable Read Only Memory) is used to store the code that is re-programmed in the FPGA each time the system is powered up.

Differences between FPGAs compared to DSP and CPU devices

DSPs and CPUs can operate with floating point numbers, while FPGA traditionally has lower performance with this type of operations, due to its lack of a hardwired FPU (Floating Point Unit). However nowadays some top end FPGAs can cope with these operations without a significant reduction of performance. If memory requirements are not so high, internal memory of FPGA can be used, so space in the electronic board can be saved, because there is no need to populate an external memory. To work efficiently, FPGAs use fixed point instead of floating point precision, but in each case design decisions have to be considered to optimize the data word length and not lose precision in the calculations. An analysis of this topic is shown in chapter 4 about the Control design.

Techniques to optimize resources

In an FPGA, two techniques can by used to optimize resources, Time Division Multiplexing (TDM) and resources sharing. Resources sharing consists in the implementation of only one functional block to perform several operations. For instance, a multiplier could be used to process two values, and then another two different values, coming from other data paths. But resource sharing increases connectivity, and connecting CLB/LUT with MAC or multipliers uses more connectivity rather than if they are connected with other CLB/LUT, so this issue has to be considered when sharing MAC or multipliers. Sometimes shared resources requires same cost than if they are used separately, for instance two adders in Xilinx technology. When sharing resources, room is improved but performance is worse.

Design workflow of digital signal processing algorithms in an FPGA

To perform digital signal processing in FPGA, regardless of the implementation technology, it is common practice to first perform a system level evaluation and verification of the algorithm, in a proper software environment as MATLAB. There are several ways to implement a DSP algorithm in a FPGA:

- Parallel, using hardware resources simultaneously. It’s fast but takes more device space.

- Serial, using resources sharing. Slow but occupies less space in the device.

- Mixed, using resources sharing in some degree but also hardware resources. It is a balanced solution between speed and device space.

To design a digital signal processing algorithm, first it is convenient to implement a floating point representation in MATLAB. After that, in order to implement it in a FPGA, a quantization of data needs to be done, namely to convert it to fixed point precision. If not, calculations in floating point in the FPGA would be very slow. An important design decision is selecting the optimized numbers of bits for the task, that would be the minimum number in order to reduce hardware resources thus accelerating processing time, but at the same time to keep enough precision to perform the required operation well.

Several design flows can be followed when a DSP algorithm has to be implemented in an FPGA, for example, one typical design flow would be:

- Algorithm verification at system level in floating point.

- Algorithm verification at system level in fixed point.

- Manual conversion from Register Transfer Level (RTL) to VHDL.

Nevertheless, digital signal processing algorithms of certain complexity are better designed with a higher level of abstraction that RTL. There are blocks that are used commonly and many times in these kinds of algorithms, as adders, multipliers, MACS or divisors, so there is no need to repeat these structures in the coding again and again. This solution, which is followed in this research, consists of the next steps:

- Algorithm verification at system level with IP blocks.

- Automatically create hardware models for these blocks, using System Generator from Xilinx.

- Manual conversion from RTL to VHDL of some blocks not converted by System Generator.

In chapter 4 about the control system these steps are explained with more detail.

2.5.2 Hardware technologies for AO Control

AO control is essentially a digital signal process, where clocked information from image sensors needs to be processed and sent, adequately conditioned, to the mechanical actuators of the deformable mirror in certain time. Different hardware solutions can be used to perform this processes, such as CPU, DSP, GPU (Graphics Processing Unit), ASIC or FPGA. All these technologies have evolved rapidly due to the advances in semiconductor integration experimented during last 50 years.

Traditionally CPU and DSP have been used widely as the real time controller (RTC) that an AO system needs, and still they are. The current models of these devices can cope with the speed requirements of an AO control loop, that typically has to perform all necessary calculations faster than the atmosphere turbulence changes, typically at 1 kHz rate. In table 1.3 of chapter 1, in the column RTC are shown the hardware architectures found in the literature for the control of the AO systems for small aperture telescopes.

In recent years, several researchers (shown in table 2.3 of next section) have propose the use of FPGA as the technological platform to implement AO real time controllers. In some cases FPGAs are complementary devices of a CPU/DSP-based system, in other cases FPGAs act as standalone devices. In the next sections are shown some results of the scientific community aimed to the use of FPGA devices in AO control systems.

As the telescope aperture size increases, more deformable mirror actuators and subapertures in the wavefront sensor are needed, and so increases the computational load. One way to design an AO control system is to use a CPU where the data processing is not performed until the image data from the wavefront sensor are stored in memory, introducing a delay. This makes more difficult to reach the goal of 1 ms processing time (1 kHz frame rate).

The implementation of high speed real time control algorithms, as the reconstruction of the wavefront in an AO system, requires high processing speed and low latency, which can be achieved with current FPGAs. Parallelization and design reuse, inherent to these digital devices, can benefit the bandwidth requirements of the real time control loop. Even FPGA can include embedded processors which along with the digital signal processing algorithm, provide the possibility to have a whole processor-based control system implemented in a standalone device, with no need to use external processing units. This decreases the cost and power consumption, and eases the portability of the control subsystem, which matches the requirements of the present research: an AO system applied to small aperture telescopes. This is due to the low cost, easy programming and dedicated architecture based on pipeline and parallel processing of FPGAs.

In an AO control several stages are included, some of them with high computational requirements, such as as multiplications of matrices in order to obtain the reconstructed wavefront, where clearly some parts can be identified as bottlenecks in the process flow. Regarding this aspect, it's clear that the use of pipeline and parallel features of FPGA is a great advantage when repeated operations need to be done, involving operations with pixels, and mathematical operations with matrices.

2.5.3 FPGA in AO control systems

In table 2.3 is shown some of the research efforts towards the use of FPGA in AO control systems. In some cases FPGA is a processing aid to the system but the main control is performed in other devices. In a few cases FPGA is used as a standalone device.

Wang et al.[73] used a systolic array implemented in a Xilinx Virtex4 FPGA to reduce the wavefront reconstruction latency to 3µs. Their experimental results are based in a SH wavefront sensor with 54 subapertures and a deformable mirror with 61 actuators.

In IAC (Instituto de Astrofísica de Canarias) and Universidad de La Laguna in Spain, research has been performed in the use of FPGA for AO systems, building firstly a test bench [55], for its application in a later stage to real telescopes. Also they have done some research in the internal FPGA architecture, evaluating the performance when using floating point or fixed point operations [40]. Mainly his efforts have been aimed to the use of adaptive optics in big telescopes. (Refs. [56], [39], [17], [57].)

In Durham University researchers have developed AO systems [4], mainly aimed for their use in real big aperture telescopes, as TMT or GTC, with complex and extensible architectures. Also they have accomplished some efforts in more simple systems that could be applied for low cost AO applications. (Refs. [61], [24], [62].)

Table 2.3: AO systems for astronomy with FPGA control architecture as reported in literature at January 2015.

Year	Ap[1]	WFS[2]	DM[3]	RTC [4]	Status[5]	Ref
2004	–	SH 54	61	FPGA Virtex2	lab	Wang[73]
2005	30-100	SH 64	MM 37	FPGA Virtex4	lab	R-Ramos[55]
2005	8-10	SH 400	MM 37	FPGA Spartan3	lab	Saunter[62],[24]
2007	0.4-1.5	SH 256	PDM 19	FPGA Virtex2	lab	Terrier[68],[71]
2008	–	SH 400	–	FPGA Virtex4	lab	Kepa[31]
2008	–	SH 256	–	FPGA Virtex4	lab	Peng[49]
2008	4.2	SH 256	PDM 121	–	on-sky	Guzman[27]
2010	30	5792	7500	FPGA Virtex6	arch	Hovey[29]
2010	–	SH 49	52	CPU+FPGA+GPU	arch	Basden[4]

Kepa [31] et al. implemented an AO control system in a Xilinx Virtex4LX-25 FPGA, as a first stage with the aim to develop in the future a full low cost AO system. They showed a flexible design that can support up to 400 subapertures, with geometries ranging from a quad cell to 64x64 pixels per subaperture in the WFS. They presented results about resource usage and processing time in FPGAs, stating that the processing time bottleneck has moved from the data processing to the readout image sensor speed.

Peng [49] et al. developed an AO controller for its use in solar imaging. They used an absolute difference algorithm to calculate the positions of the centroids in the SH wavefront sensor, and a systolic array implementation in the FPGA, and obtained a processing latency of 7µs in a system with 16x16 subapertures of 16x16 pixels each.

Hovey [29] et al. proposed a control architecture for the TMT telescope based in FPGAs, stating that the fast development of this processing technology will make possible the design of a AO control systems based on FPGA for big aperture telescopes.

[1]Aperture diameter of telescope primary mirror in metres.

[2]Type of wavefront sensor (SH: Shack-Hartmann) and number of subapertures.

[3]Type of deformable mirror (MM: Membrane Micromachined, PDM: Piezoelectric Deformable Mirror) and number of actuators.

[4]RTC: Real Time Control hardware (FPGA model).

[5]Status (Lab: Laboratory demonstrator, on-sky: demonstrator in real telescope, arch: proposed electronic architecture).

In UNSW Canberra, several efforts have been done in this area, developing a SH wavefront sensor based in an FPGA, and also a laboratory testbench to integrate this system in a real control loop for adaptive optics, installed in laboratory [68, 71]. The work of Terrier [68] established the base for the development of an AO system based in FPGA, with a SH wavefront sensing implemented in a low cost FPGA. This work was extended subsequently by Visser [71], where a complete electronic architecture control was implemented in two FPGAs connected through a LVDS (Low Voltage Differential Signaling) bridge.

In figure 2.12 is shown the integrated FPGA+CMOS sensor developed by my supervisor, Dr. Andrew Lambert, in UNSW Canberra, with the purpose to obtain a small form factor board, that could be implemented in an image processing system, as is the case of the present research. Also interface and driver boards were developed, which are used in several parts of the AO system developed in this thesis. More details about these boards can be found in chapter 4 about the control system.

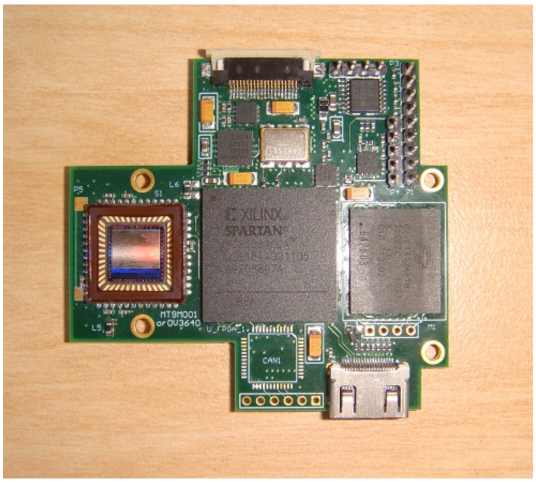

Figure 2.12: FPGA+CMOS sensor board developed by supervisor in UNSW Canberra.

Also in UNSW Canberra research efforts have been accomplished in post processing algorithms in open loop for image processing, and architectures based in CMOS technology image sensors that has been demonstrated to be successful compared to their counterpart CCD technology [35].

2.6 Summary

Taking these summative steps and technologies and building a low cost AO system with modest performance is the subject of this endeavour. Care has been taken throughout to engineer rather than craft a testbed, so others may follow and adapt their designs. Subsequent chapters address incremental steps, starting with the design of an opto-mechanical system in the next chapter.

CHAPTER 3

Opto-Mechanical Design

3.1 Optical and mechanical specifications

One of the main challenges of this research is the integration of the three main disciplines that form an AO system: mechanics, optics and electronics. Regarding the first two, a common design workflow would start with the optical design based in the optical constraints and specifications determined in a previous theoretical study. Then a mechanical design would be developed trying to accommodate the components of the previous optical configuration, with relaxed constraints in the positions of the different optical components. But one particularity of the current research is that both mechanical and optical constraints are closely interrelated, which complicates the design stage of the development process.

Below a list of the opto-mechanical specifications is presented, which defines the system design and determines its constraints and limitations.

Lightness

The structure should have a relative low weight compared to the telescope, thus having the lowest possible impact in the overall system weight, in order to ease the balance of the system. At the same time, the mechanical junction between the AO system and the telescope rear port should be solid enough to support the AO system weight, around 10 kg, which is the expected average weight, including optical components and the mechanical structure itself. On the other hand, a lightweight design would ease the portability of the AO system, as one of the segments where the system is intended to be used is amateur astronomy, where usually the transportation of the telescope and auxiliary systems are important factors.

Flexibility and modularity

The system should be designed to be attached to different telescopes, each of them with different characteristics, among others: aperture size, F number and static aberrations. Also the AO system is intended to be used with a broad range of astronomical targets. Because of that, the system should be flexible enough to adapt to different scenarios, the longitudinal distances between components should be easily modified, and the optical components interchangeable.

One of the advantages of this approach is that the same system could be tested and aligned in laboratory, and then be attached to the rear port of a telescope. In that case, there is no need to build two different prototypes, one for testing purposes in laboratory, and other for on-sky observations, that would increase the budget and complexity of the project. The AO system should be attached to the telescope in only one spot in its rear port, usually a tubular shape of different diameters, which would ease the installation of the system across different telescopes. This should help in the future to obtain a commercial product that would be available for different types of telescopes.

As well, the system should show certain degree of modularity, hence the AO correction section should be easily attached and detached, and optical components interchangeable, depending on the telescope used, and the target under observation.

Cost

Low cost is one of the main constraint of the AO system in this research, as the potential users are amateur astronomers, or modest facilities in research centres and universities. Therefore the system ideally should be designed with off-the-shelf components, which will reduce the overall cost and would ease the obtaining of spare parts that could be used to improve, repair or extend the design. The materials of the optical components should be standard and computing devices to perform the control should be found in the consumer market.

Wavelength

The system is intended to be used in the visible spectrum, to include amateur astronomy applications, although it can be adapted to more professional wavelength applications, such as infrared. Usually turbulent effects are lesser in infrared, but the clients of this system most require correction in the visible spectrum.

Telescope aperture

Due to the small aperture of the telescopes where the AO system is intended to be used, the number of photons is significantly lower than in larger apertures. To compensate this drawback, one of the design considerations is the use of the less possible number of optical components, in order to prevent attenuation losses due to reflections and partial transmissions in these components. Also this lack of photons will necessarily influence in the algorithms developed in the control section to interpret the order and extent of the aberrations caused by the atmosphere turbulence.

3.2 Mechanical design

3.2.1 Configurations

The mechanical design of the AO system is divided in two sections, magnification and AO correction, as shown in figure 3.1. The former holds the components that will work as a magnification system without atmosphere turbulence correction. The output of this stage is the magnified astronomical object image in observation which will be recorded or visualized with a science camera, or just simply observed by eye. When the AO correction section is not attached nor active, the system works as defined by the optical components of the magnification section, as a standard telescope eyepiece works. When the AO correction section is attached and active, the aberrations are corrected, and the images can be observed in the AO system output. The magnification section support the main weight of the AO system and includes the junction between the AO system and the rear port of the telescope. Its center of gravity should be as close as possible to the rear port to reduce flexions in the joining parts of the AO system.

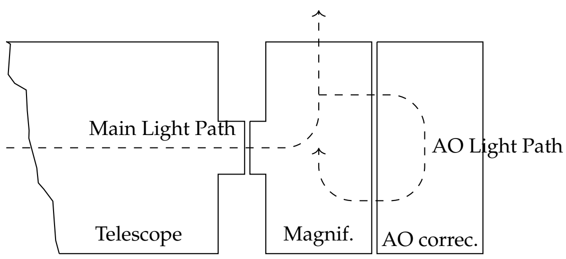

Figure 3.1: Mechanical sections of AO system.

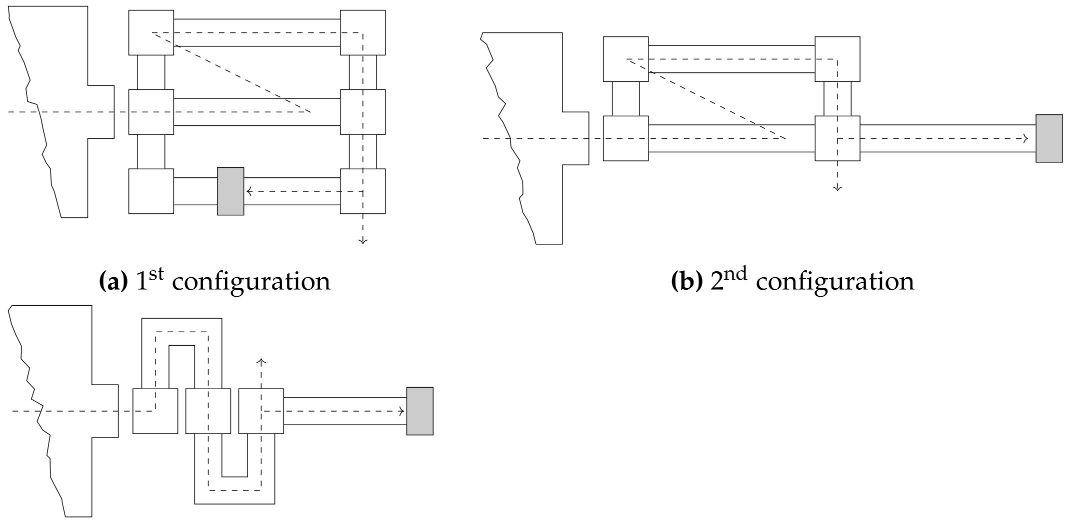

(a) 1st configuration

(b) 2nd configuration

(c) 3rd configuration

Figure 3.2: Different mechanical configurations of AO system (grey box is the Shack-Hartmann wavefront sensor).

Three different mechanical configurations were initially considered for the magnification section, which are represented in figure 3.2.

In the configurations represented in figures 3.2.a and 3.2.b, the number of fold mirrors is less than in the 3rd one in figure 3.2.c. A lower number of fold mirrors eases the system alignment, nevertheless these two first designs are not symmetrical respect the telescope axis, but it is in the third design. In this one, the center of gravity of the AO system is closer to the rear port of the telescope compared to 1st and 2nd designs, which makes the system less prone to effects of vibrations, created mostly by the tracking motors of telescope axes or the wind. Also this 3rd configuration prevents a lengthy system, which could collide with other parts of the telescope facility when this is tracking astronomical objects. Furthermore this configuration includes an even number of steering mirrors in symmetrical positions, so that in the WFS a circular shape of the wavefront is obtained regardless of the incident angles in these steering mirrors. The light beam reflects in 6 mirrors at 45 degrees angle each of them, so in the SH wavefront sensor, the light beam enters the CMOS image sensor at 0 degrees angle (the same direction of the telescope axis) with a circular shape.

For the AO correction section, a linear design with a tubular shape without bending in the light beam was chosen, to ease the alignment. This design avoids excessive mechanical flexions when the telescope is tracking sidereal objects, and therefore modifying continuously the angular position of the AO system in space. This makes the structure more rigid, and minimises flexions, although makes the system more complicated to adjust and align in the initial calibration process. This tubular design is reinforced with stainless steel rods, because once calibrated, it turns out to be a much more rigid system, and as well is a more modular design, because the whole AO section could be exchanged with a different one, without making a complete disassemble of the system.

Taking all these factors in consideration, and after some trial experiments with the three configurations, the third design was selected for the development due to its better flexibility and modularity compared to the rest of configurations, mechanical symmetry, which provides a better weight balance, and because the center of gravity is more conveniently situated. One of the drawbacks of this configuration is the effect of higher incidence angles of light beam on the deformable mirror. This could be fixed with a software solution, modifying the influence functions of this mirror according to this angle. In figure 3.3 a picture of the selected configuration for the AO system is shown, where the exaggerated length of the rear tube containing the SH sensor is because the available components sizes must be adjusted to fit the microlens array, the image sensor and so on.

Regarding the temperature influence in the material of the mechanical testbed, the linear thermal expansion for the stainless steel tubular AO section has been calculated with the next formula:

$$dl = \alpha \times L_0 \times dt = 17.8 \times 10^{-6} \times 0.225m \times 54F^\circ = 0.21mm$$

This linear expansions corresponds to 0.09% of the optical path length in the tubular AO section, so stainless steel thermal expansions effects in the optical path length of the tubular AO section are negligible

3.2.2 General description of mechanical design

In figure 3.4 is shown the 3D model of the mechanical configuration developed for the AO system. All components except the joining rods are aluminium, made to provide the necessary rigidity, while keeping a minimum weight. The dimensions of the platform are 700 mm length (in the direction of the telescope optical axis), 600 mm width and 70 mm thickness. The square flange at left is the only spot where the AO system is attached to the telescope.

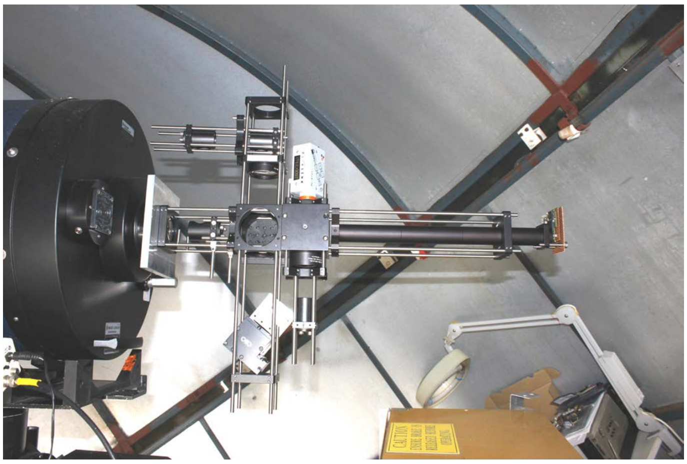

Figure 3.3: Mechanical testbed developed for AO system.

The main structure is formed by two aluminium cubes, which can hold lenses if necessary. An extra lens holder was placed next to the junction part with the telescope rear port, to provide extra rigidity to the structure. The lens holders are supported by stainless steel rods, which form the basic joining mechanism for the magnification stage. All optical components of this stage can be shifted longitudinally, to provide flexibility when needed. The first fold mirror after the telescope rear port is situated in a holder that can be rotated, so if the AO system is not used, a standard eyepiece or camera can be attached directly to a C-Mount adapter included in the structure, without removing the AO system.

The holders of 2nd and 3rd fold mirrors are situated in a independent module, to facilitate the substitution of this part for a tip-tilt correction mirror in a later stage, which is not in the scope of the present research. The first cube holds three fold mirrors and the deformable mirror, while the second one holds the fourth fold mirror, the science camera, and the tubular AO system. This cube also holds the beam splitter inside, where the light beam is divided between the AO section and the science camera.

All mechanical parts are off-the-shelf from Thorlabs (`http://www.thorlabs.com`).

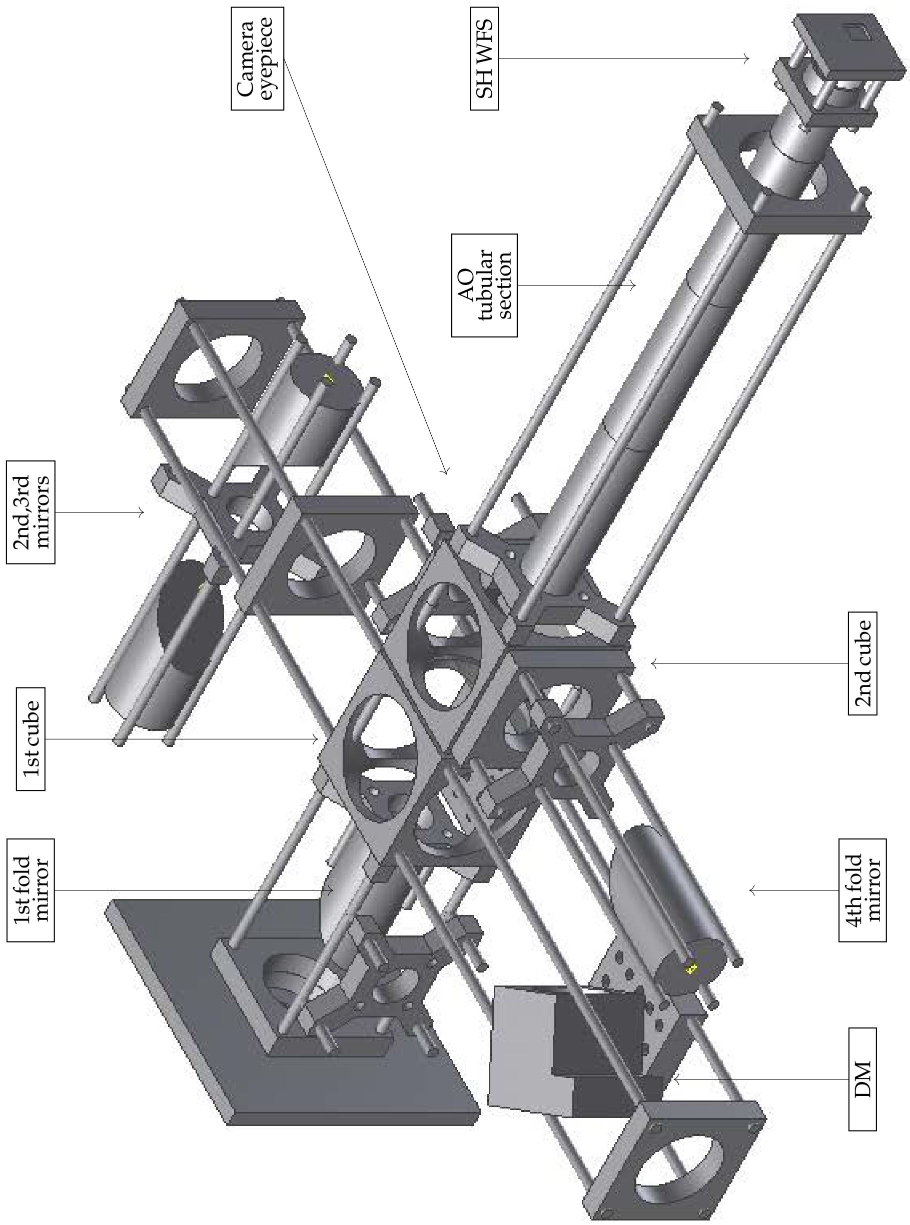

Figure 3.4: 3D model of mechanical testbed developed for the AO system.

3.2.3 Mechanical components description

Next is a more detailed description of each of the mechanical components of the AO system:

Junction with telescope rear port

The union between the AO system and the telescope rear port consists in an aluminium square plate of dimensions 150 x 150 x 12 mm. It includes four threaded holes for screwing the AO system, reinforced with an attached square flange. This junction plate has a threaded hole in the center where is screwed to the rear port of the telescope. If the system is used in other telescope, this flange is the only part that has to be adapted to the size and screw type of the corresponding telescope rear port, because the AO system is not attached to the telescope in any other spot.

Connection between components

The connections between the mechanical parts of the AO system consist on stainless steel rods of diameter 6 mm with different lengths. The use of these rods keeps AO system light while is a suitable way to increase the flexibility in the optical components positions. Lenses holders and the deformable mirror platform can be shifted along the rods, to adapt to different configurations. All rods include 4-40 removable studs in their ends, so they are stackable and also can be screwed to the different cube faces. In each end of the AO system, the rods are joined by square aluminum plates, which provide extra rigidity.

Fold mirror holders

The four fold mirrors are situated in circular holders with three worms each, which permit to situate each mirror in a precise and stable position, at a 45 degrees angle. These lens holders can be moved along the rods which hold them, and then fixed in a stable position. The mirror closest to the telescope can be rotated in 90 degrees increments, which allows the use of other components different from the AO system, like standard eyepieces or cameras.

Central structure

The AO system includes two aluminium cubes with 76 mm of edge size, which form up the central structure. Optics can be mounted in the different cube faces and inside them with the aid of the appropriate platform, as for instance the beamsplitter included in one of the cubes. Rods can be screwed to the cubes, or they can slide in through bore holes.

30mm to 60 mm adapters

The standard distances between rods are 30 mm and 60 mm, hence to join systems of different sizes, adapter plates are needed. These aluminium plates include threaded holes of 1" diameter, that could hold optics if necessary.

Optics holders

The lenses of the magnification section are contained in plates that can accommodate optics of 2" in diameter. These plates can be shifted longitudinally in order to change the optical configuration of the system.

Tubular section (AO correction section)

The AO stage of the system is included within a tube of 1" diameter, which is formed by sections of 2" and 4" length aluminium tubes, which can hold optics inside. The tubular section is attached to a 30 to 60 mm adapter plate, that can be shifted longitudinally through four rods, to adjust distances between lenses when required.

Wavefront sensor section

The holder of the wavefront sensor is supported by a small aluminium plate that can slide and rotate with respect the tubular section. This rotation provides a easy way to adjust accurately the angle and position of the wavefront sensor.

In the appendices is shown a list with all components of the system, with their corresponding weight.

3.3 Optical design

3.3.1 Global setup

In figure 3.5 is shown the optical setup of the AO system.

Essentially the optical setup consists on fold and deformable mirrors to adapt the light beam to the mechanical structure and compensate for aberrations respectively, lenses with different functions, a beamsplitter to divide the incident light beam, and

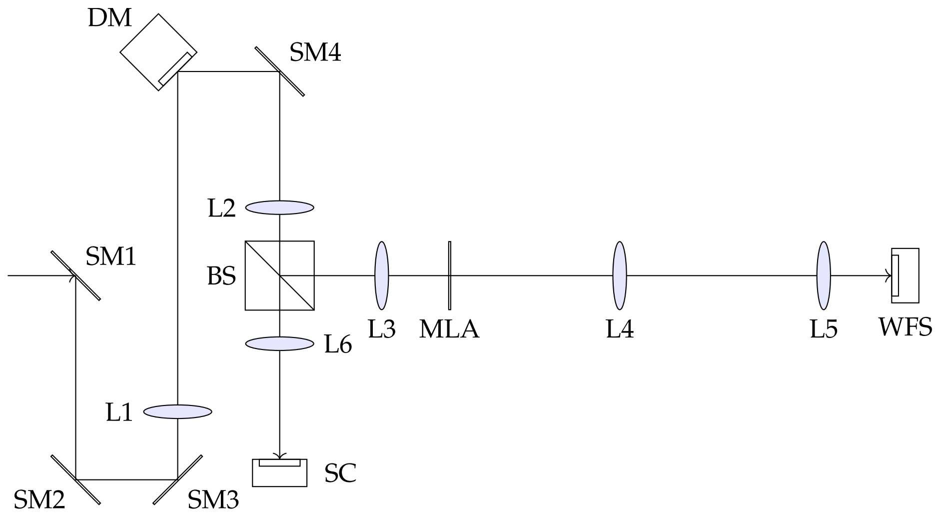

Figure 3.5: Optical setup of AO system. SM1-SM4: Fold Mirrors, L1: Collimation lens, L2-L3: Kepler system, L4-L5: Telecentric system, L6: Focal length adjust lens, DM: Deformable Mirror, BS: Beam Splitter, SC: Science Camera, MLA: Micro Lenslet Array, WFS: Wavefront Sensor.

an image sensor to extract the information of the aberrated beam and visualize or record the output of the AO system.

The DM is situated in the back focal distance of L1, and MLA in the back focal distance of L3, This way both components, DM and MLA, are situated in the pupil plane of the telescope primary mirror. Also back focal distance of MLA is coincident with the focal distance of the first lens of the telecentric system L4, and WFS is situated in the back focal distance of L5. The calculation of these positions is supported by simulations in ZEMAX for different light beam input angles within the field of view.

First an initial design was developed based in the opto-mechanical specifications. After this stage, the optical system was simulated and analyzed in a ray tracing software (ZEMAX), which results are shown in the analysis of subsection 3.3.3. In the next stage the system was tested in laboratory with a laser source, and results obtained in the previous stage with ZEMAX were validated. Finally the AO system was attached to the telescope and a series of on-sky observations were performed. Results from laboratory and on-sky observations are presented in chapter 5 about experimental results.

The first stage of this workflow permits to test the performance of the different blocks of the optical system and to take the appropriate design decisions without considering issues concerning real components. In the laboratory the optical system can be assessed, avoiding issues such as the weak photon flux, the telescope static aberrations, the light incoherence inherent to real astronomical objects, and the tip and tilt images shifting caused by atmosphere turbulence, inaccuracies in the telescope tracking system or the wind. Also the laboratory stage provides an easy way to pre-align the optical path, and then the system can be adjusted on site in the telescope with slight corrections.

Two types of lenses were considered for the design, spherical singlets and achromatic doublets. The former are more appropriate for coherent light as a laser due to the chromatic aberration that doesn't show. The achromatic doublets are more appropriated to work in a broader spectrum, as the light emitted by astronomical objects, due to their lower chromatic aberrations compared to spherical singlets. In subsection 3.3.3 is shown a detailed analysis of the lenses chromaticism.

Both type of lenses, spherical and achromatic doublets, are coated for visible spectrum wavelengths. This improves the transmission percentage, an important factor when dealing with low photon flux, as in the case of small aperture telescopes. In figure 3.6 is shown the theoretical transmission percentage of an uncoated lens of N-BK7 material compared to a coated AC508-200-A lens from Thorlabs. The transmission percentage difference in the visible spectrum is around 8% in average, and considering that the light beam has to go through five lenses apart from the beamsplitter and the mirrors, the use of uncoated lenses would reduce significantly the transmitted signal that reaches the wavefront sensor, worsening the performance of the AO system.

In table 3.1 are shown the main specifications of the optical components of the AO system.

Table 3.1: Main parameters of AO system optical components.

Ref[1]	Item	Shape[2]	Material	D[3]	λ (nm)	FL(mm)[4]
L1(S)	LA1979A	P-C	N-BK7	2"	350-700	200
L1(A)	AC508-200A	n/a	N-BK7/SF2	2"	400-700	200
L2(S)	LA1050A	P-C	N-BK7	2"	350-700	100
L2(A)	AC508-100A	n/a	N-BAF10/SF10	2"	400-700	100
L3(S)	LA1131A	P-C	N-BK7	1"	350-700	50
L3(A)	AC254-030A	n/a	N-BAF10/N-SF6HT	1"	400-700	30
L4(S)	LA1050-A	P-C	N-BK7	2"	350-700	100
L4(A)	AC254-100A	n/a	N-BAF10/SF5	1"	400-700	100
L5(S)	LA1951-A	P-C	N-BK7	1"	350-700	25.4
L5(A)	AC254-30A	n/a	N-BAF10/N-SF6HT	1"	400-700	30
SM1-4	Fold Mirr.	P	Aluminium	1"	-	n/a
DM	PDM30-19	P	Metal	1.2"	-	n/a
BS	BP245B1	P	Nitrocellulose	2"	400-700	n/a
MLA	AOA	P-C	Fused silica	1"	-	23

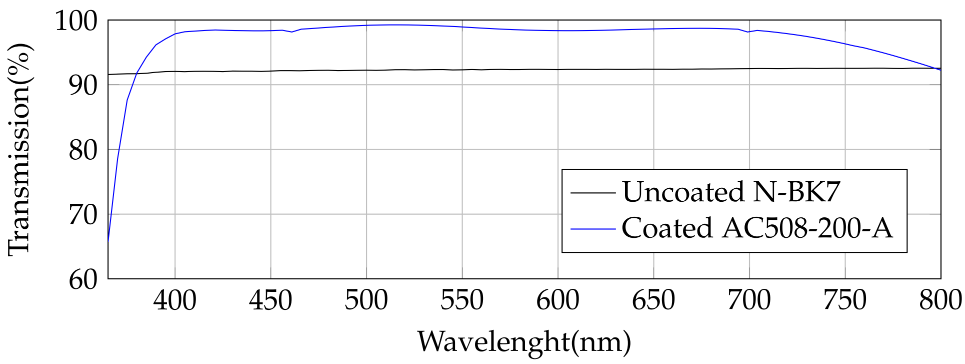

Figure 3.6: Theoretical transmission of an uncoated sample of N-BK7 material of 10 mm thick, and a coated AC508-200-A lens in visible spectrum (Source:www.thorlabs.com).

[1]Reference and type of lens: (S: singlets, A: achromatic, DM: deformable mirror, BS: beamsplitter, MLA: micro lenslet array).

[2]Lens shape: (P: plane, C: convex.).

[3]Lens diameter in inches.

[4]Focal length in millimetres.

3.3.2 Optical components description

Next the funcionality and features of each of the components in the optical setup is described.

Fold mirrors: SM1 to SM4

The AO system includes four fold mirrors, SM1 to SM4, orientated in a 45°angle. These flat surface mirrors redirect the light beam adapting it to the mechanical structure. The first mirror, SM1, can be rotated in 90°increments, thereby if the AO system is not used, other devices with different functions can be attached to the AO mechanical structure, as eyepieces or cameras.

The second and third mirrors, SM2 and SM3, are situated in an independent structure that can be removed easily. In a later stage but not in the scope of this thesis, it is planned to exchange one of these fold mirrors by a tip tilt stage, which will correct the shifting in the images created by low order atmosphere turbulence aberrations or vibrations of the telescope tracking system. One of the priorities of this research was the evaluation of the viability to correct aberrations of orders greater than tip and tilt, so at first the tip-tilt stage mirror was not considered. Besides tip-tilt correction can be acheived easily using speckle post-processing techniques provided the beam doesn't wander too much in the system.

These mirrors include an adjustable platform in their base which includes 3 worms, which permits to move the mirrors spatially with three degrees of freedom. Also the mirror holders can be displaced longitudinally to align accurately the light beam angles.

Collimator: L1

The lens situated in L1 position in figure 3.5 collimates the beam light coming from the telescope to a diameter appropriate to illuminate the deformable mirror effective surface. The focal length of this lens is 200 mm, a relatively high value compared to the rest of the system lenses. This length was chosen to try to minimize the effect of spherical aberration, more pronounced in short focal length lenses.

The focal plane of the telescope is situated between fold mirrors SM1 and SM2. This distance can be adjusted if necessary with the manual focus knob of the telescope, which moves its primary mirror in a finely controlled motion. The collimation lens is situated at 200 mm of this focal plane of the telescope, in order to get a collimated light beam of approximately 20 mm in diameter, since the F number of the telescope is F/10. This beam will illuminate an area of approximately this diameter in the deformable mirror, in order to cover its effective surface.

Two different lenses were tested in this position, LA1979-A and AC508-200-A from Thorlabs (see table 3.1 for more information). Both can get a collimated beam at the output but with different optical features, as it will be analyzed in subsection 3.3.3 of this chapter.

In both cases, to reduce the spherical aberration, the lenses always will be orientated with their more curved surface facing the collimated beam.

Deformable mirror: DM

The deformable mirror used in the optical setup is the PDM30-19 of OKO Technologies. In table 3.2 are shown its main technical parameters. It consists of 19 piezoelectric column actuators tied to a base holder. The mirror plate is bonded to the actuators and coated with a metal layer. Its shape is controlled through the voltages applied to the actuators. With no voltages in the actuators the mirror plate shows a slight sphericity in its surface. To compensate this curvature the distance between the collimator and the mirror will be altered to reach the desired focal length. Also due to the actuators hysteresis, the initial shape of the mirror plate could be different from the reference sphere, but this effect will be irrelevant when the system is working in closed loop control.

Table 3.2: Main specifications of deformable mirror OKO PDM30-19 (Source: www.okotech.com).

Parameter	Value
Aperture shape	Circular 30 mm diameter
Mirror coating	Metal or Metal+dielectric
Actuator voltages	0..+300V
Number of electrodes	19
Actuator capacitance	5 nF
Main initial aberrations	Sphere
Initial RMS deviation from reference sphere	less than 1 µm
Maximum stroke	8 µm at +400V
Actuator pitch	7 mm
Hysteresis	< 10%
Package dimensions	76 x 60 x 24 mm
Weight	320 g

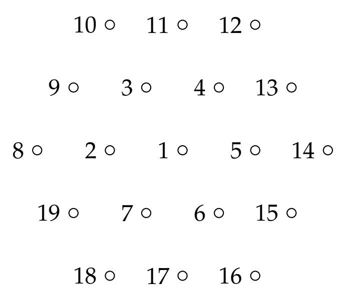

Figure 3.7: OKO PDM30-19 DM actuators geometry(source www.thorlabs.com).

In figure 3.7 is shown the hexagonal pattern of the actuators geometry. These actuators are controlled by a driver board. In chapter 4 which describes the control architecture it is detailed the hardware connections and the influence functions used to drive these actuators.

The input diameter beam in the mirror plate is 20 mm, not enough to illuminate completely its effective surface, but moving slightly the position of the collimator lens, this effective surface will be fully covered, and also the initial spherical shape can be compensated, so that a collimated beam can be obtained at the output of the deformable mirror.

Kepler system: L2-L3

In order to illuminate the desired numbers of micro-lens of the lenslet array, the beam diameter needs to be reduced from 20 mm to an appropriate value. To get this reduction, two lenses in a Kepler telescope configuration are used, as shown in figure 3.8. If back focal distance $f_2^{'}$ of L2 is overlapped with front focal distance f_3 of L3, the output of the system will be a collimated beam with a magnification equal to $f_3/f_2^{'}$.

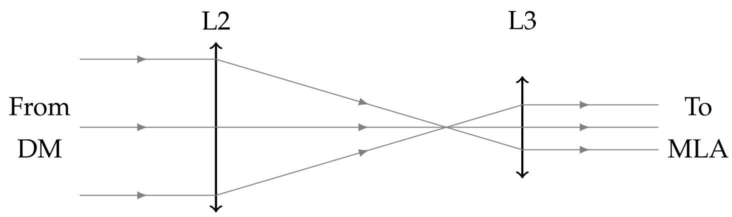

Figure 3.8: Lenses in Kepler telescope configuration.

L2 focal length is 100 mm in both lenses versions, spherical (LA1050-A) or achromatic (AC254-100-A). If L3 is LA1131-A of focal length 50 mm, the magnification is 1/2, therefore the diameter of the output beam is 10 mm. The distance between lenslets in the micro-lens array is 0.5 mm, so in that case the output of this array will be a grid of 20 lenslet focal points in diameter. If L3 is AC254-30-A of focal length 30 mm, the magnification is 1/3, and the grid will consist on 13 lenslet focal points in diameter.

Beamsplitter: BS

The beamsplitter divides the incoming light in two beams, one used to obtain information about wavefront aberrations in the WFS, and the other to register or visualize the corrected images in the science camera.

In this system a pellicle beamsplitter (BP245B1 from Thorlabs) is used, because it eliminates the ghosting created in other types of beamsplitters, and also it doesn't show chromatic aberration when incident beams are not perfectly collimated. Its diameter is 2", the split ratio is 45% Reflectance - 55% Transmission, and is coated for maximum performance in the visible spectrum.

The main disadvantages of this type of beamsplitter are their fragility and the sinusoidal oscillations resulting from thin film interference effects. In this AO system, the pellicle beamsplitter is situated inside one of the aluminium cubes, so once mounted, fragility is not an issue. Figure 3.9 shows the transmission percentages where sinusoidal oscillations can be observed. The AO system is intended to be used with natural light from astronomical sources in the visible spectrum. Sinusoidal oscillations are averaged over the whole visible spectrum, so the quality in the detection of centroids won't be affected by these oscillations.

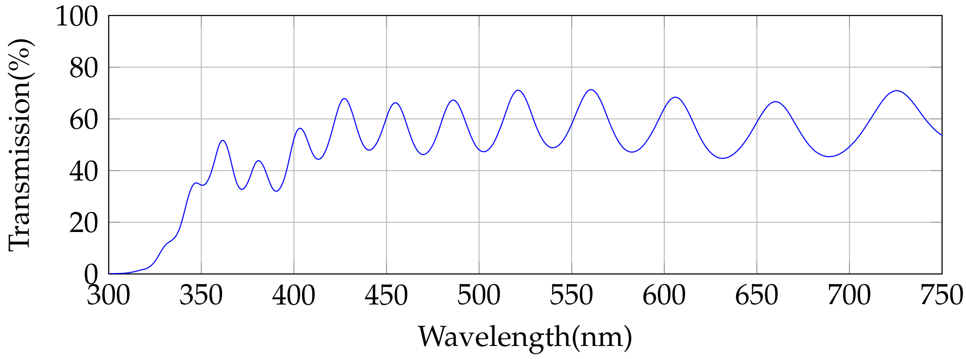

Figure 3.9: Transmission percentage of BP245B1 beamsplitter in visible spectrum (Source:www.thorlabs.com).

Focal length adapter lens: L6

This lens is situated between lens L2 and the science camera, to match the focal length of the incident beam in this camera, in order to sample the images at diffraction limit.

Science camera: SC

The camera used to register the output of the system is the monochrome PixeLINK PL-A741 Machine Vision Camera, with 1.3 megapixels resolution. It includes a CMount adapter to attach it to the AO system, and a Firewire interface to connect to the support computer. Although this camera is not one of the best options for astronomical observations, its good enough in order to evaluate the performance of the developed AO system. Table 3.3 shows its specifications.

Micro lenslet array: MLA

The MLA consists on a plano-convex 0.5 x 0.5 mm square array of micro-lenses with focal distance 23 mm, commercialized by AOA (Adaptive Optics Associates).

Telecentric system: L4-L5

This system, formed by two lenses in a bi-telecentric arrangement, is used to scale the MLA output to the pixel size of the wavefront sensor. A telecentric system has a constant magnification regardless of the distance to the object under study or its location within the field of view. In a bi-telecentric system, front and back focal planes of both lenses are overlapped thus the positions of the object (focal plane of MLA) or the image (wavefront sensor) won't affect the magnification. Figure 3.10 shows the bi-telecentric configuration adopted in this AO system.

Table 3.3: Main specifications of PixeLINK PL-A741 camera (source:www.pixelink.com).

Parameter	Value
Optical format	2/3"
Image sensor type	CMOS
Active imager size	8.576 mm x 6.912 mm, 11.01 mm diagonal
Active pixels	1280 x 1024
Pixel size	6.7 µm x 6.7 µm
Shutter type	Synchronous shutter (global)
Frame rate	25 fps (ROI 1280x1024), sub-windowing available
Spectral Sensitivity Range	350 - 1000 nm
Dynamic Range	$\approx$ 60 dB
ADC Resolution	8 - 10 bits
Output Interface	FireWire (IEEE 1394) IIDC 1.3
Optical Interface	Standard C-Mount 2/3"
Max. Power Consumption	4.2 W
Housing size	35 mm x 50 mm x 100 mm
Weight	190g
Vibration	up to 10G (20 to 200 Hz)
Operating temperature	0°C to 50°C (non-condensing)

In the MLA focal plane are represented three lenslet focal points equally spaced. In the output, back focal plane of L5, is situated the wavefront sensor. In this plane, the lenslet focal points are re-imaged. They are equally spaced at a distance f_5/f_4, that is the ratio between focal lengths of lenses L5 and L4.

This constant magnification reduction is obtained through lenses L4 and L5, that is 1/3 (or 1/4 if LA1951-A is used as L5). To obtain the bi-telecentric system, front focal plane of L4 is overlapped with back focal plane of MLA, and back focal plane of L4 is overlapped with front focal plane of L5. The wavefront image sensor will be situated in the back focal plane of L5.

Wavefront sensor: WFS

The CMOS image sensor that forms part of the Shack-Hartmann wavefront sensor is the MT9M001 commercialized by Aptina (formerly Micron). Table 3.4 shows its main parameters.

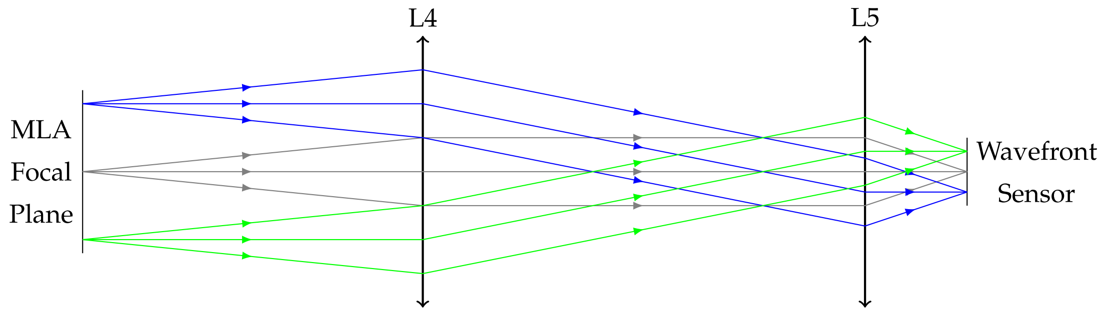

Figure 3.10: Bi-telecentric system section of AO optics configuration (adapted from www.thorlabs.com)

Telescope

The telescope used in this research is the 16" LX200-ACF from Meade. A list of its main specifications are shown in table 3.5. However other telescopes with different F numbers can be used, provided that the distances between optical elements are modified accordingly (such as the 1 metre McLellan telescope sited in Mt.John Observatory (New Zealand) with F/7.7, where this AO system was also tested).

3.3.3 Analysis

In this section a detailed analysis of the optical system is shown. Optical quality and parameters in both outputs of the optical path, the scientific camera and the wavefront sensor, will be obtained and analyzed. To assist the calculations, both optical systems are modeled in ZEMAX, an industry standard for optical analysis. This software will ease the calculation of the optical components positions in the optical path, and also it will provide a estimated performance and optical quality of the system in both outputs. It will permit to evaluate the influence of the different parameters, as the effect to use spherical singlets or achromatic doublets as lenses, or aberrations introduced in the wavefront by the telescope. In appendix A.2 is shown a detailed table introduced in ZEMAX to model the AO system. In figure 3.11 is shown a 3D model of the AO system.

Field of view estimation

The lenslet array is the optical component which limits the maximum input angle in the optical system. Considering the size and focal length of this array of micro-lens and the magnification obtained in the wavefront sensor, it follows that the

Table 3.4: Main specifications of Aptina MT9M001 CMOS image sensor (source:www.aptina.com).

Parameter	Value
Optical format	1/2" (5:4)
Image sensor type	CMOS
Active imager size	6.66 mm x 5.32 mm
Active pixels	1280 x 1024
Pixel size	5.2 µm x 5.2 µm
Shutter type	Electronic Rolling Shutter (ERS)
Frame rate	30 fps (ROI 1280x1024), sub-windowing available
Spectral Sensitivity Range	350 - 1000 nm
Dynamic Range	$\approx$ 68.2 dB
ADC Resolution	10 bits
Output interface	Parallel 10 bits
Power consumption	363mW at 3.3V (Operating)
Operating temperature	0 °C to 70 °C

maximum input angle with respect to the optical axis is 0.01°, so the Field of View (FOV) is ± 0.01°. This will be the value used as maximum input angle of field of view in ZEMAX, noting this field changes with various magnifications in the system.

Optical quality and analysis in scientific camera

According to the Rayleigh criterion, to consider that an optical system is limited by diffraction, static aberrations introduced by all optical components in the light path should be less that one quarter of the incident wavelengths. One way to check this constraint is with the Optical Path Difference (OPD) curves. In this optical setup, the OPD are calculated in both sagittal and tangential fans, in the science camera position, under two different fields, 0 and +0.01°, and results are shown in figure 3.12. It can be observed that in all of them except tangential fan at +0.01°in figure 3.12c, number of wavelengths are below the value 0.25.

To avoid losing data, images need to be spatially sampled at Nyquist frequency. The diffraction limit of the telescope used in the research, with an aperture of 16" (406.4 mm), is obtained through the Rayleigh criterion for circular apertures and small angles: $\theta = 1.22 \times (\lambda/D)$, with (λ/D) the FWHM of the Airy pattern.

Table 3.5: Main specifications of Meade LX200-ACF telescope (source:www.meade.com).

Parameter	Value
Focal ratio	f/10
Optical design	Ritchey-Chrétien
Clear aperture	406.4 (16")
Focal length	4064 mm
Resolution	0.28 arcsec at 550 nm
Coating	Meade Ultra-High Transmission Coatings
Net telescope weight	318 lb (144 kg)
Spectral Sensitivity Range	350 - 1000 nm
Dynamic Range	$\approx$ 60 dB

In this formula λ is the wavelength and D the telescope aperture. For a wavelength of 550 nm, the angular resolution is $\lambda/D = 0.28$ arc sec, that is the FWHM of the Airy pattern. Another parameter to express the diffraction limit of a telescope is the Dawe's limit[15], based on empirical data, which gives as result the resolving power of the telescope R, according to the formula $R = 11.6/D$, where D is the telescope aperture in mm. For this particular telescope, the resolving power would be R = 0.28 arcsec, matching the value of the manufacturer specifications.

The pixel size in the science camera is 6.7 µm x 6.7 µm. Applying the Nyquist theorem to the image sampling, the maximum pixel size should be half the size of the Airy disk. In the science camera image sensor, the pixel size is about the same size of the Airy disk. To sample at Nyquist frequency, the focal distance to the science camera should be modified. In the first case, a plano-convex lens, L2, is situated before the science camera, resulting in a F/5 system. When L6 is included, the working focal ratio of the system is modified to F/25, enough to satisfy the Nyquist theorem ($\lambda \times F = 0.550 \times 10^{-6} \times 25 = 13.75m > 13.4 = 2 \times 6.7m$).

To evaluate the optical quality of the system different criteria can be used. The Modulation Transfer Function (MTF) is one of the most comprehensive ones. It provides information about how the optical system transfers the modulation from the object to the image, as a function of the spatial frequency. In figure 3.13 is shown the MTF of the optical system at the science camera output. The computation is based in an Fast Fourier Transform (FFT) algorithm applied in the pupil data. The MTF obtained is calculated relative to unit in the pupil plane, and it is function of the spatial frequency for a sine wave object, expressed in cycles per millimeter.

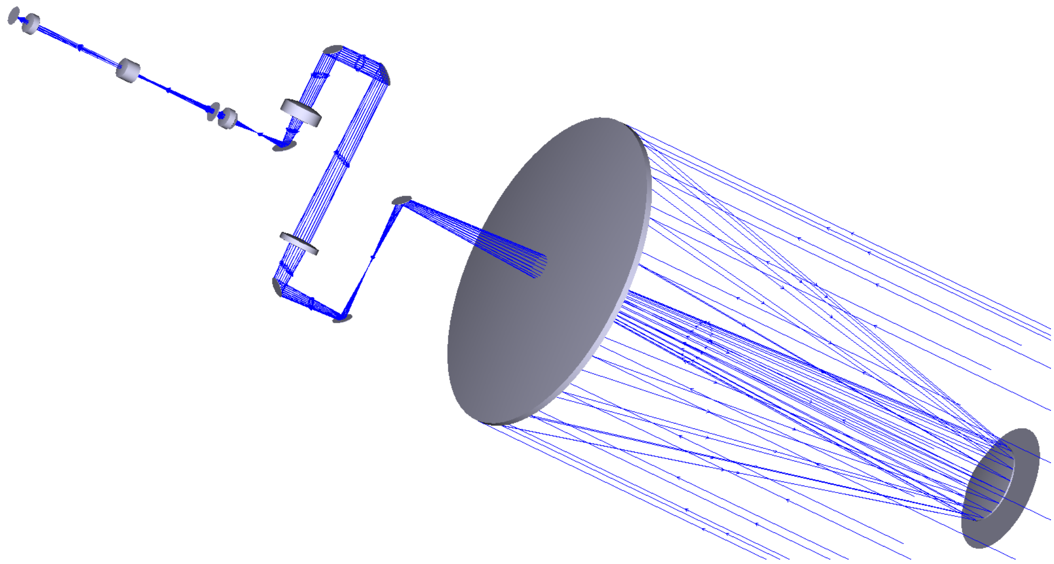

Figure 3.11: 3D Model of AO system in ZEMAX.

Three different sets of MTF have been obtained, each of them calculated for both tangential and sagittal fans, at limit of diffraction, for 0°and +0.01°fields. Sampling over the pupil is 128 × 128 in the visible spectrum.

In figure 3.13 it is observed that the system has a moderate performance at 0°field, but this trend degrades as the field increases. In diffraction limit and 0°field, both tangential and sagittal fans are coincident, but at +0.01°field fans have different modulus, indicating some degree of aberrations in the incident light. For a resolution of 55 cyles/mm, the maximum achievable value of the MTF is 0.48, which corresponds to the diffraction limit of the telescope. For this resolution, values of MTF of 0.38 and 0.15 (averaged between tangential and sagittal fans) are obtained when lights traverses the AO optical system, for a 0°and +0.01°field respectively . This means a brightness reduction in contrast to 80% for light rays on axis and 31% for light rays in the maximum FOV. This reduction in contrast of the image will spread the diameter of the image size if a point source as a star is considered, that will reduce the capability of the system to correct aberrations. But depending on the value of the relation D/r_0, that is, if the turbulence is not too strong, still the AO system will be capable to perform partial correction of the aberrations introduced by atmosphere turbulence. When comparing figure 3.13 curves with figure 3.9 in Roggemann work [44] and figure 7 in Fraser work [19], which represent the short exposure OTF versus the normalized spatial frequency, we observe that this contrast decrease is equivalent approximately to a value in the

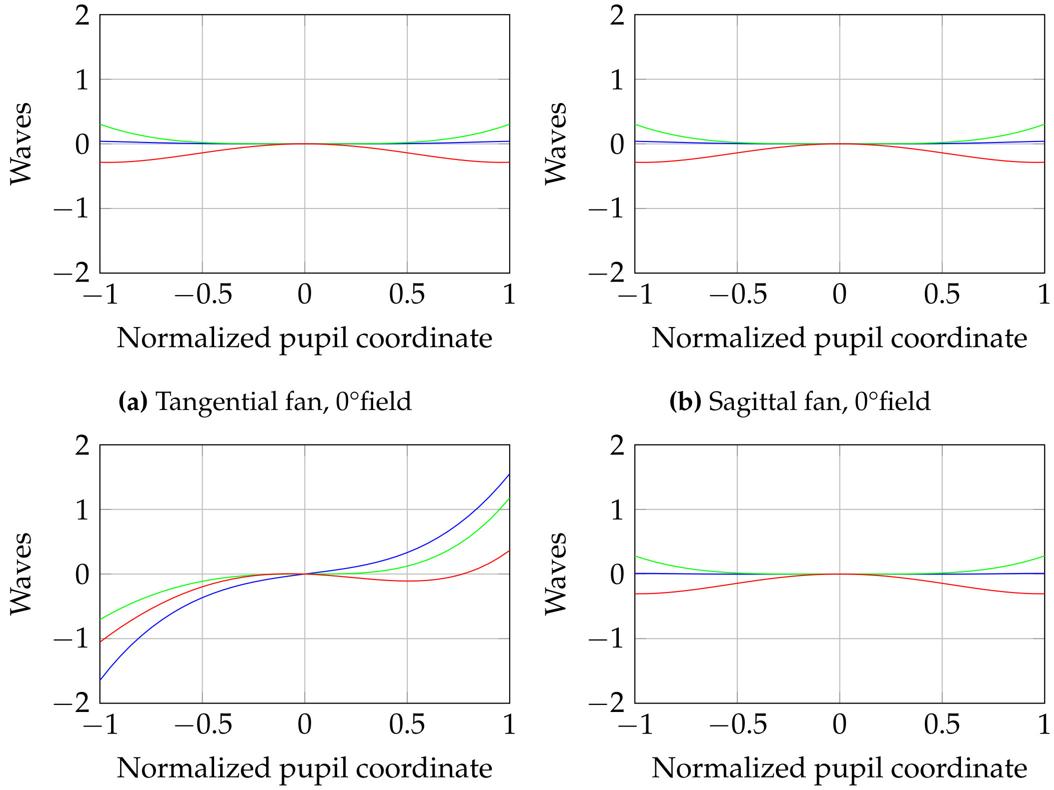

(a) Tangential fan, 0°field

(b) Sagittal fan, 0°field

(c) Tangential fan, +0.01°field

(d) Sagittal fan, +0.01°field

Figure 3.12: OPD as a function of pupil coordinate in science camera at fields 0°and +0.01°. Wavelengths: 486 nm; 588 nm; 656 nm.

normalized aperture dimension l/r_0 of 2 , which means that the correction degree will be limited by the severity of the aberration for a particular aperture size, and it won't be better than this approximate value of $l/r_0 = 2$.

The optical path to the science camera is not optimized for image forming, but this was not a priority in this research, where the control system performance will be evaluated with other more significant parameters as we will see in chapter 4 about the control system. The science camera in this case has also a complementary functionality as an aid for optical alignment or deformable mirror tests. Nevertheless, the system could be enhanced with a better camera, or modify the optical components in the optical path of the science camera.

In figure 3.14 is shown the Point Spread Function (PSF) cross section for both 0°and +0.01°fields, calculated by a FFT algorithm. In figure 3.14a is represented the cross section according X axis in the central column, and in figure 3.14b according Y axis. A shift around 5 µm in Y coordinate can be observed, when the maximum

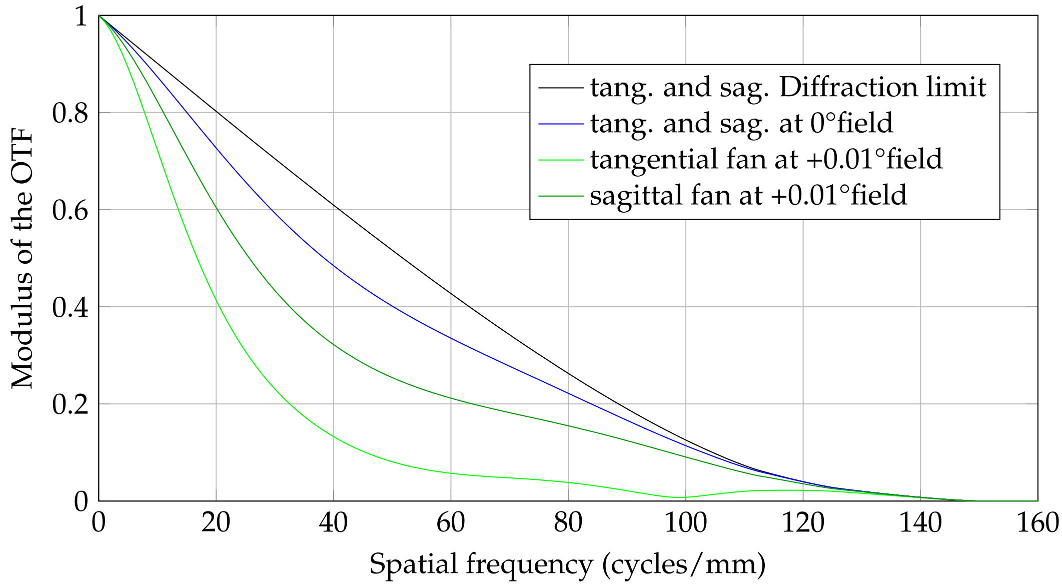

Figure 3.13: FFT MTF at science camera (wavelengths: 486nm to 656 nm, Pupil Sampling 128 x 128).

+0.01°field is applied. FWHM in these PSF are of same order of magnitude for X and Y axes and for different angle of arrival. The use in ZEMAX of accurate models of lenses provided by the manufacturer, contrary to use ideal lenses surfaces, can create the difference in magnitude and the shift in Y axis when angle of arrival is +0.01°.

Optical quality and analysis in wavefront sensor

The telescope is an F/10 focal ratio system. After attaching the adaptive optics system, the focal ratio at the wavefront sensor is incremented to working focal ratio of F/112 for each of the beams coming from the lenslet array. This increase of the F number is more than enough to satisfy Nyquist theorem, so that no information in lost in the spatial sampling in the wavefront sensor.

In the Shack-Hartmann wavefront sensor, the aim is to detect the shift of the focal points of the different subapertures, through centroiding algorithms, to measure wavefront phase aberrations. To get the best possible performance in these measurements, the PSF of these lenslet focal points should aim for Gaussian curve shapes with ideally no aberrations. The output of the system in the wavefront sensor is a grid of focal points, so multiple images are formed. In figure 3.15 is shown the output at the wavefront sensor obtained in ZEMAX, when the input

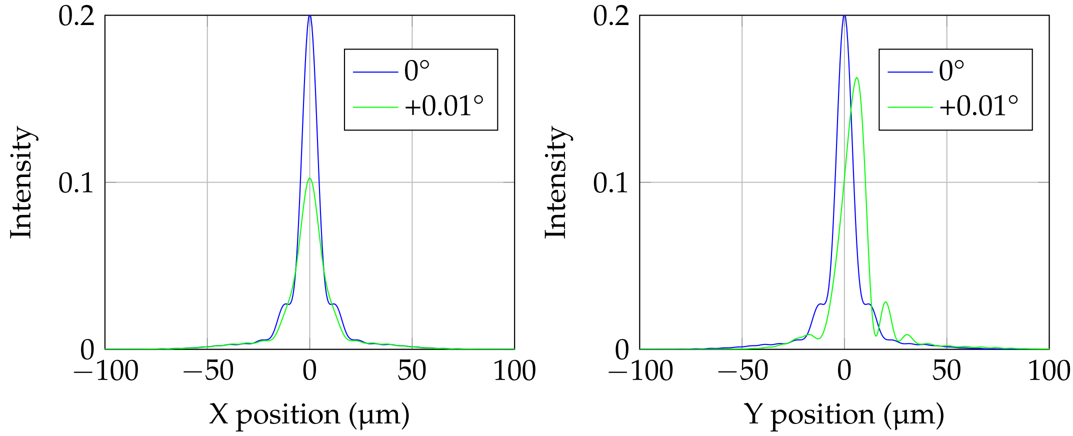

(a) X axis **(b)** Y axis

Figure 3.14: PSF cross section in science camera (pupil sampling 256 x 256, Central Column, Wavelengths: 481nm to 656nm).

is an ideal circular shape situated at infinity in the object plane, with fields 0°and +0.01°.

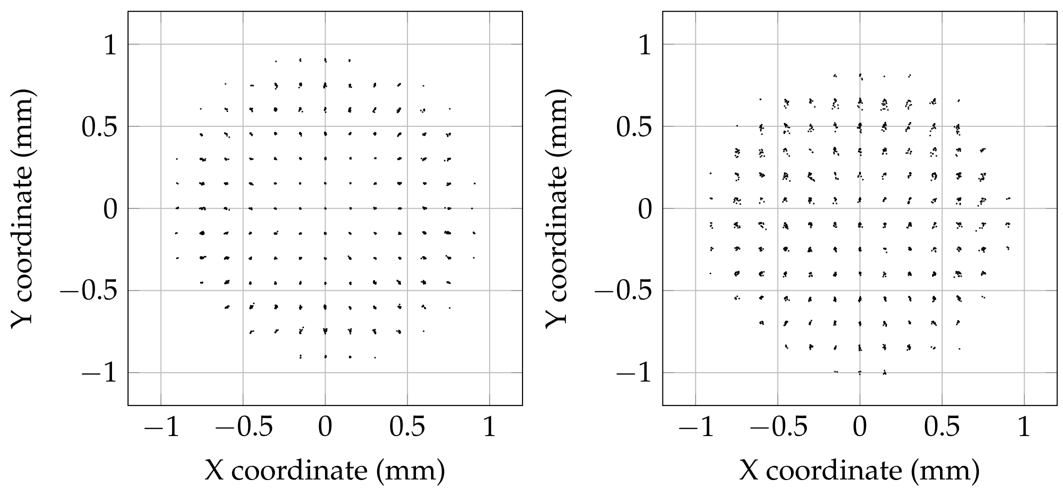

(a) field 0° **(b)** field +0.01°

Figure 3.15: Geometrical image output in wavefront sensor when input is a ideal circle in infinite at object space without telescope (wavelengths: 486nm to 656 nm).

The methods to evaluate the image quality in the science camera where based in image formation, but in the case of the wavefront sensor, geometrical methods give us more useful information to analyze the optical properties of the system. Moreover, in the science camera FFT calculations were made with reference to a single sphere located in the exit pupil of the system. In this case, the wavefront does not converge in a single image, so now this criterion can no longer be applied. Nevertheless, OPD curves can be obtained for the on-axis centroid, corresponding to the central microlens of the MLA. The result is shown in figure 3.16, where according to Rayleigh criteria, the optical system could ideally work on the axis in diffraction limited conditions, as the maximum value is under one quarter of the different wavelengths, except at 486nm wavelength at field +0.01°. It is noteworthy to say that in the wavefront sensor the lenslet focal point shapes in the image are more important than the image quality, as we want to detect shifts in this focal points with the appropriate centroids algorithm, that will be described in chapter 4 about the control system.

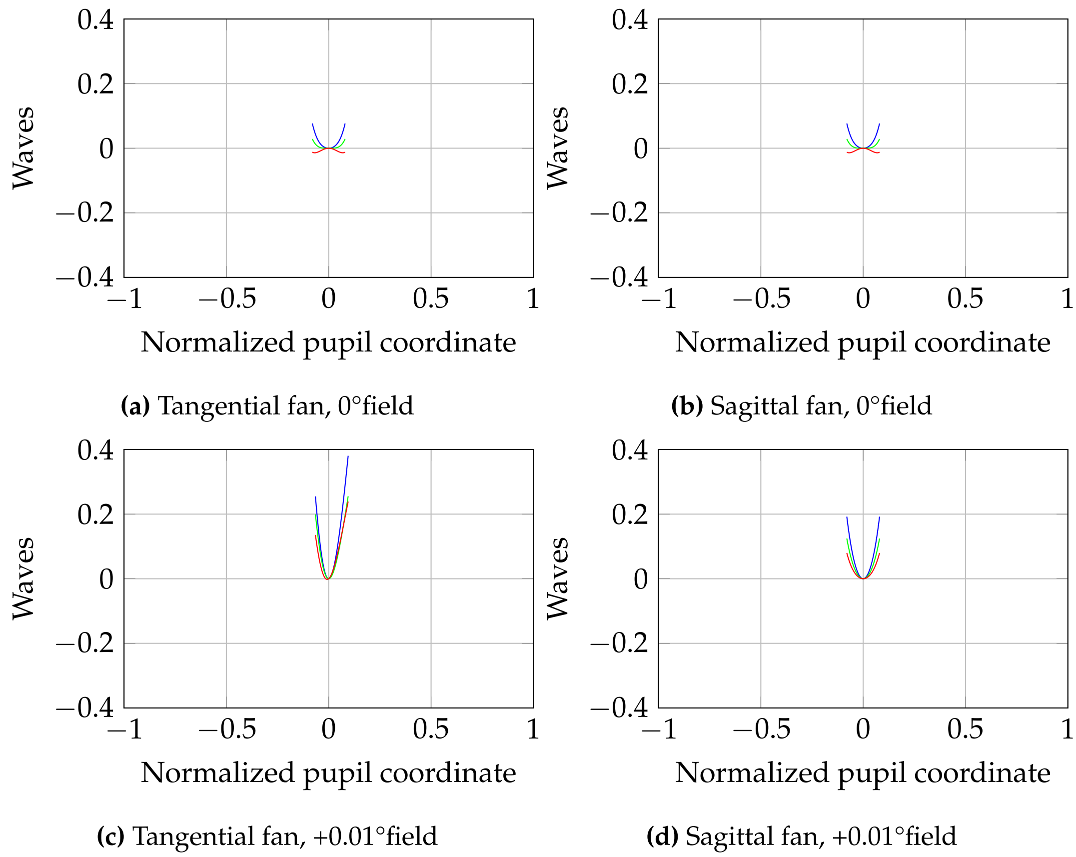

(a) Tangential fan, 0°field

(b) Sagittal fan, 0°field

(c) Tangential fan, +0.01°field

(d) Sagittal fan, +0.01°field

Figure 3.16: OPD as a function of pupil coordinate in WFS for on-axis lenslet at fields 0°and +0.01°. Wavelengths: 486 nm; 588 nm; 656 nm.

To analyze the aberrations in the rest of centroids in the image plane which are not on-axis, a geometrical analysis is performed through the transverse ray aberration curves, that are shown in figure 3.17. These curves represent geometrically the aberrations in tangential and sagittal planes as a function of pupil coordinates. The vertical gap between horizontal segments correspond to the intermediate space between lenslet focal points, approximately 166 µm. The horizontal segments shapes indicate the type and the severity of the aberrations in the image plane. From these curves it was measured a small degree of aberration at the 0°field, with a value around 23 µm for the peripheral focal points. This aberration is around 68 µm in the case of +0.01°field. The distance between centroids in the wavefront sensor is approximately 166 µm, since a 1/3 magnification has been applied with the telecentric system to the image plane of the lenslet array, with 500 µm distance between lenslets. 23 µm and 68 µm correspond with approximately 14% and 40% of the subaperture lateral size for the central and peripheral centroids respectively, which will be the maximum values of static aberrations introduced by the optical system in the WFS.

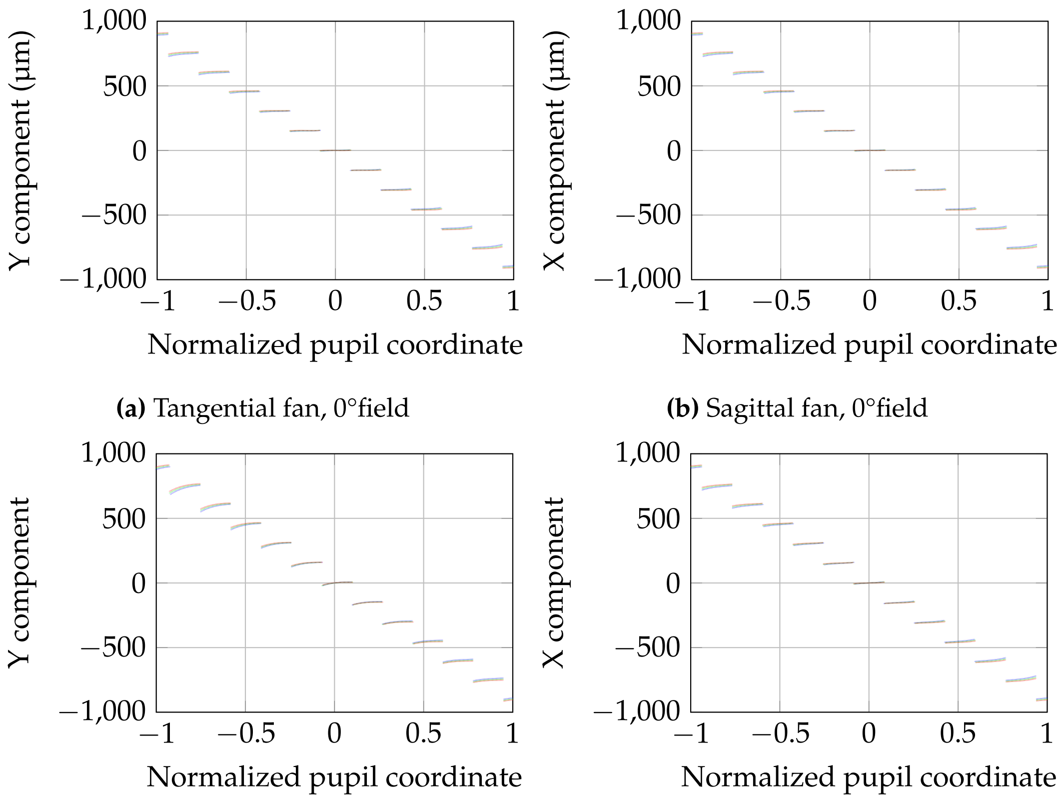

(a) Tangential fan, 0°field

(b) Sagittal fan, 0°field

(c) Tangential fan, +0.01°field

(d) Sagittal fan, +0.01°field

Figure 3.17: Transverse ray fan aberration curves as a function of pupil coordinate in WFS at fields 0°and +0.01°, without telescope. Wavelengths: 486 nm; 588 nm; 656 nm.

In figure 3.18 is shown the PSF cross section curves for both 0°and +0.01°fields, only for the on-axis subaperture, which show an adequate Gaussian shape.

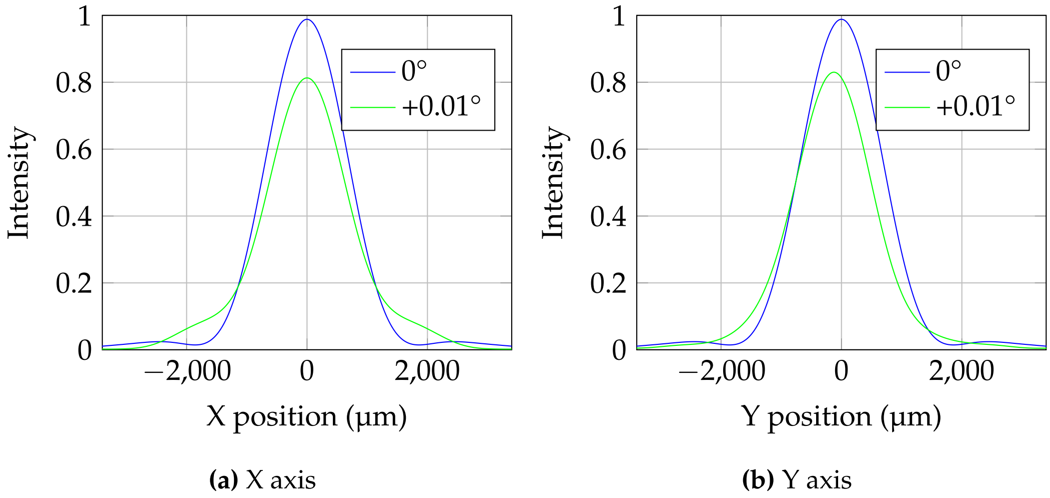

Figure 3.18: PSF Cross Section in wavefront sensor image plane (pupil sampling 256 x 256, Central Column, Wavelengths: 481nm to 656nm).

Influence of lenses chromaticism

Two sets of lens were used in the optical design, spherical singlets and achromatic doublets. When analyzed in ZEMAX, lenslets focal points in image plane obtained with spherical singlets shown a adequate shape when used with a source light at only one specific wavelength, as a laser. When used with natural light, covering all visible spectrum, peripheral focal points show a high degree of chromatic aberration, visualized as stripes or line segments, rather than points. This could drastically degrades the output of the centroids algorithm. When achromatic doublets are used, this aberrations is significantly lower, being a more reliable image to detect centroids. This effect can be observed in figure 3.19, where the lenslet focal point shapes in the image plane are shown, when used the two different sets of lenses.

Influence of telescope

To evaluate the influence of the telescope in the optical path, a model of the 16" Meade LX200 telescope used in this research has been introduced in ZEMAX. Some of the aspects to evaluate were the influence of the primary and secondary mirrors in the aberrations, and the effect of the central obscuration in the image plane. When the telescope model is included, aberrations have approximately the same values, as is shown in figure 3.20. From these curves, at 0°now aberration of the SH spot is an elongation of around 23 μm and at +0.01°is 70 μm, approximately the same values when the telescope model was not included in the analysis.

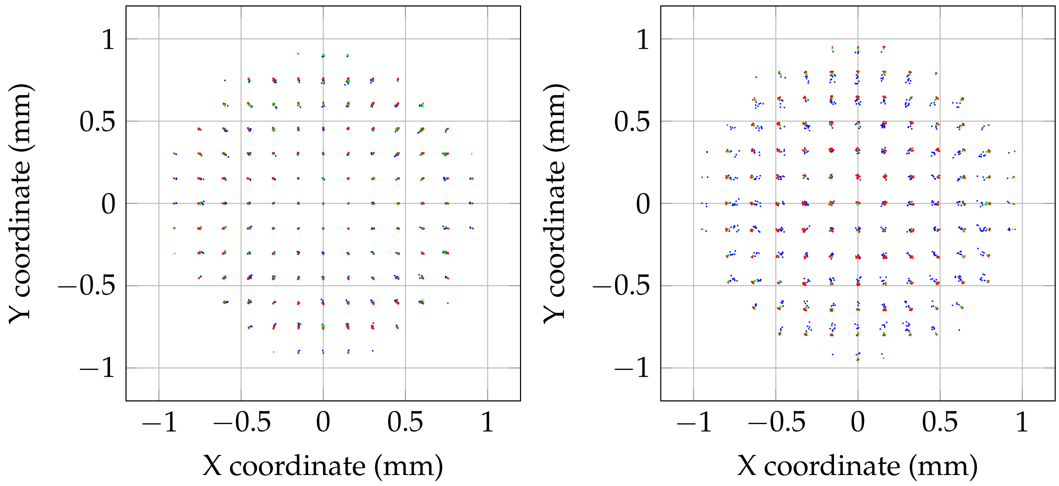

(a) achromatic doublets **(b)** spherical singlets

Figure 3.19: Geometrical image output in WFS when input is a ideal circle in infinite at object space (wavelengths: 486nm to 656 nm) at 0°field. Wavelengths: 486 nm; 588 nm; 656 nm.

The effect of the central obscuration in the wavefront sensor image plane is shown in figure 3.21, where the image of the MLA now is an annular area, that shows a enough lenslet focal points to perform the reconstruction efficiently, as we shall see in chapter 4 about the control system.

Other effect of the obscuration that can be evaluated is the degradation in the MTF curve, that can be observed in figure 3.22. Due to the absence of chief ray, the FFT algorithm can not be applied to calculate the MTF. Instead direct integration of Huygens wavelets method was applied. In this figure is shown the degradation in the MTF, that eventually will reduce moderately the image contrast at the output.

3.4 Summary

Following the design considerations of the opto-mechanical design presented in this chapter, the AO system shows a high degree of flexibility that makes it suitable to be used in any amateur or research grade telescope. Particularly optical components as lenses, microlens array, deformable mirror and steering mirrors can be easily shifted to adapt to different telescope F numbers, and exchanged in order to adapt to various photon flux constraints and different atmosphere turbulence severity degrees, depending on telescope diameter, height above sea level and local conditions of a particular site.

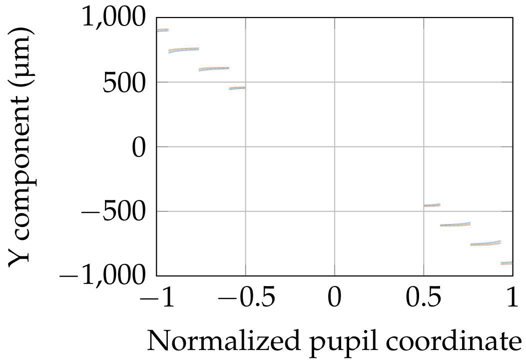

(a) Tangential fan, 0°field

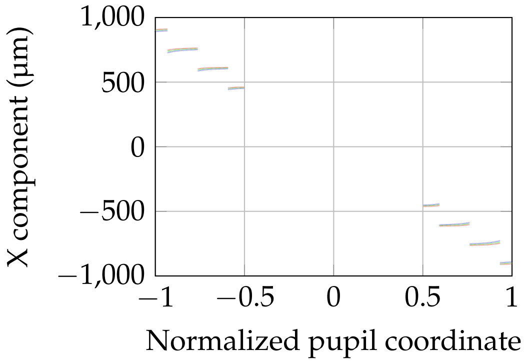

(b) Sagittal fan, 0°field

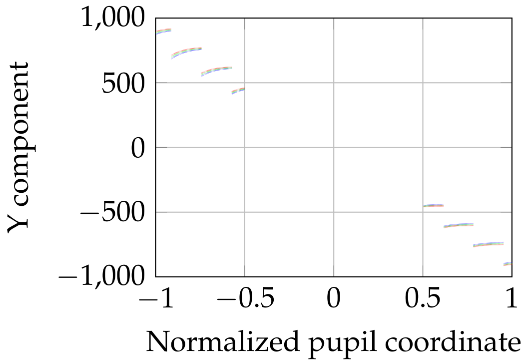

(c) Tangential fan, +0.01°field

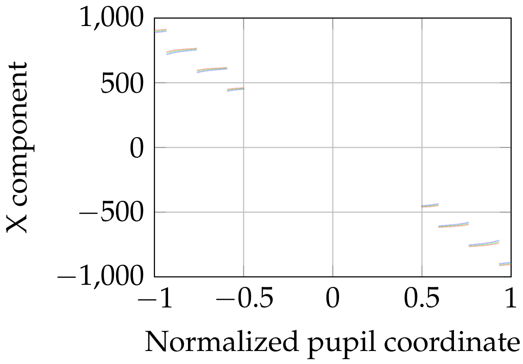

(d) Sagittal fan, +0.01°field

Figure 3.20: Transverse ray fan aberration curves as a function of pupil coordinate in WFS at fields 0°and +0.01°with telescope. Wavelengths: 486 nm; 588 nm; 656 nm.

All optical and mechanical components are off-the-shelf and low cost, which directs this design towards the amateur and moderate budget research community use. The continuous price decline during the last few years in optics, electro-mechanical components and image sensors, suggests that AO systems as the one describe in this thesis will reduce even more their cost and will approach this design to the general amateur and scientific astronomical community.

The opto-mechanical AO system design description and the subsequent analysis accomplished in this chapter, establish the necessary background and constraints in which the AO control design is supported, that is undertaken in the next chapter.

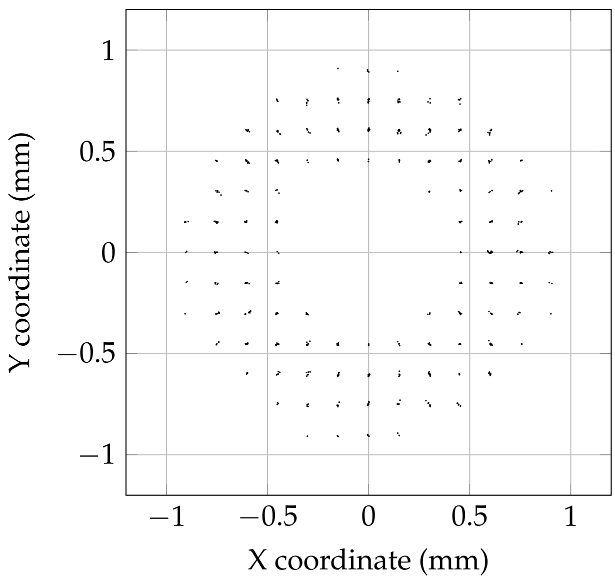

Figure 3.21: Geometrical image output in WFS when input is an ideal circle at infinite in object space at 0°field, in visible light, with telescope.

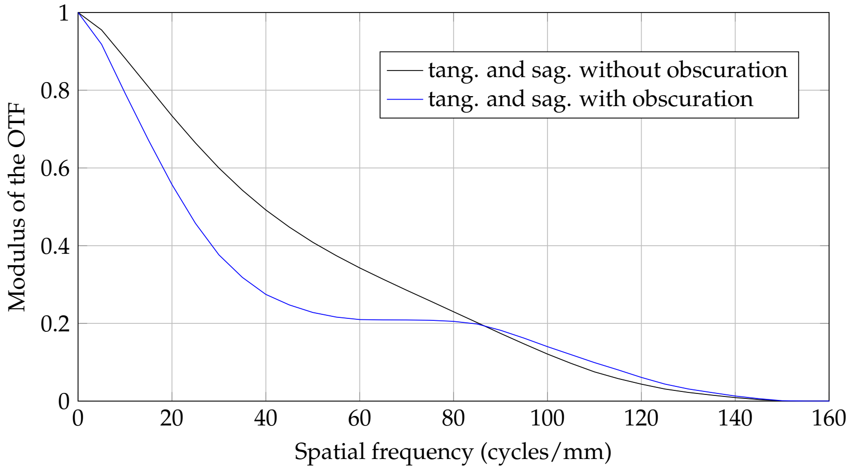

Figure 3.22: Huygens MTF at science camera (wavelengths: 486nm to 656 nm, Pupil Sampling 128 x 128, field 0°).

CHAPTER 4

Control Design

4.1 Introduction

This chapter details the design of the control stage of the AO system. Firstly the global control architecture is detailed, and then the workflow and hardware utilized in each of the stages implemented in the FPGA are shown. In the Centroids stage, two algorithms were implemented, the CoG (Center of Gravity) and 1FC (1st Fourier Coefficient). The principles, operation and hardware implementation of both algorithms are shown. Chapter 5 about experimental results later shows a comparative study of both algorithms.

Then the global hardware architecture is shown, providing details of the modules of which is formed, and the electronics specifications. The real time control software implemented in MATLAB is described, including its operation.

It is important to note that while this is described as a complete and functional system there are a number of novel and unique contributions: all processing is done in real time in small electronic devices, with only a software interface to guide the process, contrary to the usual AO control systems; the development and testing of the design is rigorous with parallel simulation using real data in MATLAB; the use of alternative methods to determine centroids are employed in simulation and real time hardware; and the addressing of numerical precision within the design is a priority.

In appendices A.1 and A.6 more details are provided about the Real-Time control software and relevant code respectively.

4.2 Control architecture

4.2.1 Global control architecture

In figure 4.1 is shown the global control architecture of the AO system.

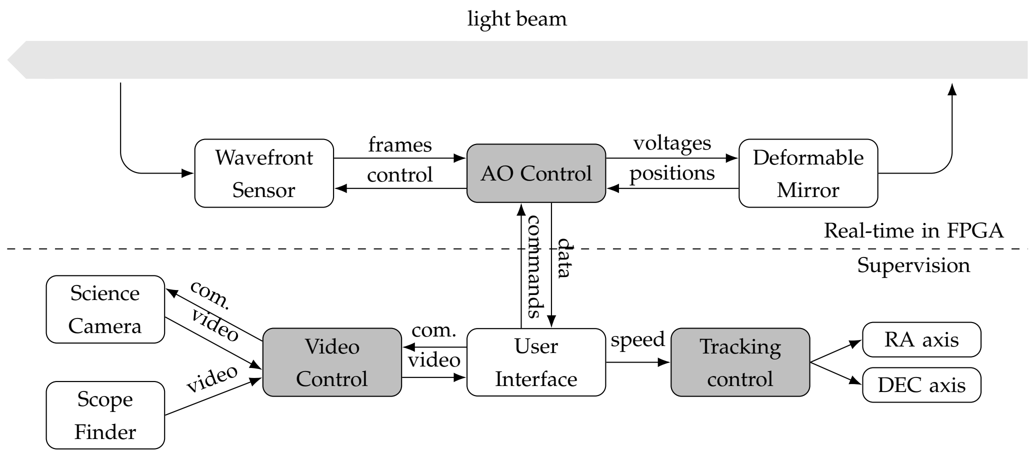

Figure 4.1: Global control architecture.

The control architecture is divided in three main modules, AO control, Tracking control and Video control (shaded in gray in figure 4.1), all of them attached to a User interface. The AO control is a closed loop adaptive optics system, fully implemented in a standalone FPGA, which essentially receives frames from the wavefront sensor and sends the appropriate voltages to the deformable mirror actuators. The AO control module sends control signals to the WFS in order to change its parameters and initiate, stop or reset the frame capture. From the User Interface, parameters of the AO system can be modified in real time, and also data from intermediate sections of the AO control stage can be displayed or stored for later analysis. In subsection 4.2.2 is detailed the AO control architecture.

The Tracking control module provides signals to Right Ascension (RA) and Declination (DEC) axes of the telescope mount, keeping a sidereal tracking speed, or any other speed, to track other objects such as satellites. The video control module receives image streaming from the science camera which is shown in the display of the User Interface. Also from this interface, parameters of the science camera can be modified in real time, and video streaming from the finderscope camera is received. Details of the tracking control module are shown in appendix A.3.

4.2.2 AO Control module

Figure 4.2 shows the global AO control architecture implemented in the FPGA. There are several stages that form the closed loop reconstruction algorithm: calculation of centroids and their gradients with respect to a reference image, determination of the first 10th Zernike coefficients excluding piston mode, obtaining of DM actuator voltages, and lastly interface signaling. In figure 4.2 these stages are split up in their Intellectual Property (IP) blocks. On top and bottom of the figure are the control, clocks, frame and command stages, which for clarity of the figure, their main blocks are explained in their corresponding sections.

Next is a description of the inputs and outputs of the AO control architecture.

INPUTS:

CLK_{in}: Clock signal which comes from the wavefront sensor along with H_{sync}, V_{sync} and D_{IN} signals. It is used to synchronise all blocks in the design.

CLK_{50}: Clock signal generated externally to the FPGA from an 50 MHz frequency oscillator.

H_{sync}: Horizontal synchronism signal from the wavefront sensor. It's a logic signal of value 1 when pixels read in a row are active, and 0 otherwise.

V_{sync}: Vertical synchronism signal from the wavefront image sensor. It's a logic signal of value 1 when pixels read in a frame are active, and 0 otherwise.

D_{IN}: Pixels intensity data coming from the wavefront sensor, one value per clock tick, and with selectable resolution of 8 to 10 bits, that is 256 to 1024 grayscale possible values.

COM: Command data in serial RS232 protocol format coming from the User Interface.

OUTPUTS:

CLK_{out}: Clock signal generated inside the FPGA, which feeds the input clock of the wavefront sensor. From this input clock, the wavefront sensor generates the CLK_{in} signal that feeds all the clocked blocks in the FPGA.

SYNC: Signal generated each frame of the wavefront sensor, to synchronize snapshot frames that are transmitted from the FPGA to the User Interface, used for data logging.

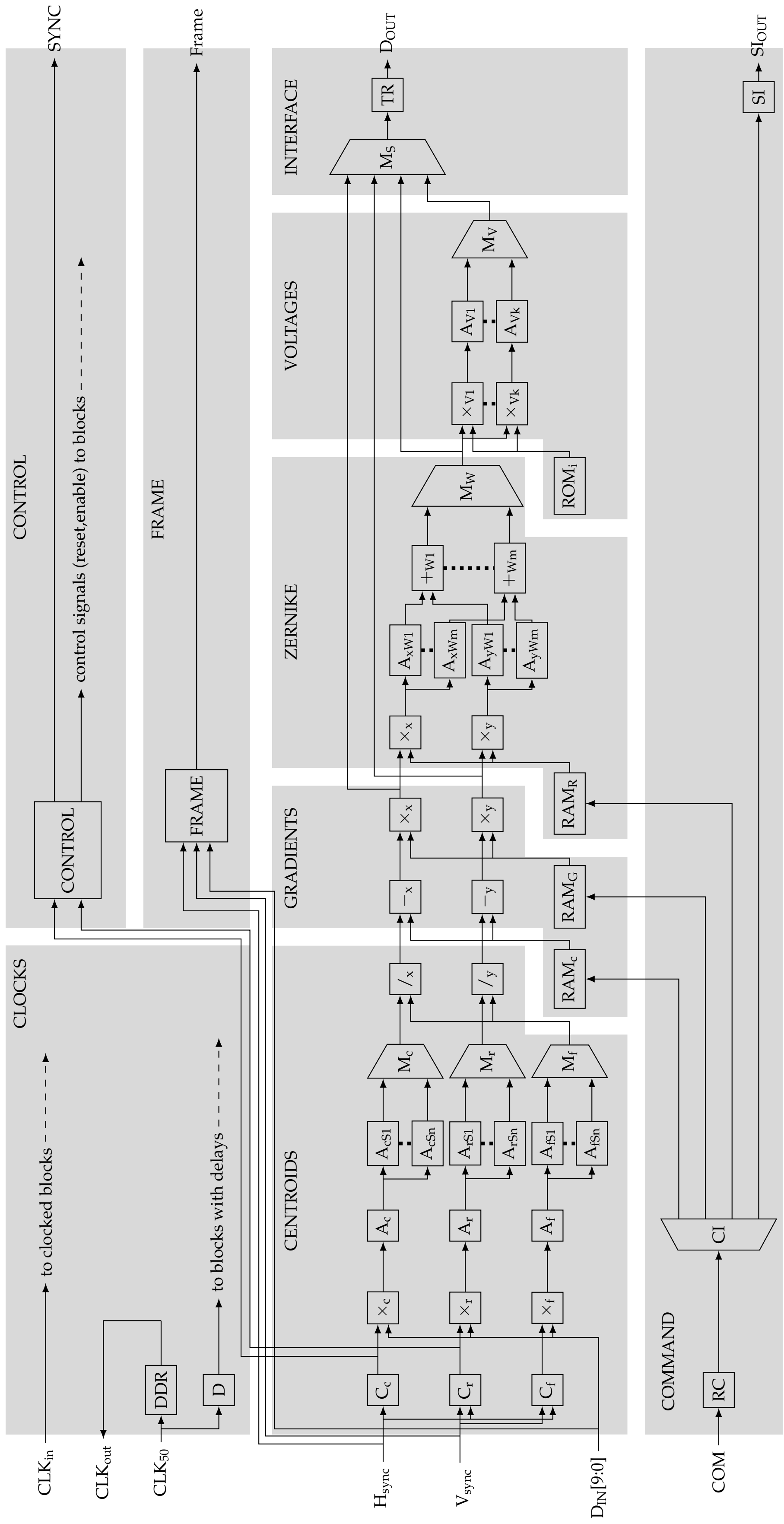

C: Counter ×: Accumulator M: Multiplexer /: Divider −: Subtraction +: Addition TR: Transmitter RAM_c: RAM centroids RAM_g: RAM gradients RAM_R: RAM zernike ROM_I: ROM influence functions RC: Receiver CI: Command Interface SI: Serial Interface DDR: Double Data Rate module D: Delays

Figure 4.2: AO control architecture implemented in FPGA.

Frame: Here a snapshot frame from the wavefront sensor is generated, when the appropriate command is sent from the User Interface to the FPGA. It's then transmitted in RS232 serial protocol format.

D_{out}: Real time high speed serial transmission of gradients, Zernike coefficients and actuator voltages given to the deformable mirror through an SPI interface, and to the User Interface through a USB communication link.

SI_{out}: Serial interface transmission of command data to control the wavefront sensor and modify its parameters.

In the five reconstruction stages is where the phase information of each of the subapertures of the WFS is converted to the actuator voltages of the deformable mirror, which are sent to to it through the signal D_{out} in the Interface stage. The Command stage provides communication with the user interface, which consists of a command interpreter implemented in the FPGA. The Clocks section generates the clock signals required by the rest of the blocks of the design, from an external oscillator of 50 MHz. In the Control stage is where the reset and enable signals of rest of blocks are generated, and also the SYNC signal to synchronize the output data D_{OUT}. The Frame section provides a capture frame from the wavefront sensor through a serial interface from D_{IN}, H_{sync} and V_{sync} signals. In the next subsections, each of these stages are detailed, showing their control architecture and providing details of their corresponding hardware implementation. To optimize the design, two techniques are combined in the FPGA, time division multiplexing[77] and resource sharing[42], each applied in the design where more convenient.

- Centroids stage
  An accurate centroid calculation of the Shack-Hartmann subaperture focal points in the wavefront sensor is a crucial part of the wavefront reconstruction and also an important error source. Different researchers have investigated the importance of this calculation in the AO reconstruction process. Stone [66] made a comparison of centroiding algorithms, and stated that the Gaussian fit is a good centroiding method, and that a method based in moments (as the Center of Gravity(CoG)) suppressing the sky background below a certain threshold shows good performance when that background level is significant. Fusco [22] also compared different centroiding methods, specifically for a SH wavefront sensor. In his research is shown that different methods work better than others for diverse turbulence conditions, background noise and

photon flux. Fusco stated that there is no a perfect centroiding method for every conditions, and established a methodology to calculate the error due to centroiding in a SH wavefront sensor. Ruggiu [60] investigated the use of centroiding methods based on a Gram-Charlier expansion, and he obtained more accurate centroiding results in low light level conditions, when compared with the standard CoG estimation.

From this previous research it is deduced in general terms, that high computational methods as the Gram-Charlier expansion or the Gaussian fit result in higher accuracy in the centroids calculation, compared to more simple methods in computational load, as the CoG. For our purpose, a fast and simple computational calculation of the centroid is a must, due to the limited computational capability of the chosen hardware platform. This leads to the need of a optimised and fast implementation in the FPGA. For this purpose, an algorithm based in the 1st coefficient of the Fourier expansion was implemented (more details provided below in 1FC algorithm epigraph of this section). Also a standard CoG algorithm was implemented for its simplicity and speed. For comparison purposes, a Gaussian fit algorithm was developed but not implemented in the FPGA. These three algorithms were tested in floating point calculations in a post process flow, and also the 1st Fourier Coefficient (1FC) and the CoG algorithms were tested on-sky in the FPGA in real time, and experimental results are shown in chapter 5. The operation of both centroiding algorithms, 1FC and CoG is now detailed.

CoG algorithm

The center of gravity algorithm is one of the fastest calculations that can be performed to obtain the centroids corresponding to the SH wavefront sensor focal points. The formulas used to calculate the centroids in axes x and y are as follows:

$$Cent_x = \frac{\sum_{i=1}^{N} x_i I(x_i, y_i)}{\sum_{i=1}^{N} I(x_i, y_i)}, Cent_y = \frac{\sum_{i=1}^{N} y_i I(x_i, y_i)}{\sum_{i=1}^{N} I(x_i, y_i)}, \tag{4.1}$$

where x_i, y_i are the pixel coordinates of the WFS, and $I(x_i, y_i)$ the intensity values in each of these coordinates.

In figure 4.3 is shown the centroids stage of the AO control system for the CoG algorithm.

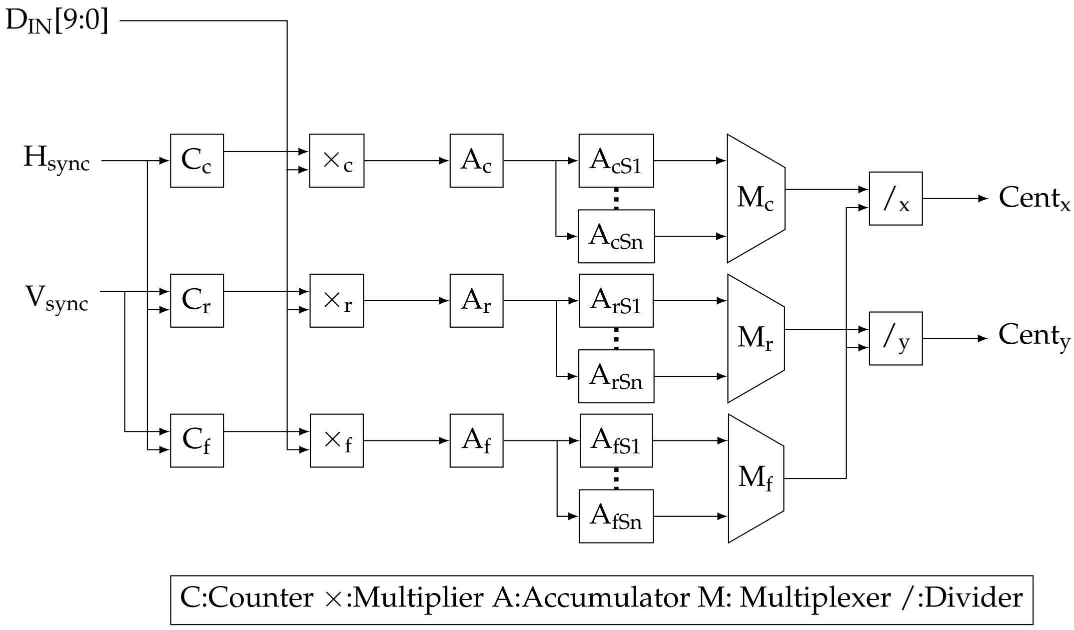

Figure 4.3: Control architecture of Centroids stage with CoG algorithm.

The input data from the wavefront sensor are represented by the signal D_{IN}, which is the intensity level of each pixel with a maximum resolution of 10 bits, while H_{sync} and V_{sync} are generated along the signal D_{in} in the wavefront sensor to synchronize pixel rows and columns with the intensity data. C_c and C_r are the column and row counters respectively. C_f creates a boolean signal that is 1 when the read pixels are active, and 0 otherwise. The number of columns and rows are also used by the Control block to generate the appropriate reset and enable signals for the rest of blocks (see figure 4.2).

In the multipliers x_c and x_r, intensity data is multiplied by the number of column and row respectively. In x_f intensity data are multiplied by 1 when the pixel is active, and by 0 otherwise. A_c, A_r and A_f accumulate this products until the number of rows of each subaperture is reached. A_{cS1} to A_{cSn} accumulates again this products until the number of columns of each subaperture is reached, where n is the number of columns. A similar process is followed for A_{rS1} to A_{rSn}, and for A_{fS1} to A_{fSn}. The enable signals for these accumulators are generated by the control block. All these signals are multiplexed in M_c, M_r and M_f, with the aim to use only two dividers in the process, that otherwise would use a lot of resources of the FPGA, so a resource sharing approach is used here. The output of dividers $/_x$ and $/_y$ yield in the computed centroids Cent_x and Cent_y, in axes x and y respectively.

Regarding the hardware, C_c is implemented with a Xilinx IP Counter as a 9 bits counter with synchronous reset, while C_r and C_f are implemented as MCode Xilinx blocks (blocks coded in MATLAB scripting language and translated to hardware by Xilinx software tools in a later stage). x_c, x_r and x_f are FPGA embedded multipliers with full precision and a latency of 3 clock cycles. All the accumulators are implemented with the Xilinx IP accumulator, with 24 bits depth the row accumulators and 29 bits depth the column accumulators, with reset and enable input ports. The multiplexers are implemented with Xilinx IP multiplexers. Dividers are implemented with Xilinx Divider Generator 3.0, with a output fractional width of 16 bits, enough to get the required precision. The analysis of the required precision is detailed later in section 4.5.2 of this chapter.

Appropiate delays are included in the different data paths in order to synchronize the intensity data from the wavefront sensor with signals H_{sync} and V_{sync}. In the similar software solution these are implemented as blocks in Simulink/System Generator.

1FC algorithm

To optimize the centroids calculation for low S/N ratio intensity data, an algorithm based in the 1st Fourier coefficient was implemented in the FPGA. This algorithm was proposed by Küveler in 1998 as an automatic guiding method of primary images in solar Gregory telescopes for a one dimensional profile [32], that later was extended to two dimensions [74]. Mackey et al. proposed the use of this algorithm to measure the image motion caused by turbulence for a free-space optical link over water [37]. In the previous cases, the algorithm was implemented in CPUs, but not in FPGA devices. In this research this algorithm is implemented in the FPGA, and next is shown the derivation of the formulas used to measure the centroids based on the 1FC algorithm.

The amount of asymmetry in an sample of 2N discrete data points in a profile f(x) can be defined in one dimension as a Fourier sequence as follows:

$$f(x) = \sum_{k=-N}^{N} C_k \, e^{2\pi i k x/N}, \tag{4.2}$$

where $C_k = a_k + ib_k$ are complex Fourier coefficients. If f(x) is symmetric with respect the origin x=0, then the imaginary parts of C_k disappear, and therefore the next expression can be used as a measure of asymmetry of function f(x) with respect to the origin x=0, denominating

$$A = \sum_{k=1}^{N} (IM[C_k])^2. \tag{4.3}$$

If the shifting theorem of Fourier transform is applied to the previous equation, for a shift of value Δx, we obtained:

$$A(\Delta x) = \sum_{k=1}^{N} (IM[C_k\, e^{-2\pi i k \Delta x/N}])^2. \tag{4.4}$$

If A is minimized with respect to Δx, the more symmetrical point in the sample of 2N discrete data points is obtained.

To obtain a feasible implementation in the FPGA, fast enough to cope with the atmosphere turbulence variation rate, this algorithm should be as simple as possible. With this aim, only the 1st Fourier coefficient (k = 1) will be considered, yielding in the next expression:

$$IM[C_1\, e^{-2\pi i \Delta x/N}] = a_1\, sin(2\pi \Delta x/N) - b_1\, cos(2\pi \Delta x/N) = 0 \tag{4.5}$$

From this expression the value of Δx, the location of the centre of symmetry, is obtained:

$$\Delta x = \frac{N}{2\pi}\, arctan \frac{b_1}{a_1} + C_x \tag{4.6}$$

where C_x can be named as the phase correction term for x axis, with its values expressed in the next table:

Table 4.1: Values of the phase correction term C_x as a function of a_1 and b_1.

b_1	a_1	C_x
> 0	> 0	0
any	< 0	N/2
< 0	> 0	N

Extending these results for two dimensions, a similar expression would be obtained for a shift of value Δy in y axis, and the corresponding values of the phase correction term in y axis C_y in table 4.2:

$$\Delta y = \frac{N}{2\pi} arctan \frac{b_1}{a_1} + C_y. \tag{4.7}$$

Table 4.2: Values of the phase correction term C_y as a function of a_1 and b_1.

d_1	c_1	C_y
> 0	> 0	0
any	< 0	N/2
< 0	> 0	N

In figure 4.4 is shown the centroids stage implementation for the 1FC algorithm.

The input data from the wavefront sensor are the intensity data represented by the signal D_{IN}, and the synchronism signals H_{sync} and V_{sync}. The output of column and row counters of CoG algorithm (C_c and C_r) now are the indexes of four ROM memories, that are initialized when the FPGA is programmed at the beginning of the AO control operation, according to the next formulas:

$$SIN_A = sin(\frac{(j-1) \times 2 \times pi}{Columns - 1}) \qquad COS_A = cos(\frac{(j-1) \times 2 \times pi}{Columns - 1}) \tag{4.8}$$

$$SIN_B = sin(\frac{(j-1) \times 2 \times pi}{Rows - 1}) \qquad COS_B = cos(\frac{(j-1) \times 2 \times pi}{Rows - 1}) \tag{4.9}$$

where j is the number of column (for ROM_{cosB} and ROM_{sinB}) or row (for ROM_{cosA} and ROM_{sinA}). The outputs of these ROMS are multiplied by the intensity data in the multipliers x_c, x_d, x_a and x_b. The result of multiplier x_c

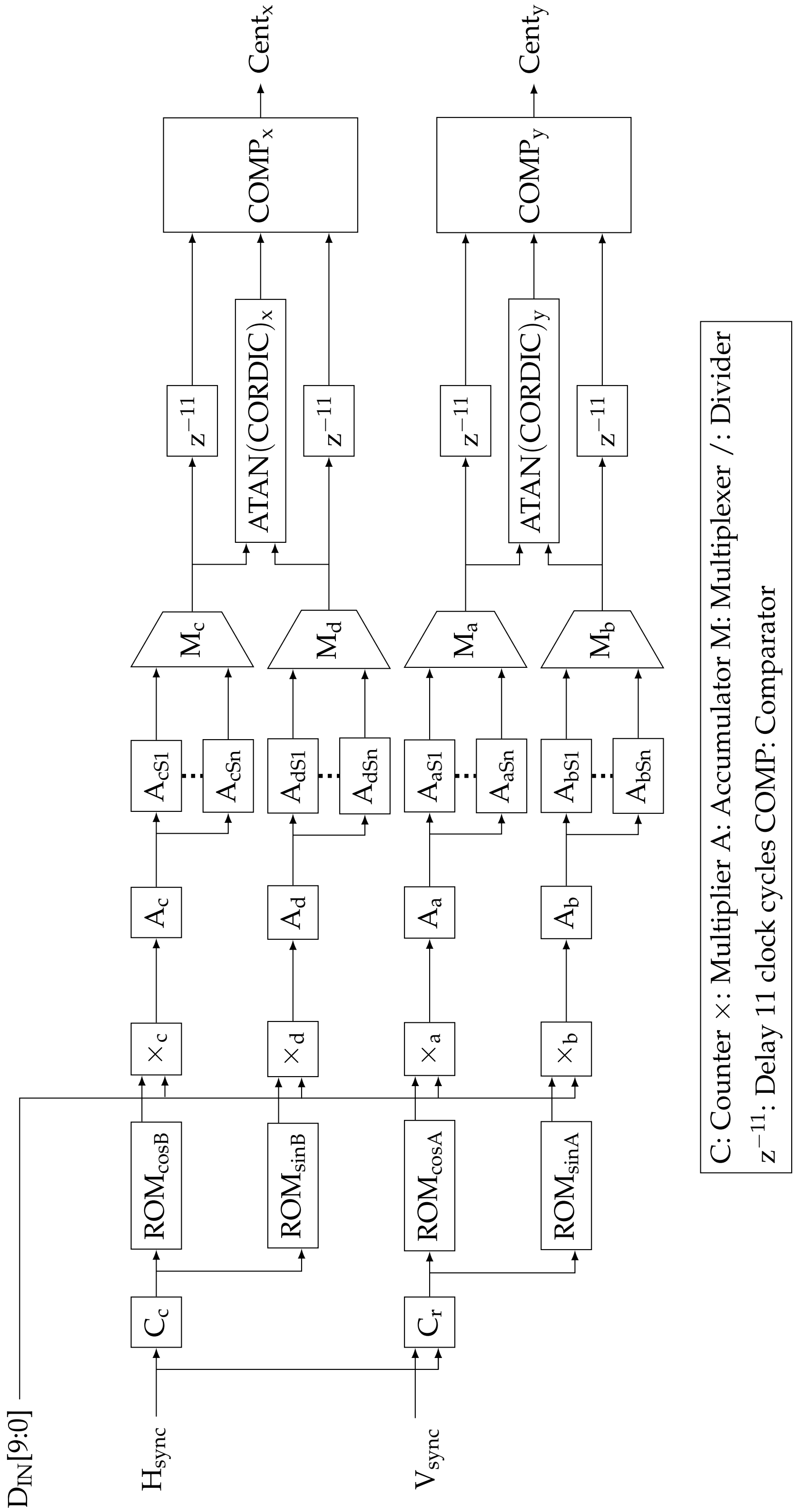

Figure 4.4: Control architecture of Centroids stage with 1FC algorithm.

are accumulated by column and row in the accumulators A_c, A_{cS1}, A_{cSn}, and a similar process occurs in the outputs of the rest of the multipliers. These values are then multiplexed in M_c, M_d, M_a and M_b in order to share the blocks of the next stage. The arctangent is calculated through a CORDIC (Coordinate Rotation Digital Computer) algorithm, an efficient method to implement trigonometric functions [72]. The output values of the multiplexers are delayed 11 clock cycles in order to be synchronized with the outputs of the CORDIC algorithms, before reaching the comparators ($COMP_x$ and $COMP_y$) where the appropriated phase correction term is added. The output of the comparators are the centroids $Cent_x$ and $Cent_y$ in axes x and y respectively.

As in the CoG algorithm implementation, C_c is implemented as a Xilinx IP Counter and C_r as a MCode Xilinx block. Also multipliers, accumulators, multiplexers and delays are implemented as Xilinx IP blocks. The arctangent CORDIC algorithm is implemented with a Xilinx block with 20 processing elements, 31 bits data width and binary position of 14 bits. Comparators, $COMP_x$ and $COMP_y$, are implemented as MCode Xilinx blocks.

- Gradients stage
  In figure 4.5 is shown the gradients stage of the control algorithm implemented in the FPGA. In this stage is where the gradients in axes x and y are calculated for each subaperture of the SH wavefront sensor, from the absolute centroids shift in pixels obtained in the Centroids stage.

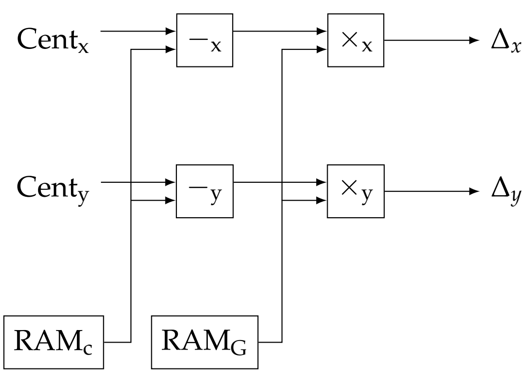

x: Multiplier −: Subtraction RAM_c: RAM centroids RAM_g: RAM gradients

Figure 4.5: Control architecture of Gradients stage.

In blocks $-_x$ and $-_y$ are where the absolute value of centroids shifts are subtracted from a reference centroids matrix stored in RAM memory (RAM_c).

Initial reference centroids values are preloaded in RAM_c when FPGA is programmed in the initialization stage, corresponding to a perfectly flat and non aberrated wavefront. These values can be modified in real time from the User Interface, when a snapshot reference image is selected by the user. Due to the small size and reduced weight of the telescope-AO system tandem, these are more affected by inertial forces when telescope is tracking sidereal objects, or external sources as wind, which can create misalignment on the opto-mechanical design, which can be compensated in real time, just loading a new centroids reference into the FPGA.

The output of the $-_x$ and $-_y$ blocks is measured in pixels. To change the scale of these measurements, outputs of these blocks are multiplied by a constant value stored in RAM_G in x_x and x_y multiplier blocks, and therefore the gain of the control loop is modified. The gain value stored in RAM_G can be modified in real time from the User Interface, that provides and efficient way to deal with the reference variability in the AO system. At the output of this stage the gradients in axes x and y are obtained, which are sent to the Zernike stage, and also to the interface multiplexer M_s as shown in figure 4.2, in order to send the gradients in real time to the User Interface.

Regarding the hardware, subtractors and multipliers; these are implemented with Xilinx IP blocks. RAM_c is implemented as two dual port RAMs with depth 100 addresses, corresponding to 100 centroids on each axis, using block RAM of FPGA. RAM_G is implemented as two single port RAMs, for axis x and y, using distributed memory of the FPGA.

- Zernike stage
  In figure 4.6 is shown the Zernike stage of the AO control implemented in the FPGA. In this stage gradients are multiplied by the calibration matrix, yielding to the Zernike coefficients of the first n polynomials, where n is the number of classic aberration modes. In this AO control algorithm, the chosen number of Zernike coefficients is 9, that following the terminology used in this thesis based in Noll's index [47], range from Z_2 to Z_{10} as shown in table 2.2 of chapter 2. Z_1, piston mode, is deprecated, because its Zernike coefficient is constant so it is not sensed in the SH sensor. This matrix is calculated offline (see later description of Offline stage in its corresponding epigraph of this section), due to the difficulty of the calculation in a FPGA of a high dimension

inverse matrix in the available gap of time, to cope with the changing rate of atmosphere turbulence.

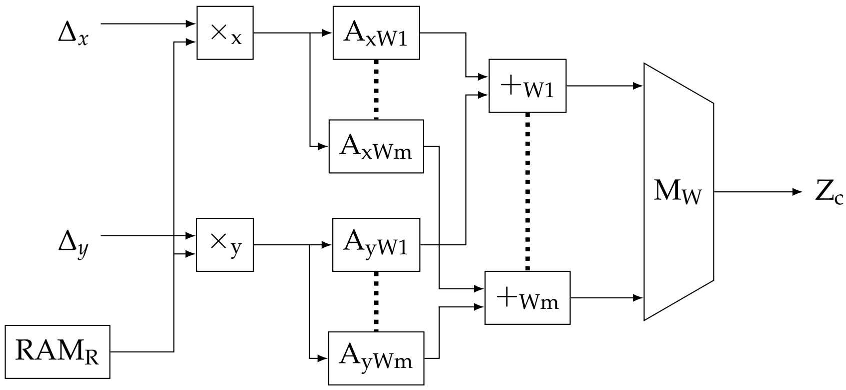

$\times$: Multiplier A: Accumulator M: Multiplexer +: Addition RAM_R: RAM zernike

Figure 4.6: Control architecture of Zernike stage.

The reconstruction matrix has dimensions equal to the number of Zernike polynomials multiplied by the total number of centroids in x and y axes. In this implementation the number of Zernike polynomials chosen is 9, which doesn't put an excessive computational load in the FPGA. If needed, this number of modes can be modified in the code, just changing the dimensions of the matrices and adding the polynomials in offline calculations. For a 10 x 10 subaperture layout in the wavefront sensor, the total number of dots representing the centroids is 200 (100 for x axis and 100 for y axis), so the calibration matrix has dimensions 9 x 200. RAM_R is implemented as two dual port RAMs with depth 9 x 200 = 1800 addresses, both memories with the same data. At first these two RAMs are initialised with the calibration matrix calculated offline from the initial centroids reference.

The gradients Δ_x and Δ_y are multiplied sequentially by the calibration matrix loaded in RAM_R. These values are accumulated in 9 blocks for each axis (A_{xW1} to A_{xW9} for x axis, and A_{yW1} to A_{yW9} for y axis), corresponding to the 9 Zernike polynomials. In $+_{W1}$ are added A_{xW1} and A_{yW1}, and an analogue process occurs for adders $+_{W2}$ to $+_{W9}$. The Zernike coefficients are multiplexed in M_W, and its output are the 9 Zernike coefficients calculated from the centroids gradients of a particular frame, each one in a clock cycle. The Zernike coefficients are sent to the next stage, Voltages, and simultaneously to the multiplexer interface M_S, in order to debug and measure the quality of the reconstruction from the User Interface (UI).

- Voltages stage
  In figure 4.7 is shown the Voltages stage of the AO control.

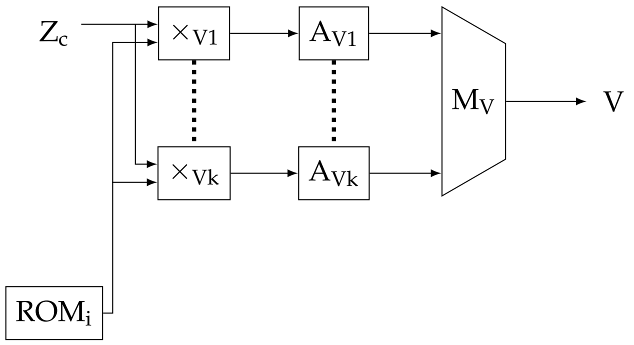

×: Multiplier	A: Accumulator	M: Multiplexer	ROM_I: ROM influence functions

Figure 4.7: Control architecture of Actuators stage.

In ROM_i is stored the influence matrix, where its rows are formed by the influence functions of the deformable mirror used in the AO control (see later description of offline stage in its corresponding epigraph of this section). The deformable mirror of the AO system has 19 actuators, therefore, the influence matrix has dimensions 19 x 9, assuming linearity of the mirror as is commonly done (we recognise crosstalk occurs in deformable mirror but ignore here). There is no need to store this matrix in RAM, because once obtained, it is formed by constant values which depend on this particular deformable mirror. This matrix is stored in Read Only Memory (ROM) memory, and loaded whenever the FPGA is programmed.

In the 19 multipliers x_{V1} to x_{V19}, the Zernike coefficients coming from the previous stage are multiplied by the influence functions values stored in ROM_i. The output of the multipliers are accumulated in blocks A_{V1} to A_{V19}, and then multiplexed in M_V, in order to obtain the 19 voltages sequentially at the output, one voltage per clock cycle. Next these values are sent to the multiplexer M_s of the Interface stage, that later will be sent out of the FPGA through the TR block, in a high speed serial communication.

ROM_i is implemented in 19 ROM blocks of distributed memory in the FPGA with depth 9 addresses each. Multipliers, accumulators and the multiplexer M_V is implemented with Xilinx IP blocks.

- Interface stage
  The interface stage is formed by the multiplexer M_s and the block TR, that in figure 4.8 is splitted in its main blocks: FIFO, C_{TR} and RS232.

  Signals from gradients (Δx and Δy), Zernike coefficients (w_i) and voltages (V) are multiplexed in a single data line, which is the input of a FIFO of depth 256 bytes, which is connected to an RS232 transmitter block. Those two blocks are controlled by block C_{TR}. When the data (centroids, Zernike coefficients and actuator voltages) of a full frame have been received in the FIFO, C_{TR} send a control signal to RS232 block, and this in turn sends the data out of the FPGA in RS232 protocol format. Instead of using one of the standard bauds rate of this protocol, the data are sent at higher speed, 1 Mbps, in order to be able to send the data from this frame on time before the next frame results arrive. Blocks C_{TR} and RS232 are programmed in VHDL.

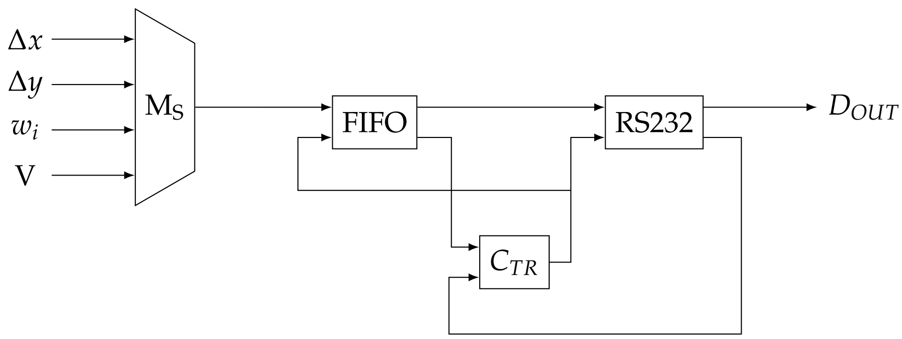

M: Multiplexer	C_{TR}: Transmission Control	FIFO: FIFO memory
RS232: Conversion to RS232		

Figure 4.8: Control architecture of Interface stage.

- Command stage
  In figure 4.9 is shown the Command stage of the AO Control implementation in the FPGA.

  Commands are sent from the User Interface, including information about the actions to perform and companion data if necessary. These data are sent in RS232 protocol. In the RS232 block, that information is converted to a parallel

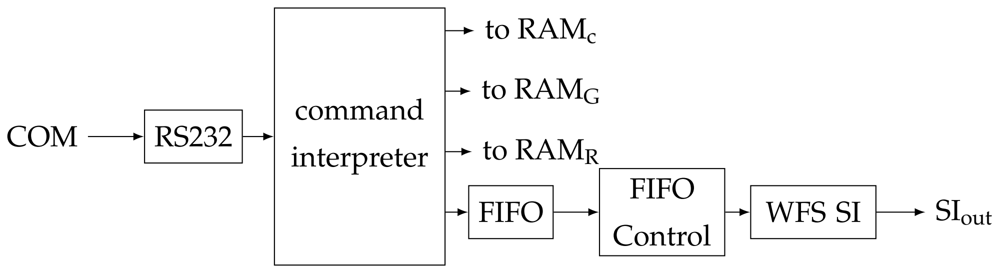

Figure 4.9: Control architecture of Command stage.

data bus and the appropriate sync signal is generated. These signals are sent to the Command Interpreter block, which according to the command sent from the UI, different actions are performed. There are four types of actions that can be accomplished in the Command Interpreter: Reference centroids data sent to RAM_c; Gain data sent to the RAM_G; Calibration Matrix data sent to the RAM_R; or configuration parameters to the wavefront sensor through a FIFO. These four actions can be performed simultaneously with the closed loop AO algorithm running.

Control signals and data for the three RAM memories are generated in the command interpreter, but parameters to configure the wavefront sensor needs to be converted to the serial interface format of this sensor. This function is performed by a FIFO, along with the FIFO Control and the WFS SI blocks. The later block stores a initial configuration for the wavefront sensor, and also converts data coming from the FIFO to the serial protocol required by the wavefront sensor.

Regarding the hardware, all blocks in this stage are code blocks (in MATLAB and VHDL), except the FIFO block, that is implemented with an IP Xilinx block. MATLAB and VHDL blocks are synthesized by Xilinx software tools previously to the implementation.

- Clock stage
  In figure 4.10 is shown the Clocks stage of the FPGA AO Control implementation.

  CLK_{50} is the signal coming from an 50 MHz external oscillator. This clock signal is the input for a DDR (Double Data Rate) block, and a D block. The latter generates different timing delays to required blocks in the FPGA, in order to have an adequate power up of the FPGA. The DDR block generates

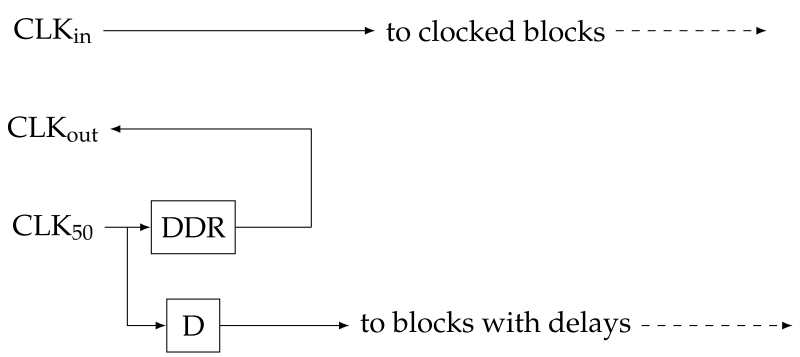

Figure 4.10: Control architecture of Clocks stage.

a 50 MHz clock signal within the FPGA, CLK_{out}, that is the clock input signal of the wavefront sensor. The wavefront sensor generates and output clock synchronized with the rest of its output signals, D_{IN}, H_{sync} and V_{sync}. This output clock of the wavefront sensor is the input clock of the FPGA, CLK_{in}, which synchronize all the blocks that form the AO control loop.

D and DDR blocks are synthesized from VHDL code to hardware with Xilinx software tools.

- Control stage
  In figure 4.11 is shown the Control stage of the FPGA AO Control implementation.

Figure 4.11: Control architecture of Control stage.

The Control block provides reset and enable signals to the rest of blocks in the AO control loop as needed. These signals are generated from the column counter (C_c) and the row counter (C_r) blocks. Also this block provides a SYNC signal, that will be an output of the FPGA, to synchronize signal D_{OUT} of the Interface stage. The Control block is generated from MCode blocks, that are translated to hardware by Xilinx software tools.

- Frame stage
  In figure 4.12 is shown the Frame stage of the FPGA AO Control implementation.

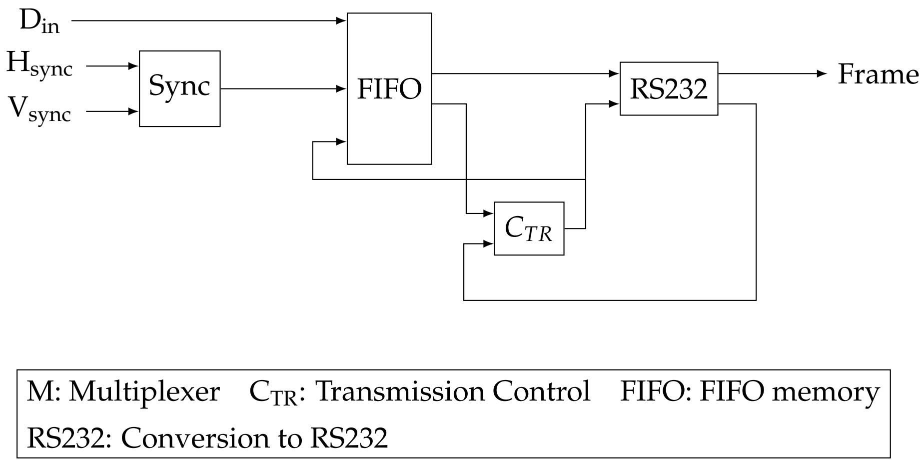

Figure 4.12: Control architecture of Frame stage.

This stage generates a 300 x 300 pixels snapshot frame, when the corresponding command is sent from the User Interface. The FIFO memory of depth 128 KBytes stores the frame, which is sent through a serial interface out of the FPGA through the Frame signal, controlled by blocks C_{TR}, and translated to RS232 protocol in block RS232. Sync block generates the write enable signal of the FIFO, from H_{sync} and V_{sync} signals. The transmission of a frame can be performed simultaneously with AO control loop algorithm running. For this purpose, the Frame signal and D_{OUT} signal of Interface stage, have dedicated and independent serial communication channels to send data, that can be accepted and managed simultaneously by the USB Controller of the UI implemented in MATLAB. MATLAB can also store such data for offline processing.

- Offline stage

  In figure 4.13 is shown the Offline stage of the FPGA AO Control implementation.

  In this stage, data to be calculated in real time are computed, which alleviates the processing load of the FPGA, that otherwise would struggle to perform these calculations in the time gap available before the next frame arrives to the WFS. These calculations are the reference centroids to be stored in RAM_c, the reconstruction matrix calculated by a least mean square algorithm, and storage of the Interaction matrix.

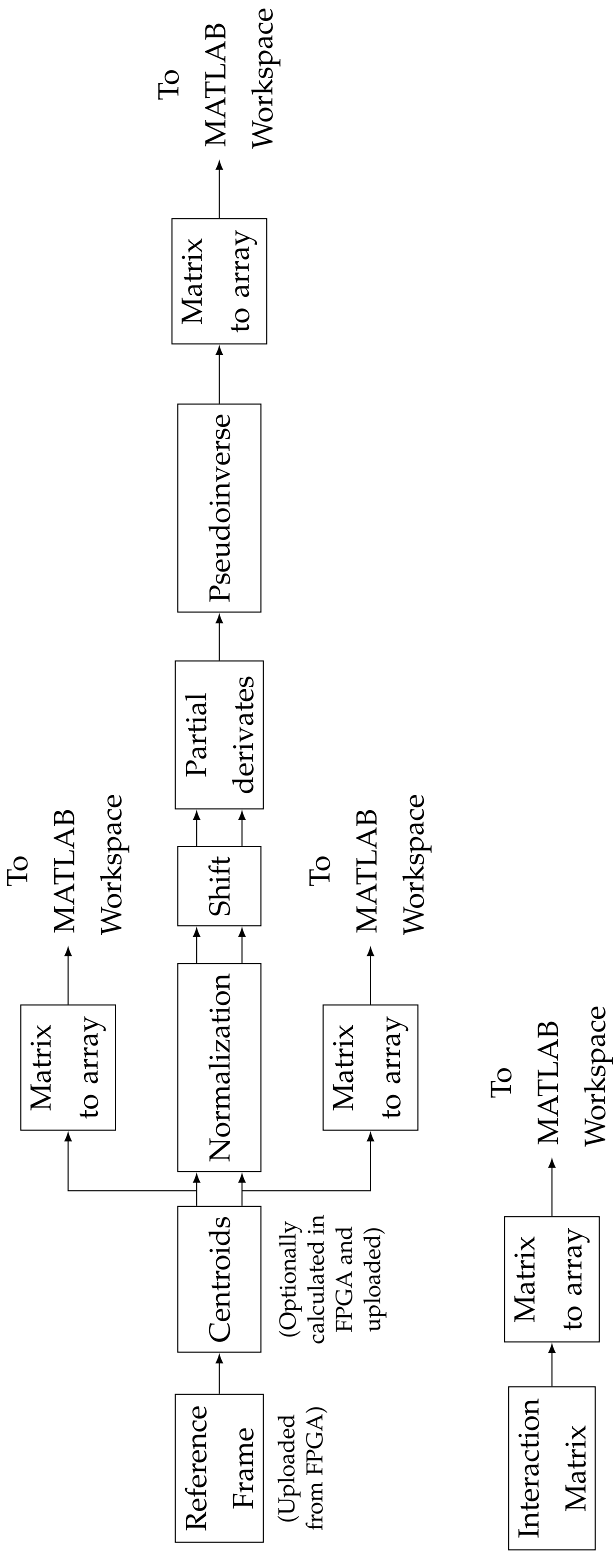

Figure 4.13: Control architecture of Offline stage.

Reference centroids are calculated initially from a non aberrated reference wavefront frame, that are loaded in RAM_c when FPGA is programmed. Later, these reference centroids can be recalculated during normal operation of the AO control loop, and stored on-the-fly in RAM_c, when the user select an appropriate new centroids reference in the User Interface.

From these centroids reference, the Zernike polynomial coefficients are calculated. First the reference centroids are normalized to unity, and then shifted in order to have a Cartesian reference in the center of a circle of diameter unity. From this reference, Zernike coefficients are obtained through the partial derivatives in X and Y axes, as shown in table 4.3, according to Noll index [47]. Normalizing parameters are not included in table 4.3, because they just scale the obtained values, but they will be included in the calculations.

Mode number	Polynomial (cylindrical)	Polynomial (cartesian)	X derivative	Y derivative
1	1	1	0	0
2	$r\,cos\theta$	x	1	0
3	$r\,sin\theta$	y	0	1
4	$2r^2-1$	$2x^2+2y^2-1$	$4x$	$4y$
5	$r^2\,cos2\theta$	x^2-y^2	$2x$	$-2y$
6	$r^2\,sin2\theta$	$2xy$	$2y$	$2x$
7	$(3r^3-2r)cos\theta$	$3x(x^2+y^2)-6x$	$3(3x^2+y^2-2)$	$6xy$
8	$(3r^3-2r)sin\theta$	$3y(x^2+y^2)-6y$	$6xy$	$3(x^2+3y^2-2)$
9	$r^3cos3\theta$	$x(x^2-3y^2)$	$3(x^2-y^2)$	$-6xy$
10	$r^3sin3\theta$	$y(3x^2-y^2)$	$-6xy$	$3(x^2-y^2)$

Table 4.3: Zernike polynomials in cylindrical and cartesian coordinates and their derivatives in X and Y axes (adapted from [13].

The calibration matrix is calculated through the pseudo inverse matrix (Moore-Penrose pseudo inverse) in the next stage, as shown in equation 2.39 in chapter 2. This matrix is initially loaded in RAM_R. During normal operation of the AO Control loop, a new reconstruction matrix associated to a particular snapshot frame can be calculated and sent to the FPGA on-the-fly from the UI.

The Interaction matrix stored in ROM_i is also generated offline. These data are loaded initially in ROM memory when FPGA is programmed. Once obtained, an adequate Interaction matrix for a particular deformable mirror doesn't need to be modified, so there is no need to store it in RAM memory. In subsection 4.5.5 is detailed the process to obtain the Interaction matrix, including simulations for any particular Zernike classic aberration and error analysis.

All offline calculations, reference gradients, calibration matrix are processed in floating point precision in MATLAB running in the support computer. In order to be used in the FPGA, floating point precision data are converted to fixed point precision in the Command Interpreter block of the Command stage, previously to be loaded in RAM memory of the FPGA.

4.3 Hardware and specifications

We briefly describe the electronic hardware used to implement our small scale AO system based in WFS with an microlens array and a OKO 19 channel DM. The hardware is generic enough to work with a range of microlens and deformable mirrors. It is important to reflect on the spatial form factor of this complete AO control system, which open avenues for use in other instrumentation.

4.3.1 Global hardware architecture

In figure 4.14 is shown the global hardware architecture of the AO control, divided in the main boards that form the system.

In the FPGA control board, the FPGA manages the communication with the CMOS image sensor that forms part of the SH wavefront sensor. After one frame from the wavefront sensor is processed in the AO algorithm in the FPGA, D_{out} will output the voltages to be applied to the deformable mirror actuators at TTL (Transistor-Transistor Logic) level. This voltages are encapsulated in an SPI protocol bus and sent to the High Voltage DM Board, which in turn converts these voltages to analog values in the D/A stage, and increases the voltage level that the deformable mirror needs, through the OA (Operational Amplifier) stage.

The voltages obtained in Teensy1 board are sent simultaneously to the support computer, along with the gradients in axes x and y, and the Zernike coefficients,

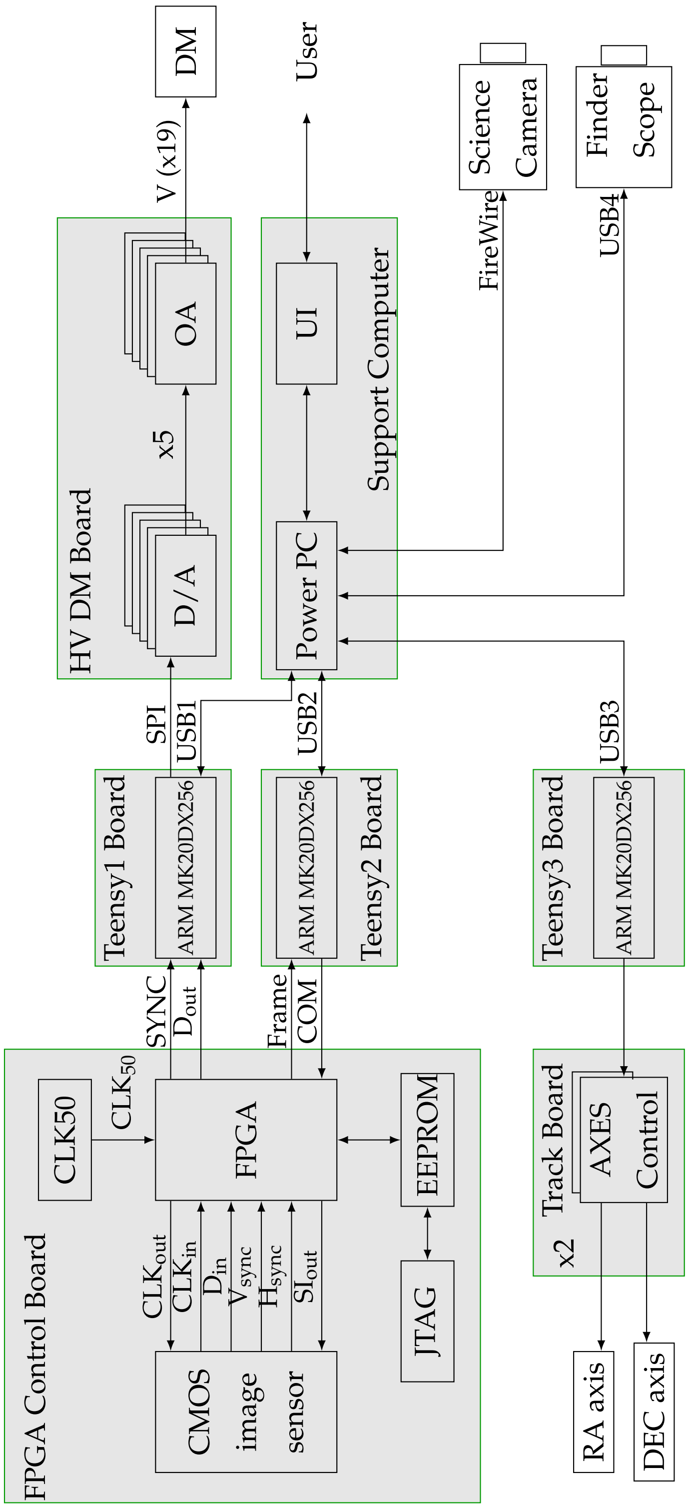

Figure 4.14: Global Hardware Architecture.

corresponding to a particular frame through USB1 interface. These data can be observed in real time in the User Interface of the support computer, and also parameters of a selected number of frames can be stored in local memory.

The FPGA is programmed through a JTAG interface, with stores the last code in an EEPROM memory, so that next time the FPGA is powered-up, the program stored in this memory is loaded automatically in the FPGA.

Teensy2 board provides another serial interface between the FPGA Control Board and the support computer. Through USB2 interface, commands can be issued from the UI, and also a snapshot frame can be received through this interface. USB1 and USB2 are managed simultaneously in the support computer, allowing these communications to be concurrent.

The support computer controls the AO system, but also manages the control of the RA and DEC telescope axes, through the Teensy3 interface board and the Track Board. It also receives and visualize real time streaming video from the Science Camera through a FireWire port, and from the Scope Finder through USB4 interface.

Next the hardware boards including their main characteristics are described.

4.3.2 FPGA control board

The main components of the FPGA Control Board includes the FPGA itself, a CMOS image sensor of the SH wavefront sensor, a 50 MHz oscillator and an EEPROM memory to program the FPGA through the JTAG interface. In figure 4.15 is shown a picture of the board with its main components indicated.

The FPGA chosen for the implementation of the AO control algorithm is a Xilinx Spartan3A XC3SD3400A. Below there is a list of its main features:

- Dimensions: 55 x 55 mm.
- FPGA: Xilinx XC3SD3400A.
- Package CSG484: Dimensions 19 x 19 mm, 484 balls in a BGA (Ball Grid Array) configuration.
- 3400K system gates.
- 5.968 CLBs.

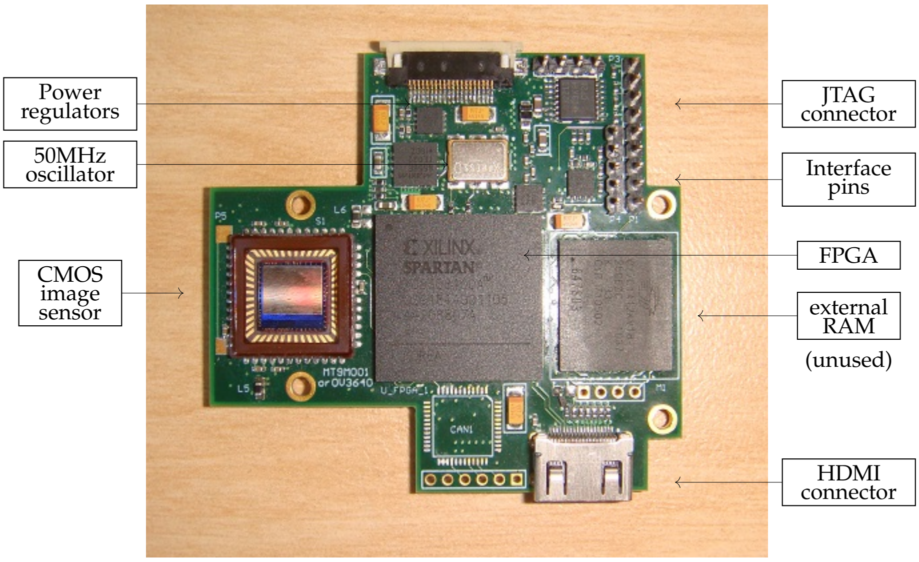

Figure 4.15: FPGA+CMOS sensor board with its main components indicated.

- RAM Memory: 373Kbits of distributed memory, 2.268Kbits of Block memory.
- 126 DSP48 blocks.
- 8 DCM (Digital Clock Manager).
- 469 User Input/Output.

Details of CMOS image sensor were given in table 3.4 of chapter 3. The FPGA control board is designed and provided by my supervisor.

4.3.3 Interface boards

The interface between the FPGA Control Board and other boards of the rest of the system, is provided by Teensy boards from PJRC (www.pjrc.com). These boards include a ARM processor with built-in standard serial interface protocols, as USB, SPI or UART, programmed in an Arduino software environment, which ease its programmability and also alleviate the FPGA from communication tasks. In figure 4.16 is shown a picture of the version 3.1 of this board with its main components indicated.

Below are enumerated the main features of this board:

- Dimensions: 36 x 18 mm.
- Processor MK20DX256 32 bits ARM CORTEX-M4 72 MHz.

Figure 4.16: Communications interface board (source www.pjrc.com/teensy/).

- Memory: RAM 64 Kbits, Flash 256 Kbits, EEPROM 2Kbits.
- Interfaces: 3 UART ports, 2 I2C ports, 1 SPI port.
- 34 Input/Output.
- USB powered.

4.3.4 High voltage deformable mirror board

The HV DM Board receives the voltages to apply to the deformable mirror actuators in digital format, converts these values to analog voltages, and them amplifies them to the required high voltage values for the piezoelectric actuators of the deformable mirror, ranging from 0V to 300V. In figure 4.17 is shown a picture of this board, where the five digital to analog converters are shown in the upper part of the board, and below them the five operational amplifiers. Each of the D/A converter and OAs provides four channels, so for the 19 signals required for the deformable mirror actuators, 5 chips of each device are needed.

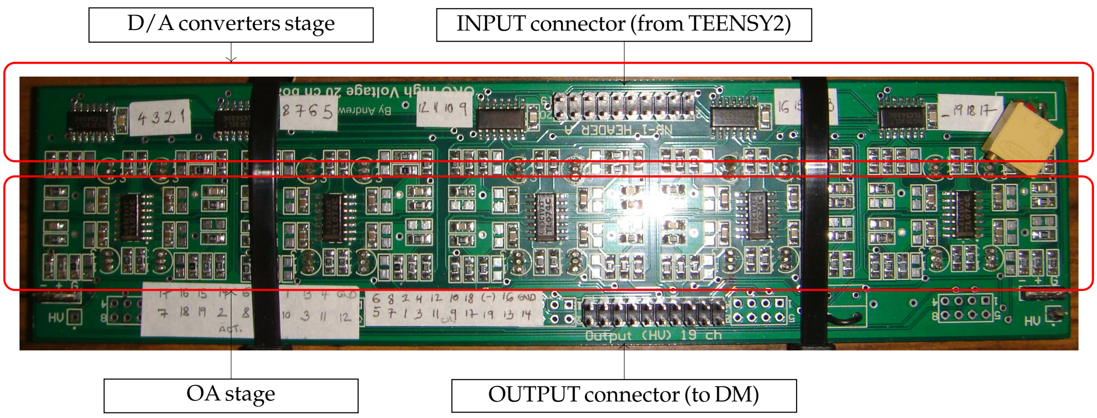

Figure 4.17: High Voltage Deformable Mirror board

Below is a list of the main features of this board:

- Dimensions: 190 x 48 mm.

- 5 TLC5620 TI Quad D/A Converters, 8-bit, Serial input with simultaneous update, and programmable reference voltage.
- 5 TL074C Motorola Quad JFET Input Operational Amplifiers.
- 20 high voltage A44 BJT (Bipolar Junction Transistor) class A amplifiers (reverse side).
- 20 TCLT1000 optocouplers for monitoring actuator signals electronically for MOAO (Multiple Object Adaptive Optics) applications (not used, reverse side).

This board was designed and supplied by my supervisor.

4.3.5 Support computer

The computer which serves as support for the AO system has the next characteristics. Its configuration is by convenience to support all the peripheral connections.

- Dimensions 197 x 197 x 36 mm.
- Model Apple Mac mini Server (Late 2012).
- Weight 1.3 Kg.
- Processor 2.3 GHz quad-core Intel Core i7.
- Intel HD Graphics 4000.
- 4 GB of 1600 MHz DDR RAM memory.
- 1 FireWire 800 port.
- 4 USB version 3 ports.

Below are enumerated the main functions of this computer:

- Interaction with the user through the UI.
- Receive AO control real time data through USB1 interface.
- Receive snapshot frames through USB2 interface.
- Send commands to FPGA Control Board through USB2 interface.

- Store AO Control data and frames for their subsequent analysis and debugging.
- Control tracking motors of RA and DEC axes of Telescope mount through USB3 interface.
- Receive real time video from Finderscope through USB4 interface.
- Receive real time video from Science Camera and control its operation through a FireWire interface.

4.4 Real Time Control Software GUI

A real time control software GUI (Graphical User Interface) was implemented, based in MATLAB and running on the support computer, to control different parameters of the AO system. From this platform, the user can issue commands to the FPGA control board. It also receives data from the FPGA and extracts from them relevant information, showing different parameters of frames in real time, to support the debugging and analysis of the system. In figure 4.18 is shown a snapshot of the GUI, where the main areas are highlighted.

Below the functionality of each GUI areas is described.

In Commands area is where the user can send commands to the AO Control system, to perform the next actions:

- Initiate, pause and stop the AO control loop.
- Take snapshots of frames from the SH wavefront sensor.
- Calculate and display the reference centroids of a particular frame.
- Send reference centroids to RAM_c memory in the FPGA.
- Modify the gain of the AO control loop, storing this value in RAM_g in the FPGA.
- Initiate, pause and stop the real time display of Centroids, Zernike coefficients and Voltages for the deformable mirror.
- Store in MATLAB workspace centroids, Zernike coefficients and Voltages of a consecutive number of frames, that have been uploaded from the FPGA.

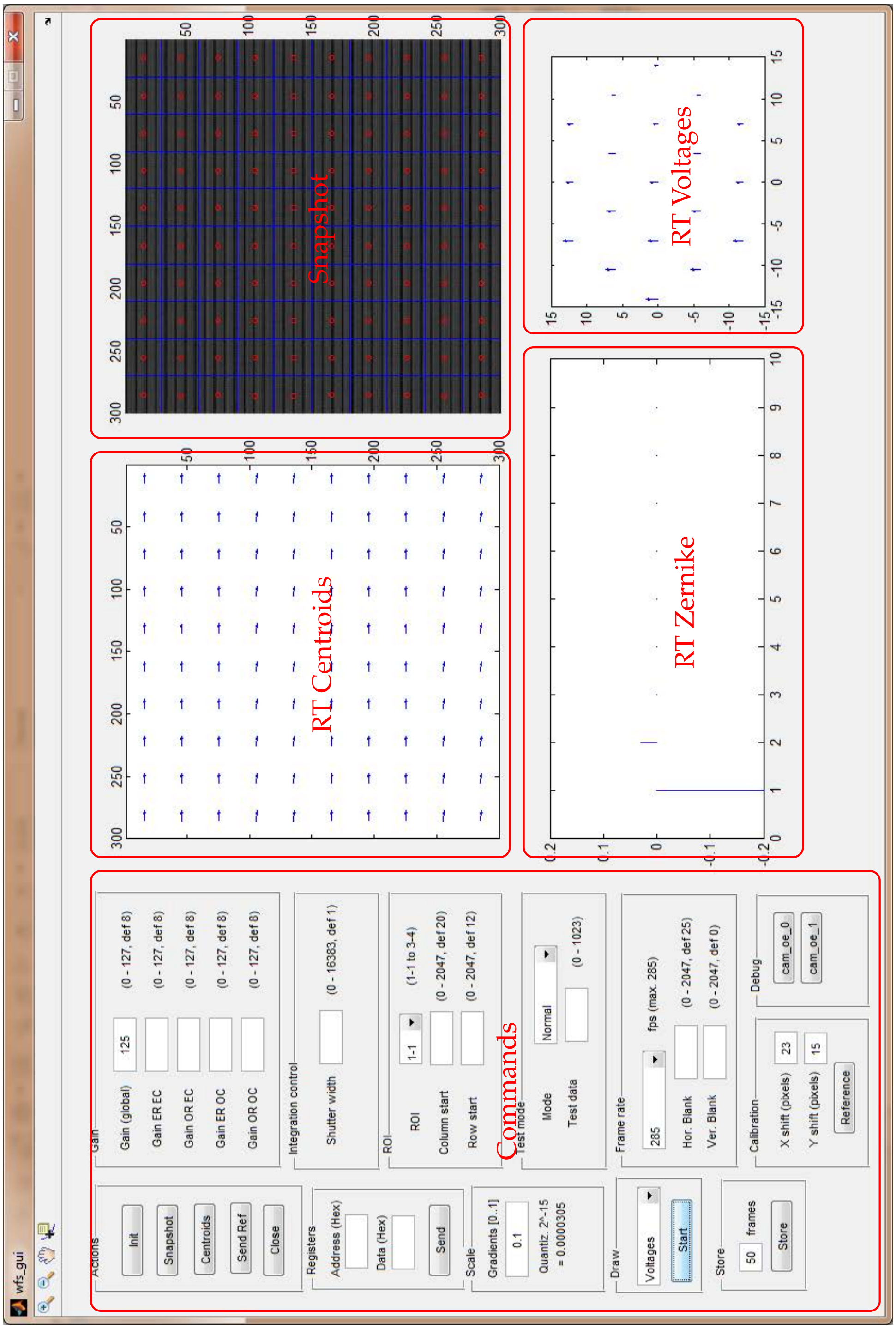

Figure 4.18: Real-Time control software interface with test of Tilt in x axis aberration (Z_2 Zernike polynomial) with background noise in SH wavefront sensor.

- Modify all parameters of the wavefront sensor, among them: Gain, Shutter, ROI (Region of Interest), Test mode, Frame rate and Blanking periods.

In RT Centroids area is where the gradients, that is, the differences between calculated and reference centroids are shown in real time. Gradients are represented as arrows indicating the centroids shift direction for all subapertures in the wavefront sensor.

In RT Zernike area is where the first 10 Zernike coefficients are shown in real time. The length of each bar is proportional to the corresponding coefficient.

In RT Voltages area is where the voltages applied to the deformable mirror actuators are shown. Their values are expressed as vertical arrows with length proportional to calculated values. Their layout in the display follows the geometry of the deformable mirror.

In Snapshot area is where the snapshot of a particular frame uploaded slowly from the FPGA is shown. When the reference centroids for a particular frame is calculated offline, these are shown as red dots in a grid which corresponds to the geometry of the subapertures in the wavefront sensor.

A more detailed description of the GUI is shown in appendix A.1.

4.5 Summary

In this chapter a complete AO control system has been described and analysed, including different novel contributions, both in the design approach followed and in the analysis of the critical parts of the system.

The AO closed loop real time control algorithm with low latency time is fully implemented in a low cost FPGA device (using approximately 50% of resources), in contrast to the usual AO control system which normally include external CPU/GPU architectures with last generation computing devices.

A support computer running MATLAB is used only to perform non critical timing tasks, control different parameters of the process, visualize and store results and debug intermediate stages of the AO reconstruction.

An alternative method to determine centroids based in Fourier decomposition has been implemented and tested successfully, which shows some advantages over more traditional methods such as the threshold CoG, that will be analysed in next chapter about experimental results.

According to the timing analysis accomplished, the maximum latency time for the AO closed loop process in the FPGA is 2μs at 50 MHz. The FPGA used in this design is capable to run its DSP blocks at 250 MHz, that will yield in a maximum latency time of 0.4μs. Current models of FPGA are capable of reaching maximum working frequencies of 638 MHz. That clock speed is more than enough to cope with the atmosphere rate change, in average 1kHz. The control system implemented in the FPGA is ready and capable to cope with readout speed upgrades in the CMOS image sensor, and improvements in the dynamic performance of the actuators of the deformable mirror.

CHAPTER 5

Analysis and Experimental results

5.1 Introduction

In this chapter experimental results obtained with the AO system and its subsystems, tested in laboratory and on-sky are shown. First a description of the laboratory and on-sky setups are shown, detailing the used devices and the followed procedures, and then different analyses are performed; Firstly an analysis of different sections of the control architecture is shown, addressing timing issues, the influence of using fixed point precision instead of floating point precision, the FPGA utilization, and the linearity in the DAC converters of the deformable mirror driver board. Then the performance of the Zernike stage is assessed, using a laser source in laboratory, where accuracy of the wavefront shape generated with Zernike coefficients, obtained with floating point and fixed point models, is evaluated. Then the different implementations of centroiding algorithms will be evaluated and compared with a Gaussian fit model, where the behaviour of these algorithms under different scenarios will be considered. Finally the performance of the AO control loop is evaluated, through measurements of gradients, Zernike coefficients and actuator voltages, both in laboratory and on-sky.

The experimental procedures followed here are uniquely conducted on a small-medium scale telescope, as are evidence of the developments required to log imagery, centroids, and mirror signals for concurrent confirmation of performance in MATLAB.

5.2 Laboratory setup

In this setup issues related with the weak photon flux, optical alignment, obscuration of secondary mirror of telescope and the light incoherence coming from astronomical sources will be avoided, so that the AO control performance in ideal conditions can be evaluated. This avoids the need for a dedicated mirror for tip-tilt correction, so that the limitations of the deformable mirror can be evaluated for high order aberrations modes, but inclusion of a tip-tilt corrector is planned in the future. The laser light source generates a high intensity and correctly aligned beam, to evaluate the capacity of the optical system and to generate a valid centroids pattern, which will be used by the control system to generate the appropriate signals for the deformable mirror actuators.

In figure 5.1 is shown the AO system installed in a platform in the laboratory.

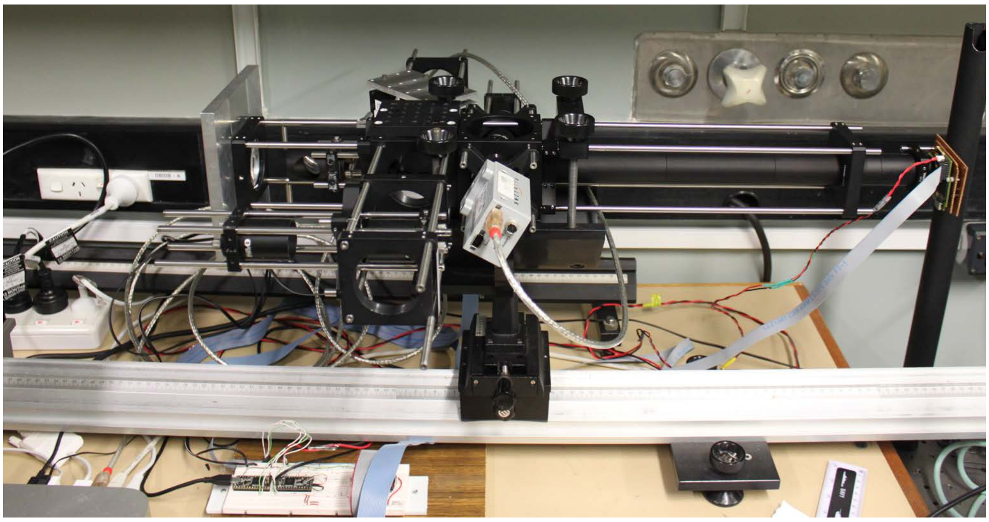

Figure 5.1: AO system installed for laboratory laser tests.

The mechanical structure is supported in a holder that can be shifted along a rail. A F/10 system was simulated through the use of an optical setup situated before the beam enters the AO system, to emulate the configuration of the telescope that will be used in the on-sky setup. Also neutral density filters are used to decrease the laser intensity which could saturate the image in the CMOS sensor of the SH WFS. The laser used is a HeNe Class 2, with 0.5 mW output power and λ = 632.8 nm.

5.3 On-sky setup

In figure 5.2 is shown the AO system installed in the 16" Meade LX200ACF telescope sited in UNSW Canberra, where the on-sky experiments were held.

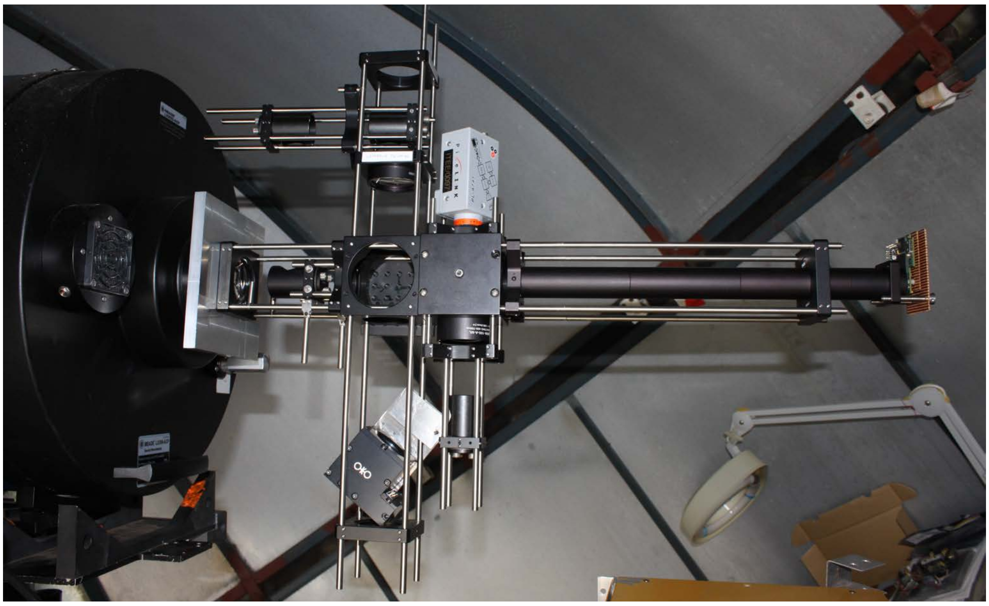

Figure 5.2: AO system installed in 16" Meade LX200ACF Telescope sited in UNSW Canberra.

This telescope is sited in UNSW Canberra, at coordinates latitude $-35.292°$ S, longitude $149.165°$ E, and 600 metres above sea level. In figure 5.2 can be observed that the AO system is attached to the rear port of the telescope through an aluminium flange, which is the only contact point with the telescope. Other components that can be observed in the figure are the science camera in upper part, the OKO deformable mirror in the bottom part, and the WFS in the right part.

5.4 Analysis of the control system

Having described the control system in the previous chapter, its control and implementation, we now provide performance results. Three critical aspects of the design have been addressed, which can have an important effect in the overall performance of the system: The influence of the use of fixed point precision instead floating point precision, which confirms that this shortcoming of FPGAs doesn't affect too much the AO control performance; The performance of the digital to analog conversion of the actuator voltages; and the accuracy in the calculation of the interaction matrix, including a detailed error analysis of the wavefront conjugate shapes obtained when these voltages are applied.

5.4.1 Timing analysis

The AO control loop needs to be executed with a latency able to cope with the rate change of the atmosphere turbulence. In figure 5.3 are shown the timing delays between wavefront sensor readout, CZV (Centroids, Zernike and Voltages) calculations and CZV serial send, for a frame rate of 250 frames/s.

The frame rate selected for the analysis is 250 frames per second, that is, each frame is read in 4 ms, indicated in gray in figure 5.3 as readout time. This is the time that the wavefront sensor takes to read a frame of 300 x 300 pixels, plus horizontal and vertical blanking times (time that the wavefront sensor is reading inactive pixels to synchronize rows and columns). As soon as the first row formed by 10 subapertures is read, the FPGA AO control algorithm starts to process these data, obtaining gradients, Zernike coefficients and voltages for this row of subapertures, indicated in blue in figure 5.3. Both processes, the frame readout and the calculation of gradients, Zernike coefficients and voltages, are performed in parallel, so that, only after a delay of 60 to 100 clock cycles (1.2 to 2µs for a clock frequency of 50 MHz) after the frame readout is finished, the CZV calculations are completed, giving enough time to the next frame to arrive without interfering the closed loop process.

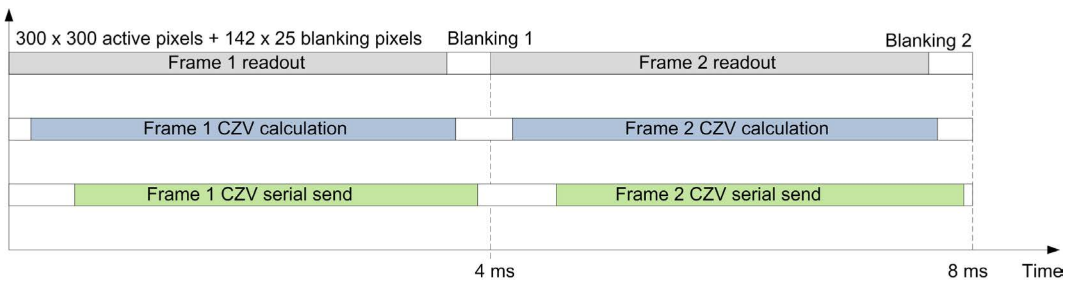

Figure 5.3: Comparative of readout time of the wavefront sensor and processes running in the FPGA, at 250 frames/s.

The time to read one row of pixels (300 active + 25 horizontal blanking) at 50 MHz is 6.5 µs. The readout time of the whole ROI is 4 ms, which corresponds to 250 fps, and this will involve one frame delay. With the rolling shutter the required exposure time is taken just prior to read out each line. If we don't increase the exposure time beyond the number of rows of the selected ROI (in our case 300 active rows + 21 blanking rows), the added temporal delay will be the readout time of 1 row, which is 6.5 µm, and there is not extra delay. So in this case the total delay would be 1 frame, which corresponds to the readout time of the ROI. If we apply more rows of integration time than the numbers of rows of the ROI, the image sensor will add more blanking rows accordingly, and the frame rate will decrease depending the number of added rows, with one row time 6.5 µs. Experiments carried out with a LED driven from the FPGA which illuminated the CMOS sensor and observing saturated pixels in the data coming from the CMOS image sensor, showed that the delay between LED activation edge and image sensor data was 6.5 µs, which correspond with the readout of one row of the sensor.

The deformable mirror used in this research has a published response time faster than 150 µs, though typically control electronics would limit this time to 0.5 ms (or even faster with our own deformable mirror driver board), so the total estimated temporal delay would be:

frame readout time + 1 row delay + FPGA control AO delay + DM control electronics and actuator time response: $4ms + 6.5s + 2s + 0.5ms = 4.5085ms$

Note that line exposure and readout can begin immediately after the last row of readout, in parallel with mirror actuators. So the latency reported here is solely the 4 ms of exposure time.

Analogously, as soon as the gradients, Zernike coefficients and voltages of one frame are calculated, they are sent out of the FPGA through the signal D_{OUT}, process indicated in green in figure 5.3. The sending process also will be finished before the next frame arrives, to avoid conflicts with the computation of the next frame.

The process is performed with a external oscillator of 50 MHz, which results in a frame rate of 250 frames/s. If a faster oscillator is used the frame rate could be raised to 1KHz frame rate, that is the expected variation rate of atmosphere turbulence, as this FPGA model is capable to manage signals up to 250 MHz.

5.4.2 Influence of fixed point precision in Zernike coefficients

The FPGA shares resources in a time division multiplexing process, taking advantage of the per clock basis nature of the implemented algorithm, using pipeline stages when is required. Parallel processing is performed in the x and y axes computation blocks, with the aim to get the minimum latency time at the end of each frame. In order to get high computation speed, FPGA operations are performed with a fixed point resolution. To assess the accuracy of the obtained data, two models were designed, one implemented in MATLAB with double floating point precision, and the other implemented in the FPGA with fixed point precision. In the whole computational process, the selection of the number of bits for the fractional part of the divisions is a key parameter which affects both resolution and utilization of hardware FPGA resources.

A synthetic image was created, in order to generate centroids in random positions, which is formed by 300 x 300 pixels, subdivided in 10 x 10 subapertures, hence each of the subapertures consist of 30 x 30 pixels squares.

To illustrate the influence of the number of bits in the fractional part when fixed point precision is used, three different gradients ranges have been considered for a subaperture. Three synthetic subapertures of 30 x 30 pixels have been created, where the centroids are at 1, 7 and 14 pixels separation from the geometrical center of the subaperture, which is shown in figure 5.4a.

The Zernike coefficient w_2 of Z_2 (tilt in x axis) has been calculated, comparing the floating point result obtained in MATLAB, with the fixed point results obtained in the FPGA, with a number of bits in the fractional part ranging from 4 to 12 bits, with a step of 2 bits. The results are shown in figure 5.4b.

Figure 5.4 shows that the error introduced by the use of fixed point resolution with 10 bits or more in the fractional part of the centroids is independent of the number of extra bits. On the other hand, the relative error in this case is constant and with values around 0.03% for separations of 1 and 7 pixels, and 0.08% for 14 pixel separation. When the number of bits in the fractional part is less than 10 bits, the error is variable and becomes larger as the number of bits decreases, with errors in excess of 2% for 14 pixel separation and 4 bits in the fractional part. These results agree with Martin-Hernando et al.[40] where errors of this order where obtained when 10 bits where used in the fractional part of the centroids calculation.

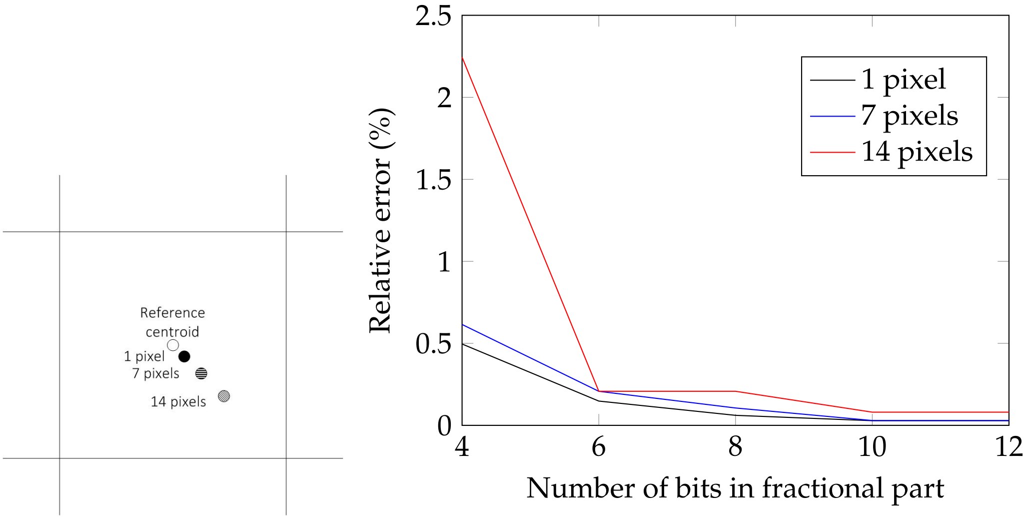

(a) synthetic subaperture **(b)** relative error

Figure 5.4: Relative error in calculation of Zernike coefficient W2 (tilt in x axis) when using fixed point precision compared to floating point precision, for 3 different positions of centroids in a synthetic subaperture of 30 x 30 pixels.

5.4.3 FPGA utilization

In figure 5.5 is shown the percentage utilization of the FPGA, for the two AO control designs implemented: AO control with CoG algorithm, and AO control with 1FC algorithm.

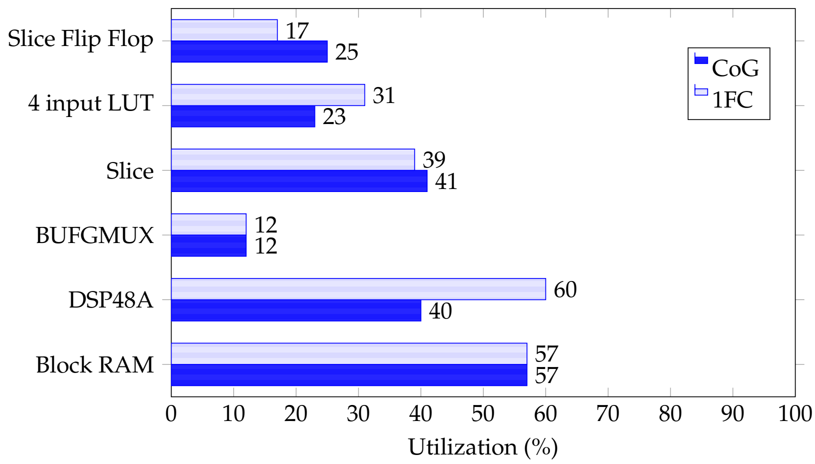

Figure 5.5: FPGA percentage utilization with CoG and 1FC centroiding algorithms.

The FPGA utilization results show that even though the use of DSP48A blocks (combination of multipliers and adder optimized for digital signal processing) is higher in the case of 1FC algorithm, in both cases there is still half of the FPGA not used. Also the number of slices in both cases is below half of the FPGA total utilization. Block RAM is used to store frames before sending them out of the FPGA, with the reconstruction matrix and the reference centroids matrix for diagnostic purposes only. If it is required to store more than one frame or apply digital filters, an external high capacity RAM existent in the FPGA Control Board could be used for this purpose.

5.4.4 Linearity in D/A converters

An analysis of the behaviour of the D/A converters was accomplished, as this conversion is an important stage which influences in the final precision of the voltages applied to the deformable mirror actuators. With the next formula the TLC5620 TI D/A converter transforms digital inputs to analog outputs:

$$V_{out} = V_{Ref} \times \frac{CODE}{256} \times (1 + RNG) \tag{5.1}$$

where V_{out} is the output analog voltage, V_{Ref} is the reference voltage which defines the output analog range, CODE is the digital input with 8 bits resolution (range 0 to 255), and RNG is the range bit, which defines if the output ranges between one time (RNG=0) or two times (RNG=1) the reference voltage.

In figure 5.6 is shown V_{out} for V_{ref}=3.3V (green and red curves) and for V_{ref}=5V (blue curve).

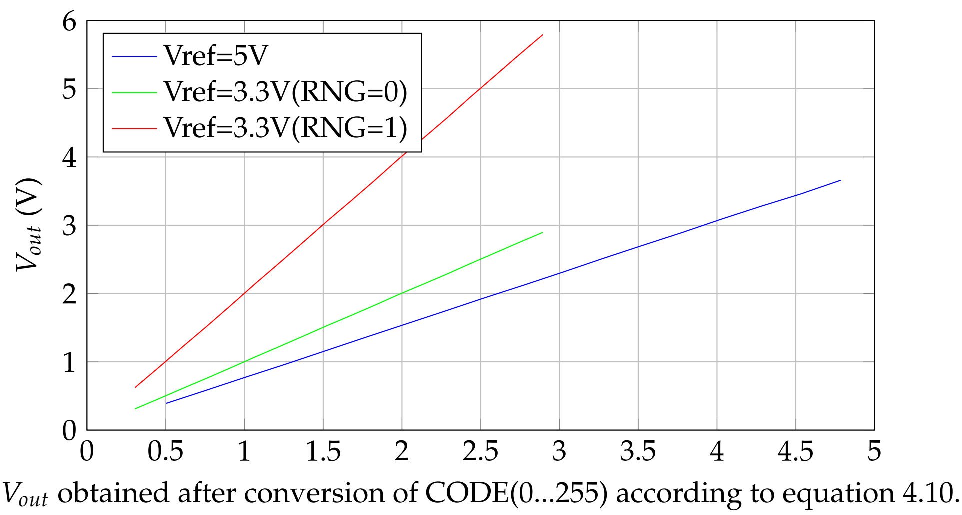

Figure 5.6: Output voltage of the D/A converters of the HV DM board, when an input signal ranging from 0 to 3.3V (for V_{ref}=3.3V) or ranging from 0 to 5V (for V_{ref}=5V).

This curves were obtained applying digital voltages values which range from 0 to 255 (8 bits) as the digital input of the converters, which correspond to V_{in} ranging from 0 to 3.3V when V_{ref} = 3.3V, an ranging from 0 to 5V when V_{ref} = 5V. Although the V_{out} curves are linear, an offset voltage in the curve corresponding to V_{ref} = 5V can be observed, so that when V_{in} = 4.8 then V_{out} = 3.7V. In curves corresponding to V_{ref} = 3.3V, there is no offset voltage, so for V_{in} = 3V then V_{out} = 3V. To reach the whole dynamic range of the operational amplifiers of the next stage, V_{out} has to reach its nominal input voltage, 5V, that can be achieved if bit RNG is set to 1. This will be the configuration selected in the converters to reach the dynamic range of the operational amplifiers.

5.4.5 Interaction matrix: calculation and simulation

The interaction matrix expresses the relation between the Zernike coefficients and the voltages applied to the deformable mirror actuators. Enough precision in the surface shape of the mirror for a particular set of voltages is important to get the better possible conjugate shape of the aberrated wavefront. This accuracy depends on the mechanical properties, geometry and layout of a particular deformable mirror. The knowledge of the influence functions, that is the shape created in the mirror for each actuator when one is forced to its maximum stroke and the others are not active, is crucial to reproduce with enough accuracy a particular shape in the mirror.

For the deformable mirror used in this AO system, the PDM19-30 from OKO Technologies, the manufacturer provides these influence functions. In the MrFit software provided by OKO Technologies, when the input is a set of Zernike coefficients corresponding to an aberrated wavefront, the output are the voltages to apply to the deformable mirror, in order to get the best possible conjugate shape for that set of aberrations.

The relation between Zernike coefficients and voltages is shown in the equation 5.2, similar to equation 2.40 of chapter 2, this time showing the elements of the matrix:

$$\begin{bmatrix} V_1 \\ V_2 \\ \vdots \\ V_{19} \end{bmatrix} = \begin{bmatrix} I_{1\,1} & I_{2\,1} & & \cdots I_{9\,1} \\ I_{1\,2} & I_{2\,2} & & \cdots I_{9\,2} \\ \vdots & \vdots & \ldots & \vdots \\ I_{1\,19} & I_{2\,19} & & \cdots I_{9\,19} \end{bmatrix} \cdot \begin{bmatrix} w_2 \\ w_3 \\ \vdots \\ w_{10} \end{bmatrix} \tag{5.2}$$

In equation 5.2, V_1 to V_{19} are the voltages to apply to the deformable mirror actuators, w_2 to w_{10} are the nine Zernike coefficients considered excluding piston mode w_1, and the matrix with values from $I_{1\,1}$ to $I_{9\,19}$ is the interaction matrix.

If a finite non-zero value for a Zernike coefficient is provided in equation 5.2 when the rest are zero, from the voltages obtained in MrFit software, each of the rows of the interaction matrix can be obtained from voltages obtained in MrFit software, as shown in equation 5.3.

$$\begin{bmatrix} V_1 \\ V_2 \\ \vdots \\ V_{19} \end{bmatrix} = \begin{bmatrix} I_{1\,1} & I_{2\,1} & & \cdots I_{9\,1} \\ I_{1\,2} & I_{2\,2} & & \cdots I_{9\,2} \\ \vdots & \vdots & \cdots & \vdots \\ I_{1\,19} & I_{2\,19} & & \cdots I_{9\,19} \end{bmatrix} \cdot \begin{bmatrix} 10^{-6} \\ 0 \\ \vdots \\ 0 \end{bmatrix} \tag{5.3}$$

The relation between the input Zernike coefficients and the output voltages is linear, so any value of Zernike coefficient can be used to obtain the Interaction matrix, but the value of 10^{-6} m is used, because it won't reach the dynamic range of the deformable mirror for the maximum voltage applied, which is 300V according to the manufacturer specification.

For a value of $Z_i = 10^{-6}$ m in each of the Zernike coefficients when the rest are zero, the Interaction matrix shown in equation 5.4 is obtained following the Noll criteria in the Zernike order.

In the Interaction matrix of equation 5.4, which is shown transposed for convenience, each column represents the voltages that should be applied to the deformable mirror actuators, to obtain each of the Zernike aberrations modes Z_2 to Z_{10}. Columns represent the voltages from V_1 the first element to V_{19} the last one. This is the matrix that will be stored in ROM memory of the FPGA, when this is programmed.

MrFit software also provides a simulation of the obtained surfaces with the Zernike mode and the resulting shape in the mirror after we apply the actuator voltages, showing the expected error between both surfaces. In figures 5.7 to 5.9 are shown the simulated surfaces for the first 10 Zernike classical aberration, Z_2 to Z_{10}, excluding the piston mode Z_1, for a reference wavelength of 638 nm.

The subfigures at the left are the fitted wavefronts, that is, the simulated wavefronts when the voltages of matrix 5.4 are applied to the deformable mirror actuators. The error wavefront results were obtained, displayed and assessed assuming that

$$I^T = \begin{bmatrix} 68.5 & 51.7 & 54.7 & 62.4 & 55.7 & 154.7 & 184.5 & 128.8 & 169.1 \\ 42.8 & 54 & 10.6 & 68.2 & 68 & 143.6 & 290.1 & 145.9 & 162 \\ 55.2 & 28.9 & 1.2 & 71 & 50.2 & 252.9 & 245.4 & 151.9 & 175.1 \\ 84.5 & 29.8 & 11.1 & 66.1 & 63.5 & 252.9 & 95.4 & 146.8 & 156.3 \\ 107.5 & 53.9 & 6.7 & 67.2 & 58.4 & 139.9 & 3.1 & 149.3 & 181.9 \\ 83.6 & 82.4 & 7.7 & 75.9 & 55.9 & 10.4 & 97 & 148 & 158.1 \\ 56 & 83.1 & 7 & 59 & 54.1 & 0.9 & 243.8 & 149.6 & 172.5 \\ 1 & 54.6 & 160 & 65.9 & 141.4 & 126.4 & 36.2 & 183.7 & 2.6 \\ 33 & 27.6 & 142.4 & 118.7 & 87.8 & 122.1 & 131.8 & 0.3 & 228.6 \\ 35.7 & 2.5 & 162.3 & 138.2 & 19.5 & 16.8 & 88.4 & 179.6 & 232.1 \\ 76.2 & 0.2 & 142.1 & 60.5 & 0 & 95.3 & 182.4 & 185.1 & 219.7 \\ 98.7 & 2.4 & 159.5 & 0.1 & 3.1 & 18 & 220.2 & 175.8 & 20.8 \\ 121.2 & 27.7 & 139.4 & 1.8 & 101.4 & 120.9 & 246.9 & 6.2 & 220.3 \\ 121.2 & 54.6 & 162.3 & 76.4 & 130 & 131.7 & 290.1 & 177.8 & 232.1 \\ 121.2 & 80.8 & 139.6 & 111.8 & 97.8 & 177.8 & 247.7 & 185.1 & 217.7 \\ 98.7 & 105.2 & 162.3 & 138.3 & 12.4 & 251.3 & 218.2 & 177.2 & 21.2 \\ 76.4 & 105.2 & 139.6 & 63.6 & 0.2 & 212.5 & 182.8 & 6.7 & 220.1 \\ 35.9 & 105.2 & 162.3 & 0.1 & 16.3 & 252.9 & 89.5 & 174.3 & 232.1 \\ 32.7 & 80.8 & 139.2 & 9.8 & 87.6 & 182.3 & 132.3 & 185.1 & 230.3 \end{bmatrix} \tag{5.4}$$

the illuminated area is 66% of the full aperture of the DM. Subfigures in the right are the error wavefronts, that is, the difference between the wavefront obtained mathematically with the Zernike functions, and the fitted wavefronts obtained through the influence functions. For each fitted wavefront, data of the difference between maximum and minimum value (peak-to-peak) in z axis (z_{pp}) are provided and also the root mean square deviation (z_{rms}) of the wavefront according to the next equation:

$$z_{rms} = \frac{\int_S (z - z_0)^2 \, ds}{S}, \tag{5.5}$$

where S is area of the mirror aperture. Similarly this data are also provided for the error wavefronts (e_{pp}, e_{rms}).

In figure 5.10 are shown the errors (e_{pp} and e_{rms}) for Zernike modes Z_2 to Z_{10}, compared with the visible spectrum wavelengths.

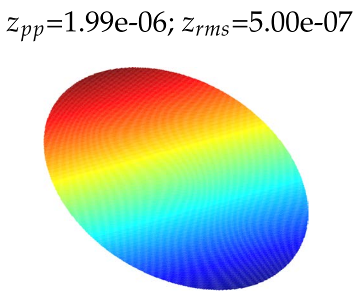

(a) Z_2 fitted wavefront

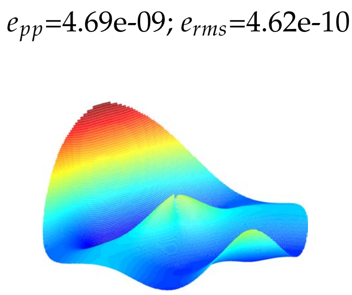

(b) Z_2 error wavefront

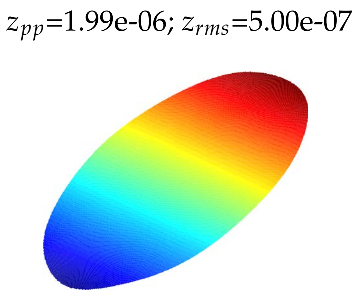

(c) Z_3 fitted wavefront

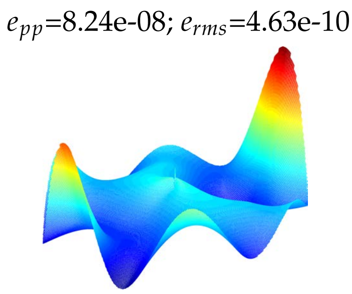

(d) Z_3 error wavefront

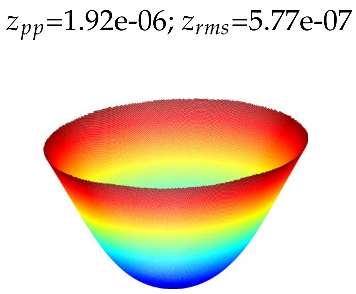

(e) Z_4 fitted wavefront

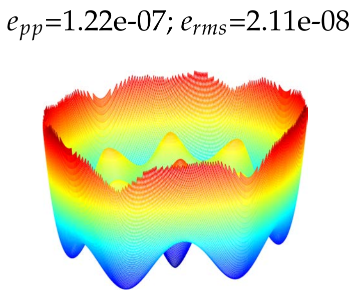

(f) Z_4 error wavefront

Figure 5.7: Simulated fitted wavefront (left) and error wavefront (right) corresponding to Zernike modes Z_2 to Z_4, obtained with software MrFit, provided by the manufacturer of the mirror, OKO Technologies. This wavefronts are obtained with Zernike coefficients values of 10^{-6}m. Units of z_{pp},z_{rms},e_{pp} and e_{rms} are metres.

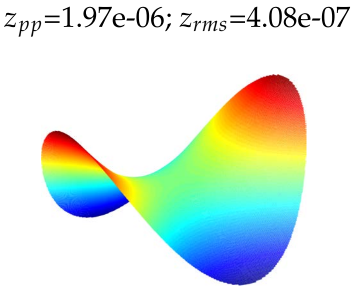

(a) Z_5 fitted wavefront

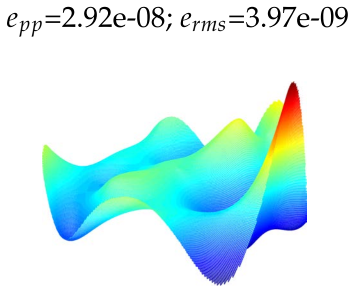

(b) Z_5 error wavefront

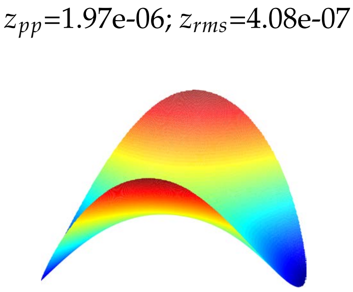

(c) Z_6 fitted wavefront

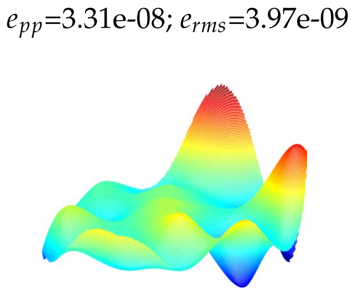

(d) Z_6 error wavefront

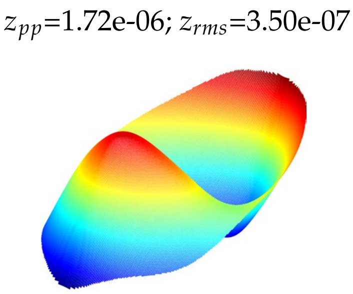

(e) Z_7 fitted wavefront

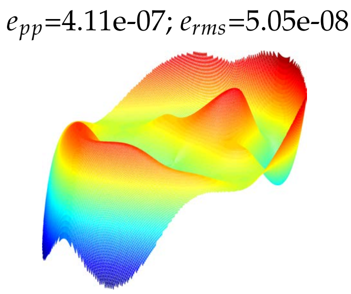

(f) Z_7 error wavefront

Figure 5.8: Simulated fitted wavefront (left) and error wavefront (right) corresponding to Zernike modes Z_5 to Z_7, obtained with software MrFit, provided by the manufacturer of the mirror, OKO Technologies. This wavefronts are obtained with Zernike coefficients values of 10^{-6}m. Units of z_{pp},z_{rms},e_{pp} and e_{rms} are metres.

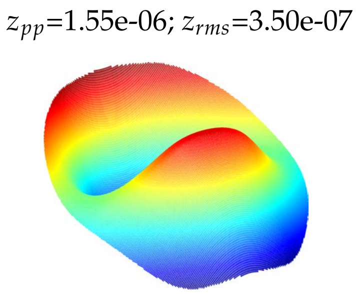

(a) Z_8 fitted wavefront

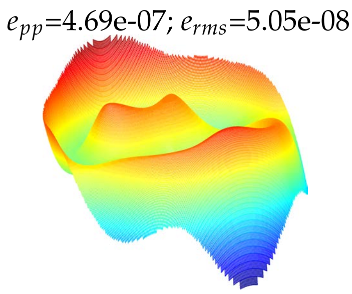

(b) Z_8 error wavefront

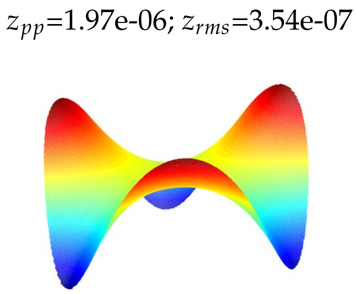

(c) Z_9 fitted wavefront

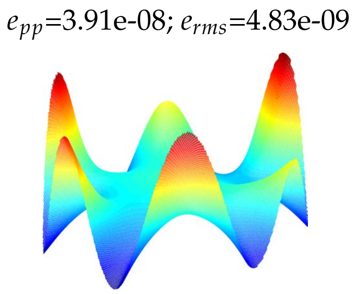

(d) Z_9 error wavefront

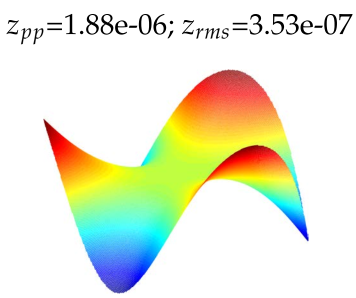

(e) Z_{10} fitted wavefront

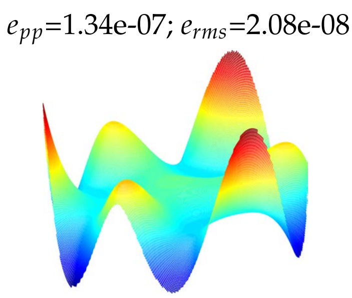

(f) Z_{10} error wavefront

Figure 5.9: Simulated fitted wavefront (left) and error wavefront (right) corresponding to Zernike modes Z_8 to Z_{10}, obtained with software MrFit, provided by the manufacturer of the mirror, OKO Technologies. This wavefronts are obtained with Zernike coefficients values of 10^{-6}m. Units of z_{pp},z_{rms},e_{pp} and e_{rms} are metres. Colour scales are different for fitted and error wavefronts.

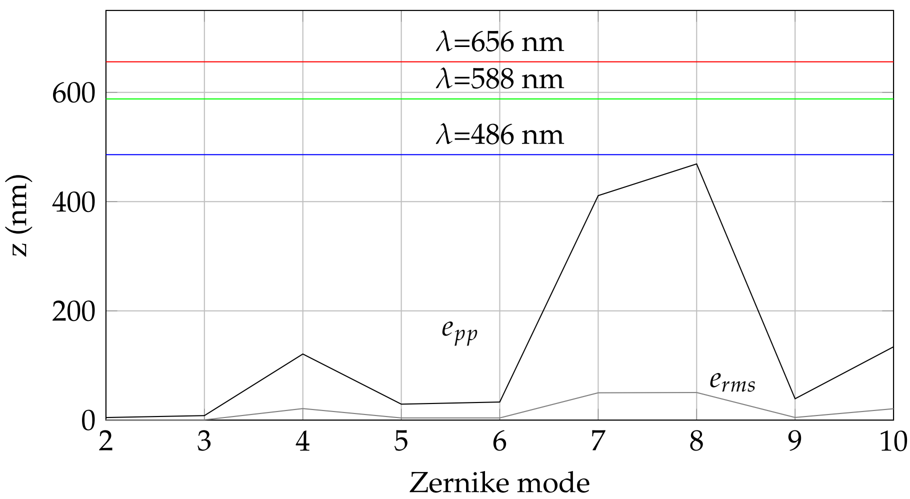

Figure 5.10: Errors, e_{pp} and e_{rms}, in DM wavefront for Zernike modes Z_2 to Z_{10}.

In this figure is shown that the error is always below visible spectrum wavelengths.

5.5 Analysis of Zernike stage

In this analysis, the performance of the calculation of the Zernike coefficients, both in floating point precision with a model implemented in MATLAB, and in fixed point precision obtained from the FPGA, is evaluated in the laboratory with a laser source. For each experiment, first a reference image of the centroids in the camera is obtained, and then the laser input angle is modified in x and y axes directions and another image of the centroids is obtained. From this two images, the centroids gradients are calculated in both floating point and fixed point models. From here, Zernike coefficients are calculated and the result can be observed in the corresponding tables. From the obtained Zernike coefficients in both models, wavefront surfaces are obtained through Zernike polynomials computations, and 3D graphical representations of the surfaces are shown.

All images in the camera have a size of 300 x 300 pixels, divided in a layout of 10 x 10 subapertures of 30 x 30 pixels each. Experiments are performed with different laser source intensities, with the use of different neutral density filters, to evaluate the influence of the S/N ratio.

In the next figures are shown the experiments conducted with the discussed parameters.

TILT IN X AXIS WITH HIGH INTENSITY LASER SOURCE

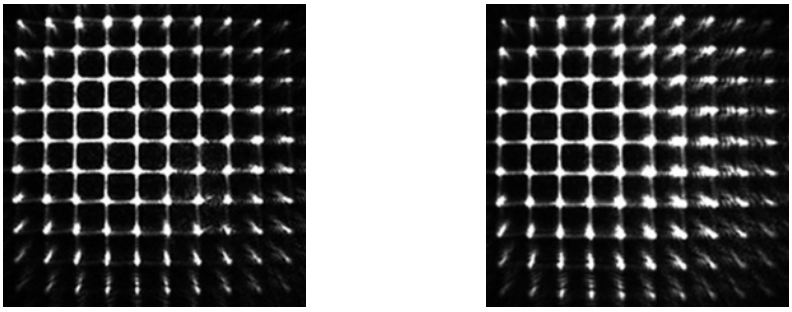

(a) Reference centroids (b) Shifted centroids

Figure 5.11: Reference centroids (left) and shifted centroids (right) in the camera with high intensity laser source.

Table 5.1: Floating point and fixed point values of Zernike coefficients for high intensity laser. Units in $m \times 10^{-3}$.

Zernike mode	Floating point (MATLAB)	Fixed point (FPGA)	Rel. Error (%)
Z_2	-0.0465	-0.0417	10.3
Z_3	0.1391	0.1356	2.5
Z_4	-0.0179	-0.0182	-1.7
Z_5	0.0452	0.0468	-3.5
Z_6	-0.0093	-0.0092	1.1
Z_7	0.0071	0.0075	-5.6
Z_8	-0.0071	-0.0068	4.2

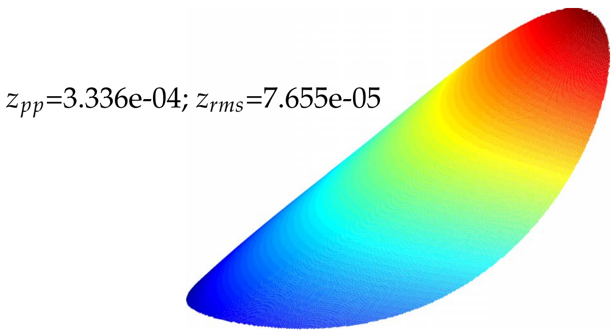

Figure 5.12: Wavefront obtained applying the Zernike coefficients obtained with floating point (MATLAB) to Zernike polynomials series, indicating z_{pp} and z_{rms} for high intensity laser source (units in metres).

TILT IN Y AXIS WITH MEDIUM INTENSITY LASER SOURCE

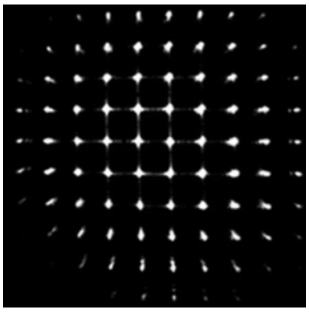

(a) Reference centroids

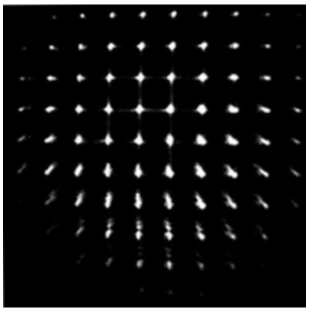

(b) Shifted centroids

Figure 5.13: Reference centroids (left) and shifted centroids (right) in the camera with medium intensity laser source.

Table 5.2: Floating point and fixed point values of Zernike coefficients for medium intensity laser. Units in $m \times 10^{-3}$.

Zernike mode	Floating point (MATLAB)	Fixed point (FPGA)	Rel. Error (%)
Z_2	-0.2773	-0.2754	0.7
Z_3	0.0949	0.0964	-1.6
Z_4	0.0145	0.0143	1.4
Z_5	0.1142	0.1129	1.1
Z_6	0.1513	0.1533	-1.3
Z_7	-0.0220	-0.0204	7.3
Z_8	-0.0246	-0.0221	10.2

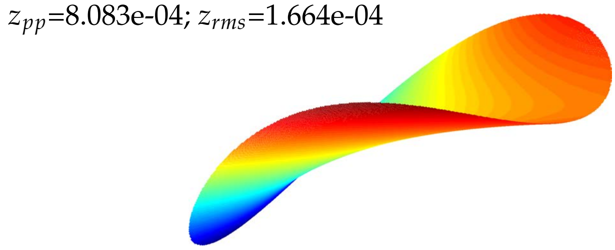

Figure 5.14: Wavefront obtained applying the Zernike coefficients obtained with floating point (MATLAB) to Zernike polynomials series, indicating z_{pp} and z_{rms} for medium intensity laser source (units in metres).

TILT IN X AND Y AXIS WITH LOW INTENSITY LASER SOURCE

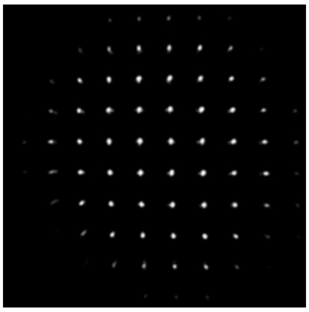

(a) Reference centroids

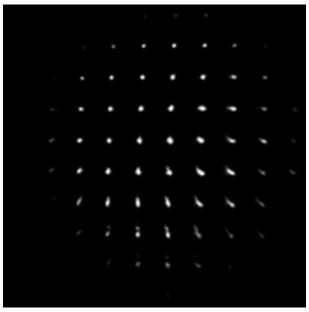

(b) Shifted centroids

Figure 5.15: Reference centroids (left) and shifted centroids (right) in the camera with low intensity laser source.

Table 5.3: Floating point and fixed point values of Zernike coefficients for low intensity laser. Units in $m \times 10^{-3}$.

Zernike mode	Floating point (MATLAB)	Fixed point (FPGA)	Rel. Error (%)
Z_2	-0.1040	-0.0995	4.3
Z_3	0.1131	0.1158	-2.4
Z_4	-0.0035	-0.0038	-8.6
Z_5	-0.0140	-0.0126	10.0
Z_6	-0.0664	-0.0664	0.0
Z_7	0.0079	0.0075	5.1
Z_8	-0.0136	-0.0117	14.0

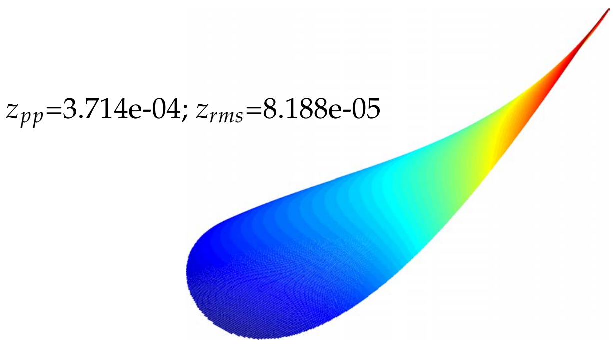

Figure 5.16: Wavefront obtained applying the Zernike coefficients obtained with floating point (MATLAB) to Zernike polynomials series, indicating z_{pp} and z_{rms} for low intensity laser source (units in metres).

According to these previous results, the relative error in the computation of Zernike coefficients, when floating point precision is compared to fixed point precision is below 14%.

5.6 Analysis of centroiding algorithms

To analyse the performance of the centroiding algorithms, post processing was performed on videos of two real sidereal sources. The video frames are of 60 x 60 pixels. The first analyzed video has frames with a profile of a narrow source with a maximum intensity value of 89 in 8 bits resolution (255 values). The second video has frames with a profile of a extended source with a maximum intensity of 255, that is the maximum value of the image sensor. Each of the video streams has three types of processing: raw data, 2D convolution filtering with a kernel dimension of 3 x 3 pixels, and 2D convolution filtering with a kernel dimension of 5 x 5 pixels. These filters were applied to measure the influence on the centroid results of the white noise that the image sensor shows. The post processing was analyzed with a program coded in Python, which is provided in appendix A.6.

All time series have been linearly detrended, that is, the output is the input minus a best fit line of the input, so that the high frequency components of the curve can be observed properly.

According to Stone [66], Gaussian fit is a reliable centroiding method. In this analysis, three different centroiding methods that can be implemented in the FPGA are compared to a Gaussian fit method, that herein is denominated GFiT. The centroiding methods that can be implemented in the FPGA are: Center of Gravity (CoG), Threshold Center of Gravity (TCoG) and First Fourier Coefficient (1FC).

The threshold in the analysis of the centroiding algorithms is applied with the OpenCV function (coded in Python, see appendix A.4) cv2.threshold(THRESH TOZERO) and its function is:

$$f_{out} = \begin{cases} f_{in}(x,y) & \text{if } f_{in}(x,y) > \text{threshold} \\ 0 & \text{otherwise} \end{cases}$$

At a first glance to the temporal series of figures 5.17 to 5.22, it is observed that TCoG for certain threshold level and 1FC, follow to a greater or lesser degree the GFiT. This is only true for the TCoG algorithm for an optimized threshold, th=20

LSB (in case of the narrow source, and th=50 LSB in case of the extended source. When threshold is different than these optimized values, the difference with the GFiT curve is higher. In the case of the narrow source, an optimized threshold in the TCoG algorithm of 20 LSB was applied, while in the extended source the optimized value was 50 LSB. This way, the threshold was adapted depending on the centroid shape, giving a better performance of the centroiding calculation.

An advantage of the 1FC algorithm over the TCoG is that there is no need to select a determinate threshold depending on the centroid shape, while in the case of the TCoG this value affects severely the computed centroids values.

To analyze closely the difference in the performance of TCoG and 1FC, compared to the GFiT, the absolute differences TCoG - GFiT and 1FC - GFiT for different threshold levels in the time series are represented in figures 5.23 for the narrow source, and 5.24 for the extended source. These curves were obtained from the non filtered data of the image, because the filtered images are very similar and do not provide relevant information. In the case of the narrow source, a different shifting range between axes x and y can be observed, that is due to inaccuracies in the tracking system in the 16" Meade telescope. Nevertheless, this differences don't affect the high frequency components of the curves, which are the relevant data to evaluate the comparative performance of the centroiding algorithms.

As a measure of the variation in these curves, the standard deviation is obtained to evaluate the performance in a convenient way. Standard deviation values for the narrow source are shown in tables 5.4 (x axis) and 5.5 (y axis), and for the extended source in tables 5.6 (x axis) and 5.7 (y axis). From the standard deviation values is deduced that the TCoG algorithm with a optimized threshold show the best results in the difference with the GFiT approximation. Standard deviation values of the 1FC algorithm are in general higher that the TCoG with optimized threshold, but not in all cases. But when the threshold of the TCoG algorithm is different from the optimized value, the dispersion of data is higher, worsening severely the detection of centroids.

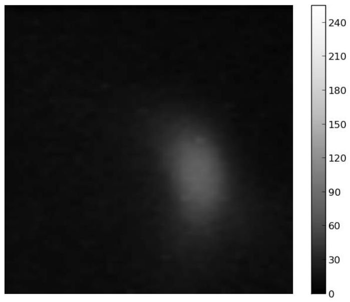

(a) 2D frame of time series

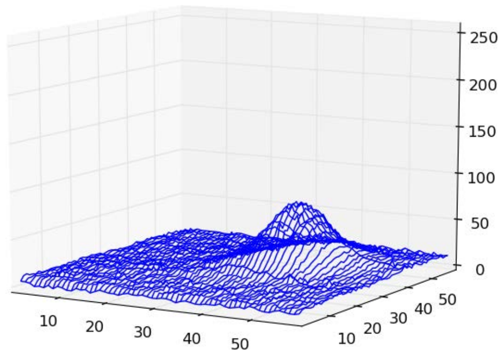

(b) 3D frame of time series

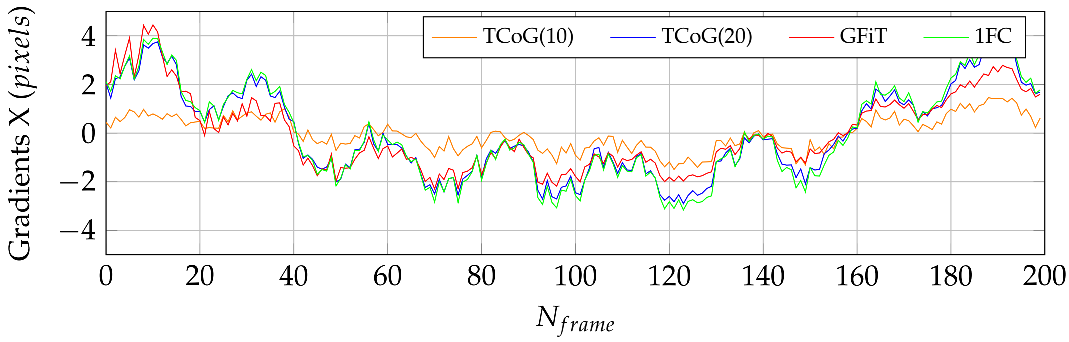

(c) X axis

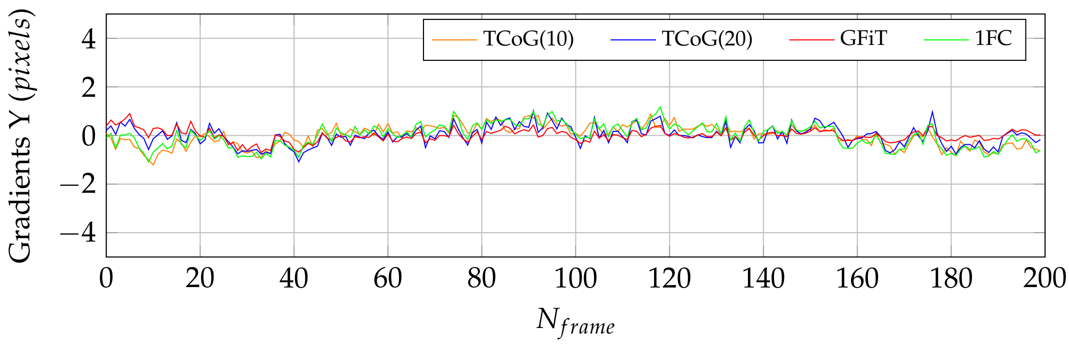

(d) Y axis

Figure 5.17: Time series of centroids for narrow source without filter. (a): 2D frame no.20 of time series. (b): 3D frame no. 20 of time series. (c),(d): Time series of centroids calculated by TCoG (th=10), TCoG (th=20), GFiT and 1FC in Python (floating point, detrended). 200 frames. Science camera. Telescope Meade LX200ACF. Object: narrow source. Window: 60 x 60 pixels. Frame rate 15 frames/s.

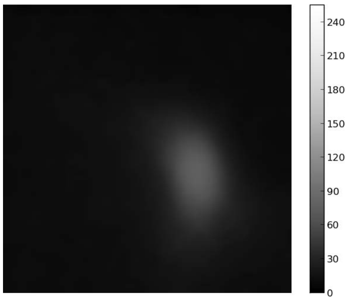

(a) 2D frame of time series

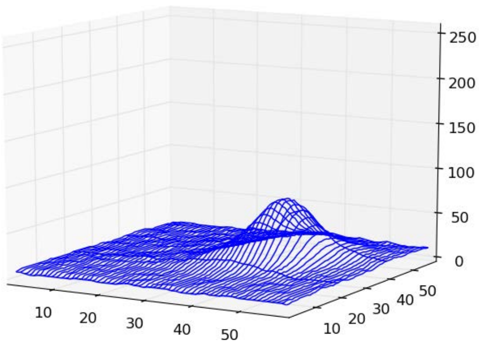

(b) 3D frame of time series

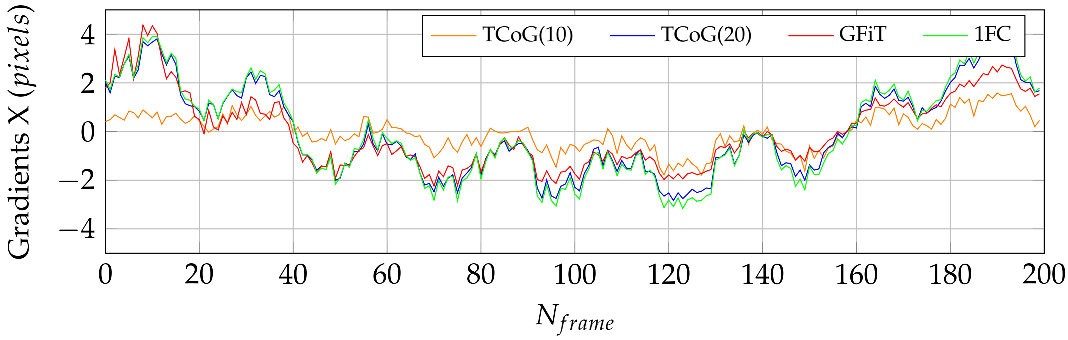

(c) X axis

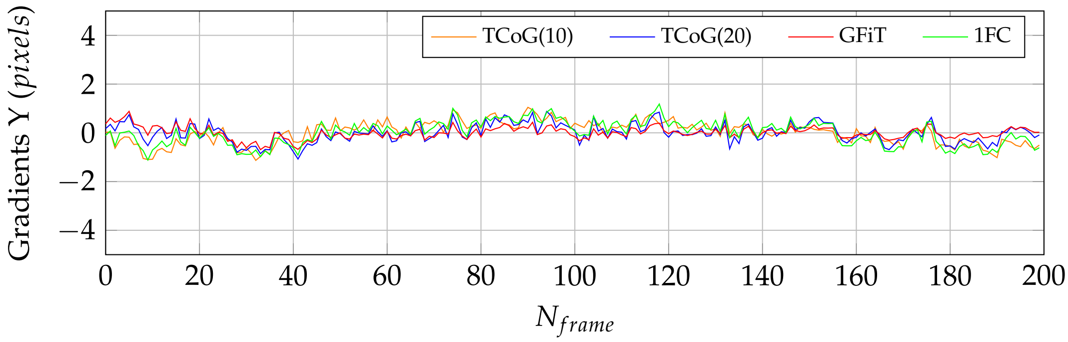

(d) Y axis

Figure 5.18: Time series of centroids for narrow source with 2D convolution filter (3x3). (a): 2D frame no.20 of time series. (b): 3D frame no. 20 of time series. (c),(d): Time series of centroids calculated by TCoG (th=10), TCoG (th=20), GFiT and 1FC in Python (floating point, detrended). 200 frames. Science camera. Telescope Meade LX200ACF. Object: narrow source. Window: 60 x 60 pixels. Frame rate 15 frames/s.

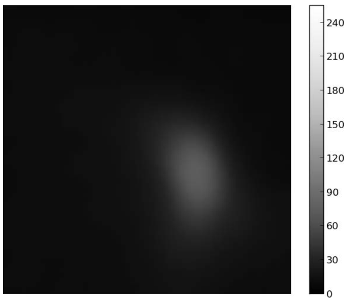

(a) 2D frame of time series

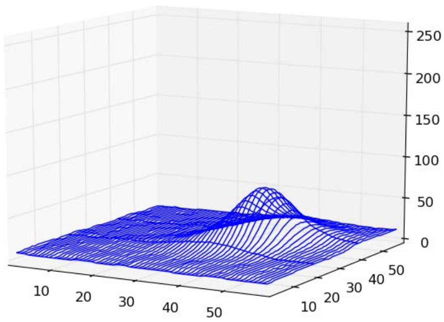

(b) 3D frame of time series

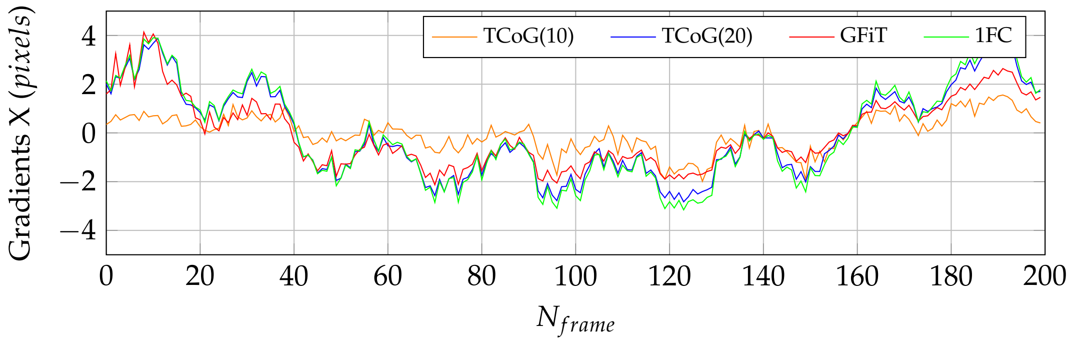

(c) X axis

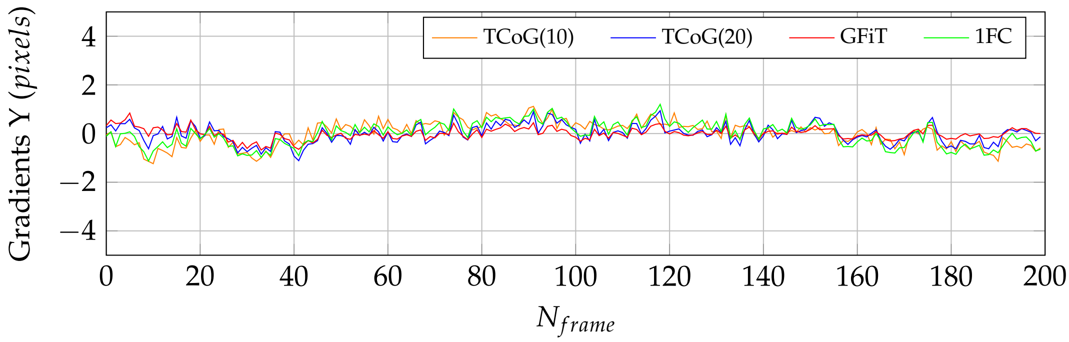

(d) Y axis

Figure 5.19: Time series of centroids for narrow source with 2D convolution filter (5x5). (a): 2D frame no.20 of time series. (b): 3D frame no. 20 of time series. (c),(d): Time series of centroids calculated by TCoG (th=10), TCoG (th=20), GFiT and 1FC in Python (floating point, detrended). 200 frames. Science camera. Telescope Meade LX200ACF. Object: narrow source. Window: 60 x 60 pixels. Frame rate 15 frames/s.

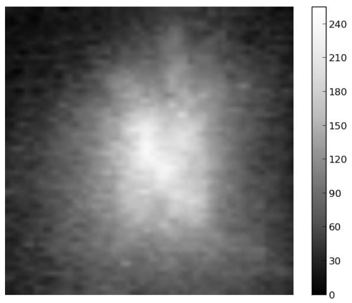

(a) 2D frame of time series

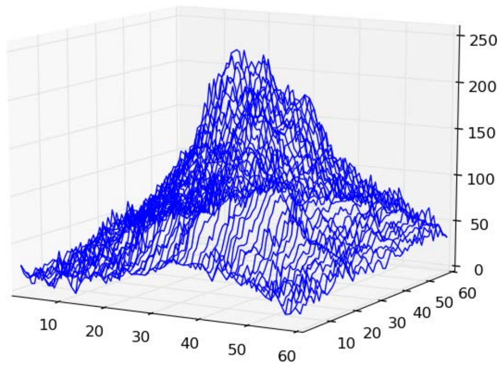

(b) 3D frame of time series

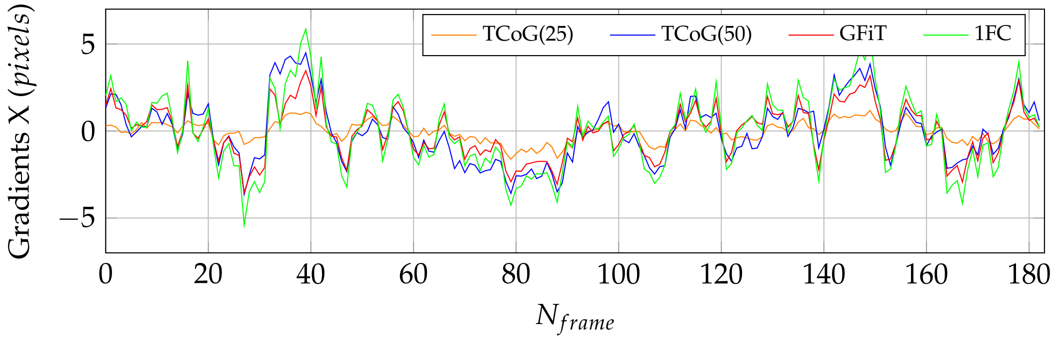

(c) X axis

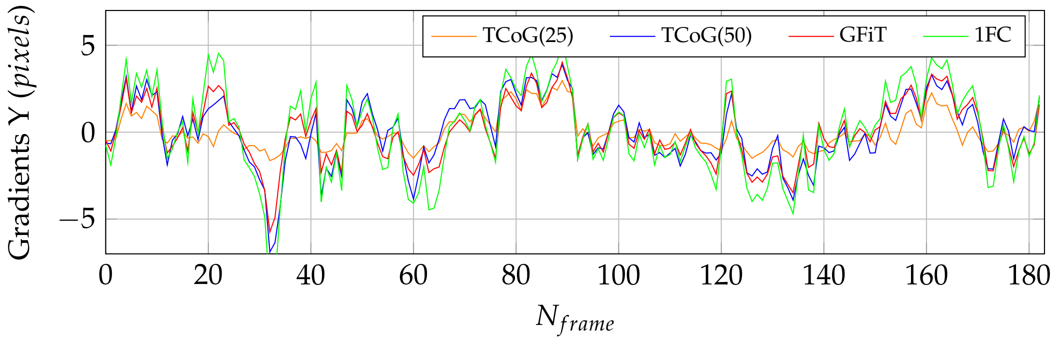

(d) Y axis

Figure 5.20: Time series of centroids for extended source without filter. (a): 2D frame no.20 of time series. (b): 3D frame no. 20 of time series. (c),(d): Time series of centroids calculated by TCoG (th=25), TCoG (th=50), GFiT and 1FC in Python (floating point, detrended). 183 frames. Science camera. Telescope 1m McLellan Mt.John (NZ). Object: extended source. Window: 60 x 60 pixels. Frame rate 15 frames/s.

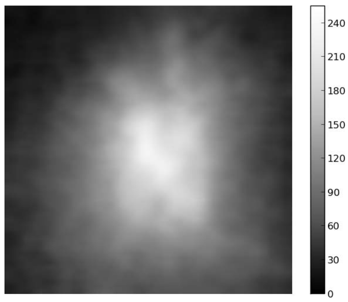

(a) 2D frame of time series

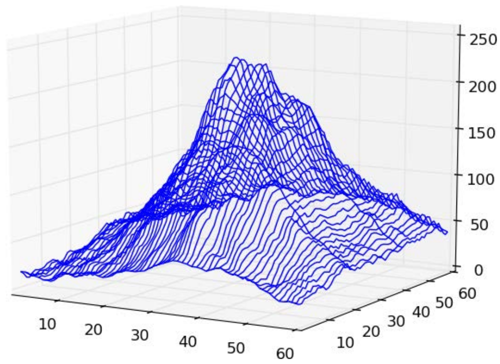

(b) 3D frame of time series

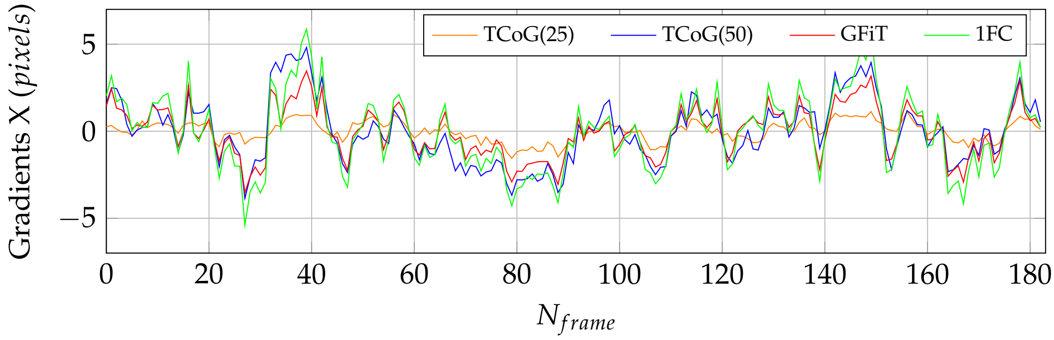

(c) X axis

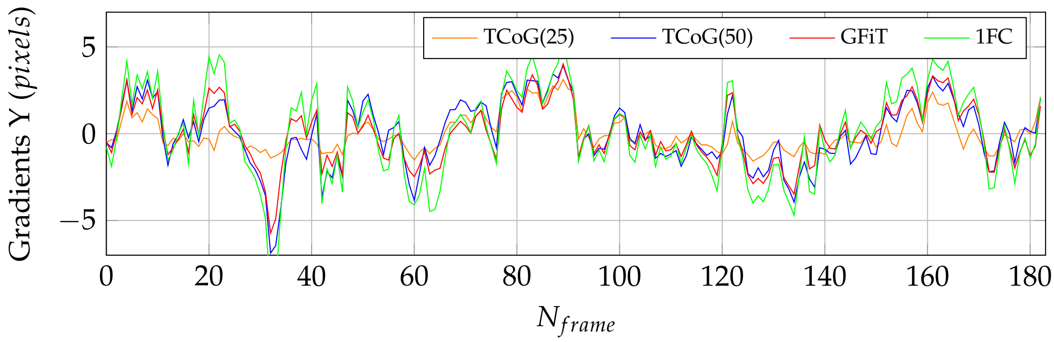

(d) Y axis

Figure 5.21: Time series of centroids for extended source with 2D convolution filter (3x3). (a): 2D frame no.20 of time series. (b): 3D frame no. 20 of time series. (c),(d): Time series of centroids calculated by TCoG (th=25), TCoG (th=50), GFiT and 1FC in Python (floating point, detrended). 183 frames. Science camera. Telescope 1m McLellan Mt.John (NZ). Object: extended source. Window: 60 x 60 pixels. Frame rate 15 frames/s.

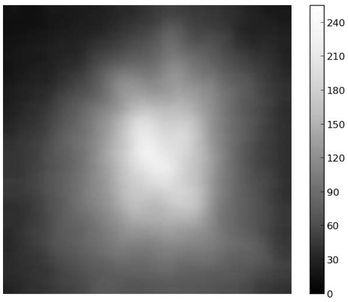

(a) 2D frame of time series

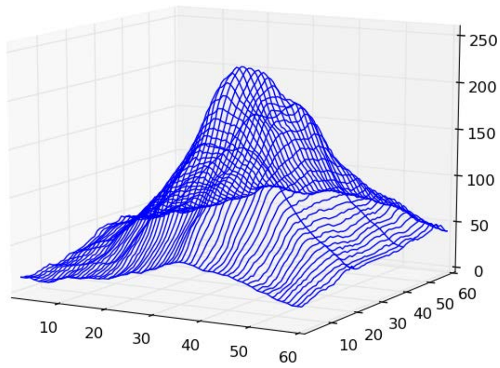

(b) 3D frame of time series

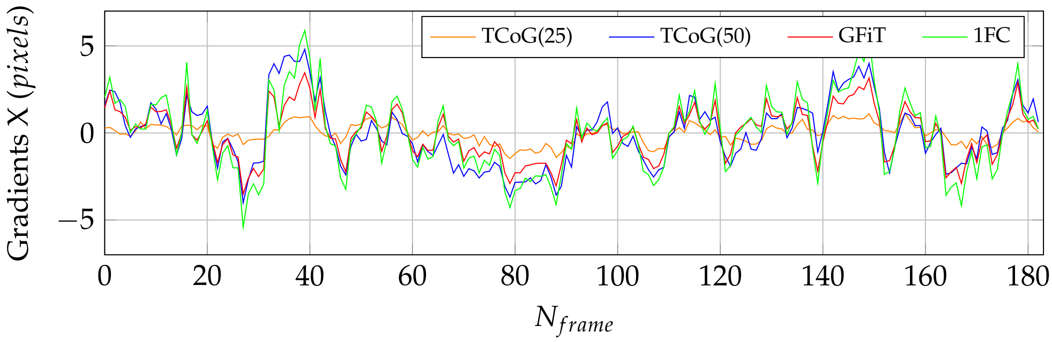

(c) X axis

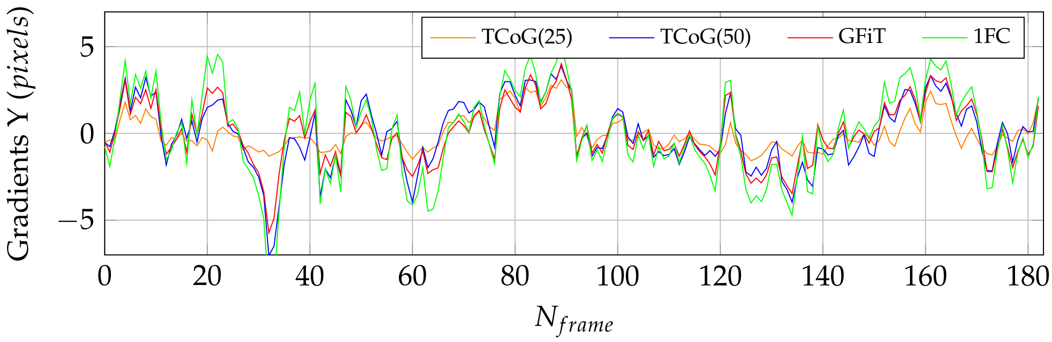

(d) Y axis

Figure 5.22: Time series of centroids for extended source with 2D convolution filter (5x5). (a): 2D frame no.20 of time series. (b): 3D frame no. 20 of time series. (c),(d): Time series of centroids calculated by TCoG (th=25), TCoG (th=50), GFiT and 1FC in Python (floating point, detrended). 183 frames. Science camera. Telescope 1m McLellan Mt.John (NZ). Object: extended source. Window: 60 x 60 pixels. Frame rate 15 frames/s.

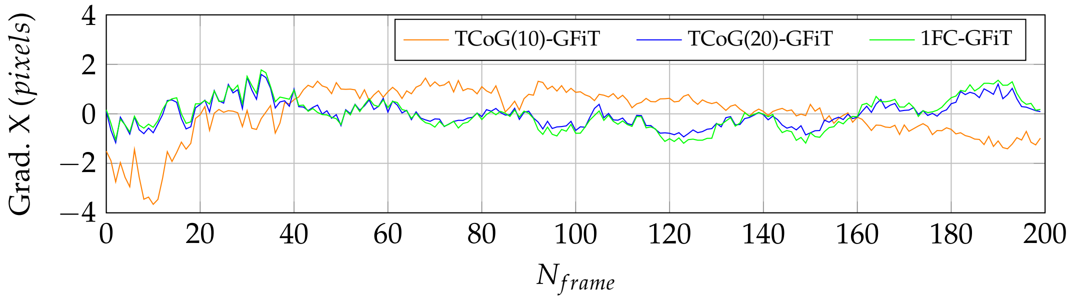

(a) X axis

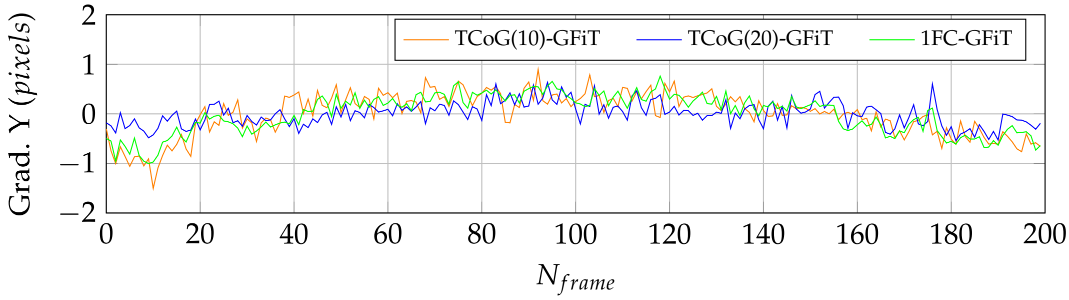

(b) Y axis

Figure 5.23: Time series of absolute differences between TCoG(10), TCoG(20), 1FC with GFit for narrow source without filter. (a): X axis. (b): Y axis.

Table 5.4: Standard deviation for narrow source in X axis, for differences between centroiding algorithms with 3 different filters.Units in pixels.

Filter	TCoG(10)-GFiT	TCoG(20)-GFiT	1FC-GFiT
No filter	1.027	0.517	0.631
2D Conv. 3x3	1.005	0.513	0.646
2D Conv. 5x5	0.927	0.529	0.681

Table 5.5: Standard deviation for narrow source in Y axis, for differences between centroiding algorithms with 3 different filters. Units in pixels.

Filter	TCoG(10)-GFiT	TCoG(20)-GFiT	1FC-GFiT
No filter	0.433	0.243	0.389
2D Conv. 3x3	0.454	0.213	0.395
2D Conv. 5x5	0.468	0.207	0.389

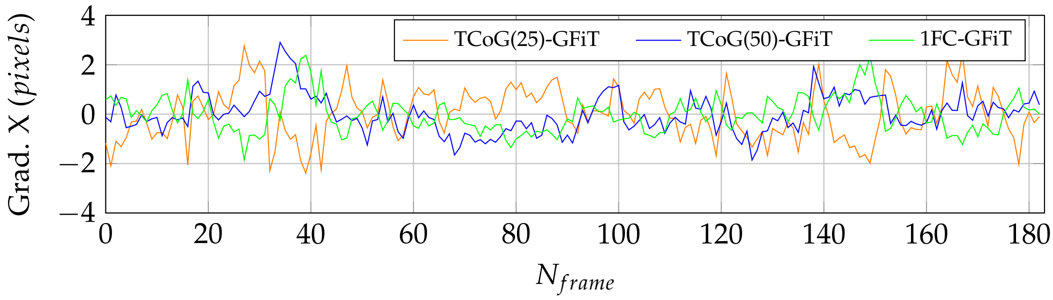

(a) X axis

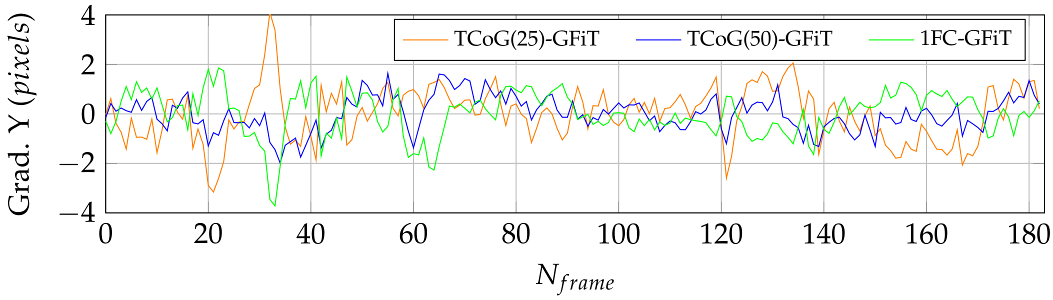

(b) Y axis

Figure 5.24: Time series of absolute differences between TCoG(25), TCoG(50), 1FC with GFit for extended source without filter. (a): X axis. (b): Y axis.

Table 5.6: Standard deviation for extended source in X axis, for differences between centroiding algorithms with 3 different filters. Units in pixels.

Filter	TCoG(25)-GFiT	TCoG(50)-GFiT	1FC-GFiT
No filter	1.015	0.769	0.718
2D Conv. 3x3	1.040	0.832	0.725
2D Conv. 5x5	1.046	0.849	0.735

Table 5.7: Standard deviation for extended source in Y axis, for differences between centroiding algorithms with 3 different filters. Units in pixels.

Filter	TCoG(25)-GFiT	TCoG(50)-GFiT	1FC-GFiT
No filter	1.088	0.695	0.899
2D Conv. 3x3	1.102	0.700	0.906
2D Conv. 5x5	1.110	0.690	0.915

The 1FC shows a moderate performance and there is no need to adapt the algorithm to certain value, hence it adapts better for changing conditions in the targets observed, both narrow or extended sources. In contrast, TCoG has a slightly better performance than the 1FC, but with the disadvantage that it needs to be adapted, changing the threshold value, depending on the noise level and the centroid width.

On the other hand, the existence of white noise in the image doesn't seem to affect the centroiding calculation for the 1FC as much as the TCoG (optimized) algorithms, which can be observed in tables 5.4 to 5.7, where the standard deviation values are very similar for any of the two sources, regardless the chosen filter.

The independence of the variability in intensity and width of the reference source shown by the 1FC centroiding algorithm, is particularly useful in the case of a NGS AO system for small aperture telescopes, where the reference is the source itself or a nearby object, which will show a strong variability depending on the source or the nearby objects, therefore extending the range of objects under study with the AO system.

5.7 Analysis of AO control loop

To analyze the behaviour of the AO control loop different tests were performed. First the gradients shift and the Zernike coefficients variability was measured when there was no target in the laser source or the telescope, hence the CMOS image sensor noise in the WFS sensor was analyzed. Then the AO loop was tested with a laser source in laboratory, under two conditions, AO activated (AO ON) and AO deactivated (AO OFF). And finally same tests were accomplished with the telescope tracking sidereal objects.

In figure 5.25 is analysed the behaviour of the AO control loop when the input is image sensor noise. It is observed that this perturbation influences the centroids shift in a subpixel scale, 0.125 pixels in both axes. Something similar happens in figure 5.26, in the analysis of the Zernike coefficients, where the more affected Zernike mode is Z_3, tilt in axis Y, due to the vertical shifting noise present in the CMOS sensor, that can be seen in figure 5.25a in the snapshot of a frame, as horizontal bars. In any case, this perturbation in the Z_2 is around 0.1µm.

The bi-state output in the time series of centroids and in calculation of Zernike coefficients when noise is the input is due to internal calculations in the FPGA.

In the subtraction block inside the FPGA (see figure 4.2 in Chapter 4), reference centroids are subtracted from calculated centroids in order to obtain the gradients, with fixed point resolution of 26 bits with 16 decimal figures. In order to transmit the Gradients out of the FPGA through the serial port, with a bit width of 8 bits, a casting block in inserted with 8 bits resolution, including 3 decimal figures. These 3 decimal positions provide a quantization of 3 bits, which yield to 8 possible values in the decimal precision, therefore with a quantization of 1/8 = 0.125. So input noise in the CMOS image sensor, the centroids values oscillates between these 2 states, 0 and -0.125, as shown in figure 5.25. Nevertheless, the gradients values to obtain the Zernike coefficients and the deformable mirror voltages have higher resolution in the decimal part, 16 bits precision.

In figures 5.27 and 5.28 is shown the analysis of the AO system with a laser source where random aberrations of average value of 2 pixels shift were introduced in the beam with a phase screen, with AO OFF and in figures 5.27 and 5.28, and AO ON in figures 5.29 and 5.30. In the Zernike coefficient curves, it is observed an initial period (approximately the first 150 frames), where Zernike coefficients curves are smoother that the rest of the time series. This is due to the time delay between the capture of frames is initiated and the aberrations are introduced with a phase screen in the wavefronts. This also explains the peaks in the time series curves of figures 5.27 and 5.29.

From the analysis of this curves, in this aberration range there is no noticeable differences between the corrected and the uncorrected centroids and Zernike coefficients values, due to the small range of variability of the gradient shifting.

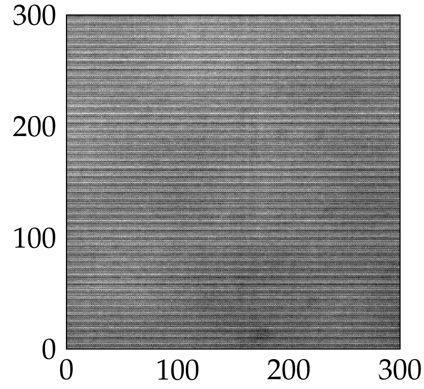

(a) Snapshot frame, grayscale [0 255], 300 x 300 pixels

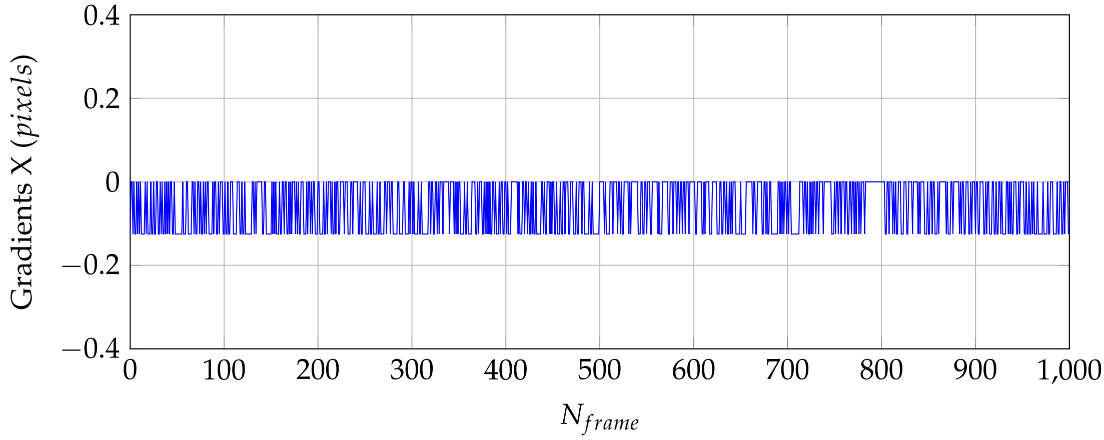

(b) X axis

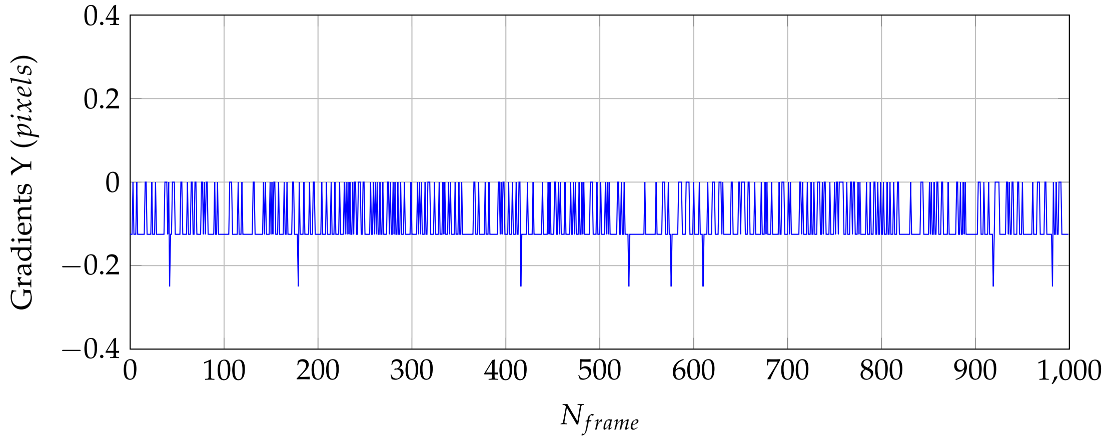

(c) Y axis

Figure 5.25: Time series of centroids for image sensor noise of AO system (FPGA). (a): Snapshot frame of time series. (b),(c): Time series of centroids in subaperture 11 in FPGA (fixed point, no detrended, no tracking, AO OFF). 1000 frames. Camera Aptina-FPGA. Object: image sensor noise. Window: 300 x 300 pixels. Frame rate 285 frames/s.

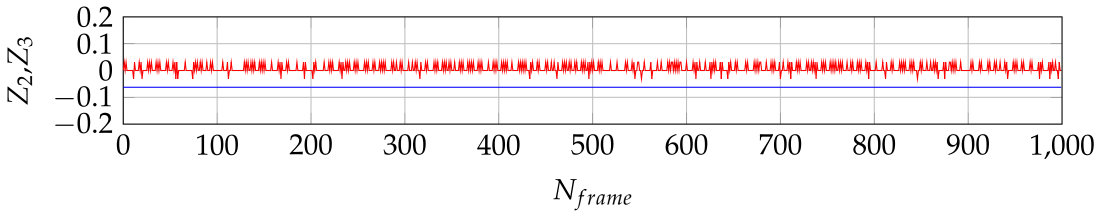

(a) Tilt x (Z_2), Tilt y (Z_3)

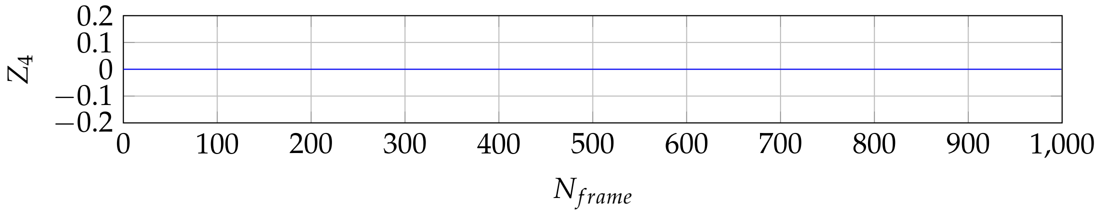

(b) Defocus (Z_4)

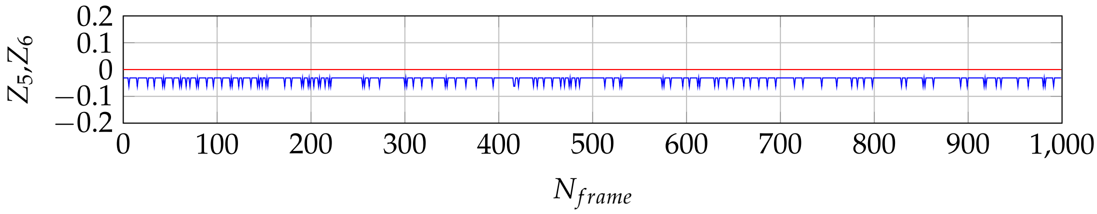

(c) Astigmatism (Z_5), Astigmatism (Z_6)

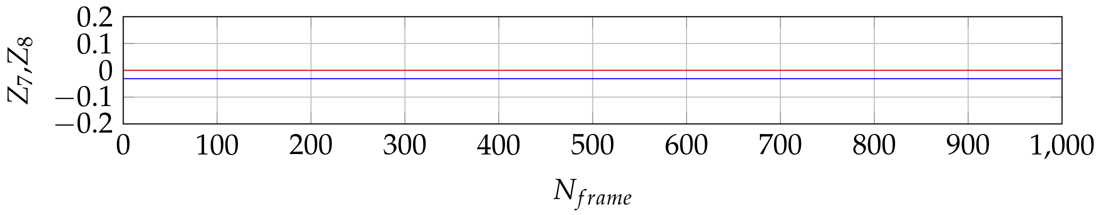

(d) Coma (Z_7), Coma (Z_8)

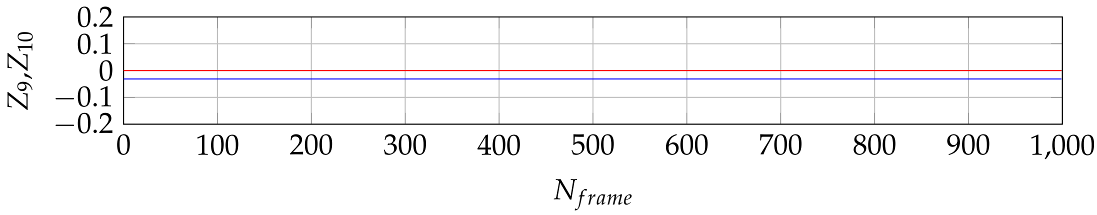

(e) Trefoil (Z_9), Trefoil (Z_{10})

Figure 5.26: Time series of classic Zernike aberrations coefficients calculated by CoG in FPGA for image sensor noise source. (fixed point, no detrended, no tracking, AO OFF). 1000 frames. Camera Aptina-FPGA. Object: image sensor noise. Frame rate 285 frames/s. Scale: x 10^{-6} m.

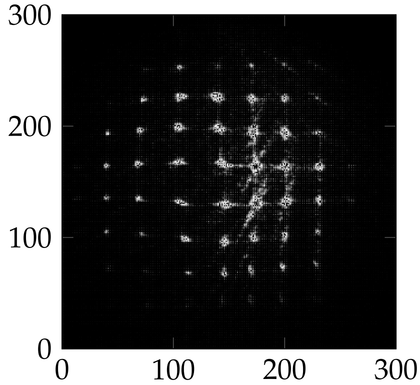

(a) Snapshot frame, grayscale [0 255], 300 x 300 pixels

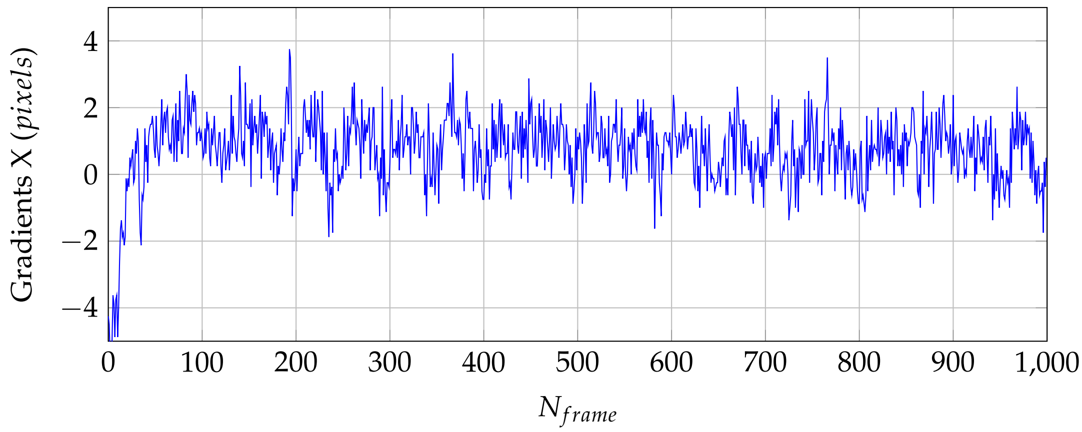

(b) X axis

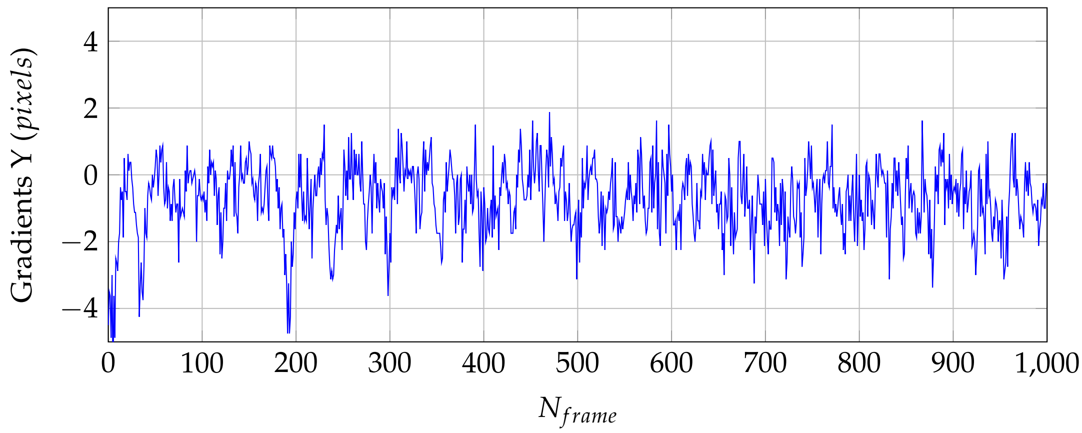

(c) Y axis

Figure 5.27: Time series of centroids for laser source through phase screen with AO OFF in CMOS image sensor of AO system (FPGA). (a): Snapshot frame of time series. (b),(c): Time series of centroids in subaperture 11 in FPGA (fixed point, no detrended, no tracking, AO OFF). 1000 frames. Camera Aptina-FPGA. Object: laser source through Lexitek phase screen. Window: 300 x 300 pixels. Frame rate 285 frames/s.

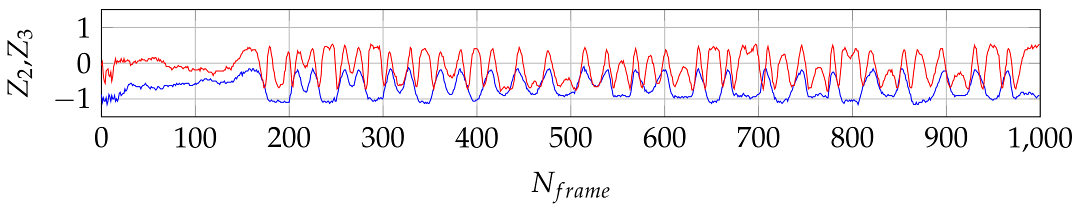

(a) Tilt x (Z_2), Tilt y (Z_3)

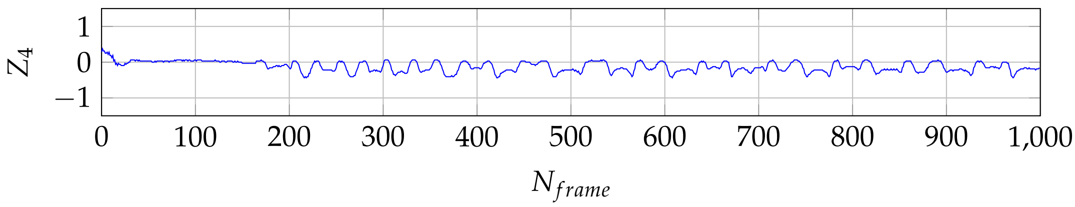

(b) Defocus (Z_4)

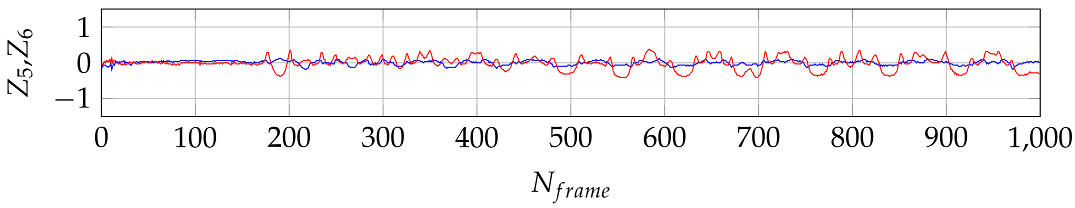

(c) Astigmatism (Z_5), Astigmatism (Z_6)

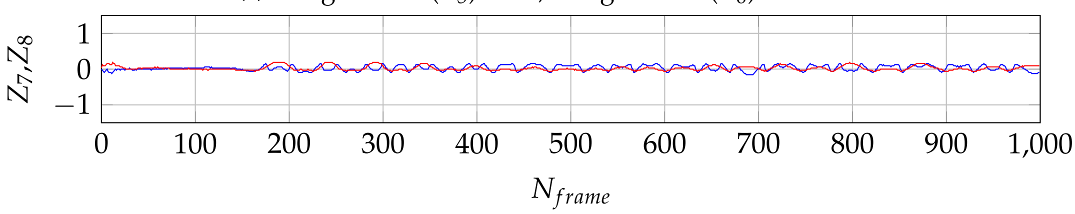

(d) Coma (Z_7), Coma (Z_8)

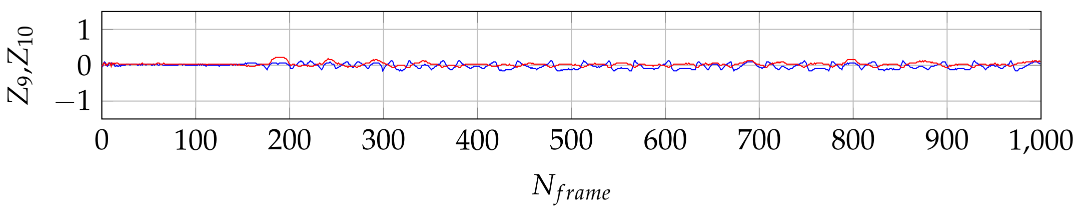

(e) Trefoil (Z_9), Trefoil (Z_{10})

Figure 5.28: Time series of classic Zernike aberrations coefficients for laser source through phase screen with AO OFF in FPGA. (fixed point, no detrended, no tracking, AO OFF). 1000 frames. Camera Aptina-FPGA. Object: laser source through Lexitek phase screen. Frame rate 285 frames/s. Scale: x 10^{-6} m.

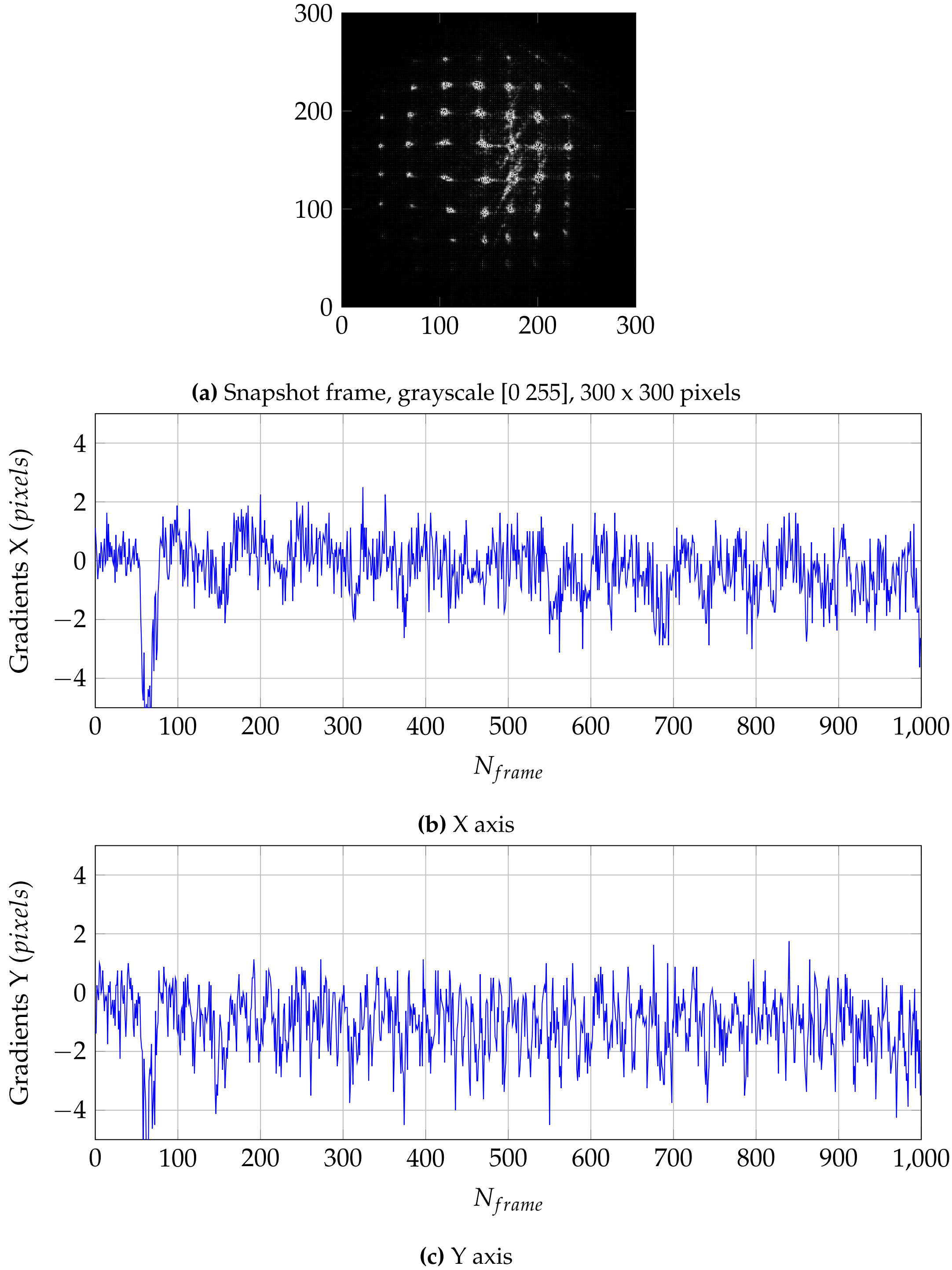

Figure 5.29: Time series of centroids for laser source through phase screen with AO ON in CMOS image sensor of AO system (FPGA). (a): Snapshot frame of time series. (b),(c): Time series of centroids in subaperture 11 in FPGA (fixed point, no detrended, no tracking, AO ON). 1000 frames. Camera Aptina-FPGA. Object: laser source through Lexitek phase screen. Window: 300 x 300 pixels. Frame rate 285 frames/s.

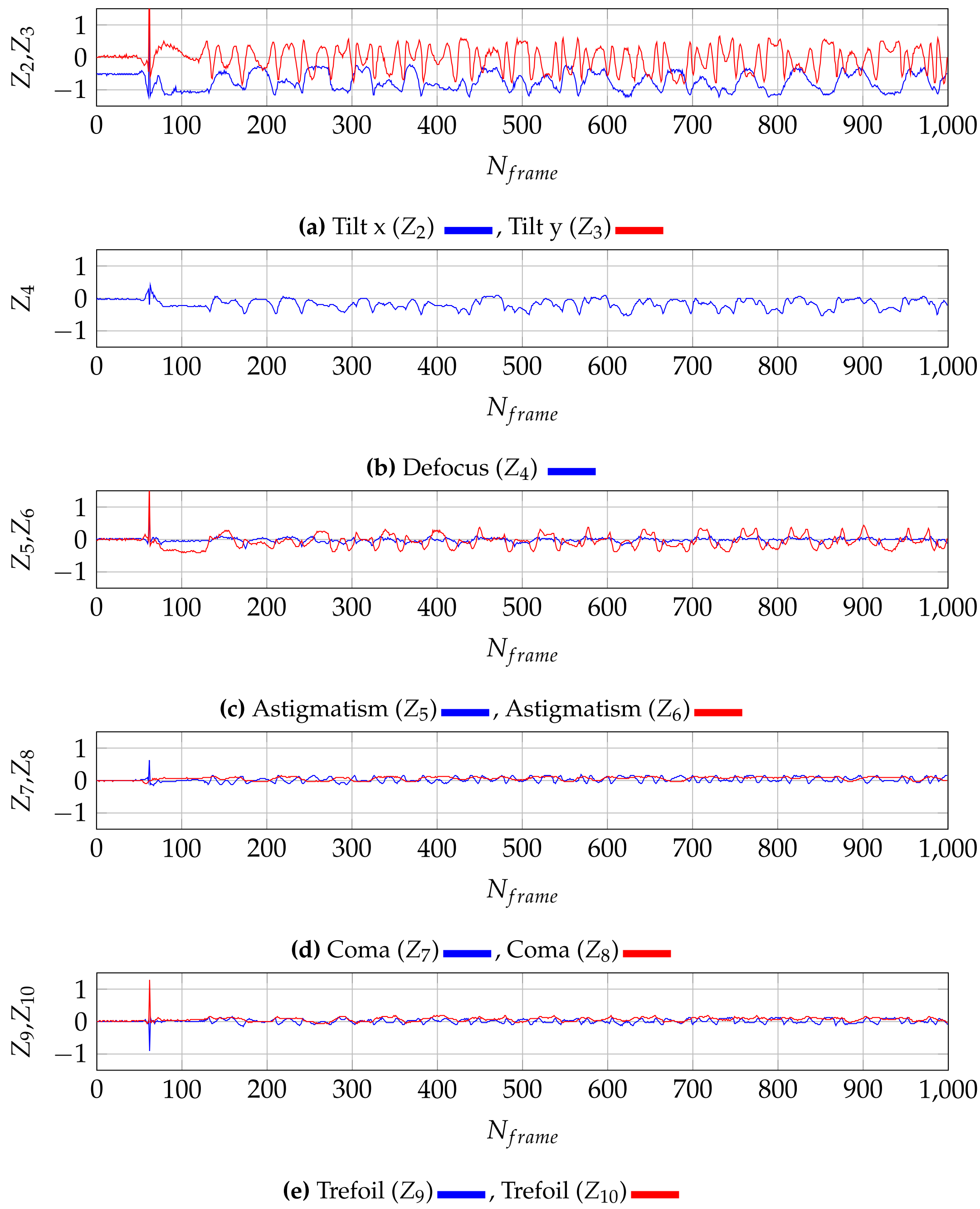

(a) Tilt x (Z_2), Tilt y (Z_3)

(b) Defocus (Z_4)

(c) Astigmatism (Z_5), Astigmatism (Z_6)

(d) Coma (Z_7), Coma (Z_8)

(e) Trefoil (Z_9), Trefoil (Z_{10})

Figure 5.30: Time series of classic Zernike aberrations coefficients for laser source through phase screen with AO ON in FPGA. (fixed point, no detrended, no tracking, AO ON). 1000 frames. Camera Aptina-FPGA. Object: laser source through Lexitek phase screen. Frame rate 285 frames/s. Scale: x 10^{-6} m.

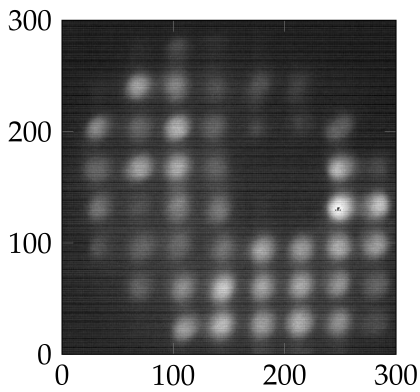

(a) Snapshot frame, grayscale [0 255], 300 x 300 pixels

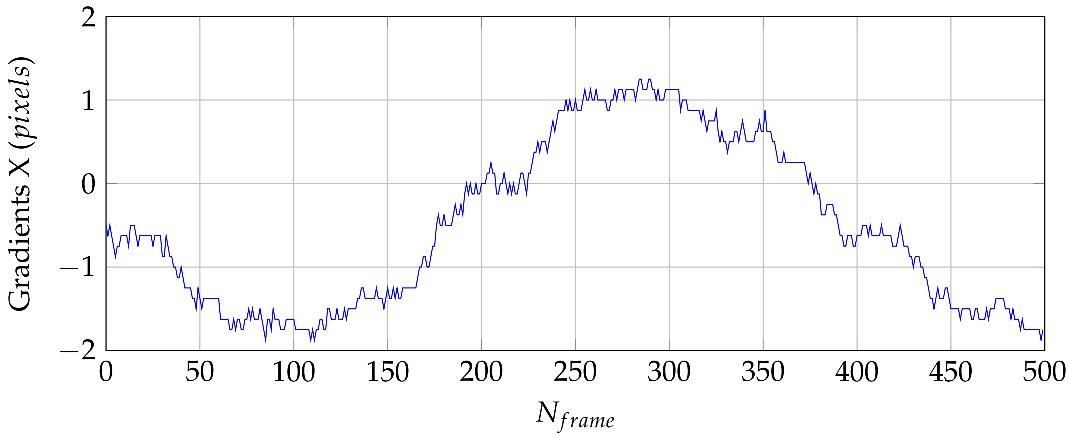

(b) X axis

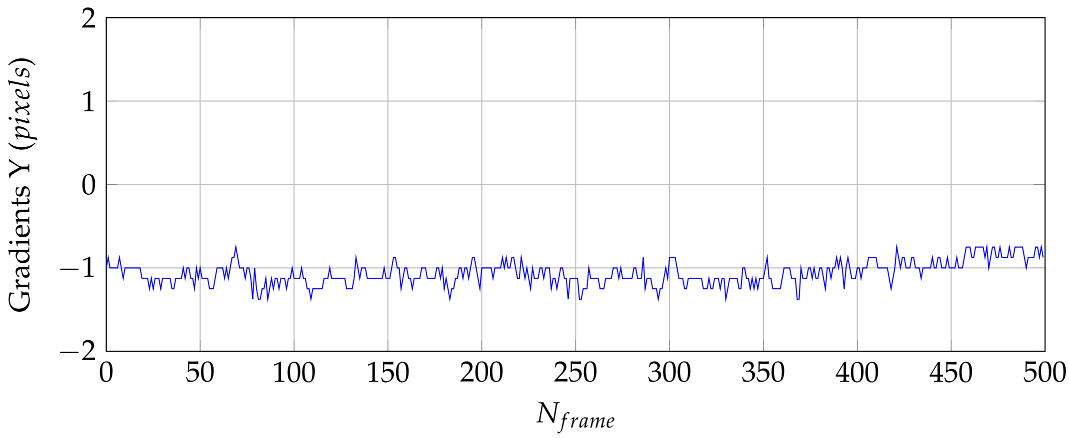

(c) Y axis

Figure 5.31: Time series of centroids for Jupiter with AO OFF in CMOS image sensor (image sensor gain=100) of AO system (FPGA). (a): Snapshot frame of time series. (b),(c): Time series of centroids in subaperture 85 in FPGA (fixed point, no detrended, tracking ON, AO OFF). 500 frames. Camera Aptina-FPGA. Object: Jupiter. Window: 300 x 300 pixels. Frame rate 285 frames/s.

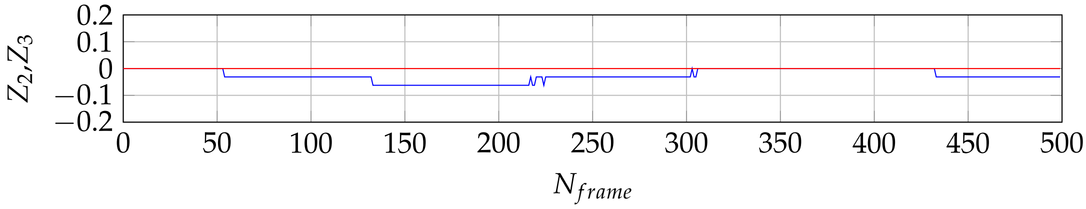

(a) Tilt x (Z_2), Tilt y (Z_3)

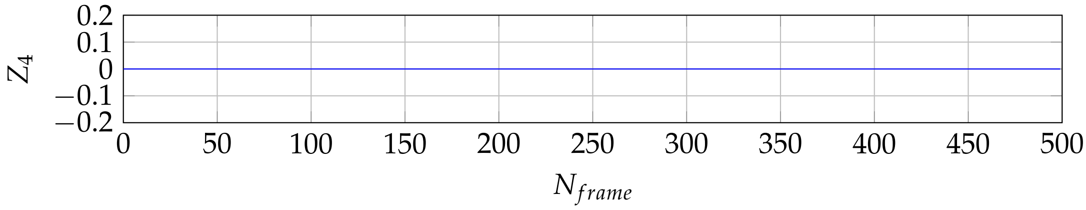

(b) Defocus (Z_4)

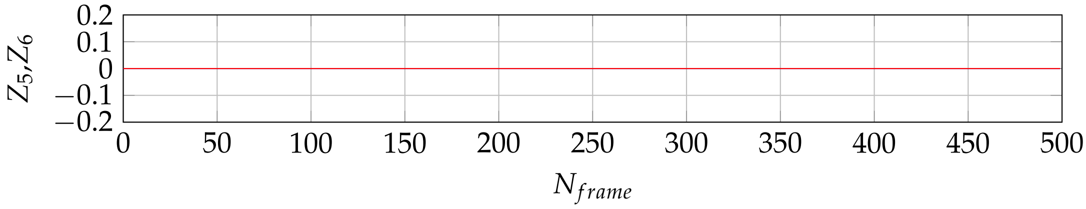

(c) Astigmatism (Z_5), Astigmatism (Z_6)

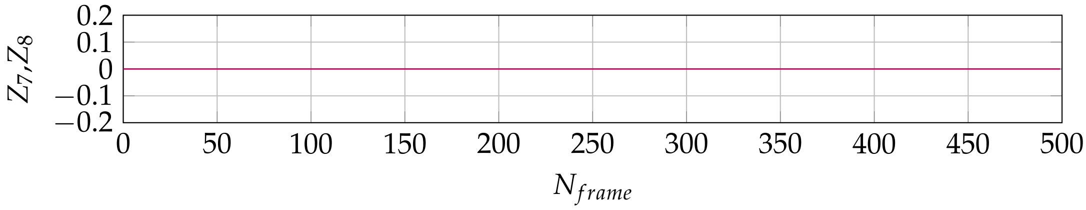

(d) Coma (Z_7), Coma (Z_8)

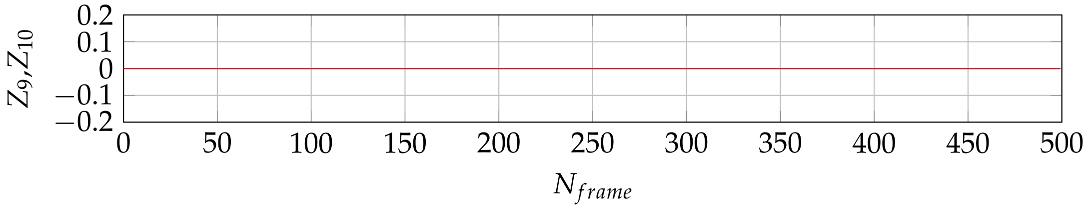

(e) Trefoil (Z_9), Trefoil (Z_{10})

Figure 5.32: Time series of classic Zernike aberrations coefficients for Jupiter with AO OFF in CMOS image sensor (image sensor gain=100) of AO system (FPGA). (fixed point, no detrended, tracking ON, AO OFF). 500 frames. Camera Aptina-FPGA. Object: Jupiter. Frame rate 285 frames/s. Scale: x 10^{-6} m.

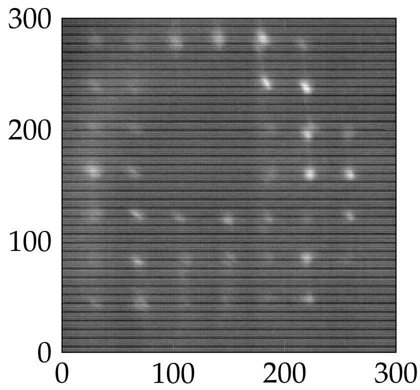

(a) Snapshot frame, grayscale [0 255], 300 x 300 pixels

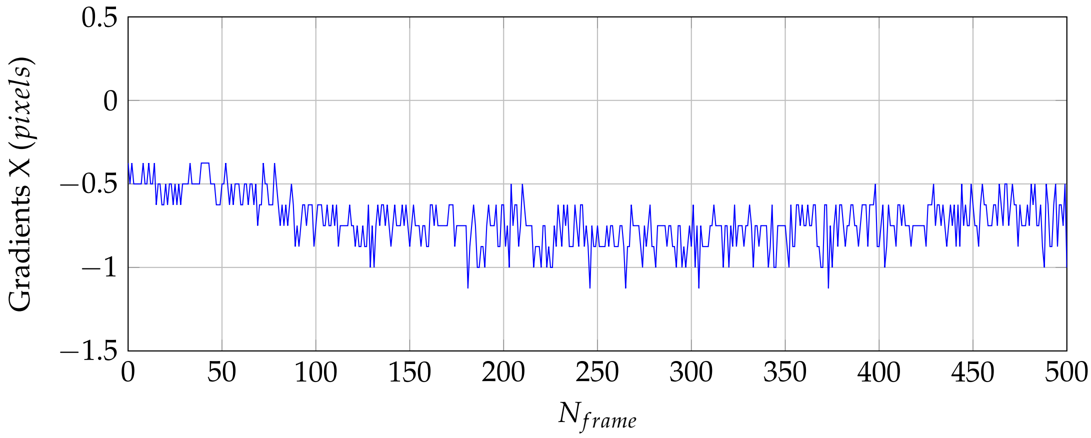

(b) X axis

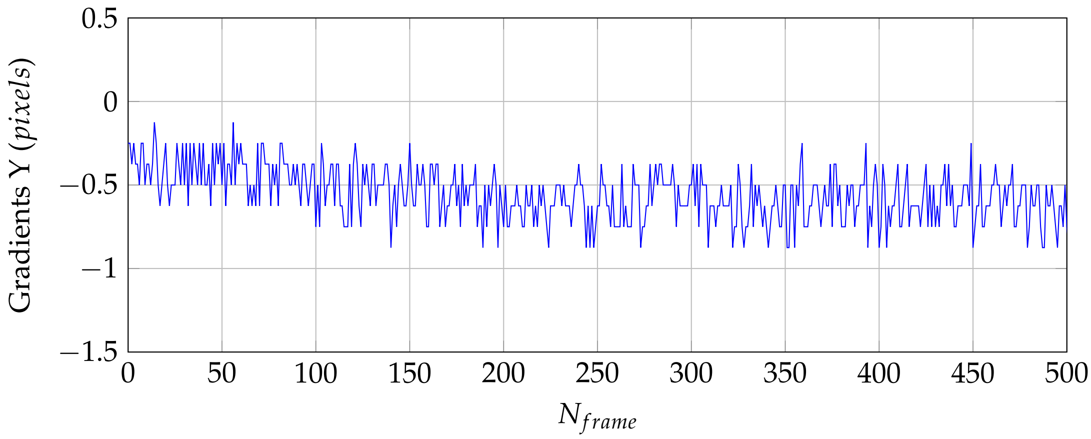

(c) Y axis

Figure 5.33: Time series of centroids for Rigel Kentaurus (m_v = 0.13) with AO OFF in CMOS image sensor (image sensor gain=100, shutter=18 ms, AO gain=0.7) of AO system (FPGA). (a): Snapshot frame of time series. (b),(c): Time series of centroids in subaperture 48 in FPGA (fixed point, no detrended, tracking ON, AO OFF). 500 frames. Camera Aptina-FPGA. Object: Rigel Kentaurus. Window: 300 x 300 pixels. Frame rate 285 frames/s.

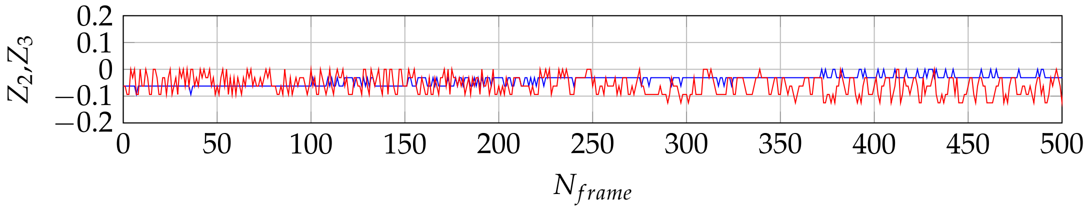

(a) Tilt x (Z_2), Tilt y (Z_3)

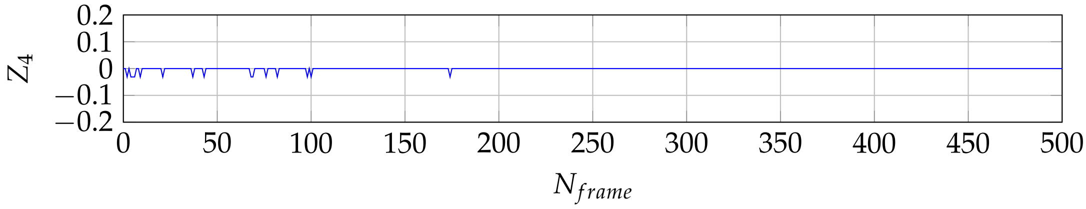

(b) Defocus (Z_4)

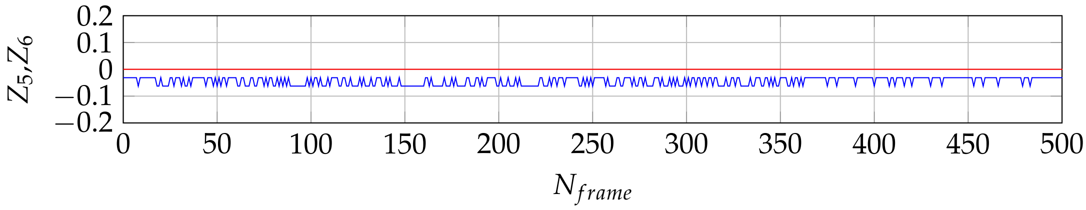

(c) Astigmatism (Z_5), Astigmatism (Z_6)

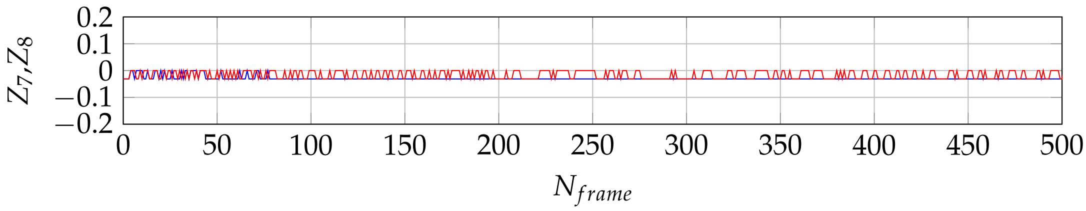

(d) Coma (Z_7), Coma (Z_8)

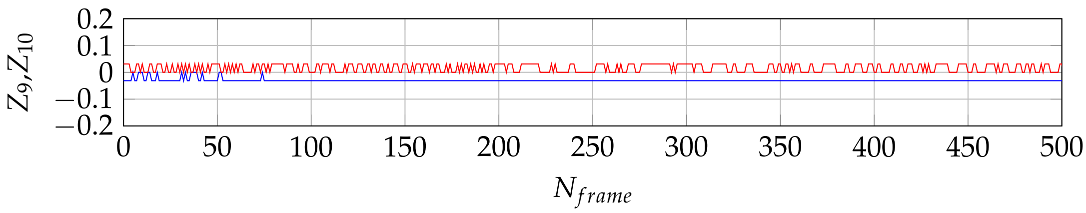

(e) Trefoil (Z_9), Trefoil (Z_{10})

Figure 5.34: Time series of classic Zernike aberrations coefficients for Rigel Kentaurus (m_v = 0.13) with AO OFF in CMOS image sensor (image sensor gain=100, shutter=18 ms, AO gain=0.7) of AO system (FPGA). (fixed point, no detrended, tracking ON, AO OFF). 500 frames. Camera Aptina-FPGA. Object: Rigel Kentaurus. Frame rate 285 frames/s. Scale: x 10^{-6} m.

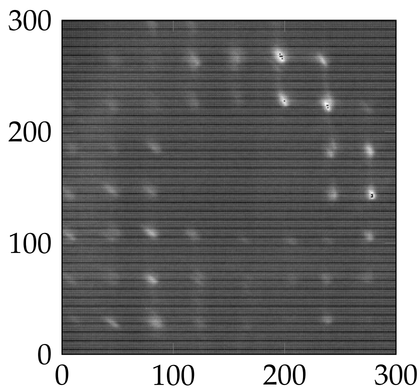

(a) Snapshot frame, grayscale [0 255], 300 x 300 pixels

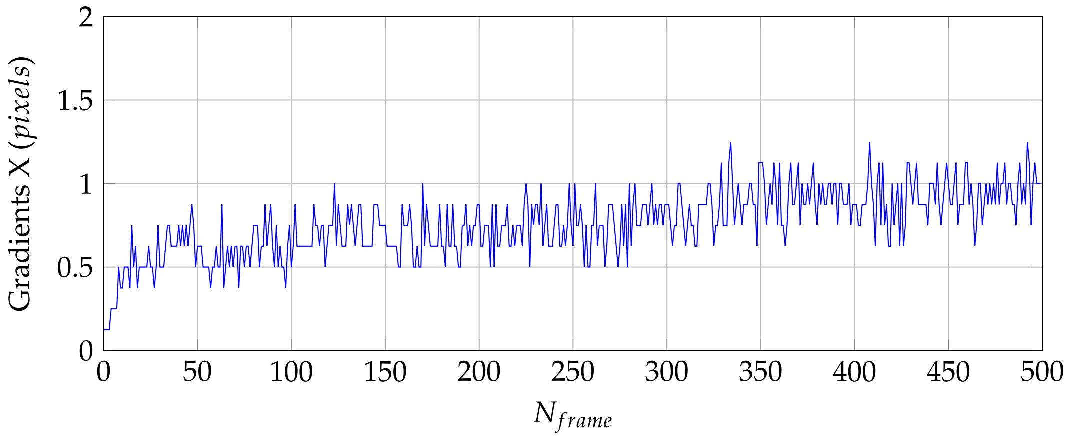

(b) X axis

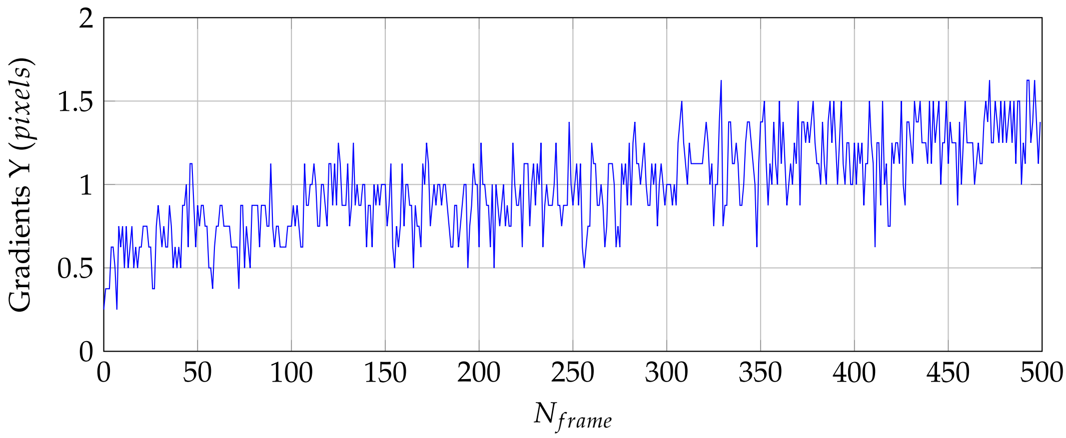

(c) Y axis

Figure 5.35: Time series of centroids for Rigel Kentaurus (m_v = 0.13) with AO ON in CMOS image sensor (image sensor gain=100, shutter=18 ms, AO gain=0.7) of AO system (FPGA). (a): Snapshot frame of time series. (b),(c): Time series of centroids in subaperture 48 in FPGA (fixed point, no detrended, tracking ON, AO ON). 500 frames. Camera Aptina-FPGA. Object: Rigel Kentaurus. Window: 300 x 300 pixels. Frame rate 285 frames/s.

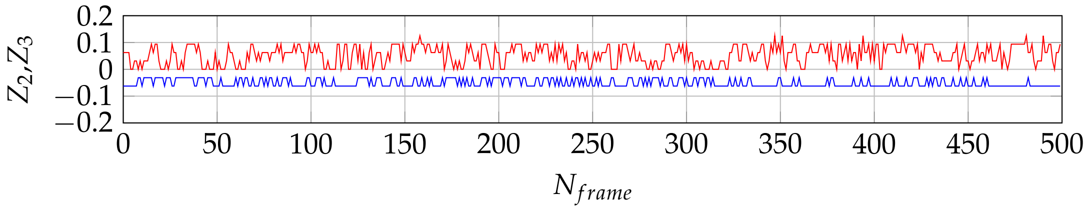

(a) Tilt x (Z_2), Tilt y (Z_3)

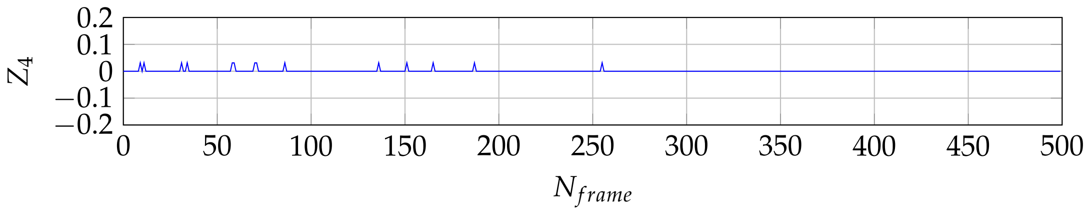

(b) Defocus (Z_4)

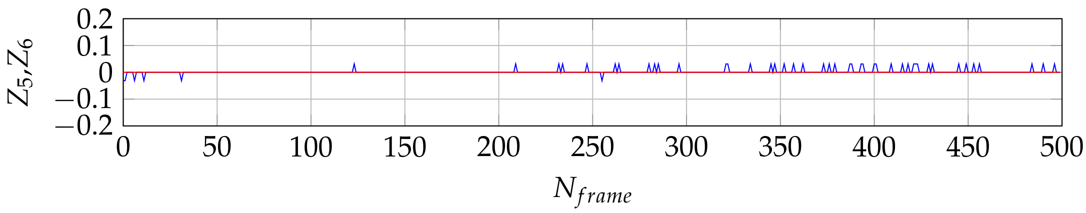

(c) Astigmatism (Z_5), Astigmatism (Z_6)

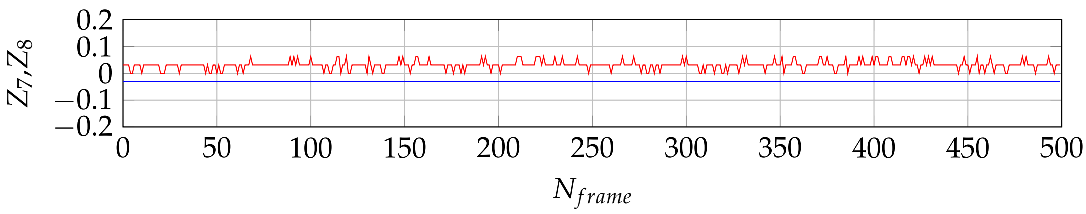

(d) Coma (Z_7), Coma (Z_8)

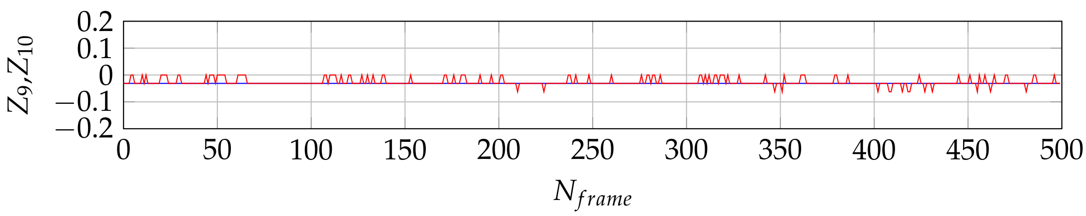

(e) Trefoil (Z_9), Trefoil (Z_{10})

Figure 5.36: Time series of classic Zernike aberrations coefficients for Rigel Kentaurus (m_v = 0.13) with AO ON in CMOS image sensor (image sensor gain=100, shutter=18 ms, AO gain=0.7) of AO system (FPGA). (fixed point, no detrended, tracking ON, AO ON). 500 frames. Camera Aptina-FPGA. Object: Rigel Kentaurus. Frame rate 285 frames/s. Scale: x 10^{-6} m.

In figures 5.31 and 5.32 are shown the results when the target is an extended source, Jupiter, which creates wider dots in the WFS focal plane, as the angle of arrival comes from different directions from the source, which makes difficult to detect high order aberrations. It can be seen a slow variation of x axis centroids, due to inaccuracies on the tracking, or effects as wind. This variation is translated to the Zernike coefficients, so in figure 5.32a, Z_2 curve (represented in blue) shows also this trend.

In figures 5.33 to 5.36 is shown the AO system operation with a star of apparent magnitude 0.13 (m_v = 0.13), with AO ON and AO OFF. The difference between a extended source as Jupiter and a narrow source as a star can be seen in the Zernike coefficients output values in figures 5.32 (Jupiter), 5.34 (Rigel with AO OFF) and 5.36 (Rigel with AO ON). In Zernike coefficients of Jupiter there is no variation in the time series (except the slow variation in Z_3 due to tracking inaccuracies or wind), but in Zernike coefficients of Rigel these variations can be observed, with different values depending on the aberration mode. Both Jupiter and Rigel time series were taken in the same night with similar atmospheric conditions.

In figure 5.37 are shown two snapshots of two video streams captured with the science camera, with the AO OFF (figure 5.37a) and with the AO ON (figure 5.37b), for Rigel Kentaurus.

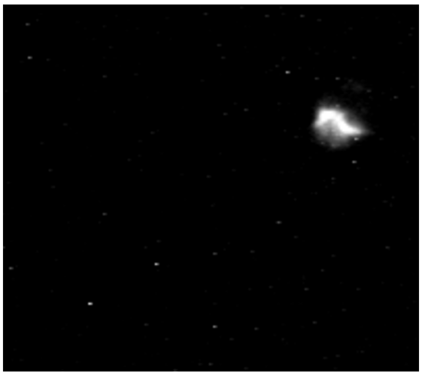

(a) AO OFF

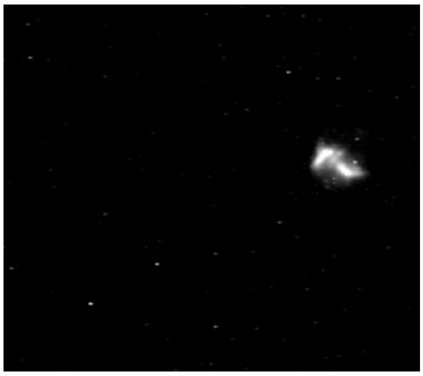

(b) AO ON

Figure 5.37: Snapshot of video streams of Rigel Kentaurus (m_v = 0.13) taken with the science camera, with AO OFF (left) and AO ON (right).

To analyse the performance of the AO system with these two video captures, we follow the next approach proposed by Fraser et al. [18]. In their research, they propose the use of a Wiener filter within a ROI to detect a space varying PSF, providing more robust tip-tilt information in images through turbulence, compared to other methods as cross correlation. According to their proposed method, to obtain the PSF we apply the next formula of the Wiener filter:

$$h = \mathcal{F}^{-1}\left\{ \frac{\mathcal{F}(f)^*}{|\mathcal{F}(f)|^2 + \phi^2} \mathcal{F}(g) \right\}, \tag{5.6}$$

where h is the PSF that we will use to evaluate the performance of the AO system, $\mathcal{F}$ and $\mathcal{F}^{-1}$ are the forward and inverse discrete Fourier transforms respectively, f is the windowed ROI of the image that we will consider as the non aberrated one (in this case with AO ON), g is the windowed ROI of the image that we will consider as the aberrated one (in this case with AO OFF), ϕ is the S/N ratio, and * indicates the complex conjugate.

In figure 5.38 are shown the windowed ROIs on which the Wiener deconvolution is applied. In figure 5.38a is represented the corrected image and in figure 5.38b the uncorrected one, both with sizes 40 × 40 pixels. A colored map has been used to get a better visualization.

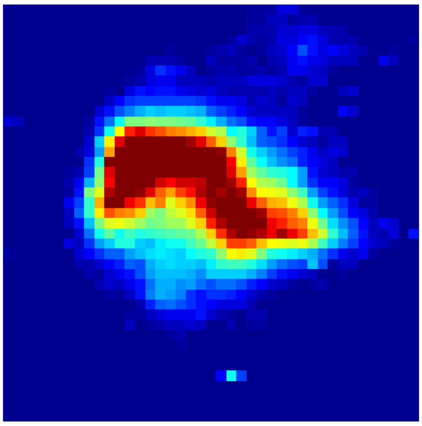

(a) f (corrected image)

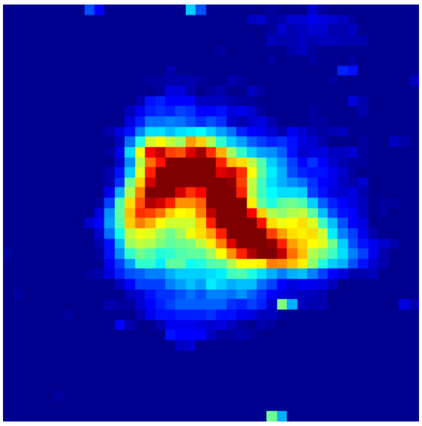

(b) g (uncorrected image)

Figure 5.38: Windowed ROIs of 60 × 60 pixels of corrected image (left) and uncorrected image (right).

A value of $\phi = 10^7$ was chosen, which gave a discernible maximum in the PSF, in order to calculate its FWHM. In figure 5.39 are shown the PSF corresponding to the four considered cases: AO ON with $\phi = 10^7$, AO OFF with $\phi = 10^7$, f=g with $\phi = 10^7$, and f=g with $\phi = 1$. In figure 5.40 are shown the FWHM values of h as time series corresponding to 100 consecutive frames for x axis (5.40a) and y axis (5.40b).

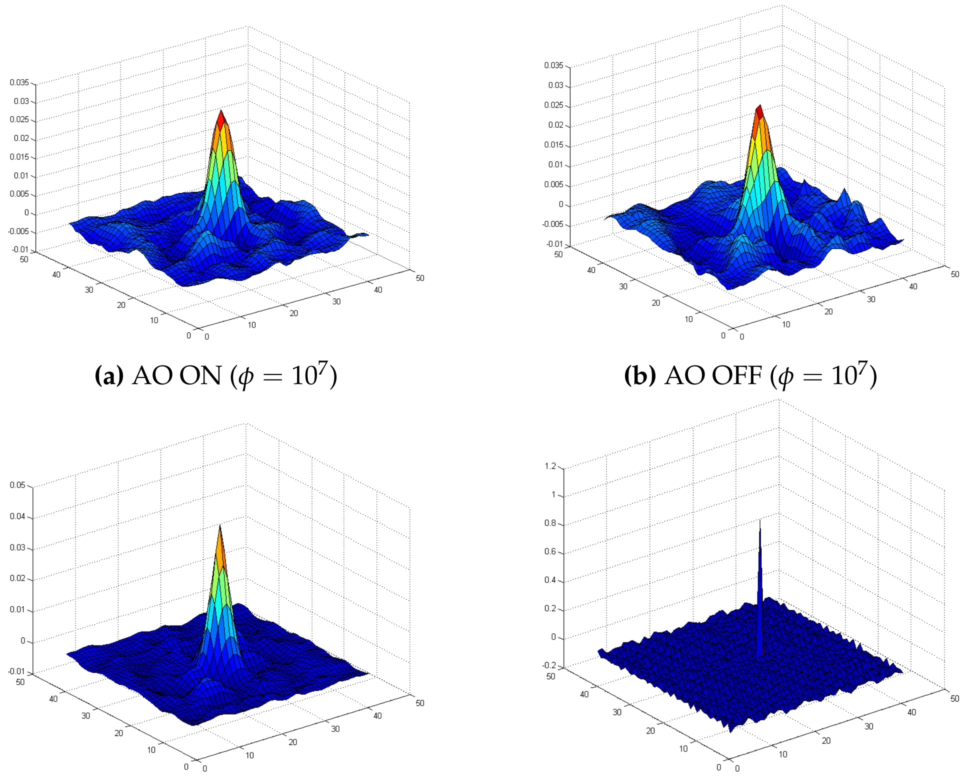

(a) AO ON ($\phi = 10^7$)

(b) AO OFF ($\phi = 10^7$)

(c) f = g ($\phi = 10^7$)

(d) f = g ($\phi = 1$)

Figure 5.39: PSF of frames in the science camera generated with Wiener deconvolution.

From this curves, apparently it doesn't seem to exist an improvement in the FWHM when the AO system is active, but different factors can influence these results: level of noise in the Wiener deconvolution, resolution of the science camera, inaccuracies in the tracking system, to mention a few. Further investigation needs to be done to obtain relevant results in the AO system performance with this metodology.

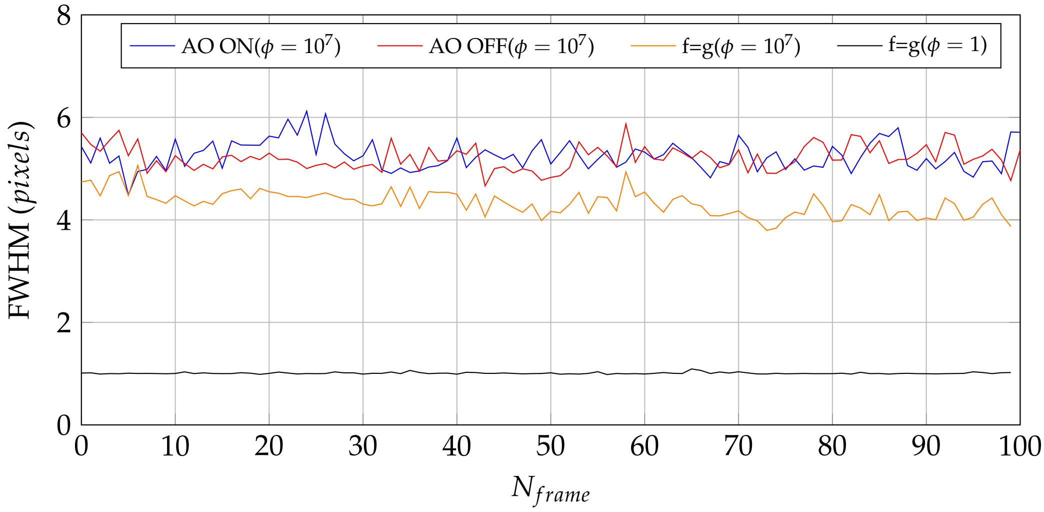

(a) X axis

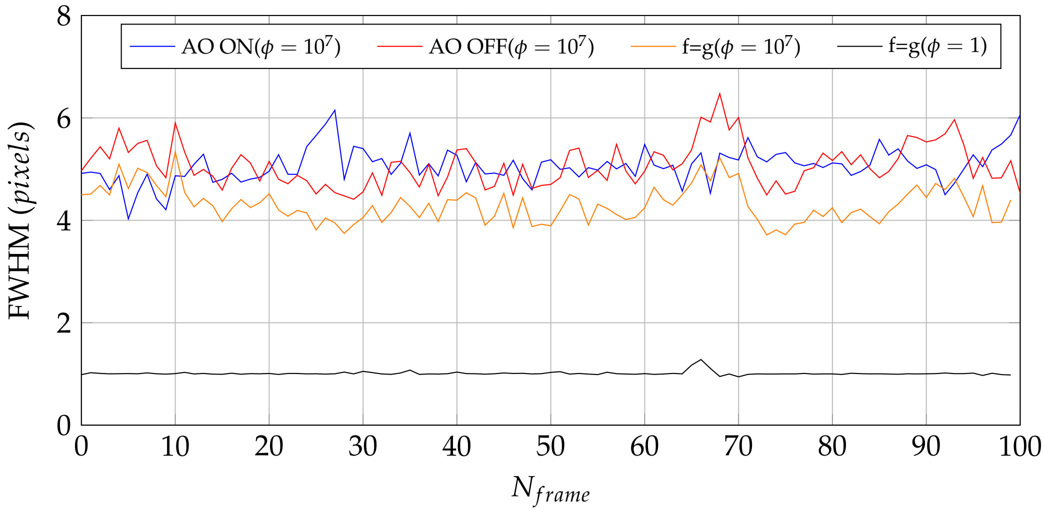

(b) Y axis

Figure 5.40: Time series of FWHM values of PSF obtained through Wiener deconvolution for video captures in the science camera with AO ON and AO OFF.

CHAPTER 6

Conclusions and Future Work

6.1 Conclusions

In this thesis the viability of a low cost portable AO system for small and moderate size aperture telescope has been investigated. Considering the design decisions and engineering technologies described in chapter 2, the characterization and performance of an AO system, that could have impact in a big potential market formed by amateur astronomy and modest facilities in research and educational organizations have been accomplished.

This AO system was supported first in an opto-mechanical testbed described and analysed in chapter 3. The system is highly configurable in the mechanical and optical components setup which makes it suitable for its use in different telescopes. The AO system is based in off-the-shelf components, portable with an overall weight around 10 kg, and low cost with an estimated cost in materials around 23900 AUD (a detailed budged is shown in appendix A.5). This estimated cost includes the DM, the MLA and the science camera. DM is by far the most expensive component, but currently new models can be found in the market with better features and lower cost than the one used in this thesis. In the future the current DM will be substituted by the Thorlabs DMP40-PO1 with a cost of 5390 AUD, and in that case the cost of the AO system will be 12611 AUD. This is possible because the microlenses array is overspecified, and we can easily exchange the deformable mirror.

The AO system is built in a modular fashion, in order to have possibilities the interchange parts of the system that could experiment a great development in the future. Also this modularity permits us to identify parts of the system that can be enhanced.

Regarding the AO control, this is fully implemented in a low cost standalone FPGA, a Xilinx Spartan XC3S3400A, with only a support computer as an interface with the user. The sensing control code can be easily exported to higher performance Xilinx FPGAs as it is based in VHDL language, which as a high level abstraction paradigm makes the control algorithm independent of the physical device. With the current clock rate of 50 MHz, the latency of the control algorithm is below 2µs, but this can be improved with higher clock rates or faster FPGAs. The additional sensing process is of course function of the capture time, and it will affect loop performance, as well as the dynamic response of the deformable mirror. For instance, experimental results of the star Rigel showed in chapter 5 have an image sensor integration time of 18 ms, which is several orders of magnitude higher than the latency of the control algorithm.

The FPGA architecture is aimed towards the use of digital signal processing algorithms, which facilitates the use of pipeline and parallel structures, which definitely contributes to an improvement in the performance of the system, related with the resolutions of the wavefront sensor, the size of the deformable mirror used and the hardware resources used by the system.

One of the problems associated to small aperture telescopes is the low photon flux that reaches the WFS. For that purpose, different centroiding algorithms were implemented and tested in the control stage, some of them standard approaches (as the CoG or the TCoG), but also novel approaches were evaluated, as one based in Fourier decomposition. This algorithm has been applied before implemented in a CPU as the hardware platform, but in this thesis as a novelty a low latency algorithm implemented in FPGA based in Fourier decomposition, named 1FC, has been accomplished. In the comparative analysis performed in chapter 5, the 1FC algorithm shows similar performance to the standard optimized TCoG, but 1FC is better suited for the telescopes where this AO system is intended to be used, a NGS AO system, with strong variability in the astronomical references found in these kind of systems.

A real-time software platform in MATLAB installed in a support computer was developed. The tasks performed in this software platform are among others: Configuration of the AO closed loop algorithm; Visualization of (i) frame snapshots from the WFS; (ii) Real-time gradients between centroids compared to a reference stored in FPGA memory; (iii) Real-time Zernike coefficients corresponding to the calculated gradients of the current frame; (iv) Actuator voltages to apply to the deformable mirror through the computation of the Zernike coefficients, and (v) the influence functions of each of the actuators. In addition the software provides a logging function to store the previous real-time data in local memory of the support computer, in order to their subsequent debugging and analysis. Finally it controls all parameters of SH WFS.

The design of each of the main technologies on which this AO system is based; opto-mechanical design, control implementation and centroiding algorithms are supported by the analysis of their critical parts in the corresponding chapter, as ZEMAX simulation of the optical setup including the performance in the WFS sensor and in the science camera, the influence of fixed point precision in the control algorithm instead floating point precision, and the accuracy of the wavefront conjugated shapes in the deformable mirror.

The AO system was installed in a 16" Meade LX200ACF telescope for most of the experimentation stage, but also was tested in a professional telescope, the 1 metre McLellan telescope, sited in Mt. John Observatory in New Zealand. As a result of the experimentation stage, both in laboratory and on-sky, performance results of different stages of the process are shown in chapter 5. However it should be emphasized the significant contribution herein is in the engineering repeatability, and these on-sky results are simply the indication of the success of this engineering.

6.2 Future Research

The research accomplished in this thesis establishes a first step in the development of a full AO system that has a potential impact for its use for the amateur and scientific astronomy community. Some parts of the system are susceptible to improvements, and also supplementary systems can be included in order to ease the operation or to enhance the performance. The improvements themselves will provide for novel science and engineering research:

- The influence of the dynamic performance of the deformable mirror actuators needs to be addressed more rigorously, in order to characterise the delays introduced by its operation.
- It is planned to include a tip-tilt stage mirror, that will improve the performance of the existing deformable mirror, as it will be only dedicated exclusively to correct higher order aberrations. Very recent products in this

area include the Thorlabs DMP40-P01 DM, with integrated tip-tilt stage, meaning that the system as a whole doesn't need redesigning.

- Different CMOS image sensors have to be tested, and also more intensification or high quantum efficiency sensors can be incorporated, in order to improve their pixels readout speed and performance of the AO system.
- A way to get a better alignment of the optical components of the system needs to be addressed, as the unit is portable and misalignment must be quickly corrected each observation. This could be obtained with an optical fiber situated in the image plane of the telescope, and it will reduce the time that the AO systems needs to be calibrated and in operation.
- It is planned to add a feedback of the actuators positions of the deformable mirror. This way signals from the actual positions of the actuators obtained by non-optical methods can be applied to the AO control module, but this enhancement is not yet implemented in this prototype. Such capability is needed for MOAO research.
- As a testbed the WFS can be removed and alternative types of WFS can be tested inmediately on-sky.
- It is planned to evaluate the size of the isoplanatic patch which will limit the field of view angle where the image can be corrected with the AO system.

Bibliography

[1] Robin Arsenault, Jaime Alonso, Henri Bonnet, Joar Brynnel, Bernard Delabre, Robert Donaldson, Christophe Dupuy, Enrico Fedrigo, Jacopo Farinato, Norbert N. Hubin, L. Ivanescu, Markus E. Kasper, J. Paufique, S. Rossi, Sebastien Tordo, Stefan Stroebele, Jean-Luis Lizon, Pierre Gigan, Francoise Delplancke, A. Silber, Marco Quattri, and Roland Reiss. Macao-vlti: an adaptive optics system for the eso interferometer. In *Proc. SPIE*, volume 4839, pages 174–185, 2003.

[2] Vanessa P. Bailey, Philip M. Hinz, Alfio T. Puglisi, Simone Esposito, Vidhya Vaitheeswaran, Andrew J. Skemer, Denis Defrère, Amali Vaz, and Jarron M. Leisenring. Large binocular telescope interferometer adaptive optics: on-sky performance and lessons learned. In *Proc. SPIE*, volume 9148, pages 914803–914803–11, 2014.

[3] Christoph Baranec, Reed Riddle, Nicholas M. Law, Mark R. Chun, Jessica R. Lu, Michael S. Connelley, Donald Hall, Dani Atkinson, and Shane Jacobson. Second generation robo-ao instruments and systems. In *Proc. SPIE*, volume 9148, pages 914812–914812–11, 2014.

[4] Alastair Basden, Deli Geng, Richard Myers, and Eddy Younger. Durham adaptive optics real-time controller. *Appl. Opt.*, 49(32):6354–6363, Nov 2010.

[5] Jacques M. Beckers. Adaptive optics for astronomy: Principles, performance, and applications. *Annual Review of Astronomy and Astrophysics*, 31(1):13–62, 1993.

[6] Max Born and Emil Wolf. *Principles of Optics*. Pergamon Press, 5th edition, 1975.

[7] Antonin H. Bouchez, D. S. Acton, Roberto Biasi, Rodolphe Conan, Brady Espeland, Simone Esposito, Jose M. Filgueira, Daniele Gallieni, Brian A. McLeod, Enrico Pinna, Fernando Santoro, Gelys Trancho, and Marcos A. van Dam. The giant magellan telescope adaptive optics program. In *Proc. SPIE*, volume 9148, pages 91480W–91480W–19, 2014.

[8] C. Boyer, Sean Adkins, David R. Andersen, Jenny Atwood, Yong Bo, Peter Byrnes, Kris Caputa, Jeff Cavaco, Brent Ellerbroek, Luc Gilles, James Gregory, Glen Herriot, Paul Hickson, Zoran Ljusic, Darren Manter, Christian Marois, Angel Otárola, Hubert Pagès, Matthias Schoeck, Jean-Christophe Sinquin, Malcolm Smith, Paolo Spano, Kei Szeto, Jinlong Tang, Tony Travouillon, Jean-Pierre Véran, Lianqi Wang, and Kai Wei. Adaptive optics program at tmt. In *Proc. SPIE*, volume 9148, pages 91480X–91480X–15, 2014.

[9] James B. Breckinridge. *Basic Optics for the Astronomical Sciences*. SPIE Press, Bellingham, Washington, 2012.

[10] Rick S. Burruss, Richard G. Dekany, Jennifer E. Roberts, J. C. Shelton, J. K. Wallace, Jonathan A. Tesch, Dean L. Palmer, David Hale, Randall Bartos, Kevin M. Rykoski, Carolyn M. Heffner, Jamey E. Eriksen, and Fred Vescelus. Status of the palm-3000 high order adaptive optics instrument. In *Proc. SPIE*, volume 9148, pages 914827–914827–8, 2014.

[11] Jesús Aceituno Castro. *Prototipo de un sistema de óptica adaptativa basado en un espejo deformable de membrana para aplicación astronómica*. PhD thesis, Universidad de Granada, 2009.

[12] Yann Clénet, Tristan M. Buey, Gérard Rousset, Mathieu Cohen, Philippe Feautrier, Eric Gendron, Zoltan Hubert, Fanny Chemla, Damien Gratadour, Pierre Baudoz, Sylvestre Lacour, Anthony Boccaletti, Arnaud Sevin, Fabrice Vidal, Raphaël Galicher, Denis Perret, Bertrand Le Ruyet, Frédéric Chapron, Eric Stadler, Patrick Rabou, Laurent Jocou, Sylvain Rochat, Gaël Chauvin, and Richard Davies. Overview of the micado scao system. In *Proc. SPIE*, volume 9148, pages 91480Z–91480Z–14, 2014.

[13] Ronald Cubalchini. Modal wave-front estimation from phase derivative measurements. *J. Opt. Soc. Am.*, 69(7):972–977, Jul 1979.

[14] Marcos A. Van Dam, Antonin H. Bouchez, David Le Mignant, Erik M. Johansson, Peter L. Wizinowich, Randy D. Campbell, Jason C. Y. Chin, Scott K. Hartman, Robert E. Lafon, Paul J. Stomski Jr., and Douglas M. Summers. The

w. m. keck observatory laser guide star adaptive optics system: Performance characterization. *Astronomical Society of the Pacific*, 2006.

[15] W.R. Dawes. Catalogue of micrometrical measurements of double stars. *Memoirs of the Royal Astronomical Society*, 35:137–502, 1867.

[16] Emiliano Diolaiti, Carmelo Arcidiacono, Giovanni Bregoli, Reginald Christopher Butler, Matteo Lombini, Laura Schreiber, Andrea Baruffolo, Alastair Basden, Michele Bellazzini, Enrico Cascone, Paolo Ciliegi, Fausto Cortecchia, Giuseppe Cosentino, Vincenzo De Caprio, Adriano De Rosa, Nigel Dipper, Simone Esposito, Italo Foppiani, Enrico Giro, Gianluca Morgante, Richard Myers, Fabien Patru, Roberto Ragazzoni, Armando Riccardi, Marco Riva, Filippo Maria Zerbi, Mark Casali, Bernard Delabre, Norbert Hubin, Florian Kerber, Miska Le Louarn, Enrico Marchetti, Suzanne Ramsay, Stefan Stroebele, and Elise Vernet. Preparing for the phase b of the e-elt mcao module project. In *Proc. SPIE*, volume 9148, pages 91480Y–91480Y–8, 2014.

[17] José Javier Díaz-García, Alberto Dávila-González, Luis-Fernando Rodríguez-Ramos, José-Manuel Rodríguez-Ramos, Yolanda Martín-Hernando, and Juan-José Piqueras-Meseguer. Performance of a modal zone wavefront recovery algorithm (hudgin) implemented on fpgas for its use in elts. In *Proc. SPIE*, volume 7439, pages 74390K–74390K–11, 2009.

[18] Donald Fraser, Andrew J. Lambert, and M. Reza Sayyah Jahromi. Position-varying tip-tilt estimation and region-of-interest psf derivation by wiener filter. In *Proc. SPIE*, volume 5562, pages 50–57, 2004.

[19] Donald Fraser, Andrew J. Lambert, M. Reza Sayyah Jahromi, David Clyde, and Nikila Donaldson. Can broad-band image restoration rival speckle restoration? In *Proc. SPIE*, volume 4792, pages 185–192, 2002.

[20] David L. Fried. Post-detection wavefront distortion compensation. In *Proc. SPIE*, volume 0828, pages 127–133, 1988.

[21] Naofumi Fujishiro, Eiji Kitao, Tomo Shimizu, Takuya Matsui, Yuji Ikeda, Hideyo Kawakita, and Shin Oya. Crao: a compact and refractive adaptive-optics. In *Proc. SPIE*, volume 9148, pages 91485W–91485W–10, 2014.

[22] T. Fusco, S. Thomas, M. Nicolle, A. Tokovinin, V. Michau, and G. Rousset. Optimization of center of gravity algorithms in a shack-hartmann sensor. In *Proc. SPIE*, volume 6272, pages 627219–627219–11, 2006.

[23] Eric Gendron, Jean Gabriel Cuby, Francois J. Rigaut, Pierre J. Lena, Jean-Claude Fontanella, Gerard Rousset, Jean-Paul Gaffard, Corinne Boyer, Jean-Claude Richard, M. Vittot, Fritz Merkle, and Norbert N. Hubin. Come-on-plus project: an upgrade of the come-on adaptive optics prototype system. In *Proc. SPIE*, volume 1542, pages 297–307, 1991.

[24] S. J. Goodsell, N. A. Dipper, D. Geng, R. M. Myers, and C. D. Saunter. Darts: a low-cost high-performance fpga implemented real-time control platform for adaptive optics. In *Proc. SPIE*, volume 5903, pages 59030E–59030E–9, 2005.

[25] Darryl P. Greenwood. Bandwidth specification for adaptive optics systems. *J. Opt. Soc. Am.*, 67(3):390–393, Mar 1977.

[26] Olivier Guyon, Yutaka Hayano, Motohide Tamura, Tomoyuki Kudo, Shin Oya, Yosuke Minowa, Olivier Lai, Nemanja Jovanovic, Naruhisa Takato, Jeremy Kasdin, Tyler Groff, Masahiko Hayashi, Nobuo Arimoto, Hideki Takami, Colin Bradley, Hajime Sugai, Guy Perrin, Peter Tuthill, and Ben Mazin. Adaptive optics at the subaru telescope: current capabilities and development. In *Proc. SPIE*, volume 9148, pages 91481R–91481R–10, 2014.

[27] Dani Guzmán, Andrés Guesalaga, Richard Myers, Ray Sharples, Tim Morris, Alastair Basden, Christopher Saunter, Nigel Dipper, Laura Young, Luis Rodríguez, Marcos Reyes, and Yolanda Martin. Deformable mirror controller for open-loop adaptive optics. In *Proc. SPIE*, volume 7015, pages 70153X–70153X–12, 2008.

[28] John W. Hardy. *Adaptive Optics for Astronomical Telescopes*. Oxford University Press, 1998.

[29] G.J. Hovey, R. Conan, F. Gamache, G. Herriot, Z. Ljusic, D. Quinn, M. Smith, J.P. Veran, and H. Zhang. An fpga based computing platform for adaptive optics control. In Array, editor, *1st AO4ELT conference - Adaptive Optics for Extremely Large Telescopes*, page 07006, 2010.

[30] Liviu Ivanescu, Rene Racine, and Daniel Nadeau. A simplified adaptive optics system. In *Proc. SPIE*, volume 4839, pages 99–106, 2003.

[31] K. Kepa, D. Coburn, J. C. Dainty, and F. Morgan. High speed optical wavefront sensing with low cost fpgas. *Measurement Science Review*, 8:87–93, 2008.

[32] G. Küveler, E. Wiehr, D. Thomas, M. Harzer, M. Bianda, A. Epple, P. Sütterlin, and E. Weisshaar. Automatic guiding of the primary image of solar gregory telescopes. *Solar Physics*, 182(1):247–255, 1998.

[33] Olivier Lai, Jean-Pierre Véran, Glen Herriot, John White, Jesse Ball, and Chad Trujillo. Altair performance and upgrades. In *Proc. SPIE*, volume 9148, pages 914838–914838–13, 2014.

[34] Andrew Lambert, Benjamin J. Birt, David A. Atchison, and Huanqing Guo. Applying slodar to measure aberrations in the eye. *Opt. Express*, 16(10):7309–7322, May 2008.

[35] Andrew J. Lambert, James Webb, and Donald Fraser. Fast intelligent image sensor with application to image restoration. In *Proc. SPIE*, volume 4796, pages 246–254, 2003.

[36] Mikhail Loktev, Gleb Vdovin, and Oleg Soloviev. Integrated adaptive optics system for small telescopes. In *Proc. SPIE*, volume 7015, pages 70153K–70153K–7, 2008.

[37] Ruth Mackey, Mingzhou Chen, Andrew Lambert, David Mackey, and Alexander Goncharov. Study of turbulence effects for a free-space optical link over water. In *Proc. SPIE*, volume 7828, pages 782808–782808–12, 2010.

[38] Justin D. Mansell, Brian Henderson, Brennen Wiesner, Robert Praus, and Steve Coy. A low-cost compact metric adaptive optics system. In *Proc. SPIE*, volume 6711, pages 67110K–67110K–11, 2007.

[39] José G. Marichal-Hernández, Luis F. Rodríguez-Ramos, Fernando Rosa, and José M. Rodríguez-Ramos. Atmospheric wavefront phase recovery by use of specialized hardware: graphical processing units and field-programmable gate arrays. *Appl. Opt.*, 44(35):7587–7594, Dec 2005.

[40] Yolanda Martín-Hernando, Luis F. Rodríguez-Ramos, and Marcos R. Garcia-Talavera. Fixed-point vs. floating-point arithmetic comparison for adaptive optics real-time control computation. In *Proc. SPIE*, volume 7015, pages 70152Z–70152Z–12, 2008.

[41] André Maréchal. *Rev. d'Optique*, 26(257), 1947.

[42] Clive Maxfield. *The Design Warrior's Guide to FPGA*. Elsevier, 2004.

[43] Rosalie McGurk, Constance Rockosi, Donald Gavel, Renate Kupke, Michael Peck, Terry Pfister, Jim Ward, William Deich, John Gates, Elinor Gates, Barry Alcott, David Cowley, Daren Dillon, Kyle Lanclos, Dale Sandford, Mike Saylor, Srikar Srinath, Jason Weiss, and Andrew Norton. Commissioning sharcs: the shane adaptive optics infrared camera-spectrograph for the lick observatory shane 3-m telescope. In *Proc. SPIE*, volume 9148, pages 91483A–91483A–9, 2014.

[44] Byron Welsh Michael C. Roggemann. *Imaging through turbulence*. CRC Press LLC, 1996.

[45] Tim Morris, Eric Gendron, Alastair Basden, Olivier Martin, James Osborn, David Henry, Zoltan Hubert, Gaetano Sivo, Damien Gratadour, Fanny Chemla, Arnaud Sevin, Matthieu Cohen, Eddy Younger, Fabrice Vidal, Richard Wilson, Tim Butterley, Urban Bitenc, Andrew Reeves, Nazim Bharmal, Henri-François Raynaud, Caroline Kulcsar, Jean-Marc Conan, Jean-Michel Huet, Denis Perret, Colin Dickson, David Atkinson, Tom Bailie, Andy Longmore, Stephen Todd, Gordon Talbot, Simon Morris, Gérard Rousset, and Richard Myers. Canary phase b: on-sky open-loop tomographic lgs ao results. In *Proc. SPIE*, volume 9148, pages 91481I–91481I–12, 2014.

[46] Peter Nisenson and Richard Barakat. Partial atmospheric correction with adaptive optics. *J. Opt. Soc. Am. A*, 4(12):2249–2253, Dec 1987.

[47] Robert J. Noll. Zernike polynomials and atmospheric turbulence. *J. Opt. Soc. Am.*, 66(3):207–211, Mar 1976.

[48] Carl Paterson, Ian H. Munro, and Christopher Dainty. Low-cost adaptive optics systems. In *Proc. SPIE*, volume 4007, pages 185–193, 2000.

[49] Xiaofeng Peng, Mei Li, and ChangHui Rao. Architecture design of a fpga-based wavefront processor for correlating a shack-hartmann sensor. In *Proc. SPIE*, volume 7156, pages 71561B–71561B–8, 2008.

[50] K. Powell. Mmt ao performance: Analysis and status. Technical report, Smithsonian Institution and The Unversity of Arizona, 2012.

[51] Roberto Ragazzoni. Pupil plane wavefront sensing with an oscillating prism. *Journal of Modern Optics*, 43(2):289–293, 1996.

[52] Deqing Ren, Rong Li, Xi Zhang, Jiangpei Dou, Yiangtian Zhu, Gang Zhao, Zhen Wu, Rui Chen, Chengchao Liu, Feng Yang, and Chao Yang. The first

portable solar and stellar adaptive optics. In *Proc. SPIE*, volume 9148, pages 91482W–91482W–7, 2014.

[53] F. Roddier. The effects of atmospheric turbulence in optical astronomy. *Progress in optics. Volume 19. Amsterdam, North-Holland Publishing Co., 1981, p. 281-376.*, 19:281–376, 1981.

[54] Francois Roddier. Curvature sensing and compensation: a new concept in adaptive optics. *Appl. Opt.*, 27(7):1223–1225, Apr 1988.

[55] Luis F. Rodriguez-Ramos, Teodora Viera, Jose V. Gigante, Fernando Gago, Guillermo Herrera, Angel Alonso, and Nicolas Descharmes. Fpga adaptive optics system test bench. In *Proc. SPIE*, volume 5903, pages 59030D–59030D–9, 2005.

[56] L. F. Rodríguez Ramos, J. J. Díaz Garcia, J. J. Piqueras Meseguer, Y. Martin Hernando, and J. M. Rodríguez Ramos. Fpga-based slope computation for elts adaptive optics wavefront sensors. In *Proc. SPIE*, volume 7015, pages 701530–701530–11, 2008.

[57] Luis F. Rodríguez-Ramos, Teodora Viera, Guillermo Herrera, José V. Gigante, Fernando Gago, and Ángel Alonso. Testing fpgas for real-time control of adaptive optics in giant telescopes. In *Proc. SPIE*, volume 6272, pages 62723X–62723X–10, 2006.

[58] Jean-Jacques Roland, Jean-Paul Gaffard, Pascal Jagourel, Corinne Boyer, and Patrick Gosselin. Adaptive optics: a general purpose system for astronomy. In *Proc. SPIE*, volume 2201, pages 58–76, 1994.

[59] Gerard Rousset, Francois Lacombe, Pascal Puget, Eric Gendron, Robin Arsenault, Pierre Y. Kern, Didier Rabaud, Pierre-Yves Madec, Norbert N. Hubin, Gerard Zins, Eric Stadler, Julien Charton, Pierre Gigan, and Philippe Feautrier. Status of the vlt nasmyth adaptive optics system (naos). In *Proc. SPIE*, volume 4007, pages 72–81, 2000.

[60] Jean-Marc Ruggiu and Christopher J. Solomon. Improved technique for centroiding in shack-hartmann sensing at low light level. In *Proc. SPIE*, volume 3126, pages 545–550, 1997.

[61] C. D. Saunter and G. D. Love. Low-cost high-speed control for adaptive optics. In *Proc. SPIE*, volume 6711, pages 671107–671107–7, 2007.

[62] C. D. Saunter, G. D. Love, M. Johns, and J. Holmes. Fpga technology for high-speed low-cost adaptive optics. In *Proc. SPIE*, volume 6018, pages 60181G–60181G–7, 2005.

[63] Armin Schimpf, Mickael Micallef, and Julien Charton. 1500hz adaptive optics system using commercially available components. In *Proc. SPIE*, volume 9148, pages 914851–914851–8, 2014.

[64] Scott A. Severson, Philip I. Choi, Katherine E. Badham, Dalton Bolger, Daniel S. Contreras, Blaine N. Gilbreth, Christian Guerrero, Erik Littleton, Joseph Long, Lorcan P. McGonigle, William A. Morrison, Fernando Ortega, Alex R. Rudy, Jonathan R. Wong, Erik Spjut, Christoph Baranec, and Reed Riddle. Kapao first light: the design, construction and operation of a low-cost natural guide star adaptive optics system. In *Proc. SPIE*, pages 914839–914839–13, 2014.

[65] J. C. Shelton and Sallie L. Baliunas. Results of adaptive optics at mt. wilson obseratory. In *Proc. SPIE*, volume 1920, pages 371–380, 1993.

[66] Ronald C. Stone. A comparison of digital centering algorithms. *The Astronomical Journal*, 97(4):1227–1237, April 1989.

[67] Scott W. Teare, Ty Martinez, Jonathan R. Andrews, Christopher C. Wilcox, Sergio R. Restaino, Robert Romeo, Robert Martin, and Don M. Payne. A lightweight adaptive telescope. In *Proc. SPIE*, volume 6306, pages 630609–630609–8, 2006.

[68] David Terrier. Fpga based wavefront sensing for adaptive optics. Technical report, The University of New South Wales Canberra, 2007.

[69] Paolo Turri, Alan W. McConnachie, Peter B. Stetson, Giuliana Fiorentino, David R. Andersen, Giuseppe Bono, and Jean-Pierre Véran. Photometric performance of lgs mcao with science-based metrics: first results from gemini/gems observations of galactic globular clusters. In *Proc. SPIE*, volume 9148, pages 91483V–91483V–15, 2014.

[70] Robert K. Tyson. *Introduction to Adaptive Optics*. SPIE Press, 2000.

[71] Johannes Visser. Fpga based adaptive optics system. Technical report, The University of New South Wales Canberra, 2008.

[72] Jack E. Volder. The cordic trigonometric computing technique. *Electronic Computers, IRE Transactions on*, EC-8(3):330–334, Sept 1959.

[73] Caixia Wang, Mei Li, Chunhong Wang, Luchun Zhou, and Wenhan Jiang. Real-time implementing wavefront reconstruction for adaptive optics. In *proc. SPIE*, volume 5639, pages 199–204, 2004.

[74] Eckhard Weißhaar, Gerd Küveler, and Michele Bianda. Schnelle und genaue methode zur schwerpunktfindung in messreihen. *Photonik*, pages 46–48, March 2003.

[75] Zhiying Wen, Donald Fraser, and Andrew Lambert. Restoration of atmospherically degraded images using a sparse prior. In *Proc. SPIE*, volume 7073, pages 70731P–70731P–8, 2008.

[76] Allan Wirth, Joseph Navetta, Douglas Looze, Stefan Hippler, Andreas Glindemann, and Donald Hamilton. Real-time modal control implementation for adaptive optics. *Appl. Opt.*, 37(21):4586–4597, Jul 1998.

[77] Xilinx. System generator user guide. Technical report, Xilinx, 2012.

Appendices

A.1 Real time control software

In this section a detailed study of the MATLAB Real-Time interface with the AO system running in the support computer is shown. The whole interface is shown in figure A.1, and then the operation of each of the modules is explained.

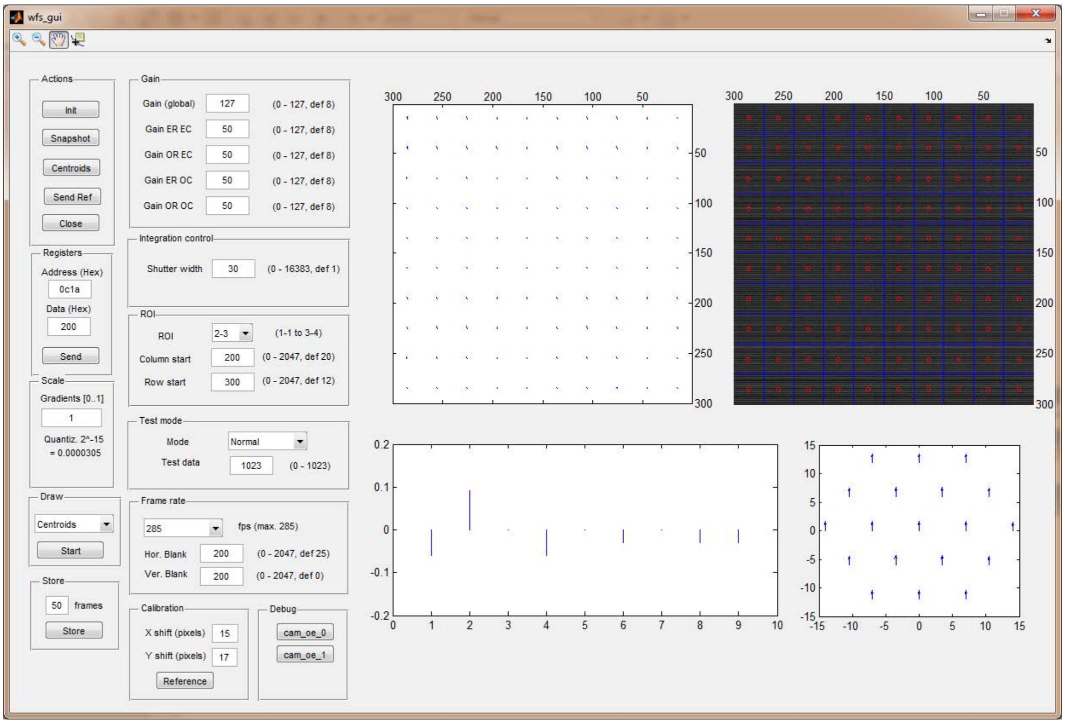

Figure A.1: MATLAB Real-Time interface of AO system.

A.1.1 Actions module

In this module the following actions can be performed:

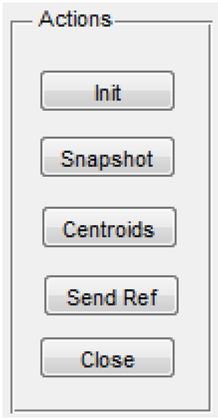

Figure A.2: Actions

Init: Initiate the AO system, deleting the communications buffers content, and reset the system with the default parameters.

Snapshot: Take a snapshot image in the SH WFS and send it to the interface display. This is used when a visual image of the reference centroids is needed, in order to align them with the subapertures grid.

Centroids: Offline computation of centroids positions of current snapshot image. When the operation is finished, the reference centroids positions are indicated with red circles, one circle per subaperture.

Send Ref: Send the reference centroids positions calculated previously with **Centroids** to the RAM_c memory of the FPGA, and also the new calibration matrix calculated offline to RAM_R.

Close: Close appropriately the AO system user interface, removing data from buffers and closing serial communications.

A.1.2 WFS parameters

This module is used to modify the parameters of the CMOS image sensor of the WFS.

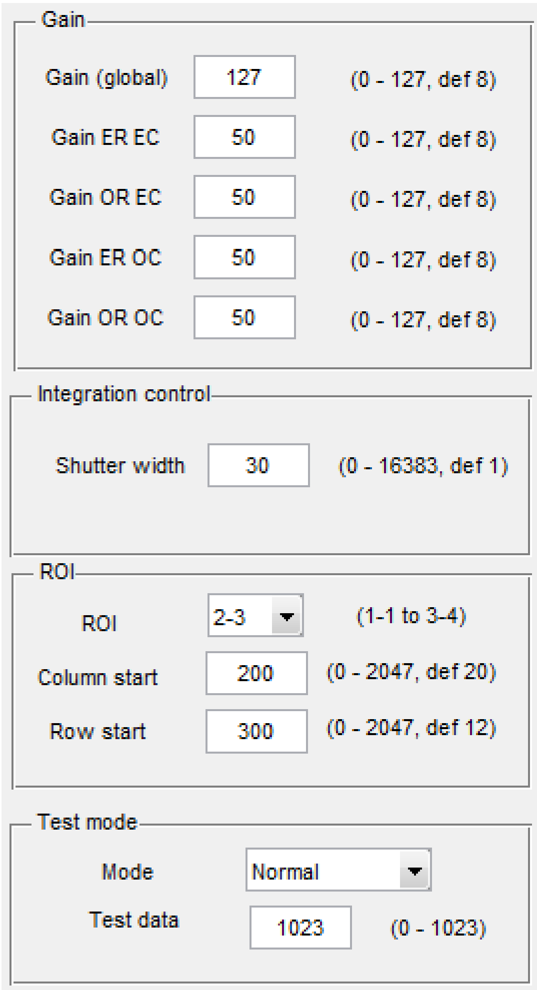

Figure A.3: WFS parameters.

Gain: In the Gain section is where the absolute gain of the CMOS image sensor is modified. The gain can be modified globally, with the same value for each active pixel, or can be modified by particular rows or columns, in the following modes:

- ER EC: Even Row, Even Column.
- OR EC: Odd Row, Even Column.
- ER OC: Even Row, Odd Column.
- OR OC: Odd Row, Odd Column.

The gain resolution is 7 bits, hence possible values range from 0 to 127.

Integration control: The integration time (Shutter width) of the CMOS sensor can be modified with this parameter, choosing certain number of rows, that typically is limited to number of rows per frame.

ROI (Region of Interest): The frame is divided in 12 regions of interest of equal size, to ease the location of the centroids. After locating the centroids, a fine tuning to align the reference centroids with the subapertures can be performed through parameters **Column start** and **Row start**.

Test mode: The operation mode can be set to **Normal** (images are acquired in the CMOS image sensor) or **Test** (to perform a test in the camera previous to the acquisition of images), to check that the camera is properly calibrated. In the test data field can be entered any value between 0 and 1023, and a pattern of columns will be generated in the CMOS sensor, with this value in even rows, and the inverse for odd columns.

A.1.3 Registers

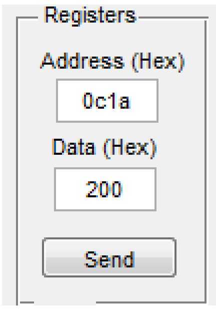

Figure A.4: Registers.

Most important parameters of the WFS can be selected in the previous section **WFS parameters**, but sometimes a more precise adjustment of the CMOS sensor is needed, and extra parameters can be modified in a one by one basis in this section, where the address and data of particular registers are introduced and sent to the sensor through the FPGA.

A.1.4 Draw and store

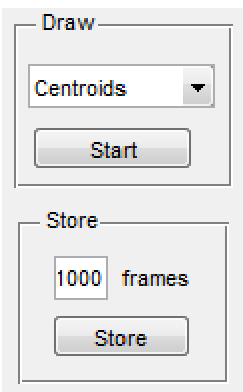

Figure A.5: Draw and store.

In this area real time video streaming of gradients, Zernike coefficients or actuator voltages is selected, and it will be shown in the corresponding areas in the right part of the display. In the store section is selected the number of data frames (gradients, Zernike coefficients and actuator voltages) to be store in MATLAB workspace.

A.1.5 Scale

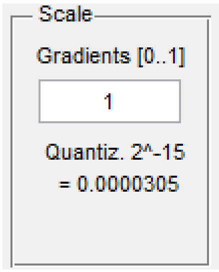

Figure A.6: Scale.

Here the gain of the AO system is selected, which is done through a value between 0 and 1 sent to RAM_G of the FPGA, where the gradients in axes x and y are multiplied by this value.

A.1.6 Frame rate

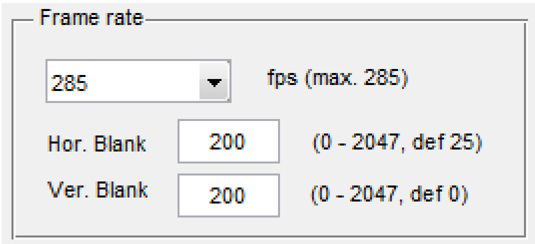

Figure A.7: Frame rate.

Frame rate is introduced in this field. Also horizontal and vertical blanking of the CMOS image sensor are introduced here, as these parameters influence the synchronization and frame rate of the system.

A.1.7 Calibration and debug

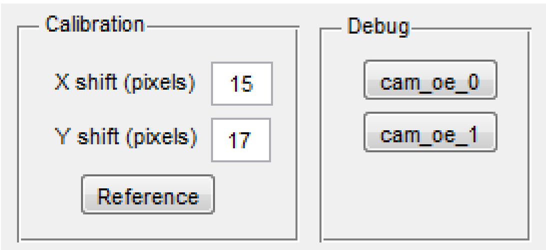

Figure A.8: Calibration and debug.

To test the different behaviour of the AO system with different reference images of centroids, in **X shift** and **Y shift** fields a number of pixels can be introduced (corresponding to a 30 x 30 pixels aperture), to generate different references centroids and send them to RAM_c of the FPGA. Also video streaming of the CMOS image sensor can be paused or resume in the **Debug** section.

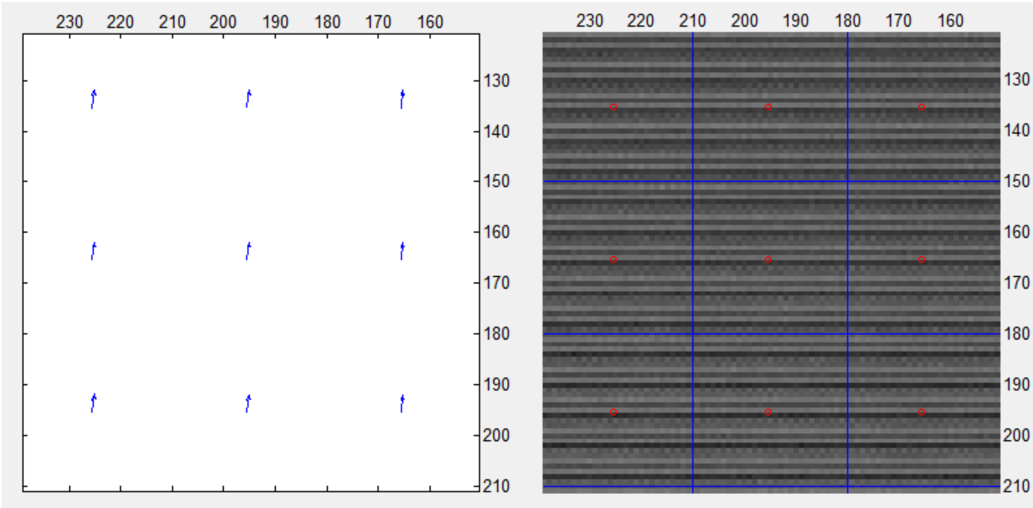

Figure A.9: Zoom in gradients and reference centroids in real time.

A.1.8 Gradients and reference centroids

Zoom can be applied to the display of gradients and frame snapshots. In left of figure A.9 is shown a zoom over the centroids gradients display. These gradients are represented through arrows with module proportional the gradient value. In the right part of the figure is shown the last frame snapshot of the CMOS image sensor, used to align correctly the centroids with the subapertures in the WFS.

A.2 Optical design ZEMAX table

In figure A.10 is shown the table with the values of the different lenses and mirror of the optical system introduced in ZEMAX software, to simulate the AO optical path. In column **Surf:type** is where the type of optical surface is declared (mirror, lens or microlens). The **Radius** column indicate the curvature radio of surfaces, being Infinity for flat surfaces, as the steering mirrors. In **Glass** column is shown the type of glass or mirror of any of the surfaces.

A.3 Tracking control module

The tracking control of the right ascension and declination axes of the telescope is an important part in the auxiliary systems of telescopes in general, and in particular for AO systems. It's important to have the more accurate possible tracking system,

Figure A.10: Tabular optical data introduced in ZEMAX to simulate the optical system.

Surf	Type	Comment	Radius	Thickness	Glass	Semi-Diameter	Conic	Par 0(unused)	Par 1(unused)	Par 2(unused)	Par 3(unused)	Par 4(unused)
OBJ	Standard		Infinity	Infinity		Infinity	0.000					
STO	Paraxial			3939.000		203.200 U			4064.000	0		
2	Coordinat..			0.000	-	0.000			0.000	0.000	-45.000	0.000
3	Standard		Infinity	0.000	MIRROR	18.484	0.000					
4	Coordinat..			-162.000	-	0.000			0.000	0.000	-45.000 P	0.000
5	Coordinat..			0.000	-	0.000			0.000	0.000	45.000	0.000
6	Standard		Infinity	0.000	MIRROR	11.151	0.000					
7	Coordinat..			100.000	-	0.000			0.000	0.000	45.000 P	0.000
8	Coordinat..			0.000	-	0.000			0.000	0.000	45.000	0.000
9	Standard		Infinity	0.000	MIRROR	20.054	0.000					
10	Coordinat..			-55.500	-	0.000			0.000	0.000	45.000 P	0.000
11*	Standard	AC508-200-A1	-376.250	-2.000	SF2	25.400 U	0.000					
12*	Standard		-93.110	-8.500	N-BK7	25.400 U	0.000					
13*	Standard		109.860	-226.000		25.400 U	0.000					
14	Coordinat..			0.000	-	0.000			0.000	0.000	-45.000	0.000
15*	Standard	DM position	2.500E+004	0.000	MIRROR	15.000 U	0.000					
16	Coordinat..			79.000	-	0.000			0.000	0.000	-45.000 P	0.000
17	Coordinat..			0.000	-	0.000			0.000	0.000	-45.000	0.000
18	Standard		Infinity	0.000	MIRROR	18.964	0.000					
19	Coordinat..			-75.000	-	0.000			0.000	0.000	-45.000 P	0.000
20*	Standard	AC508-100-A-ML	-71.120	-16.000	N-BAF10	25.400 U	0.000					
21*	Standard		44.170	-4.000	SF10	25.400 U	0.000					
22*	Standard		363.100	-37.000		25.400 U	0.000					
23	Coordinat..			0.000	-	0.000			0.000	0.000	45.000	0.000
24	Standard		Infinity	0.000	MIRROR	11.984	0.000					
25	Coordinat..			79.700	-	0.000			0.000	0.000	45.000 P	0.000
26	Standard		Infinity	0.000		5.393	0.000					
27*	Standard	AC254-030-A-ML	20.890	12.000	N-BAF10	12.700 U	0.000					
28*	Standard		-16.730	2.000	N-SF6HT	12.700 U	0.000					
29*	Standard		-79.800	15.000		12.700 U	0.000					
30*	Even Array	MLA 1ST SURF	11.260	1.200	BK7	12.700 U	0.000		51.000	51.000	0.500	0.500
31*	Even Array	MLA 2SD SURF	Infinity	21.000		12.700 U	0.000		51.000	51.000	0.500	0.500
32	Standard		Infinity	100.000		5.318	0.000					
33*	Standard	AC508-100-A-ML	363.100	4.000	SF10	25.400 U	0.000					
34*	Standard		44.170	16.000	N-BAF10	25.400 U	0.000					
35*	Standard		-71.120	130.000		25.400 U	0.000					
36*	Standard	AC254-030-A-ML	20.890	12.000	N-BAF10	12.700 U	0.000					
37*	Standard		-16.730	2.000	N-SF6HT	12.700 U	0.000					
38*	Standard		-79.800	21.200		12.700 U	0.000					
IMA	Standard		Infinity	-		1.916	0.000					

and in this way, the correction performed with the AO system can be improved, as it doesn't need to correct this extra errors caused by a non perfect tracking of a sidereal object.

In figure A.11 is shown the hardware architecture for the tracking control used in the 16" Meade LX200ACF telescope used for the main experimentation of the AO system.

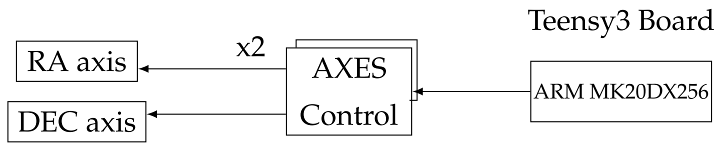

Figure A.11: Tracking telescope hardware setup.

The Teensy3 board communicates through a USB interface with the real-time control software in the support computer implemented in MATLAB. The two tracking boards (AXES Control) receive signals from the the Teensy3 board to move the motors of both axes of the telescope, right ascension and declination. The control can be adjusted up to a resolution of 16384 steps, and allows the telescope to track in a high range of velocities, from sidereal rate to fast satellites. This tracking system was designed and provided by my supervisor, and in figure A.12 is shown a picture of one the tracking boards.

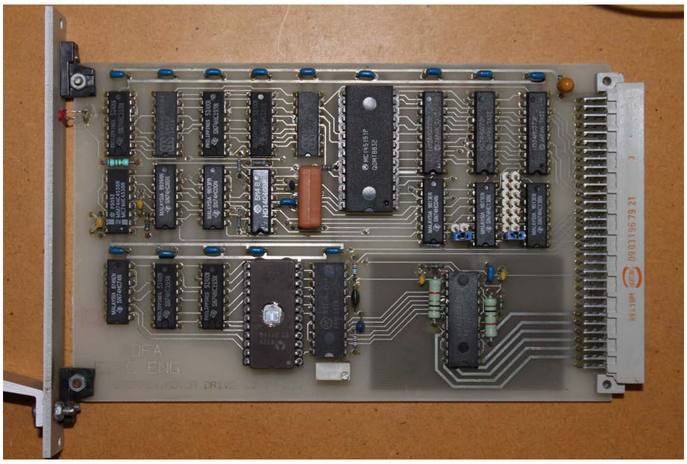

Figure A.12: Board to control tracking in one axis of the telescope.

A.4 Code to compare different centroiding algorithms (Python)

```
import cv2
import time
import csv
import matplotlib.pyplot as plt
import matplotlib.cm as cm
from matplotlib import mlab
from pylab import *
import numpy as np
from numpy import *
from scipy import optimize
from mpl_toolkits.mplot3d import Axes3D
import pdb
from scipy import stats

capture = cv2.VideoCapture('narrow.avi')
time.sleep(2)
frame_total = capture.get(cv2.cv.CV_CAP_PROP_FRAME_COUNT)

print 'Start processing video'

f = open('table.csv', 'wb')
c = csv.writer(f)
c.writerow(['#Temporal serie of centroids'])
c.writerow(['CoG_x','CoG_y','TCoG_x','TCoG_y','GFiT_x','GFiT_y','1sFC_x','1sFC_y'])

f_coord = open('../../Figures/Tables/narrow_frame_coord.csv', 'wb')
c_coord = csv.writer(f_coord)
c_coord.writerow(['#Frame with coordinates'])
c_coord.writerow(['Coord_x','Coord_y','Intensity'])
```

```
minVal=0
maxVal=0
Lx_raw = []
Ly_raw = []
Lx_th = []
Ly_th = []
Lx_gauss = []
Ly_gauss = []
Lx_fourier = []
Ly_fourier = []
j = 0
Pi = math.pi

def add_raw(i, momx, momy):
    size = len(Lx_raw)
    if i >= size:
Lx_raw.extend([None]*(i-size+1))
Ly_raw.extend([None]*(i-size+1))
Lx_raw[i] = momx
Ly_raw[i] = momy

def add_th(i, momx, momy):
    size = len(Lx_th)
    if i >= size:
Lx_th.extend([None]*(i-size+1))
Ly_th.extend([None]*(i-size+1))
Lx_th[i] = momx
Ly_th[i] = momy

def add_gauss(i, momx, momy):
    size = len(Lx_gauss)
    if i >= size:
Lx_gauss.extend([None]*(i-size+1))
Ly_gauss.extend([None]*(i-size+1))
Lx_gauss[i] = momx
Ly_gauss[i] = momy

def add_fourier(i, momx, momy):
    size = len(Lx_fourier)
    if i >= size:
Lx_fourier.extend([None]*(i-size+1))
Ly_fourier.extend([None]*(i-size+1))
Lx_fourier[i] = momx
Ly_fourier[i] = momy

def fitgaussian(data):
    params = moments(data)
    errorfunction = lambda p: ravel(gaussian(*p)(*indices(data.shape)) -
    data)
    p, success = optimize.leastsq(errorfunction, params)
    return p
```

```
def moments(data):
    total = data.sum()
    X, Y = indices(data.shape)
    x = (X*data).sum()/total
    y = (Y*data).sum()/total
    col = data[:, int(y)]
    width_x = sqrt(abs((arange(col.size)-y)**2*col).sum()/col.sum())
    row = data[int(x), :]
    width_y = sqrt(abs((arange(row.size)-x)**2*row).sum()/row.sum())
    height = data.max()
    return height, x, y, width_x, width_y

def gaussian(height, center_x, center_y, width_x, width_y):
    #pdb.set_trace()
    width_x = float(width_x)
    width_y = float(width_y)
    return lambda x,y: height*exp(
-(((center_x-x)/width_x)**2+((center_y-y)/width_y)**2)/2)

def process_frame(frame):

    # Calculate CoG
    frame_cog = frame
    flag, frame_cog = cv2.threshold(frame_cog, 10, 255, cv2.THRESH_TOZERO})

M_raw = cv2.moments(frame_cog,1)
add_raw(j-1, M_raw['m10']/M_raw['m00'], M_raw['m01']/M_raw['m00'])

# Calculate TCoG
frame_th = frame
flag, frame_th = cv2.threshold(frame_th, 20, 255, cv2.THRESH_TOZERO})

    M_th = cv2.moments(frame_th,1)
    add_th(j-1, M_th['m10']/M_th['m00'], M_th['m01']/M_th['m00'])

    # Calculate GFiT
    params = fitgaussian(frame)
    fit = gaussian(*params)(f_xx,f_yy)
    gauss_moments = moments(fit)
    add_gauss(j-1,gauss_moments[1], gauss_moments[2])

    # Calculate 1sFC
    a, b, c, d = 0, 0, 0, 0
    for l in range(1,f_height+1):
for k in range(1,f_width+1):
    a = a + COS_A[0,l]*frame[l-1,k-1]
    b = b + SIN_A[0,l]*frame[l-1,k-1]
    c = c + COS_B[0,k]*frame[l-1,k-1]
    d = d + SIN_B[0,k]*frame[l-1,k-1]
    if a > 0:
if b > 0:
    phi_row = 0
else:
```

```
    phi_row = 2*Pi
    else:
phi_row = Pi
    if c > 0:
if d > 0:
    phi_col = 0
else:
    phi_col = 2*Pi
    else:
phi_col = Pi

    Fourier_row = (math.atan(b/a) + phi_row)*(f_height-1)/2/Pi+1
    Fourier_col = (math.atan(d/c) + phi_col)*(f_width-1)/2/Pi+1
    add_fourier(j-1, Fourier_col, Fourier_row)

    print 'processing frame %0d' %frame_n

while True:

    flag1, frame = capture.read()
    frame_n = capture.get(cv2.cv.CV_CAP_PROP_POS_FRAMES)

    # flag is 0 when there is no more frames
    if flag1 == 0:
print 'frame is not ready'

    else:
j = j + 1
frame = cv2.cvtColor(frame, cv2.COLOR_BGR2GRAY)
frame_c = frame[0:59, 0:59]
frame_d = frame_c
frame = frame_d
min_val,max_val,min_loc,max_loc = cv2.minMaxLoc(frame)
print min_val, max_val

# Filtering
kernel = np.ones((5,5),np.float32)/25
dst = cv2.filter2D(frame,-1,kernel)
frame = dst

# Tasks to perform when the first frame arrives
if frame_n == 1:
    f_height = frame.shape[0]
    f_width = frame.shape[1]
    f_x = np.arange(1,f_width+1,1)
    f_y = np.arange(1,f_height+1,1)
    f_xx, f_yy = np.meshgrid(f_x,f_y)
    SIN_A = np.zeros(shape=(1,f_height+1))
    COS_A = np.zeros(shape=(1,f_height+1))
    SIN_B = np.zeros(shape=(1,f_width+1))
    COS_B = np.zeros(shape=(1,f_width+1))
```

```
    for l in range(1,f_height+1):
SIN_A[0,l] = sin((l-1)*2*Pi/(f_height-1))
COS_A[0,l] = cos((l-1)*2*Pi/(f_height-1))
    for k in range(1,f_width+1):
SIN_B[0,k] = sin((k-1)*2*Pi/(f_width-1))
COS_B[0,k] = cos((k-1)*2*Pi/(f_width-1))
    print frame_total, 'frames'

# Tasks to perform when frame n° x arrives
if frame_n == 20:

    # Shows 2d frame in matplotlib and save numpy array in csv file
    fig = plt.figure()
    ima = plt.imshow(frame, cmap = cm.Greys_r,vmin=0,vmax=255)
    fig.colorbar(ima)
    plt.axis('off')
    plt.savefig("frame.png",bbox_inches='tight')
    np.savetxt('../../Figures/Tables/dos_frame.csv', frame, delimiter=',')

    # Shows 3d frame in matplotlib
    fig = plt.figure()
    ax = fig.gca(projection='3d')
    ax.plot_wireframe(f_xx,f_yy,frame,rstride=20,cstride=1,cmap='hot')
    ax.set_zlim3d(0,255)
    plt.show()

# Processing in each frame
process_frame(frame)

# Finish processing when frame number = frame total
if frame_n == frame_total:
    # Convert vector? to numpy array
    Lxa_raw = np.array(Lx_raw)
    Lya_raw = np.array(Ly_raw)
    Lxa_th = np.array(Lx_th)
    Lya_th = np.array(Ly_th)
    Lxa_gauss = np.array(Lx_gauss)
    Lya_gauss = np.array(Ly_gauss)
    Lxa_fourier = np.array(Lx_fourier)
    Lya_fourier = np.array(Ly_fourier)

    # Perform detrend to remove continuous component
    # i.e. if telescope motors are not tracking properly
    Lxa_raw_dt = mlab.detrend_linear(Lxa_raw)
    Lya_raw_dt = mlab.detrend_linear(Lya_raw)
    Lxa_th_dt = mlab.detrend_linear(Lxa_th)
    Lya_th_dt = mlab.detrend_linear(Lya_th)
    Lxa_gauss_dt = mlab.detrend_linear(Lxa_gauss)
    Lya_gauss_dt = mlab.detrend_linear(Lya_gauss)
    Lxa_fourier_dt = mlab.detrend_linear(Lxa_fourier)
    Lya_fourier_dt = mlab.detrend_linear(Lya_fourier)
```

```
    # Calculate standard deviation
    print Lxa_raw_dt
    print std(Lxa_raw_dt-Lxa_gauss_dt)
    print std(Lxa_th_dt-Lxa_gauss_dt)
    print std(Lxa_fourier_dt-Lxa_gauss_dt)

    print std(Lya_raw_dt-Lya_gauss_dt)
    print std(Lya_th_dt-Lya_gauss_dt)
    print std(Lya_fourier_dt-Lya_gauss_dt)

    # Save temporal serie in csv file
    for k in range(len(Lx_raw)):
c.writerow(
[Lxa_raw_dt[k],Lya_raw_dt[k],Lxa_th_dt[k],Lya_th_dt[k],
Lxa_gauss_dt[k],Lya_gauss_dt[k],Lxa_fourier_dt[k],Lya_fourier_dt[k]])
    f.close()

    # Plots temporal serie in matplotlib
    fig = plt.figure()
    ax_x = fig.add_subplot(211)
    ax_x.plot(Lxa_raw_dt, label='X CoG') # blue
    ax_x.plot(Lxa_th_dt, label='X TCoG')  # green
    ax_x.plot(Lxa_gauss_dt, label='X GFiT') # red
    ax_x.plot(Lxa_fourier_dt, label='X 1sFC') # cyan
    ax_y = fig.add_subplot(212)
    ax_y.plot(Lya_raw_dt, label='Y CoG') # blue
    ax_y.plot(Lya_th_dt, label='Y TCoG')  # green
    ax_y.plot(Lya_gauss_dt, label='Y GFiT') # red
    ax_y.plot(Lya_fourier_dt, label='Y 1sFC') # cyan
    ax_x.legend(loc='best', prop={'size':8})
    ax_y.legend(loc='best', prop={'size':8})
    plt.show()
    print 'done'
    break
```

A.5 Budget of materials of the AO system

In table A.1 is shown the cost of materials of the developed AO system, excluding power supplies of the FPGA and the HV DM boards. The deformable mirror is by far the more expensive components of the AO system. If this is excluded from the budget, the cost would be 7221 AUD. In the last few years more and more deformable mirror models are manufactured with a lower cost. It is planned in the future to substitute the current deformable mirror by a cheaper one with similar features, that will reduce the total cost substantially.

Table A.1: AO system budget of materials (excluding power supplies and support computer).

Item	Part	qty	Vendor	Stock Nr.	Price (AUD)
Structure					
1	cube 60 mm	2	Thorlabs	LC6W	338
2	cube platform	1	Thorlabs	LB3C	58
3	cage plate 2"	5	Thorlabs	LCP01	238
4	cage plate 1"	3	Thorlabs	LCP02	146
5	rod 18"	4	Thorlabs	ER18	128
6	rod 10"	6	Thorlabs	ER10	96
7	rod 6"	10	Thorlabs	ER6	109
8	rod 1.5"	16	Thorlabs	ER1.5	117
9	spacer 60 mm	4	Thorlabs	ER90L	43
10	ERSCA	16	Thorlabs	ERSCA	221
11	Lens tube 4"	3	Thorlabs	SM1L40	169
12	Lens tube 2"	1	Thorlabs	SM1L20	21
13	C-Mount to SM1	1	Thorlabs	SM1A39	26
14	SM2 to SM1	2	Thorlabs	SM2A6	62
15	cage plate 1.2"	1	Thorlabs	CP12	26
16	Fold mirr.hold.	4			384
Optics					
17	Fold mirrors	4			64
18	PDM OKO 19ch.	1	OKO		16665
19	Science camera	1	Pixelink	A741	1400
20	microlens array	1	AOA		2000
21	2" col. lens	1	Thorlabs	AC508200AML	172
22	2" tel. lens	1	Thorlabs	AC508100AML	172
23	2" red. lens	1	Thorlabs	AC254100AML	123
24	1" red. lens	2	Thorlabs	AC254030AML	131
Electronics					
25	HV board	1			300
26	Teensy board	3	Teensy		77
27	FPGA board	1			600
28	Support computer	1	Apple		750
TOTAL (AUD)					24636

A.6 Pictures of details of the AO system

Different pictures of parts of the AO system are shown in this section.

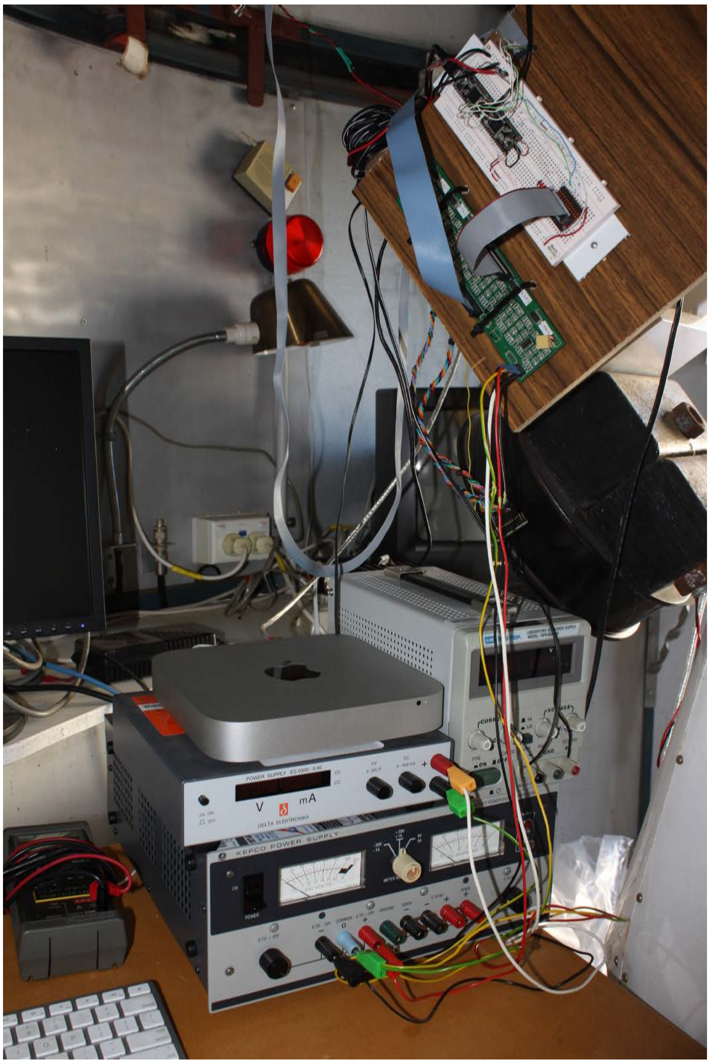

Figure A.13: Power supplies, support computer, high voltate DM driver board and interface boards.

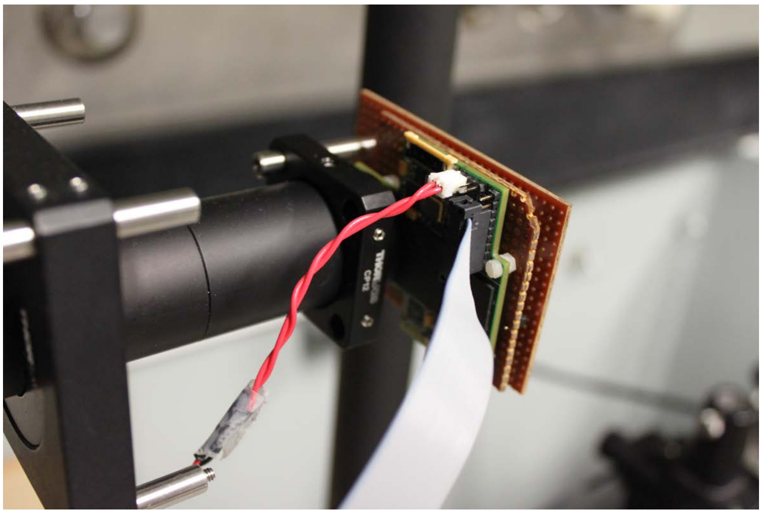

Figure A.14: WFS at the end of the tubular section of AO system. Power and data cables are connected to the FPGA board. The WFS can be rotated to get a adequate alignment with the microlens array.

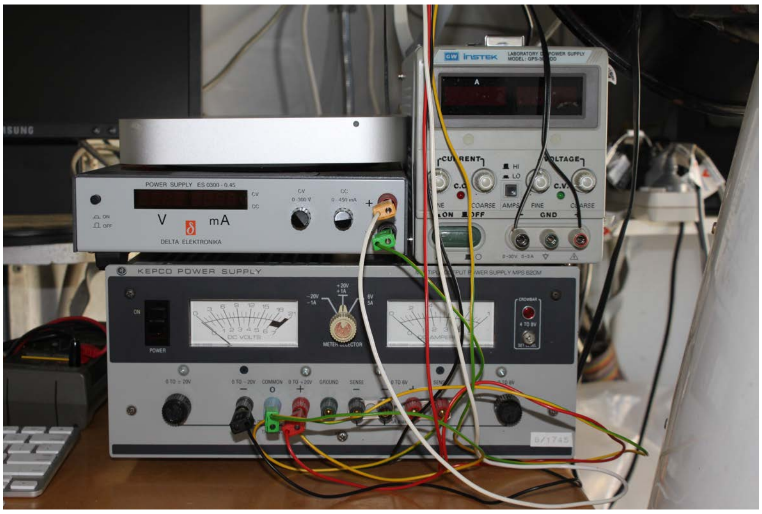

Figure A.15: Support computer (top left), High voltage power supply (below support computer), FPGA+CMOS image sensor board power supply (right of support computer) and Differential voltage power supply for operational amplifier stage of High voltage DM driver board (bottom).

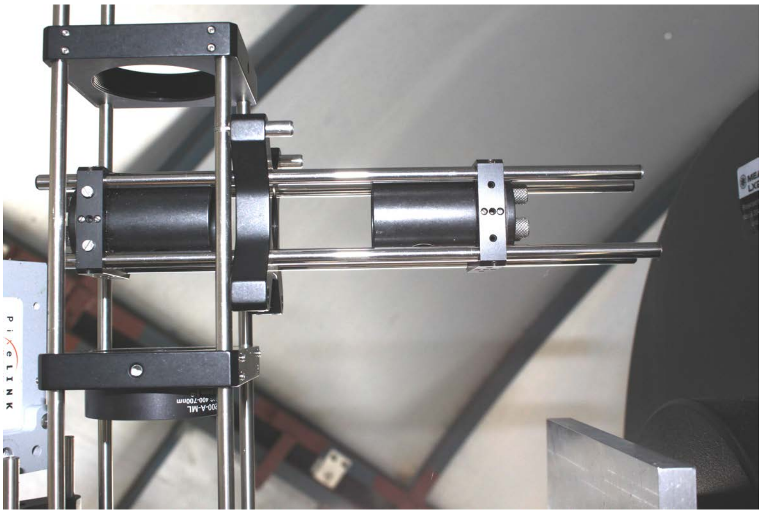

Figure A.16: 2nd and 3rd fold mirrors.

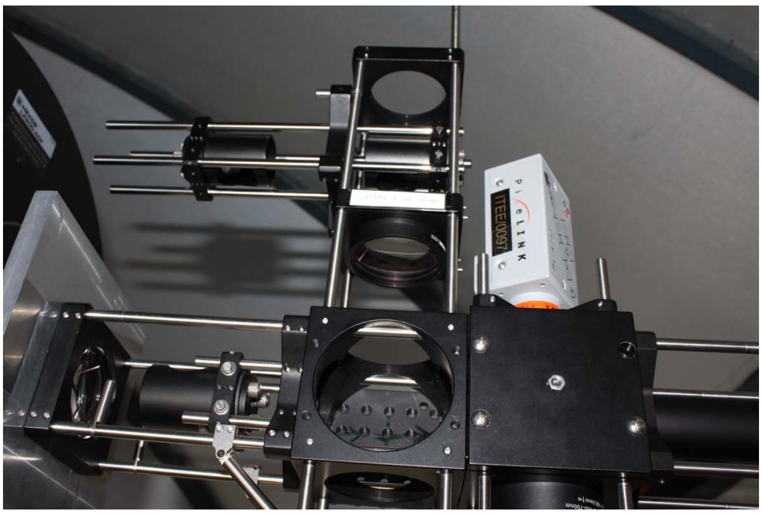

Figure A.17: Detail of 1st, 2nd and 3rd fold mirrors, collimation lens, beamsplitter (covered by platform attached to 2nd support cube) and science camera.

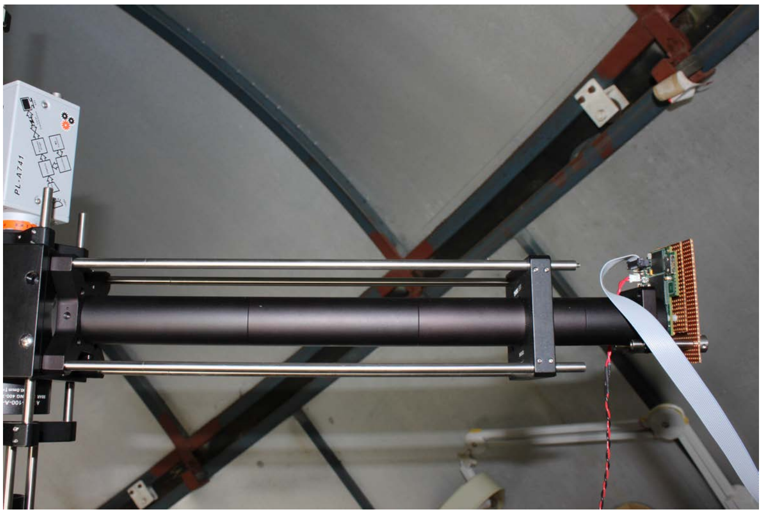

Figure A.18: AO opto-mechanical setup in a tube attached to 2nd support cube.

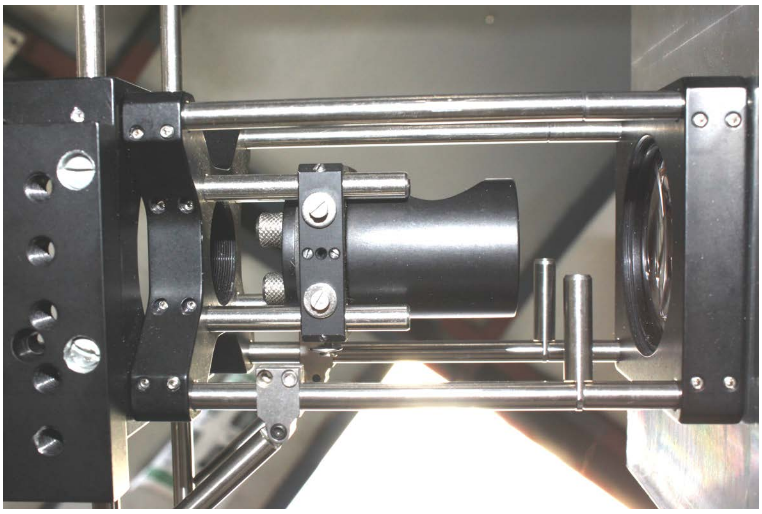

Figure A.19: Detail of 1st fold mirror. It can be rotated in increments of 90 degrees to use the telescope with other instrumentation, such as eyepieces or other cameras.

Figure A.20: AO testbed attached to 1 meter McLellan telescope in Mt.John Observatory (New Zealand).

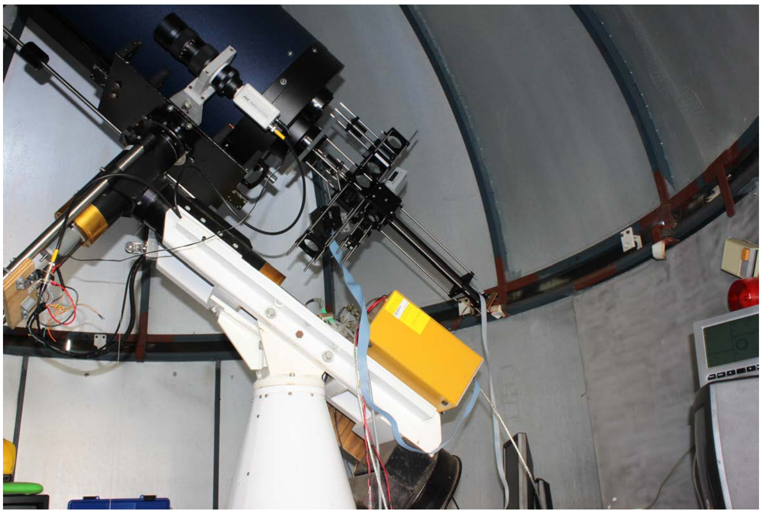

Figure A.21: AO testbed attached to 16" Meade LX200ACF telescope and tracking system (yellow box).